SORBONNE UNIVERSITÉ

THÈSE DE DOCTORAT
DE SORBONNE UNIVERSITÉ

Spécialité : Physique Quantique

École doctorale nº564: Physique en Île-de-France

réalisée sous la direction de Jean-Michel RAIMOND

au Laboratoire Kastler Brossel

Laboratoire Kastler Brossel
Physique quantique et applications

COLLÈGE DE FRANCE
1530

présentée par

Haiteng WU

Sujet de la thèse :

Millisecond-lived Circular Rydberg Atoms in a Room Temperature Experiment

soutenue le 8 décembre 2022

devant le jury composé de :

M.	ADAMS Charles,	Rapporteur
M.	BLOCH Daniel,	Examinateur
M.	GLEYZES Sébastien,	Membre invité
M.	GREFFET Jean-Jacques,	Rapporteur
M^{me}	MILMAN Perola,	Examinatrice
M.	RAIMOND Jean-Michel,	Directeur de thèse
M.	TIGNON Jérome,	President

0419082

Contents

List of Figures

Acknowledgement

This work would not have been possible without the help from my group, by which I mean everyone. I owe great thanks to all the critical ideas, inspirational discussions, and technical supports from the team's mentors and friends, to whom I shall express my gratitude.

The thesis has been an amazing journey for me. It was both the most unexpected and the most natural continuation of my education in physics: to study the atom of Bohr. It is remarkable to realize that this atomic state often associated with the founding of quantum physics is still a promising subject and an empowering tool. I have been more than fortunate to have my PhD work based on such beautiful and elegant system. For this, I must first and foremost thank Michel Brune, who admitted me as a member of the team. He is the paragon of a group leader, with an extremely humble demeanor which however never hides his brilliance. I deeply appreciate him inspecting E14 from time to time, offering guidance, morale, discussions and endless ideas.

I am indebted to Jean-Michel Raimond, the previous leader of the group and my advisor. He dragged me through the long months of the thesis writing, giving invaluable corrections and commentaries which had greatly improved the quality of my manuscript. I admire him for his sharp mind and sense of humor, which have made for countless engaging discussions in the group meetings.

The one single person who is absolutely indispensible for this experiment is my coadvisor Sébastien Gleyzes. It is eye-opening and inspiring to work with him, who always has an unexpected trick up the sleeve to solve the most challenging experimental difficulties. The mirror MOT scheme that defines this experiment came from him. Even during the COVID confinement of early 2020, when we could not do labwork, the sparks of thoughts never stopped owning to his regular online discussions with me and other PhDs. Before my defense, he also inspected my thesis, worked with me on my presentation, and offered many key advices.

I must thank Igor Dotsenko for programming my experiment control software. He is, on top of being an extraordinary experimental scientist, a great explainer. He has a striking talent to explain in plain languages and in fascinating details about any topic, be it a cutting-edge concept in physics or a fond memory of his early years in Ukraine. Last but not least, I benefited from valuable advices from Clément Sayrin. And I will not forget his warm help with my registration paperwork in my first year.

I have had the privilege to spend four years in Collège de France, sharing the same floor with many talented students and friends. I am grateful to the kindness of Arthur, who would always listen to my questions and genuinely try to help me. I vividly remember many moments with Rodrigo, a wonderful dude with insatiable curiosity about quantum mechanics and with inexhaustible energy to pursue science and other passions of his life. Then there's

Brice, he is as smart as he is dedicated, he talks softly but his work speaks thunders. I often recall Paul and his knack to simplify everything when explaining a topic. My beam-walking skill was trained by Rémi, who worked on the same experiment with me and figured out the right way to operate our laser system. I shared the same office with Andrea, our friendship made my most depressive times infinitely more bearable. In the same office, there was also Léa, who has admirable focus at work, and always trying to cheer everyone up during off time; Angelo, who plays the most enchanting guitar music; Baptiste, whose perseverance and resourcefulness at work led to the first Sr MOT in the group. I was constantly inspired by exciting results from E20's single atom arrays, enabled by Yohann's and Andrès' monumental code base. I feel happy to see the followup work of my own thesis, pioneered by Guillaume and Ankul. Finally, I have to thank Maxime and Zheng. As postdocs, they offered me valuable career advices.

I am deeply honored to have in my defense committee Pr. Charles Adams, Pr. Jean-Jacques Greffet, Pr. Perola Milman, Pr. Daniel Bloch, and Pr. Jérome Tignon.

I would also like to thank Pr. Serge Haroche, not only for his remote attendance during my defense, but also for his lecture notes from Les Houches 1990, which explained crucial points concerning the inhibition of spontaneous emission, the theoretical context of my thesis.

The work of this thesis was financially supported by China Scholarship Council, under the grant number CSC201806190206.

Finally, perhaps above all else, I thank my parents and my wife, for their unconditional love and support for my life's choices.

Notation

Listed below are some of the notations I use in this manuscript.

Constants

- c : Vacuum speed of light
- k_{B} : The Boltzmann cosntant
- ϵ_0 :Tthe vacuum permittivity
- h : The planck constant
- $\hbar = h/2\pi$: The reduced planck constant
- a_0 : The Bohr radius
- e : The elementary electric charge. $e > 0$ (an electron carries the charge of $-e$)
- $\alpha = (4\pi\epsilon_0)^{-1}e^2/(\hbar c)$: The fine structure constant

Acronyms

ARP Adiabatic Rapid Passage

AOM Acousto-Optic Modulator

BBR Black Body Radiation

CRA Circular Rydberg Atoms

FGR Fermi's Golden Rule

ITO Indium-Tin-Oxide

MOT Magneto Optical Trap

MW Microwave

rf radio frequency

TRP Total Radiated Power

UHV Ultra High Vacuum

Chapter 1

Introduction

The advent of quantum mechanics not only brought a complete [1] physical theory to describe the atomic scaled systems, but also revealed untapped resources we could take advantage of. The non-local entanglement between two quantum bits proved to be not only an asset in the long-distance quantum key distribution and teleportation [2, 3], but also a resource for quantum computation [4]. The development of modern technologies in the previous decades enabled the manipulation and detection of individual quantum systems [5, 6]. Exotic superposition states such as the squeezed states [7–9], or the Schrödinger-cat states [10–12] are used to build the quantum-limited sensors approaching the fundamental Heisenberg limit [13].

The success of quantum technologies brings the promise to build quantum machines [14] made of multiple coupled quantum objects to solve classically hard problems. These problems can have real life applications in network design or finance, such as the maximum independent (MIS) set problem [15, 16], which has the combinatorial complexity as the number of vertices grow in a graph. But more often than not, the problems to be solved are quantum ones, which have an exponential growth in computation complexity as a function of the system size. By today's standard, a quantum circuit computation task involving $\gtrsim 50$ qubits and a circuit depth of a few tens could be considered classically intractable [17]. While a fault tolerant universal quantum computer is still far from practical realization [18], tasks of this scale can already be undertaken by quantum simulators [19].

A quantum simulator produces analog results without digitally computing anything, much like a thin lens can carry out the Fourier transform of the incident light in its focal planes without really crunching any number. It is merely a controllable, modifiable, and measurable quantum system in the lab, built to emulate some other systems of interest. The latter systems are less accessible to direct study. For example, in the solids, electrons travel at a speed on the order of 10^6 m/s (Fermi velocity), the atom separations are sub-nanometer. Direct system detection would have to be repeated at least every femtosecond to barely capture electron transport. However, in an optical lattice, cold atoms (as surrogate electrons) move at a few mm/s, and the lattice potential wells are separated by a few hundred nanometers. Such a simulation system can play back the dynamics of the solids in a bloated millisecond time scale and an enlarged micrometer spatial scale, enough to be captured by an imaging camera. This leads to the successful observations of simulated quantum many-body phenomena such as Anderson localization [20] and Mott insulator [21].

The Hamiltonian engineering is another focus of the many-body quantum simulations,

during which every quantum bit is localized with controlled interactions between each other. The more widely simulated Hamiltonians are the spin models. In this category, the Rydberg atoms have long been proposed as excellent quantum bits [22–26]. These are highly excited atoms with long lifetimes ($\gtrsim 100\,\mu s$) and strong dipole-dipole interaction (a few MHz) over large separations (a few µm). In addition, the off-resonant interaction (either dipole-dipole or van der Waals) causes one excited Rydberg atom to shift the levels of another atom in a radius of typically $\approx 10\,\mu m$, preventing it from being excited by the same laser. This "Rydberg blockade" phenomenon is a very natural two-qubit controlled gate mechanism [27]. For implementing a controlled-phase gate, the qubit states $|0\rangle$, $|1\rangle$ can be encoded in two ground hyperfine levels. A "target" qubit initially in $|1\rangle_t$ gathers a phase of π (becomes $-|1\rangle_t$) after a 2π rotation between the ground state $|1\rangle_t$ and a Rydberg state $|r\rangle_t$. However, in the presence of a "control" qubit in the Rydberg state $|r\rangle_c$, the $|1\rangle_t \leftrightarrow |r\rangle_t$ transition is detuned from the laser, thus no phase is gathered for $|1\rangle_t$. The above controlled-phase gate was combined with single qubit Hadamard rotations to experimentally realize a two-atom controlled-not gate [28]. In this experiment, the two atoms are spaced by 10 µm, each trapped inside a far-off-resonant dipole trap with micrometer-sized trapping volume, the trapping laser being focused by high-numerical-aperture lenses. Such single atom dipole traps [29] are more commonly called optical tweezers in recently years. An array of optical tweezers can be achieved through shaping a laser beam's wavefront before focusing. The wavefront shaping can be done with a programmable spatial light modulator, which is an array of electrically controlled birefringence pixels. By this technique, two-dimensional neutral atom arrays are constructed. However, earlier demonstrations [30] of spin model simulation still suffered from non-deterministic loading of tweezer arrays due to light-assisted collision. This difficulty was removed by actively sorting the initially loaded atoms with dynamical optical tweezers [31]. Since then, defect free arrays of as many as > 300 atoms have been realized [32–34]. Subsequently, a number of impressive simulations have been demonstrated with this platform.

New phenomena are being revealed by the Rydberg qubit arrays. In an Ising-type spin chain simulation using ground-Rydberg qubits [35], the quantum many-body scars were observed as robust oscillations in a nine-qubit chain long after the system should have thermalized. This unusual violation of ergodicity in the presence of quenched disorder demonstrates a new universality class of quantum dynamics [36] that could be used to protect the coherence of a system. In another Ising-type simulation [37], the versatility of the programmable tweezer traps allow the adjustment of Rydberg blockade radius by setting the atomic lattice spacing. This results in a few new phases emerging in the experiment when the Rydberg blockade is extended beyond the nearest neighbors. The flexibility of the tweezer array generation does not only allow great scalability of the platform, but also brings possibility for new quantum simulation protocols. In a neutral atom quantum processor experiment [38], pairs of atoms are entangled using Rydberg blockade enabled controlled-phase gate. Afterwards, the qubit pair can be separated across a large region capable to host 2000 qubits. These entangled ancilla qubits can be shuttled to mediate entanglement between other qubits that never directly interacted. By this technique, a surface code state and a toric code state have been experimentally realized. The easy scalability of the platform already enables some classically intractable simulations. In a two-dimensional transverse-field Ising model simulation [39], defect free arrays of up to 196 atoms have been used to simulate the antiferromagnetic phase of the system, whereas the corresponding numerical simulation has to stop at ≈ 100

atoms before it becomes prohibitively resource heavy.

In the works mentioned above, two limitations are noteworthy. The first limitation is the lack of Rydberg atom trapping. The optical tweezer lights do not trap the Rydberg atoms (it even repels them), which become free as soon as they are created by laser excitation. The Rydberg interaction time is then limited to 10–20 μs even if the atoms were initially cooled to 10–20 μK. The second limitation is the Rydberg state lifetime, which is long, but still limited to typically 100 μs to 200 μs at room temperature (the condition for all the spin model simulations discussed above). To overcome the first limitation, one can either trap the Rydberg atoms using additional ponderomotive traps for low-field seekers [40, 41], or trap the ionic core of alkaline-earth Rydberg atoms using an optical tweezer, which also traps the ground state atoms before the Rydberg excitation [42]. Both are new techniques that could be implemented in spin model simulations in the near future. The Rydberg interaction time would then be longer than the Rydberg atom lifetime. The lifetime of a low-ℓ Rydberg atom, even at low temperature, is limited to typically $\lesssim 1$ ms by its optical spontaneous emissions. At room temperature, it is reduced even more by the 300 K blackbody radiation (BBR) induced transfers. The BBR induced errors in the long term can affect the gate fidelity of a fault-tolerant neutral atom computation platform [43]. In a recent experimental demonstration of the MIS quantum optimization [16], the BBR-induced violations of blockade is listed as one potential factor that limits this useful optimization, which essentially hinges on the Rydberg blockade mechanism [44]. The straightforward way to overcome the room temperature BBR is to move the platform to a cryogenic environment. There are already efforts towards this direction [34, 45]. In a 4 K environment, the low-ℓ Rydberg atom lifetime is expected to increase by a factor of 2 to 3 (depends on the n).

This 2- or 3-fold increase of Rydberg lifetime seems moderate. However, this is only for the low-ℓ Rydberg states. For the other Rydberg qubit with the potential for large-scale quantum simulations [26, 46, 47], namely the circular Rydberg atom, a 4 K environment can increase its lifetime by a factor of more than 50. Even in a 10 K environment, a lifetime in the range of a few millisecond is already reachable [48]. A circular Rydberg atom (CRA) is a Rydberg atom in the circular state, which has the longest lifetime among all the other Rydberg levels within the same manifold. It has only one weak MW spontaneous emission channel, which makes its lifetime much more sensitive to the number of BBR photons than the low-ℓ Rydberg states. In addition, a trait unique to the CRAs is that their single MW spontaneous emission channel can be inhibited by simple confinement structures [49–51], typically a plane-parallel capacitor. This would give rise to unprecedented interaction time in the range of seconds or more, which is intrinsically unreachable by the low-ℓ Rydberg atoms. A few simulation platforms of the CRA taking advantage of the inhibition feature have been proposed, such as shown in Fig. 1.1. Panel (a) is the proposal in [26]. In this poposal, the spontaneous emission inhibited CRAs in a cryostat are expected be able to simulate a Heisenberg XXZ model for seconds with a tunable interaction strength. With a chosen interacting strength of > 10 kHz, it would be possible to follow $\simeq 10^5$ spin exchange periods in a phenomenon with slow dynamics. Panel (b) is the poposal in [46]. In this proposal, the capacitor plates are glass plates with a layer of optically transparent and electrically conductive Indium-Tin-Oxide coating. This allows conventional optical tweezers to be implemented in a novel way, essentially threading the circular electron wave function with the tightly focused tweezer beam. The established dynamical tweezer sorting techniques can then be readily applied to construct defect free and trapped CRA arrays in 2D. The

proposal estimates a room temperature interaction time in the range of milliseconds, and a dipole-dipole interaction as large as 17 MHz for the high-n CRAs required for this trap. This leads to $\simeq 10^4$ to $\simeq 10^5$ cycles of a fast dynamics without a cryostat.

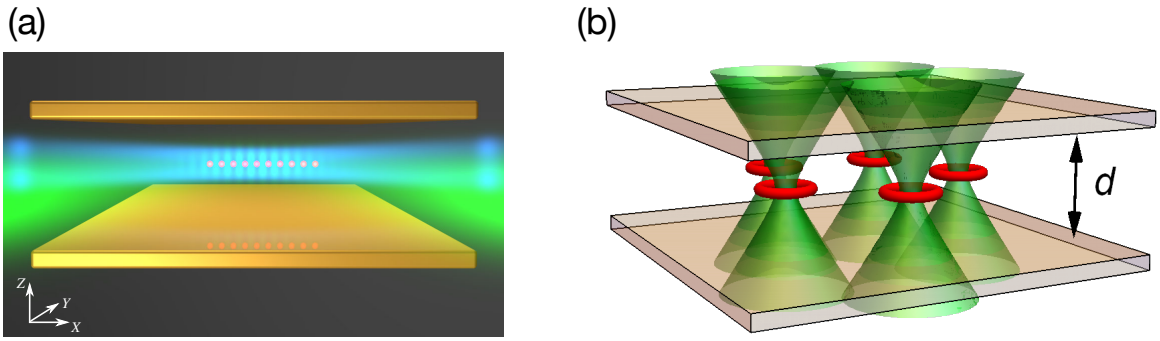

Fig. 1.1 *CRA simulation platform proposals. (a) Picture taken from [26]. Spin chain platform inside an inhibition capacitor. Single CRAs are trapped in the x direction by the fringes of two counterpropagating dipole trap beams, in the z and y directions by a Laguerre-Gauss hollow beam. (b) Picture taken from [46]. Two-dimensional array platform inside an inhibition capacitor. The tranparent electrodes enable the implementation of tweezers.*

One other unique advantage of these circular qubits is found when they are prepared from the alkali-earth elements with two valence electrons. In this case, the circular Rydberg electron is not susceptible to the auto-ionization [52], a known effect that the optically excited core electron exerts on a low-ℓ Rydberg electron. The alkali-earth CRAs thus retain an optically active and accessible core electron with potentially game changing applications. The optical transition could be used to cool the circular qubits during the runtime of a quantum simulation. The quadrupole interaction between the core electron and the circular Rydberg electron causes state dependent energy shifts in both [53]. This provides, on the one hand, the means for efficient or even QND detection of the circular Rydberg electron via optical imaging of the transition of the core electron, on the other hand, the individual MW addressability of the circular electron by optically switching the states of the core electron.

For applications in measurement and metrology, the Rydberg atoms are naturally ideal sensors of the electromagnetic fields. Being atoms, they possess stable and well-studied properties that require no calibration. The large dipoles of the Rydberg atoms couple strongly to the fields in the range from MW [54] to rf [55]. The quantum nature of these sensors allows Schrödinger-cat states to be prepared in a single atom to achieve quantum-limited sensitivity and ultra high spatial resolution at the same time [56]. In particular, the superposition of two circular states with their huge magnetic dipoles ($\simeq 50$ Bohr magnetons each) opposite in sign is a purely "circular" magnetic field sensor without any non-circular components. This "circular cat state" demonstrated a single-atom DC magnetic field detection sensitivity of $13.2 \pm 0.2\,\mathrm{nT}$, given an interrogation time of $20\,\mu\mathrm{s}$ in a cryostat [57]. The practical application of these atom-based sensors requires a miniaturized room temperature apparatus. In this scenario, the 300 K BBR becomes the limiting factor, preventing the circular cat state from existing for more than $\simeq 100\,\mu\mathrm{s}$. However, with a spontaneous emission inhibition structure, even at room temperature, this single-atom magnetometer could have an effective

interrogation time of over one millisecond [49]. The corresponding sensitivity would be less than 0.26 nT. The precise, space-resolved, and non-invasive magnetic field measurement can find real-world applications such as brain activity monitor and local mapping of fields in a nanodevice.

The increasing interest and accelerating advancement in the Rydberg technologies call for a solution to the limited atomic lifetime that would eventually become a bottleneck, limiting either the ultimate benchmark in a cryogenic environment, or the performance potential at room temperature. With this problem in mind, the work of this thesis demonstrates the inhibition of the BBR-induced transfers in a room temperature experiment to extend the lifetime of the CRA by one order of magnitude. The techniques developed in this work could contribute to overcome the lifetime bottleneck in both the experiments and the applications of the Rydberg technologies in the future.

1.1 This Work

In this thesis we experimentally realized a small-scale vapor cell experiment with excellent optical access. We prepared the CRAs from laser-cooled rubidium. We carefully characterized their lifetimes and reported for certain circular states a state-of-the-art lifetime of over 1 millisecond at room temperature.

The organization of this thesis is listed below.

Chapter 2 introduces the Rydberg atom as the quantum system we explore and exploit. The element we use in the experiment is the rubidium. Therefore, we first introduce the hydrogen model, which, paired with a model potential using the quantum defect theory, leads to the the rubidium model that we use. Afterwards, we show the principle of how we experimentally prepare the circular state. And finally, we discuss the theories regarding the characterization, derivation, and modification of the lifetime of the CRA. We put a particular stress on the mode density modification caused by a plane-parallel capacitor, and its utility in the inhibition of the decay channels of the CRA.

Chapter 3 includes all the experiment descriptions. In section 3.1, the whole setup itself was decomposed into different functional parts to be discussed separately, from the vacuum chamber to the magneto-optical trap. The central part of the experiment, the inhibition capacitor, is studied in simulation to examine the expected lifetimes of the CRAs inside it. With the composition of the experiment in mind, in section 3.2, we proceed to describe the experimental preparation of the CRA inside the plane-parallel capacitor. In this section, we first show the principle of state-selective ionization of Rydberg states. The ionization signal detected by this technique is the raw form of our data, from which we infer the state of the atoms. We then show the optimization procedures for both the field conditions of the experiment and the circularization adiabatic passage. This chapter concludes with the preparation sequences for the seven different circular states we prepare in this work.

Chapter 4 presents the data. The data is the time evolution snapshots of seven different circular states over a duration of up to 900 µs. The corresponding BBR-induced population redistributions follow from the Fermi's golden rule, and can be physically modeled by the rate equations. We thus build such a rate equation model and use it to fit a large amount of data. The obtained transition rates between the observed circular states can faithfully reproduce the dynamics in the complete data collection. From these rates we obtained the lifetimes

of the CRAs we prepared or observed in the experiment. The rates and the corresponding lifetimes reconstruct well in the frequency domain the cutoff feature of the parallel plate waveguide.

Finally, in the conclusion, we summarize this work and discuss its limitations. In addition, we give a brief account of a future experiment built to push the limit of the lifetime of a CRA to much larger values.

Chapter 2

The Quantum System: Rydberg Atom

A Rydberg atom is an atom with a highly excited electron, associated with a high principal quantum number[1] n. The atom concerned typically has one (H, Rb) or two (Sr, Ca) valence electrons. The gross structure of the atom is then given by the Rydberg formula:

$$E_n = -\frac{1}{n^2}\,\mathrm{Ry} \tag{2.1}$$

where we have used the Rydberg energy unit $1\,\mathrm{Ry} \approx 13.6\,\mathrm{eV}$, a value related to the Rydberg constant by a factor of hc. Some other systems (ion, molecule, semiconductor) with a Coulomb potential bound electron also share the same or similar Rydberg level series as in Eq. (2.1).

The simplest Rydberg system is a hydrogen atom. The essential Rydberg physics is all contained in the hydrogen model, which is discussed in section 2.1.

The quantum defect theory provides the energy corrections for the non-hydrogenic elements. The corrections for rubidium, the element used in this work, is introduced in section 2.2

In our experiment we characterize the lifetime of the circular Rydberg atoms (CRA). The principle of our circular state preparation method (circularization) is explained in section 2.3.

Finally, section 2.4 focuses on the theoretical framework of our lifetime measurement. In particular, we study the cases when a CRA's decay channels are inhibited, and the atomic lifetime is extended.

2.1 Hydrogen Atom

In a hydrogen atom, the single electron is bound by a time-independent Coulomb potential. Consequently, the wave functions of the electron found by the Schrödinger's equation are

[1] The Rydberg level series as defined by (2.1) was historically found to match precisely the hydrogen levels. Therefore an hydrogen atom, no matter the n, should always be a Rydberg atom if we stick to the textbook definition. Under modern context, alkali elements are more popular subjects of Rydberg experiments, these atoms' levels approximate that of hydrogen only at a relatively high n. We usually imply $n \geq 10$ when we refer to a Rydberg atom [58]. In addition, when dubbing an atom a Rydberg atom, we often imply other experimentally desirable high-n properties, e.g. the large coupling to the environment.

a series of stationary states. These states are the solutions to the corresponding time-independent Schrödinger's equation:

$$H\psi = E\psi \tag{2.2}$$

$$H = -\frac{\hbar^2}{2\mu}\nabla^2 - \frac{1}{4\pi\epsilon_0}\frac{e^2}{r} \tag{2.3}$$

in which $\mu = m_e/(1 + m_e/m_{core})$ is the reduced mass of the electron mass m_e and the core mass m_{core}. $r = |\mathbf{r}_e - \mathbf{r}_{core}|$ is the distance between the electron and the core. These substitutions allow us to reduce the two-body Hamiltonian to the form of Eq. (2.3), a single particle in a central potential.

The solution to (2.2) can be given in either the spherical basis (subsection 2.1.1) or the parabolic basis (subsection 2.1.2). The latter basis provides the necessary quantum numbers to describe the Rydberg energy levels in the presence of a DC electric field (subsection 2.1.3).

2.1.1 Spherical Basis

The solution to Eq. (2.2) under the Hamiltonian (2.3) is well known:

$$\psi_{nlm}(\mathbf{r}) = R_{nl}(r)Y_{lm}(\theta,\varphi) \tag{2.4}$$

$$R_{nl}(r) = \sqrt{\left(\frac{2}{na_0}\right)^3 \frac{(n-l-1)!}{2n[(n+l)!]}} e^{-r/na_0} \left(\frac{2r}{na_0}\right)^l L_{n-l-1}^{2l+1}\left(\frac{2r}{na_0}\right) \tag{2.5}$$

$$Y_{lm}(\theta,\varphi) = \sqrt{\frac{(l-|m|)!(2l+1)}{(l+|m|)!4\pi}} P_l^{|m|}(\cos\theta)e^{im\varphi} \tag{2.6}$$

in which $L_n^k(x)$ and $P_n^k(x)$ are respectively the associated Laguerre polynomials and the associated Legendre polynomials.

In the solution (2.4), a stationary state $\psi_{nlm}(\mathbf{r})$ is expressed in the spherical coordinates (r,θ,φ). This allows it to be separated into a radial part $R_{nl}(r)$ and an angular part $Y_{lm}(\theta,\varphi)$ (spherical harmonics). The three integer quantum numbers in the subscript completely determine the stationary state:

- n: The principal quantum number. It is the same n that indexes the gross structure in Eq. (2.1). For hydrogen without any core electrons, $n = 1,2,\ldots$.
- l: The angular momentum quantum number. $0 \le l < n$.
- m: The magnetic quantum number. $-l \le m \le l$

The high-m Rydberg states we focus on in this work are a simple system. The spin angular momentum quantum number $m_s = \pm 1/2$ can always be ignored, because the corresponding relativistic correction is small (kHz for $n = 50$). In addition, the MW and rf we apply to the atoms do not flip their spin states ($\Delta m_s = 0$ selection rule). The relative level transition frequencies do not change whether we start from a spin-up or a spin-down state, or a mixture of both.

Without considering the relativistic effect, the hydrogen eigenenergies E_n in the spherical basis are independent of l and m. The value of E_n coincides exactly with that given by the Bohr model ($E_n = -n^{-2}m_e c^2/2\alpha^2$), and has a n^2-fold degeneracy.

2.1.2 Parabolic Basis

The Schrödinger's equation (2.2) is also separable in the parabolic basis, which has a cylindrical symmetry and will be a more suitable basis to work with when a static external field is applied. The conversion between the parabolic basis coordinates (ξ, η, φ) and the Cartesian coordinates is given by:

$$\begin{cases} x &= \sqrt{\xi\eta}\cos(\varphi) \\ y &= \sqrt{\xi\eta}\sin(\varphi) \\ z &= \dfrac{1}{2}(\xi - \eta) \end{cases} \quad \begin{cases} \xi &= r + z = r(1 + \cos\theta) \\ \eta &= r - z = r(1 - \cos\theta) \\ \varphi &= \tan\dfrac{y}{x} \end{cases} \tag{2.7}$$

in which $r = (\xi + \eta)/2 = \sqrt{x^2 + y^2 + z^2}$.

The eigenstates in the parabolic basis are expressed as:

$$\psi_{n_1 n_2 m}(\mathbf{r}) = u_1(\xi)u_2(\eta)e^{im\varphi} \tag{2.8}$$

in which the form of the u_1 (u_2) depends on the three quantum numbers n, $n_1(n_2)$, m. The n, m here are the same quantum numbers as introduced in subsection 2.1.1. The two parabolic quantum numbers n_1, n_2, both being non-negative integers, satisfy the relation:

$$n = n_1 + n_2 + |m| + 1 \tag{2.9}$$

From the parabolic quantum numbers, the electric quantum number k is defined as:

$$k = n_1 - n_2 \tag{2.10}$$

2.1.3 Hydrogen Atom in External Electric Field

In the presence of a finite electric field $\mathbf{F} = F\mathbf{u}_z$. The Hamiltonian of a hydrogen atom reads:

$$H = H_{\text{zero}} + V_{\text{DC}} \tag{2.11}$$

$$V_{\text{DC}} = -\hat{\mathbf{D}} \cdot \mathbf{F} = -e\hat{\mathbf{r}} \cdot \mathbf{F} = -e\hat{z}F \tag{2.12}$$

in which H_{zero} is the zero field hydrogen Hamiltonian (2.3), $\hat{\mathbf{D}}$ is the electric dipole operator. Note that $e > 0$.

The interaction term V_{DC} shifts the bare eigenenergies of the zero field Hamiltonian H_{zero}, giving rise to the DC Stark shift. However, there is no analytical solution to this problem. One can instead seek a perturbative solution. The first order energy correction is found by limiting the diagonalization procedure within each n-manifold subspace. If we use the parabolic basis $|n_1,n_2,m\rangle$ in the process, we find that there is little to do: the perturbation term $\hat{z}$ is already diagonalized in the $|n_1,n_2,m\rangle$ basis for the first order correction. We can then use the approximate good quantum numbers n_1, n_2, m to label the shifted energy levels, or the "Stark levels", within one manifold. These Stark levels labeled by the parabolic quantum numbers are shown in Fig. 2.1.

In section 2.1.3.1, we introduce the most important Stark level in this work, the circular Rydberg level. In section 2.1.3.2, we discuss the higher order Stark corrections.

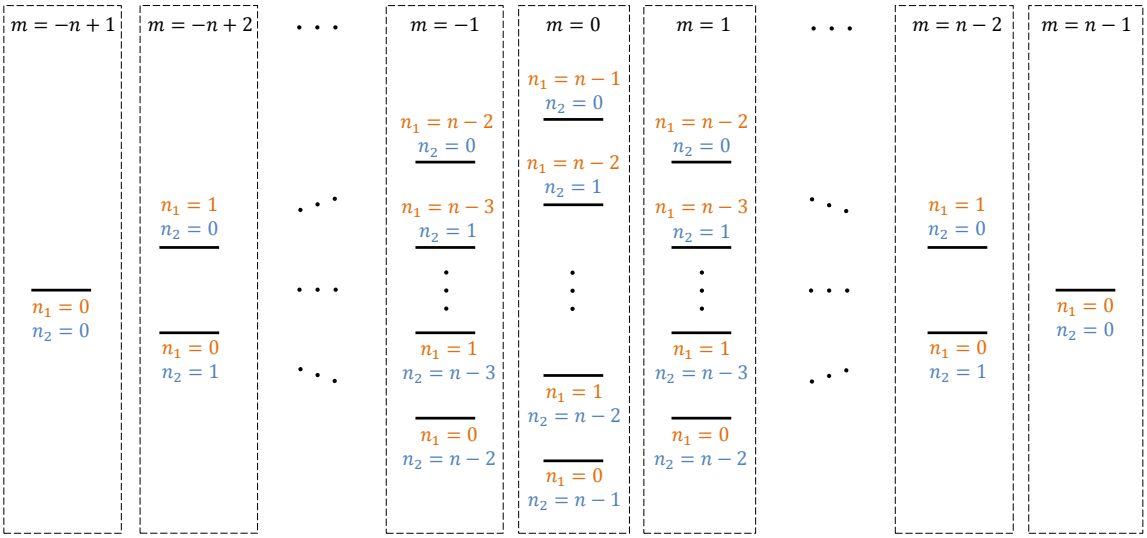

Fig. 2.1 *The Stark levels within one n-manifold are uniquely identified by the parabolic quantum numbers n_1, n_2, and the magnetic quantum number m. Notably the angular momentum quantum number ℓ becomes a bad quantum number and cannot be used to describe these Stark levels. Figure taken from [59].*

2.1.3.1 The circular state, the elliptical states

In Fig 2.1, a circular Rydberg level is the Stark level with the largest angular momentum along the quantization axis. Within one manifold this condition corresponds to the two levels at the two extremities of the Stark structure in Fig. 2.1. Due to the $\pm m$ symmetry of the Stark structure and the well-defined σ^+ polarization of our CRA preparation rf field (see subsection 3.1.1.4), the population in our system is confined in the $m \geq 0$ half of the manifold. Therefore, in this manuscript, we use the notation nC to unambiguously denote the Stark state $|n_1 = 0, n_2 = 0, m = n - 1\rangle$. The $m < 0$ half of the manifold and the other circular state $|n_1 = 0, n_2 = 0, m = -(n-1)\rangle$ never enter the picture. However, we note that one can explicitly prepare the superposition of both circular states for the application in magnetometry [57].

The wave function of the circular state nC has a simple form [60]:

$$\psi_{nC}(r,\theta,\varphi) = \frac{1}{\sqrt{\pi a_0^3}} \frac{1}{nn!} \left(-\frac{r}{na_0} \sin\theta e^{i\varphi} \right)^{n-1} e^{-r/na_0} \tag{2.13}$$

The probability distribution is localized inside a torus of radius $r_n = n^2 a_0$ and dispersion (thickness) $\Delta r_n = a_0 n^2/\sqrt{2n}$ in the $\theta = \pi/2$ plane. The torus's small angular dispersion in θ is evident from the $\sin^{n-1}\theta$ term in Eq. (2.13). The radial probability distribution of a $60C$ state is shown in Fig. 2.2, from which we see the reason for the name "circular".

For convenience, the other non-circular Stark levels in this manuscript are called the elliptical levels. The elliptical levels with the next highest m values after the nC are often discussed. Therefore we assign to them the short notations shown in Fig. 2.3.

The circular states are eigenstates in both the spherical and the parabolic basis. This

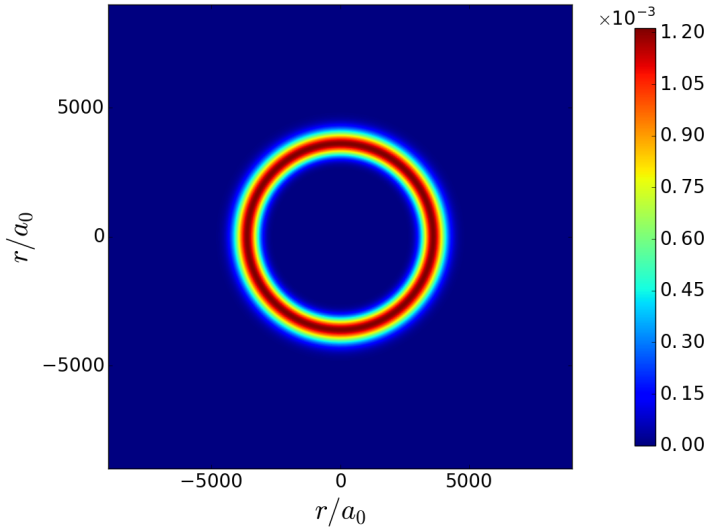

Fig. 2.2 *Radial probability of finding the outer electron of the* $60C$ *state of* ^{87}Rb. *Figure taken from [61].*

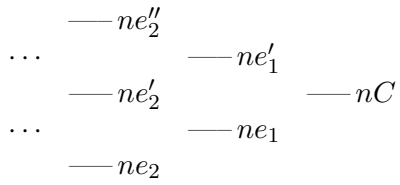

Fig. 2.3 *Notation assignment for the high-*m *states in the* n*-manifold. For an elliptical state, the subscript increases as* m *decreases. Primed states have higher energy than the unprimed*

however does not suggest that one can prepare a CRA in a zero field. The circular state is only stable in an external quantization axis field (electric or magnetic) [62]. If the magnitude of this directing field is reduced to ≈ 0, the corresponding Stark or Zeeman shifts are also vanishingly small, the slightest environment stray fields would cause an eigenbasis rotation faster than the system can adiabatically follow. Consequently, the pure circular state becomes a mixture. For this reason, we always apply a DC electric field to the atoms in the experiment.

2.1.3.2 Higher order Stark shifts

The perturbative expansion of the DC Stark energy correction up to the fourth order is given below:

$$E_n^{(0)} = -\frac{E_\mathrm{h}}{2n^2} \times F^0 \tag{2.14}$$

$$E_n^{(1)} = \frac{3ea_0}{2} nk \times F^1 \tag{2.15}$$

$$E_n^{(2)} = -\frac{(ea_0)^2}{16E_\mathrm{h}} n^4(17n^2 - 9m^2 + 19 - 3k^2) \times F^2 \tag{2.16}$$

$$E_n^{(3)} = \frac{3(ea_0)^3}{32E_\mathrm{h}^2} n^7 k(23n^2 - k^2 + 11m^2 + 39) \times F^3 \tag{2.17}$$

$$\begin{aligned} E_n^{(4)} = &-\frac{(ea_0)^4}{1024E_\mathrm{h}^3} n^{10}(5487n^4 + 35182n^2 - 1134m^2k^2 \\ &+ 1806n^2k^2 - 3402n^2m^2 + 147k^4 - 549m^2 + 5754k^2 \\ &- 8622m^2 + 16211) \times F^4 \end{aligned} \tag{2.18}$$

where we have used the Hartree energy unit: $E_\mathrm{h} \approx 27.2\,\mathrm{eV}$.

In the expansion, the zeroth order term Eq. (2.14) is the Rydberg formula (2.1). Eqs. (2.15), (2.16) respectively add to the Rydberg energies the linear Stark shift and the quadratic Stark shift. The circular state to the first order has zero electric dipole, and hence has zero linear Stark shift. The quadratic Stark shift experienced by the circular state has an intuitive classical interpretation [60]: For a circular state, the Stark field is a directing field (the quantization axis field) always perpendicular to the orbiting plane of the outer electron. The ionic core under the directing field is pushed slightly outside of the electron's orbiting plane, deviating from the zero dipole configuration and obtaining a dipole, proportional to the applied field. The induced dipole coupling gives rise to the quadratic Stark shift.

Experimentally, for the highly hydrogenic circular and the high-m elliptical states, the perturbative expansion up to the quadratic Stark shift is precise enough to predict the MW spectroscopy line shift in the regime of hundreds of V/m or less (error is less than the spectrum peak width). As a result, the quadratic Stark shift was often used as an easy means to quickly calibrate the directing field of the CRA.

Including higher order Stark shifts up to at least the fourth order is preferable when the involved field strength is approaching the ionization thresholds of the Rydberg atoms [63, 64]. This is also what we do in the calculation of the ionization signals (see subsection 3.2.1.2). Historically, the Stark shifts of the first three orders were easily obtained [65]. The fourth order shift posed a challenge. The correct form was not reached until 1974 [66]. The computer aided method was then developed to carry out the expansion to as high as twenty-fifth order [67]. But this effort was mainly to prove that the expansion should not be carried out too far, because this perturbation series is asymptotic and non-convergent.

The perturbative expansion is useful for a fast evaluation of high-ℓ Rydberg energy spectrum at relatively low fields. But when the field is large and level crossings between different terms occur, the better-suited method to comprehensively study the Stark structure of the Rydberg states is the diagonalization of the full energy matrix [63].

2.2 Rubidium Atom

The rubidium isotope ^{85}Rb is used throughout this work. It is a more abundant isotope than the other one, ^{87}Rb. Unlike hydrogen, ^{85}Rb has a ground state with $n = 5$. When its valence electron is excited to the Rydberg levels, there remains a sizable ionic core composed of 36 electrons, 37 protons, and 48 neutrons.

For a hydrogen Rydberg atom, its core is nearly point-like. A single proton's charge provides the $-e^2/r$ Coulomb potential. However, for a rubidium Rydberg atom, its low-ℓ electron wave functions can partially penetrate the non-negligible spatial extension of the core. The classical analogy is a highly elliptical orbit that has a perihelion very close to the core. In this case, the many protons' charge are not completely screened by the core electrons. As a result, the outer electron feels a stronger potential of $-Ze^2/r$. A Rydberg state with a higher angular momentum, on the other hand, has a less elliptical orbit and less wave function overlapping with the core. It thus deviates less from a hydrogenic Rydberg state. The global effect is that the low-ℓ Rydberg states have lower energy than rest of the levels in the same manifold. This breaks the n^2-fold degeneracy of the hydrogen model, and is known as the quantum defect.

The ℓ dependency of the core penetration effect can be described by assigning an ℓ-dependent effective principal quantum number $n_{\text{eff}} < n$ to a hydrogen Rydberg level. The eigenenergy of the level then becomes smaller:

$$E_{nlj} = -\frac{1}{n_{\text{eff}}^2}\,\text{Ry} \tag{2.19}$$

$$n_{\text{eff}} = n - \delta_{nlj} \tag{2.20}$$

where δ_{nlj} is the phenomenological quantum defect constant, j is the total angular momentum (orbit plus spin) quantum number. δ_{nlj} is expressed by an expansion:

$$\delta_{nlj} = \delta_0 + \frac{\delta_2}{(n-\delta_0)^2} + \frac{\delta_4}{(n-\delta_0)^4} + \cdots \tag{2.21}$$

in which all δ_i's are constants that depend on l and j. For high-n levels, the fist two terms in Eq. (2.21) provide a good approximation of δ_{nlj}. The constants δ_0 and δ_2 are reported in various sources. A summary of their values can be found in the thesis of E. K. Dietsche [59].

The quantum defect of the Rydberg states is only weakly dependent on n and j, compared to its strong l dependence. The levels are approximately hydrogenic when their quantum defect is much lower than 1. This approximation starts to be correct for $l = 3$ ($\delta_{nlj} \approx 0.016$) and becomes increasingly accurate as l rises. With the quantization axis field we routinely apply to the atoms, the corresponding Stark shifts (a few hundred MHz) are at least larger, if not much larger, than the quantum defect shifts for $l > 4$ (a few tens of MHz for $l = 5$). For this reason, in this work we consider the levels with $l > 4$ to be hydrogen-like.

In Fig. 2.4, we plot the $m_j = 1/2$ energy levels of the $n = 52$ and $n = 60$ manifolds of ^{85}Rb in the field range of 350 V/m. In this work, all the atomic state manipulations are performed below this field. The chosen energy range is enough to show the $l = 3$ levels of both manifolds. On the left of the figure, the 52-manifold is representative of the usual $n \approx 50$ Rydberg manifolds in which the CRAs are prepared in many important works [68]. Going higher in n brings the advantage of larger atomic dipole and lifetime. At the same

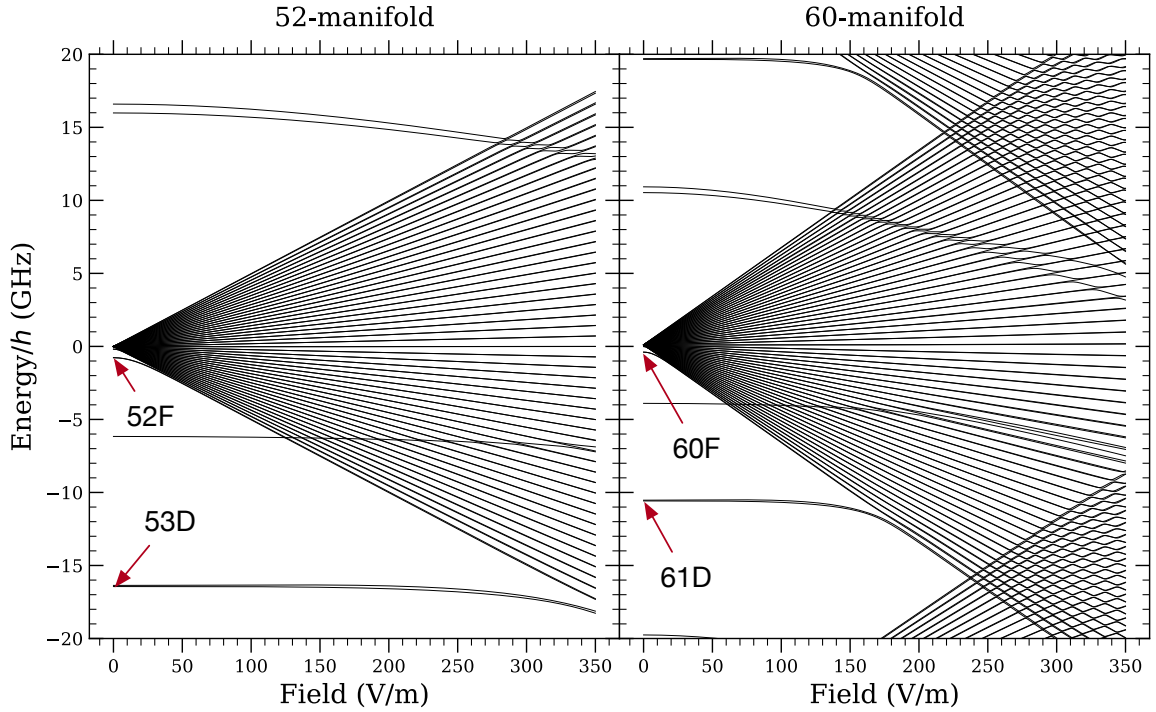

Fig. 2.4 *Numerically calculated* ^{85}Rb *levels with* $m_j = 1/2$ *as a function of the electric field. The reference energy is chosen to be the degenerate high-*ℓ *manifold levels at zero field for both* $n = 52$ *and* $n = 60$.

time, the increased sensitivity to stray fields limits one from operating at an arbitrarily high n. The $n \approx 50$ region is a compromise between the two conflicting requirements [60]. On the right of the figure, the 60-manifold is representative of the high-n Rydberg manifolds we experimentally access in this work. This is for accessing the tighter level spacings higher in the Rydberg gross structure, where the atomic decay transitions are effectively inhibited in our setup. Comparing the two manifolds, we see that the effect of the quantum defect is less at $n = 60$. On the other hand, the level crossing between the neighboring manifolds start at a smaller field. In both plots, the high-l levels shift linearly as a function of field. The quantum defect shifted D and F levels exhibit a quadratic Stark shift before joining the manifold. This is because when the off-diagonal energy matrix elements ($e\hat{z}F$) are less than the quantum defect energy shifts in the diagonal elements, the first order Stark shift does not emerge.

2.3 Reaching Circular State through Adiabatic Rapid Passage

A CRA with both a high n and a high m is prepared in two steps from the ground state. In a first step, the laser excitation increases the n; in a second step, a rf multi-photon adiabatic rapid passage (ARP) increases the m. The scheme of these two steps is shown in Fig. 2.5 for the preparation of $52C$ in a $n \approx 50$ manifold. Considerations for circularization in a $n \approx 60$ manifold will follow the discussion of the $n \approx 50$ case.

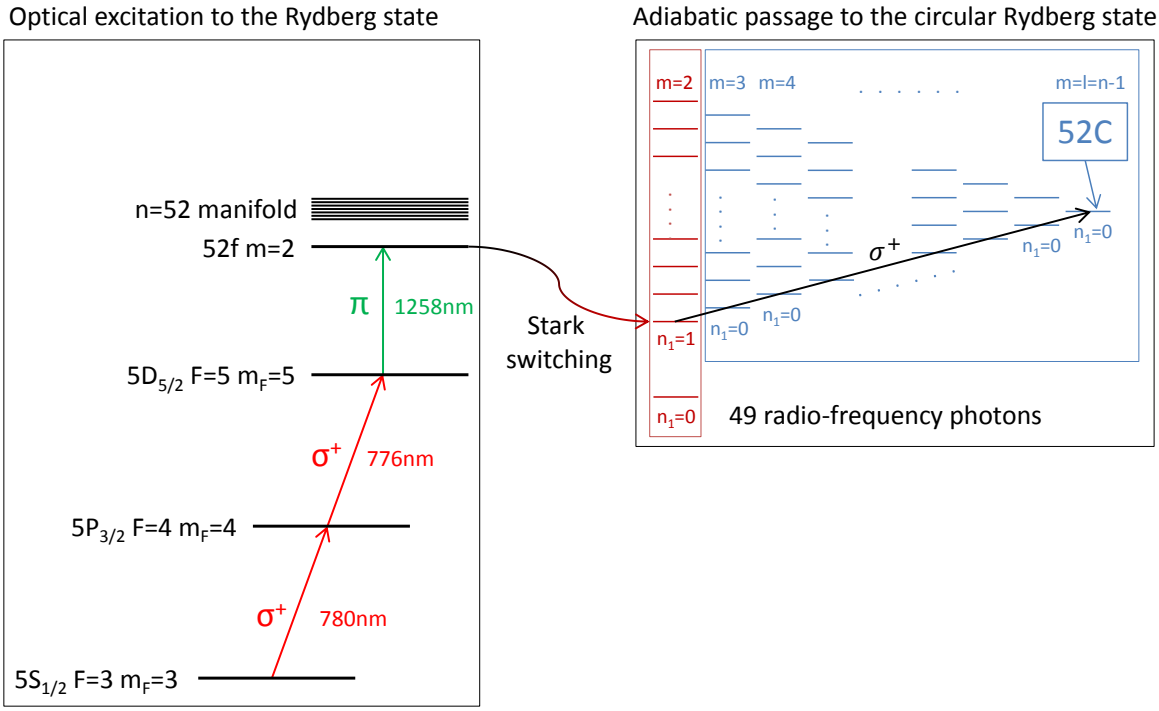

Fig. 2.5 *CRA prepration scheme: laser excitation, Stark switching, and the ARP. During the ARP stage, the absoprtion of 49 rf photons is accompanied by a down-ramped electric field (the Stark level spacings are continuously varied). Figure taken from [59].*

In the figure, the three-stage laser excitation provides the three photons needed to access the 52 F level. In the presence of a small Stark field (a few tens V/m), the degeneracy of the 52 F multiplicity is lifted. One can then choose specifically to excite the atom to the $|52\,\mathrm{F}, m = 2\rangle$ level, which, after switching to a high field (a few hundred V/m), is adiabatically connected to the $|n_1 = 1, m = 2\rangle$ Stark level. Afterwards, a σ^+-polarized rf field is applied. The pure polarization of the rf allows it to couple only the lowest diagonal levels in a Stark manifold. In this subspace, the 50 levels from $m = 2$ to $m = 51$ form an approximately harmonic ladder in the field range from at least 150 V/m to 250 V/m. They are at the same time very detuned from the last two lowest diagonal levels $|n_1 = 1, m = 0\rangle$ and $|n_1 = 1, m = 1\rangle$. In the previously given field range, down-ramping the field decreases the linear Stark shifts between the ladder levels. In the presence of a constant rf dressing frequency of 230 MHz, the ladder comes cross the resonance with the rf at[2] 230 V/m. This is equivalent to chirping the rf frequency through the ladder resonance while keeping the Stark field constant. In both cases, an adiabatic passage is accomplished. In this process, the atom absorbs 49 rf photons, each providing an increase in the angular momentum by $\Delta m = 1$. At the end of the ARP, the atom reaches $52C$.

It is more demonstrative to show the ARP in the dressed picture (Fig. 2.6). In the figure, from (a) to (b) we show the transition from the bare atom basis to the dressed atom basis.

[2] A unique property of the 52-manifold is that its linear Stark shift [0.998 MHz $(\mathrm{V/m})^{-1}$] is almost exactly 1 MHz per 1 V/m.

The latter is composed of the uncoupled atom-(rf)field levels $|k,N\rangle$, where k is the electric quantum number [Eq. (2.10)], proportional to the linear Stark shift of each bare atomic level. For the Stark structure's lowest diagonal levels involved in the ARP, each level is uniquely denoted by a $|k\rangle$ index, which also intuitively represents the level's linear Stark shift. The other index $|N\rangle$ denotes the Fock state of the rf field. We choose N to be 0 for the circular level $|k = 0\rangle$. Under this choice, for any uncoupled basis vector $|k,N\rangle$, the two indices in the ket satisfy $k + N = 0$. To obtain the energies of the dressed basis in (b), it consists in up-shifting each energy line of the bare basis in (a) by an amount of $N \times h \times 230\,\text{MHz}$. When the rf coupling is switched on in (c), an anti-crossing appears between the high field and the low field. When one scans the electric field through the anti-crossing, the lowest level in the ladder connects exactly to the highest circular level.

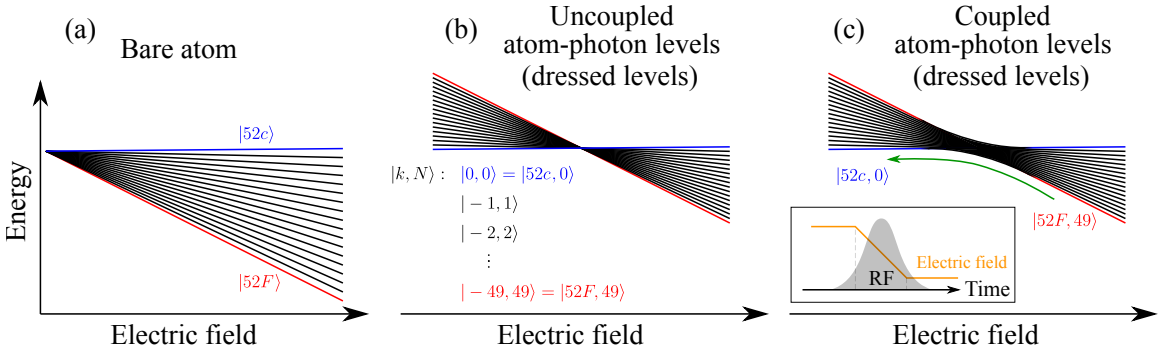

Fig. 2.6 *ARP in the dressed picture. (a) The 50 lowest diagonal levels of the 52-manifold in the bare picture as a function of the Stark field. (b) The same levels in the dressed picture (or in a rotating frame spinning at frequency* 230 MHz*) without the rf (c) The* 230 MHz *σ^+-polarized rf dressing field is switched on. An anti-crossing connects the lowest level and the highest level in the ladder. Figure taken from [69]*

The process of an ARP lasts only a few microseconds. It has been demonstrated that in the presence of a constant rf Rabi frequency of 3 MHz (equal to the level spacing at the anti-crossing), a 1.5 µs field down-ramping is enough to yield an ARP circularization efficiency of 98% in the 51-manifold [70]. In the presence of a varying rf Rabi frequency, a 1.5 µs down ramp has an estimated circularization efficiency of 99.5% [71].

We are interested in the Stark shift variations of the ARP ladder during the ramp. Therefore, we plot the Stark shifts of the $m = 0$ to $m = 6$ levels, and the corresponding $\Delta m = 1$ transition frequencies between these levels as a function of field. These numerical results are shown in Fig. 2.7. The plots in the first and second column show the levels respectively in the 52-manifold and the 60-manifold, the latter being an example of a high-n manifold that poses additional problems during circularization.

In the figure, we see that the $0 \leftrightarrow 1$ (black) and $1 \leftrightarrow 2$ (blue) transitions are greatly detuned from the rest of the transitions, therefore they never join the ARP. In the 52 manifold (bottom left plot). The higher transitions, the $3 \leftrightarrow 4$, $4 \leftrightarrow 5$ and $5 \leftrightarrow 6$, exhibit the hydrogenic degeneracy, since the concerned levels are higher in angular momentum. Transitions involving $m \geq 7$ are not plotted, since they will have the same hydrogenic behavior. The 98% circularization efficiency reported by A. Signoles et al. [70] is achieved with an ARP

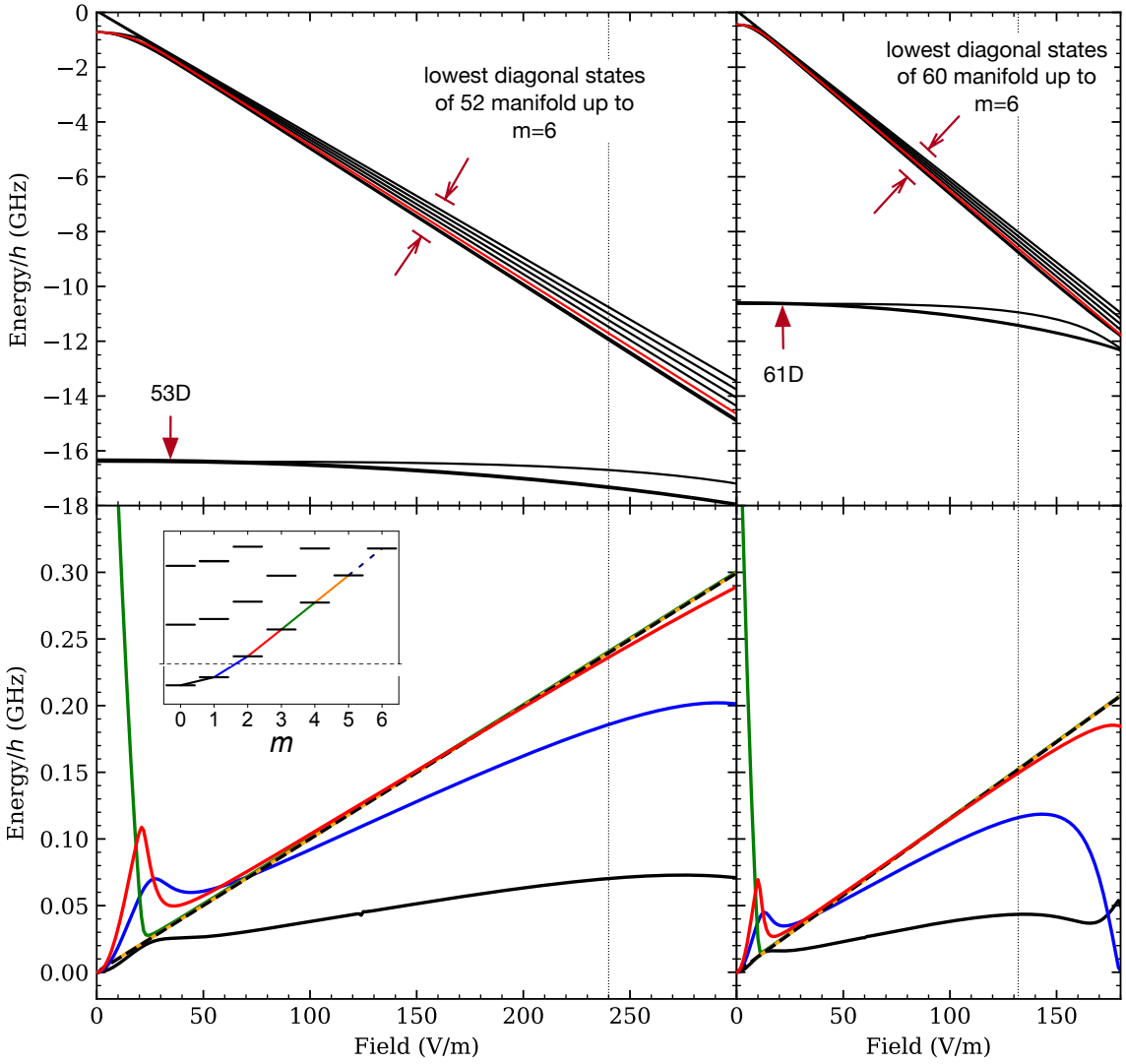

Fig. 2.7 *Numerically calculated first few lowest diagonal states of 52-manifold and 60-manifold as a function of electric field. First row: Stark shifts of the fisrt 7 lowest diagonal levels in the 52-manifold and the 60-manifold. The chosen field range ends before the D levels join the manifold. The reference energy is chosen to be the $m = 6$ level at zero field for both manifolds. The starting level of the ARP, the $|n, n_1 = 0, m = 2\rangle$ state, is colored red. Second row: the nearest-neighbor transition frequencies between the 7 levels of both manifolds in the same field range. The inset shows the color code for the transitions. The two vertical dashed lines mark the fields where the $2 \leftrightarrow 3$ transition (red curves in the second row) is detuned by 3 MHz from the higher transitions.*

that starts with a +10 MHz detuning from the 230 MHz rf dressing field, and ends with a symmetrical detuning of −10 MHz. Assuming the same dressing rf in the 52-manifold, the +10 MHz detuned field is found at 240 V/m (vertical dotted line on the left). The $2 \leftrightarrow 3$ transition at this field is detuned by 3 MHz from the rest of the ladder. The same 3 MHz detuning corresponds to a field of 130 V/m in the 60-manifold (vertical dotted line on the right). Therefore, a similar ARP carried out in a higher manifold should start the down ramp at a lower field. If the starting field is too high, the consequence is clear: the $m = 2$ level, the starting level of the ARP, would break away from the rest of the ladder. Correspondingly, the dressing rf of the ARP should have a lower frequency so that the anti-crossing appears at a field below the dashed line threshold in the figure.

The message obtained from the above comparison is relevant in this work, because we routinely perform the circularization ARP at a relatively high manifold with $n = 58$.

2.4 Lifetime of the CRA

The *lifetime* of an atom, or more specifically the lifetime of an excited atomic state, is the natural exponential relaxation time for the atom to leave that state. Note there are situations in which an atom does not experience the usual exponential relaxation of its excited levels, notably when it is strongly coupled to a single mode of a high finesse cavity [72]. In this case the *vacuum Rabi oscillation* takes place, the atom and the cavity become an inseparable whole, and the concept of a relaxation lifetime for an isolated atomic state does not apply. Therefore by considering the lifetime of the atom, we automatically put us in the perturbative regime where the atom is only weakly coupled to its environment.

All environmental parameters must be completely specified to determine the lifetime of an excited level. We consider in particular three relevant conditions in this work: the environment temperature, the physical boundary limitations set on the field, and the atom's relative position to these boundary conditions. With all conditions constant, the atomic population leaves the initial state with a constant rate Γ_{at}, the atomic lifetime τ_{at} is then defined to be the inverse of this rate:

$$\tau_{\text{at}} = \Gamma_{\text{at}}^{-1} \tag{2.22}$$

The rate Γ_{at} is a total rate that is the sum of the decay rates Γ_i's through individual decay channels: $\Gamma_{\text{at}} = \sum_i \Gamma_i$. In the regime where the non-radiative decays, e.g. collisions, are always negligible, then these individual Γ_i's are attributed to either the spontaneous emission or the stimulated emission and absorption induced by the blackbody radiation in a finite temperature environment (we will call both a *stimulated decay* when discrimination is not necessary, with the agreement that a general *decay* can go either upwards or downwards in energy). For a low-n atomic state, the stimulated decay rates are negligible, because all the decay transitions are optical, the optical thermal photon number $\ll 1$ and induce negligible stimulated decays. The resulting lifetime is only limited by the spontaneous emission channels. Early atomic lifetime measurements are mostly in this category [73, 74], and the lifetime measured is called the *radiative lifetime*. Sometimes we also see the terms like *natural radiative lifetime* [75] or *spontaneous radiative lifetime* [76] used to stress the spontaneous-emission-limited nature of the concerned lifetime. In measurement, the radiative lifetime can be strictly obtained via a simple exponential fit $e^{-\Gamma_{\text{at}} t}$ to the state population signal (e.g.

fluorescence intensity or ionization counts) as a function of time. And the exponential fit is set to converge at infinite time to zero population (or otherwise a known baseline of the experiment), due to the irreversible nature of the spontaneous emission.

However, for a Rydberg state, the rate contributions from the stimulated decays usually can not be ignored. This is well demonstrated in Fig. 2.8, in which all the individual decay rates from the $60\,S_{1/2}$ state of ^{87}Rb are shown in a bar plot to compare their relative contributions. The figure notably shows that at 300 K, more than half of the $60\,S_{1/2}$ decay rate comes from the stimulated decays, which in comparison are negligible at a low temperature. This phenomenon is caused by the abundance of the room temperature blackbody radiation thermal photons in the microwave range in which lie the typical separation frequencies between the neighboring high-n Rydberg levels: the highest two rates connecting the $60\,S_{1/2}$ to the 59P and the 60P states correspond to decay transition frequencies of $\simeq 20\,$GHz. At this frequency and at 300 K there are $\simeq 300$ thermal photons per mode. It is important to note that Fig. 2.8 shows only the first step decay. The rapidly populated 59P and 60P, for example, are still high-n Rydberg levels susceptible to the same hundreds of room temperature thermal photons which keep transferring them to the adjacent nS and nD levels, which are still Rydberg levels.... The multiplication of the populated Rydberg levels plus the directionless thermal photon transfer, i.e. the stimulated emission *and* absorption at equal rates between two levels, complicate the dynamics.

Since the stimulated decay rate is still a constant rate, formally any stimulated decay *away* from the initial level still contributes a generic Γ_i to the total $\Gamma_{\rm at}$, the lifetime definition Eq. (2.22) thus does not need to change for the Rydberg levels. But a simple one-level "radioactive" decay $e^{-\Gamma_{\rm at}t}$ can not correctly model the target state evolution anymore. Instead a complete rate equation model to include at least the significantly populated levels is needed. If the populations of the significant levels can be measured individually, the lifetime conforming to Eq. (2.22) can be strictly obtained. This is typical of a circular Rydberg state [48, 49]. On the other hand, if the BBR populated levels can not be measured separately to feed a multi-level rate equation model, one can still try an exponential fit to the target state population and obtain an exponential t_1 as a characteristic lifetime, but this lifetime does not conform to Eq. (2.22) and is dependent on the choice of the time span of the data. This is typical of a low-ℓ Rydberg state [77–79]. In the literatures, Gallagher and Cooke [80] gave the first notable acknowledgment to the BBR photons' effect to the lifetime of the Rydberg atoms. They called the effect a "reduction of the radiative lifetime". The term "radiative lifetime" has been ever since avoided to describe the Rydberg state lifetime when the BBR photons are not negligible. In this case, some use the term *effective lifetime* [76, 81] to explicitly refer to a BBR-influenced Rydberg lifetime conforming to Eq (2.22).

In general for the Rydberg atoms, the word "lifetime", alone without context, does not necessarily mean Eq. (2.22). However, when attainable, such as in this work, Eq (2.22) should be the most desirable definition of the lifetime since every individual rate Γ_i, spontaneous or stimulated, is physically a well defined rate from a time-dependent perturbation treatment to the first order (the *Fermi's golden rule*, or *FGR*) [82, 83].

In this section, we first introduce the lifetime-limiting decay rates for the Rydberg atom in subsection 2.4.1. Then we turn to the mechanisms to modify the decay rates, in particular, the waveguide structures can cause decreased mode density for the atomic decay channels below the cutoff frequency, these are discussed in subsection 2.4.2. The lifetime of the CRA in free space is examined in subsection 2.4.3. Finally, the lifetime of the CRA in a plane

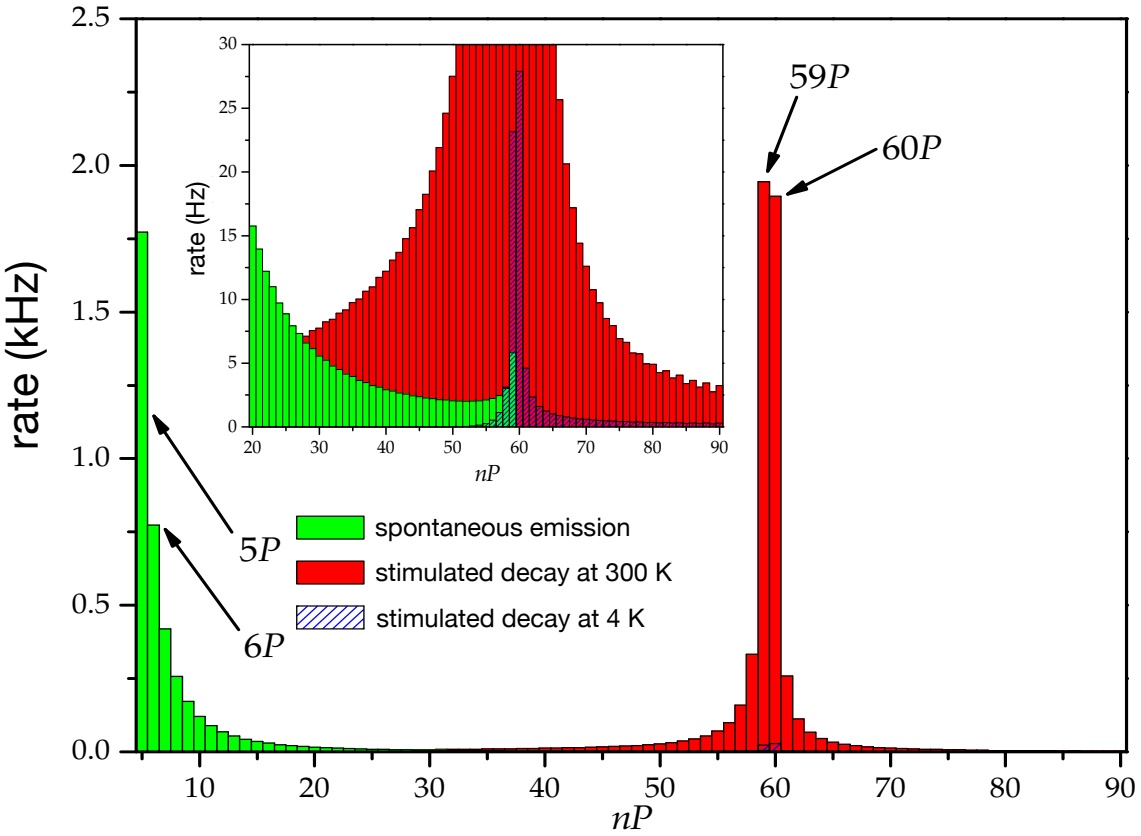

Fig. 2.8 *All the decay channels of the* $60\,S_{1/2}$ *state of* ^{87}Rb. *For* $60\,S_{1/2}$, *every decay channel ends in a* $n\mathrm{P}_{1/2,3/2}$ *state due to the selection rules. The plot shows the sum of the decay rates to* $n\mathrm{P}_{1/2}$ *and* $n\mathrm{P}_{3/2}$ *as one bar at* n. *The green, red, and striped bars represent the decay rates contributions respectively of the spontaneous emission, the stimulated decay at 300 K and 4 K. The inset is the same plot zoomed onto the high-*n *spontaneous emissions and the low temperature stimulated decays. Figure taken from [61] with adapted in-figure text.*

parallel capacitor structure that is pertinent to this work is analyzed in subsection 2.4.4.

2.4.1 Rates of Spontaneous Emission, Stimulated Emission, and Stimulated Absorption

Even in a perfect vacuum and at absolute 0 K, the lifetime of an excited atomic state is still limited by the spontaneous emission downwards from that state. A classical and a quantum effect contribute separately to this fundamental emission [84, 85]: The electron has a self-interaction with its own field (classical radiation reaction effect); the quantum fluctuations of the vacuum perturb the excited state. At the ground level however these two effects cancel out each other [86–88], giving rise to the radiative stability of atomic ground states.

On the one hand, the spontaneous emission rate can be obtained by considering the dipole couplings between the atom and all possible modes of the emitted photon. On the other

hand, the stimulated emission and absorption rates between two levels can be obtained when the field energy density at the level transition frequency is known. Assuming the known energy density is that of the thermal field, these stimulated rates are then related to the environment temperature by the Planck law. Whether spontaneous or stimulated, obtaining one leads to the other, because all these rates are correlated in the Einstein rate equation, which describes the thermalization between the atom and the environment.

2.4.1.1 The spontaneous emission rate

Historically, to characterize the intensity of the spontaneous emission phenomenon, Einstein in 1917 introduced in his rate equation a phenomenological coefficient A as the *spontaneous emission rate*, a quantity meant to be an intrinsic property of the atom. However, the A rate is not a constant, as discovered by Purcell [89]. In the presence of a cavity tuned on-resonance with a two level system, the spontaneous emission between the two levels is enhanced. This realization that the atomic lifetime is not a property of the atom itself but one of the coupled atom-field system is the starting point of the cavity quantum electrodynamics (CQED).

It thus does not change the nature of the problem whether we consider the atomic lifetime in free space or in a waveguide structure. In both cases, the field modes are propagation modes, and the spontaneous emission can be interpreted as the atom coupled to all the available propagation modes. These modes are classical modes obtained conventionally by assuming translational symmetry in space and then setting the periodic boundary conditions for propagation wave vector $\mathbf{k}$ in a virtual box of an arbitrary volume V. The $\mathbf{k}$ would then naturally take only the quantized values in a box, knowing that in the limit of a very large V, the quantized $\mathbf{k}$'s can always be as closely spaced as one needs. This discretization in a box gives rise to a set of field eigenmodes $\boldsymbol{\alpha}_{\mathbf{k},\varepsilon}(\mathbf{r})$, each $\boldsymbol{\alpha}_{\mathbf{k},\varepsilon}(\mathbf{r})$ is completely determined by the pair of indices $(\mathbf{k},\varepsilon)$ indicating the wave vector and the global structure of the eigenmode. With this eigenbasis, the decomposition of any real and sourceless field $\mathbf{E}(\mathbf{r},t)$ is equivalent to the expansion of its positive frequency part[3] $\mathbf{E}^{+}(\mathbf{r},t)$ onto the eigenbasis [90]:

$$\mathbf{E}^{+}(\mathbf{r},t)=\sum_{\mathbf{k},\varepsilon}\mathcal{E}_{\mathbf{k},\varepsilon}(t)\boldsymbol{\alpha}_{\mathbf{k},\varepsilon}(\mathbf{r}) \tag{2.23}$$

In the equation above, the expansion coefficient $\mathcal{E}_{\mathbf{k},\varepsilon}(t)$ is the electric field amplitude of the corresponding field mode. Each eigenmode basis vector $\boldsymbol{\alpha}_{\mathbf{k},\varepsilon}(\mathbf{r})$ is a complex vector function describing the spatial structure (e.g. nodes, antinodes, polarization) of the corresponding classical mode at the position $\mathbf{r}$. In free space, ε corresponds to one of the two orthogonal polarizations of any plane wave mode; in an ideal waveguide structure, ε refers to one of the many possible transverse electric (TE) or transverse magnetic (TM) modes in that waveguide.

[3]The Fourier transform of the real field $\mathbf{E}(\mathbf{r},t)$ is shown in the first equation below. The positive frequency part $\mathbf{E}^{+}(\mathbf{r},t)$ is exactly the same integration, but only over the positive half, shown in the second equation.

$$\mathbf{E}(\mathbf{r},t)=\frac{1}{\sqrt{2\pi}}\int_{-\infty}^{\infty}\tilde{\mathbf{E}}(\mathbf{r},\omega)e^{-i\omega t}\mathrm{d}\omega$$
$$\mathbf{E}^{+}(\mathbf{r},t)=\frac{1}{\sqrt{2\pi}}\int_{0}^{\infty}\tilde{\mathbf{E}}(\mathbf{r},\omega)e^{-i\omega t}\mathrm{d}\omega$$

Photon modes sharing a certain ε naturally form a family of propagation modes. The eigenmode basis is orthonormal, so that for any two basis vectors $\boldsymbol{\alpha}_{\mathbf{k},\varepsilon}(\mathbf{r})$ and $\boldsymbol{\alpha}_{\mathbf{k}',\varepsilon'}(\mathbf{r})$ we have:

$$\int_V \boldsymbol{\alpha}^*_{\mathbf{k}',\varepsilon'}(\mathbf{r}) \cdot \boldsymbol{\alpha}_{\mathbf{k},\varepsilon}(\mathbf{r}) \mathrm{d}^3 r = \delta_{\mathbf{k},\mathbf{k}'} \delta_{\varepsilon,\varepsilon'} \tag{2.24}$$

where the delta is the Kronecker symbol.

The spontaneous emission process we consider starts with an exited atom, ends with a de-excited atom and a photon emitted into one propagation mode as an elementary mode excitation. This propagation mode is always in an energy continuum of other modes. The levels in this energy continuum are naturally indexed by the mode's circular frequency ω. At the same time, an emitted photon can propagate in continuously variable directions in space. We label a propagation mode's direction with a condensed notation β, which for example can be the two angular coordinates giving the direction of the emitted photon in free space. Then all the modes of a certain frequency ω constitute a *degenerate continuum* indexed by β. One unique propagation mode can then be denoted by $(\omega,\beta,\varepsilon)$.

With the above convention of notations, we set out to find the spontaneous emission rate $\mathrm{d}A_{ij}(\beta,\varepsilon)$ when an atom decays from level $|i\rangle$ to a lower level $|j\rangle$ while releasing one photon of frequency ω_{ij} into a specific mode $(\omega_{ij},\beta,\varepsilon)$. The Fermi's golden rule for a degenerate continuum [91] gives the specific form of $\mathrm{d}A_{ij}(\beta,\varepsilon)$ as:

$$\mathrm{d}A_{ij}(\beta,\varepsilon) = \frac{2\pi}{\hbar^2} |\langle j,(\omega_{ij},\beta,\varepsilon)|H_\mathrm{I}|i,0\rangle|^2 \rho(\omega_{ij},\beta,\varepsilon)\mathrm{d}\beta \tag{2.25}$$

where $\langle j,(\omega_{ij},\beta,\varepsilon)|H_\mathrm{I}|i,0\rangle$ is the matrix element coupling the initial atom-field state $|i,0\rangle$ and the final state $|j,(\omega_{ij},\beta,\varepsilon)\rangle$ in the atom-field interaction Hamiltonian H_I. The quantity $\rho(\omega_{ij},\beta,\varepsilon)\mathrm{d}\beta\mathrm{d}\omega$ is formulated to give the number of propagation modes in the mode family ε that fall within the energy interval $\omega_{ij} \to \omega_{ij} + \mathrm{d}\omega$ and the directional interval $\beta \to \beta + \mathrm{d}\beta$ at the same time. The $\rho(\omega_{ij},\beta,\varepsilon)$ is then the mode spectral density for the modes in the family ε propagating in the direction β. Eq. (2.25) hence says that the concerned emission rate into one specific propagation mode is proportional to the corresponding mode spectral density and the square of the interaction matrix element.

In the dipole approximation regime we can specify the form of the interaction as a dipole interaction [86]:

$$\mathrm{d}A_{ij}(\beta,\varepsilon) = \frac{\pi}{\hbar\epsilon_0}\omega_{ij} |\mathbf{D}_{ij} \cdot \boldsymbol{\alpha}_{\mathbf{k},\varepsilon}(\mathbf{r}_\mathrm{at})|^2 \rho(\omega_{ij},\beta,\varepsilon)\mathrm{d}\beta \tag{2.26}$$

In Eq. (2.26), $\mathbf{D}_{ij}$ is the dipole matrix element $\langle i|e\hat{\mathbf{r}}|j\rangle$. $\boldsymbol{\alpha}_{\mathbf{k},\varepsilon}(\mathbf{r})$ is the eigenmode function introduced earlier of the emitted photon. For evaluating the emission rate, $\boldsymbol{\alpha}_{\mathbf{k},\varepsilon}$ takes the value of $\boldsymbol{\alpha}_{\mathbf{k},\varepsilon}(\mathbf{r} = \mathbf{r}_\mathrm{at})$ at the position of the atom.

The global spontaneous emission rate A_{ij} is the sum of individual rates so that the emitted photon can end up in all possible modes:

$$A_{ij} = \sum_\varepsilon \int \mathrm{d}A_{ij}(\beta,\varepsilon) \tag{2.27}$$

Eq. (2.27) involves formally all the quantities needed to estimate the spontaneous emission

rate when all field modes are propagation modes[4]. For the circular Rydberg levels, $\mathbf{D}_{ij}$ can be precisely calculated. The mode properties $\boldsymbol{\alpha}_{\mathbf{k},\varepsilon}(\mathbf{r})$ and $\rho(\omega_{ij},\beta,\varepsilon)$ also have analytical forms for simple and ideal waveguide models, open in one or two directions (e.g a circular waveguide, a parallel plate waveguide). The simplest case is a completely open "waveguide", which is the free space. The well-known free space spontaneous emission rate can be readily reached starting from Eq. (2.27):

$$A_{ij}^{(\text{freespace})} = \frac{\omega_{ij}^3 D_{ij}^2}{3\pi\hbar\epsilon_0 c^3} \tag{2.28}$$

Appendix A gives the deduction of the spontaneous emission rate for two ideal cases: the free space and a parallel plate waveguide.

2.4.1.2 The temperature stimulated transition rates

When the environment temperature is above zero ($T > 0$), the field modes, whether in free space or in a cavity, are not empty but populated by thermal photons. The *mean number of thermal photons per mode* $n_{\text{th}}(\omega, T)$ at the photon frequency $\omega/2\pi$ and temperature T is a dimensionless value given by the blackbody radiation law as[5]:

$$n_{\text{th}}(\omega, T) = \frac{1}{e^{\hbar\omega/k_{\text{B}}T} - 1} \tag{2.29}$$

An environment above 0 K necessarily subjects the atom, in addition to the spontaneous emission, to the stimulated emission and the stimulated absorption caused by the thermal photons. If we assume these BBR induced transitions are between levels with no degeneracy (corresponding to the case of our experiment), then between any two allowed levels $|i\rangle$ and $|j\rangle$, the *stimulated emission rate* B_{ij} from $|i\rangle$ to $|j\rangle$ and the *stimulated absorption rate* B_{ji} from $|j\rangle$ to $|i\rangle$ are always equal in value[6]: $B_{ij} = B_{ji}$. Given the expression Eq. (2.29) for the thermal photon number, the values of these stimulated rates at temperature T can be conveniently expressed as the corresponding spontaneous emission rate A_{ij} multiplied by a factor of n_{th}:

$$B_{ij}(T) = B_{ji}(T) = n_{\text{th}}(\omega_{ij}, T) A_{ij} \tag{2.30}$$

Importantly, Eq. (2.30) shows that, at a given temperature T, a change in the spontaneous emission rate is associated with the same change in the corresponding stimulated rates, only scaled by a factor of n_{th}. If the spontaneous emission from $|i\rangle$ to $|j\rangle$ is inhibited (enhanced), the stimulated rates for this transition are also inhibited (enhanced).

[4] It applies also to the spontaneous emission in an enclosed but highly damped cavity. In this case the directional argument β disappears, the modes are not propagation modes in an energy continuum but resonator modes separated in frequency. In the perturbative regime, each mode should have a large width due to the low quality factor. To estimate the in-cavity spontaneous emission rate of an emitter mainly coupled to one cavity mode, the $\rho(\omega_{ij},\beta,\varepsilon)$ in Eq. (2.26) is to be replaced by the 3D cavity's single mode spectral density (1 mode)/$\Delta\omega V$ [60], where V is the true cavity size. The mode width $\Delta\omega$ is obtained from the relation $Q = \omega_{\text{c}}/\Delta\omega$ with a known quality factor Q and mode frequency ω_{c}

[5] In the cavity QED experiments, one has access to the QND photon counting in a single mode [92]. The thermal photon number distribution is then measured directly to determine the temperature in the cavity [93].

[6] Here the B rates are not directly the Einstein coefficient B, which is not a rate.

2.4.2 Environment Modification to Decay Rates

How can we change the spontaneous emission rate? The FGR argument in Eq. (2.26) shows that the spontaneous emission rate for a given transition ω_{ij} depends on the values of dipole matrix element, the position of the atom, and the mode spectral density.

The dipole matrix element $\mathbf{D}_{ij}$ is considered invariant in the experiment. Changing $\mathbf{D}_{ij}$ means changing the wave function of the atom, this does not happen considering the atoms we measure are at least a few millimeters away from the boundaries of the structure, a distance far too large to ever affect the dipole matrix element $\mathbf{D}_{ij}$, which is a spatial integral localized within the $\simeq 100\,\mathrm{nm}$ span of our typical Rydberg electron's wave function.

The macroscopic position $\mathbf{r}_{\mathrm{at}}$ of the atom can modify the emission rate by yielding dipole coupling of different magnitudes at different positions in a given mode. The most basic example, amply discussed in various sources [86, 94], is the dependence of the atomic lifetime on its distance from a conductive mirror. In this scenario, no mode can have tangential electric field components along the mirror surface. For a CRA having a quantization axis normal to the mirror, the closer it is positioned to the mirror surface, the more its only σ^+ spontaneous emission is inhibited. This is because the transverse electric components of any modes can only form nodes on the mirror. As the CRA approaches these on-mirror nodes, its transition dipole moment can only couple very weakly to the field: at the zero distance limit there is zero transverse field to couple to on the mirror. This position-based rate inhibition is not the focus of our experimental work, but we give the accounts of this phenomenon in both the ideal model and the numerical simulation of our parallel plates system (see subsection 2.4.4). We note that a real mirror's surface plasmon modes would complicate the interaction, and the arbitrarily large inhibition of emission promised by an ideal surface is not guaranteed [95].

The last decay rate modifier, the mode density, can changed drastically in a cavity or a waveguide structure having the characteristic dimension of the emission wavelength. According to Eq. (2.26), the probability for a photon to be emitted at all is proportional to the number of all available photonic modes, each weighted differently by the corresponding atom-mode interaction and the mode spectral density. It follows that if there is *no* mode for a photon to be emitted into, the atom stays excited forever. Such a zero mode density regime for the inhibition of the spontaneous emission of a CRA was first proposed by Kleppner [51]. The proposed zero mode density regime occurs for instance in a circular waveguide (i.e. a metal tube) when the atomic transiton is below cut off.

The global mode spectral density of an ideal circular waveguide is shown in Fig. 2.9. The most striking feature is the complete zero mode density region below the circular frequency ω_0, which marks the cutoff of the lowest mode TE_{11} of a circular waveguide. Above the cutoff, the change in mode density is drastic, up until a few ω_0. At very high frequencies $\omega \gg \omega_0$, the mode density in the waveguide will eventually become indistinguishable from that of the free space, falling back to our common sense that a beam of laser traveling through a MW waveguide shall be indifferent to its surroundings. For a realistic metal tube which is not infinite in length and conductivity, the fundamental cutoff would tend to a Lorentzian tail towards low frequency. The ideal zero mode density does not exist in reality, but the mode density below cutoff would be greatly reduced if the conductivity of the waveguide is sufficiently high or the frequency considered is sufficiently low.

To take advantage of the low mode density below cutoff, the originally proposed experi-

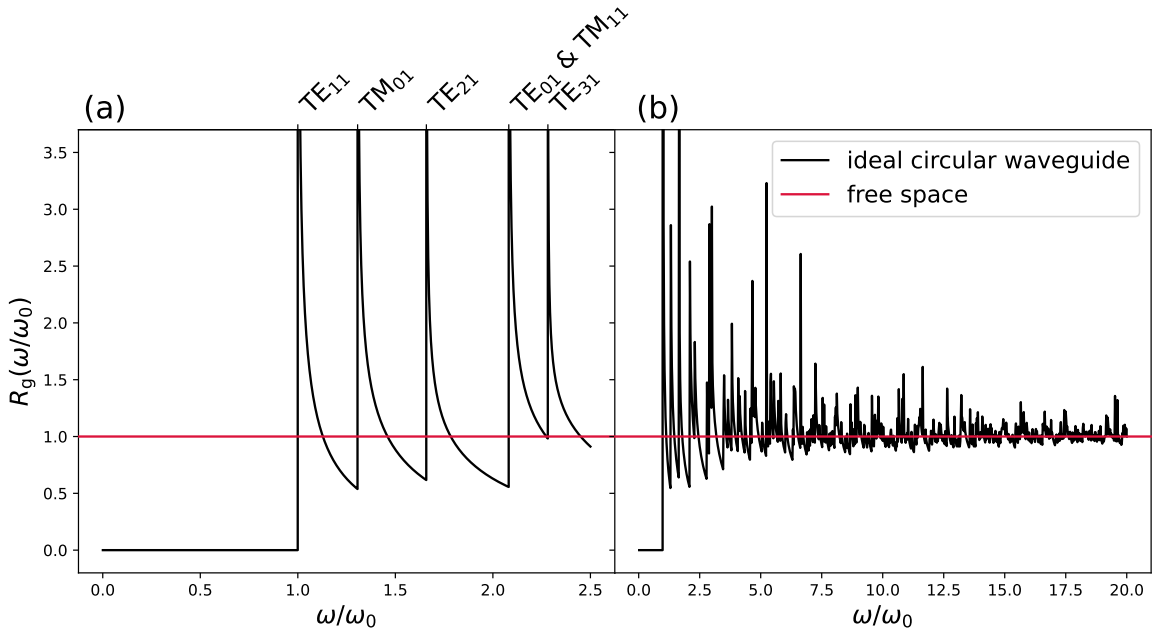

Fig. 2.9 *The mode density in an ideal circular waveguide plotted in small and large frequency range, developed from the figure 1 in the paper of Kleppner [51]. The waveguide's mode density (black curves) is normalized by that of the free space, consequently the free space mode density is represented by a straight red line at $y = 1$ in both plots. (a) The localized view in the frequency range $\omega \in [0,2.5\omega_0]$. Below the cut-off frequency ω_0 of the fundamental propagation mode TE_{11}, the mode density in the ideal waveguide is completely zero. (b) An extended view in the frequency range $\omega \in [0,20\omega_0]$. This plot captures the gradual process of the circular waveguide's mode density tending to that of the free space in the regime of $\omega \gg \omega_0$.*

ment [51] is to send a thermal beam of circular atoms through a tube, and the transition to be inhibited is $|25C\rangle \to |24C\rangle$. The tube's diameter then should be less than 0.4 mm to place the transition below the fundamental cutoff and inside the low mode density region. This would be a purely proof-of-principle experiment. In particular, the relatively low-n circular state chosen is actually for the relatively *short* lifetime of such a state (for a CRA, the higher the n, the longer the free space lifetime, see subsection 2.4.3), so that it should normally decay in free space during the travel time in the tube, the tube's inhibition effect would then be prominent in measurement. The barely machinable tube diameter 0.4 mm represents a limit that prevents one from choosing an even lower n. Indeed, the first demonstration of the inhibited spontaneous emission of a CRA [50] was later done in the transition $|22C\rangle \to |21C\rangle$ (freespace lifetime 460 µs). The thermal beam in this experiment did not travel through a tube, but between two parallel plates separated by quartz spacers to create a $\simeq 200$ µm gap, avoiding the difficulty of machining a tube of comparable size. With the relatively high-n circular states which are routinely used in all present experiments, the distance in between the plates can be much more generous, e.g. a 4 mm gap that can inhibit well the states

$|58C\rangle$ and above as demonstrated in this work. This is consistent with the change from the thermal beam paradigm: the atoms can be cooled and trapped in the center of the parallel plates, consequently one should instead prepare the CRAs with higher-n and longer free space lifetime, and extend the lifetime even longer with the inhibition structure.

In general, the parallel plates as an inhibition structure are easy to implement and pose no clear disadvantage, the reason it was not initially proposed (and even explicitly dismissed in the inhibition proposal paper of Kleppner) is probably because of its "deceptive" global mode density, which appears to have no cutoff at low frequency. This is shown in Fig 2.10.

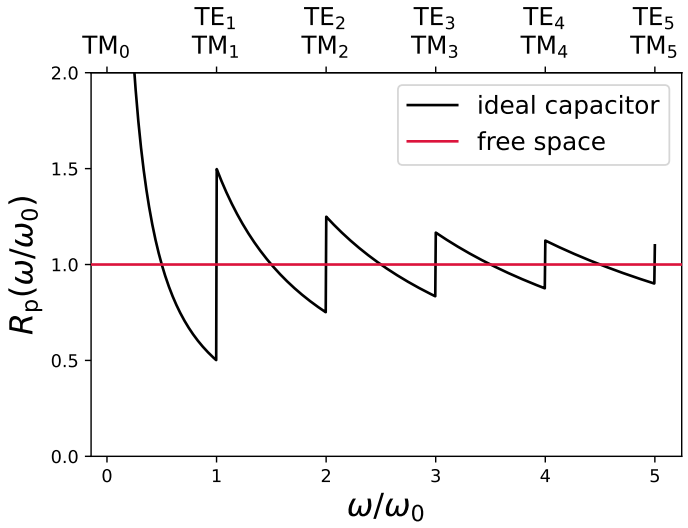

Fig. 2.10 *The global mode spectral density in an ideal parallel plate waveguide, normalized by the free space mode density.*

In a parallel plate waveguide, or a capacitor for short, a mode can only propagate in the transverse directions, and is either a TE_m mode or a TM_m mode. A TE_m (TM_m) propagation mode has its electric (magnetic) component exclusively parallel to the plates and has zero electric (magnetic) component normal to the plates. The order index $m = 0,1,2,\ldots$ is the number of the transverse electric antinodes (transverse magnetic nodes) across the spacing of the plates. A TE_m (TM_m) mode family is often referred to as "a mode" in other context, but in our case it is really a family of propagation modes, including all the TE_m (TM_m) modes propagating in the whole 2π directions transversely, and encompassing mode frequency range starting from the cutoff to infinity. The capacitor waveguide has very simple distribution of cutoff frequencies, each TE_m and TM_m with the same m are degenerate in their cutoff frequency at $m\omega_0 = mc\pi/L$ (excluding $m = 0$, since TE_0 does not exist), where L is the capacitor spacing.

In Fig. 2.10, at high frequency the capacitor mode density still tends towards that of the free space, however, below the cutoff of TE_m (TM_m), instead of reaching zero mode density as in the case of a circular waveguide, we see the curve goes to infinity at low frequency. First of all, this infinity is not to be taken literally, since what is plotted is the mode density ratio of the capacitor to the free space, the infinity only reflects that the free space mode density converges to zero faster than that of the capacitor, while none is divergent at low frequency. Secondly, the enhanced TM_0 family that cuts off at DC never couples to a CRA

with its quantization axis normal to the capacitor plates. This means for a carefully oriented CRA, it experiences the same sudden vanishing of the mode density below the cutoff of TX_1 in a capacitor as a randomly oriented CRA experiences below the fundamental cutoff in a tube. The corresponding decay rate analysis and simulation of this phenomenon is shown in subsection 2.4.4.

In our work, the capacitor inhibits both the spontaneous emission and the stimulated decays, this follows from the scaling of the stimulated rate B_{ij} as the spontaneous rate A_{ij} in Eq. (2.30) , which in our experiment is ultimately attributed to their mutual dependence on the transition mode density $\rho(\omega_{ij})$. This type of modification in decay rates is independent from the number of per-mode thermal photons n_{th}, which is a constant at a given temperature. One can of course reduce the stimulated rates through reducing n_{th}: in a Rydberg experiment this corresponds to decreasing the environmental temperature to typically a few Kelvins by using a cryostat. However a cryostat large in size approximates the free space, therefore does not alter $\rho(\omega_{ij})$, the spontaneous rate A_{ij} governed by Eq. (2.26) stays the same inside the cryostat. In this sense the modification in the mode density $\rho(\omega_{ij})$, which changes both A_{ij} and B_{ij}, is a "two birds with one stone" method compared with the modification in n_{th}, which changes only B_{ij}.

In relevant literatures reporting increased atomic lifetime in a confinement structure, language-wise, different rates tend to be addressed separately: It is either "inhibited spontaneous emission" [50, 51], when $n_{\text{th}} \ll 1$, or "inhibited stimulated absorption" [96], when $n_{\text{th}} \gg 1$. But the one underlying mechanism to encompass both would be "decreased mode density", which does not really make the difference between the A rate or the B rate, and would always change both simultaneously by the same factor.

The technical details of the figures in this subsection is found in appendix B.

2.4.3 Lifetime of the CRA in Free Space

Starting from the initial level $|i\rangle$, an atom can decay to a lower energy level $|g\rangle$, and also to a higher energy level $|e\rangle$. We express the corresponding decay rates with the notation $\Gamma_{ig} = A_{ig} + B_{ig}$ and $\Gamma_{ie} = B_{ie}$, with the spontaneous and stimulated decay rates A and B as introduced in the preceding subsections. The total decay rate Γ_{at} from the initial state $|i\rangle$ can then be written by summing over the dipole-allowed upward and downward decay channels:

$$\Gamma_{\text{at}} = \sum_{g<i} \Gamma_{ig} + \sum_{e>i} \Gamma_{ie} = \sum_{g<i} (A_{ig} + B_{ig}) + \sum_{e>i} B_{ie} \tag{2.31}$$

or if we use the mean number of thermal photon $n_{\text{th}}(\omega_{ij}, T)$ resonant with the decay transition frequency $\omega_{ij}/2\pi$ at the temperature T, with Eq. (2.30) the above equation can be expressed only in terms of the spontaneous emission rates:

$$\Gamma_{\text{at}} = \sum_{g<i} A_{ig}[1 + n_{\text{th}}(\omega_{ig}, T)] + \sum_{e>i} A_{ei} n_{\text{th}}(\omega_{ei}, T) \tag{2.32}$$

where the spontaneous emission rates (A coefficients) can be obtained by methods introduced in subsection 2.4.1.1, and the n_{th} for a certain decay channel is simply a known function of temperature. Eq. (2.32) is general not only for the free space scenario, but also for atoms in confined structures with modified spontaneous emission rates.

The total decay rate of a CRA is thus dependent on the determination of its major decay channels, corresponding to the decays to final levels $|g\rangle$'s and $|e\rangle$'s in the general equation (2.32). For the situation concerned in this work and for the clarity of analysis, we give in Fig. 2.11 the dipole-allowed decay channels starting from the initial level $|60C\rangle$ at room temperature 300 K and in free space. The manifold selection ends at a lower bound of 59 because there is no selection-rule allowed transitions below, and at a higher bound of 62 because the decay rates to levels above are negligible. The calculated transition rates shown in red numbers in Fig. 2.11 is the direct analytical result from the individual terms in Eq. (2.32), in which the spontaneous emission rates are obtained from the Eq. (2.28). The only parameter to obtain numerically [61] in this rate calculation is the radial part of the dipole matrix element D_{ij}. The resulting $|D_{ij}|$'s used are given in the figure in units of ea_0.

In this figure, we see the absolute dominant decays from the $|60C\rangle$ are the downward and upward transitions to the neighboring circular states. In particular, the BBR-stimulated upward transitions can be open to many decay channels, but in practice the σ^+ transition to $|61C\rangle$ is still the dominant compared to the π and σ^- transitions to the same 61-manifold. For these thermal-induced decays from $60C$ to the immediate next 61 manifold, the difference in the energies of the end levels ($61C$, $61e_1$, $61e_1'$, $61e_2$, $61e_2'$, $61e_2''$) are small (a few hundred MHz of linear Stark shift) compared to the $\Delta E/h \simeq 30\,\mathrm{GHz}$ energy difference between the two manifolds. For these transitions, the similar transition frequencies result in the similar free space mode densities and number of thermal photons. Consequently, the transition matrix element is the main parameter that causes the difference in the transition rates ($\propto D_{ij}^2$). If we inspect the upward transitions from $60C$ to the levels in the 61-manifold, we find that σ^+, π, and σ^- transitions rates increasing smaller by orders of magnitude. This comes from the fact that, for these nearest-manifold upward transitions, the dipole matrix elements are very different: $D_{\sigma+}^2 \gg D_{\pi}^2 \gg D_{\sigma-}^2$. Each term is >100 times larger than the next, resulting in the same scaling in the corresponding transition rates.

In the experiments of the CRA at room temperature, the π transitions are often neglected for its $\simeq 1\%$ contribution in the total decay rate, we however label the π transitions' rates in Fig. 2.11 because it belongs to the next leading decay rates and will play an important part when the circular-to-circular σ^+ transitions are inhibited (subsection 2.4.4). The π transition we mention in this work, without specific context, will be exclusively a nearest-manifold $n \to n+1$ transition, the other π transitions spanning 2 and more manifolds being always negligible in comparison. There are, however, two high frequency σ^+ transitions ($n \to n+2$) that bear the similar rates of tens of Hz as those of the π transitions. In Fig. 2.11 these transitions correspond to a one-photon decay in the channel $60C \to 62e_1$ and $60C \to 62e_1'$. We denote such a transition as a "2σ" transition[7] for the ease of discussion, while the notations σ^+, σ^- or their common notation σ are reserved only for the nearest manifold $n \to n \pm 1$ transitions.

We now focus back on the dominant circular-to-circular σ^+ transitions which determine the lifetime of the CRA in free space. It is instructive to first examine the CRA's spontaneous emission at 0 K when all the upward decays are zero. The scaling law of the CRA's radiative lifetime limited by the spontaneous emission can be found with a semi-classical argument [60]: The lifetime τ_n of the nC state is considered to be the time during which the spontaneous

[7]The naming follows from the convention used in the thesis of R. G. Cortiñas [69], who made a detailed analysis concerning the lifetime limiting effect of these high frequency σ^+ decays of the CRAs in an ideal capacitor and in the high-temperature limit.

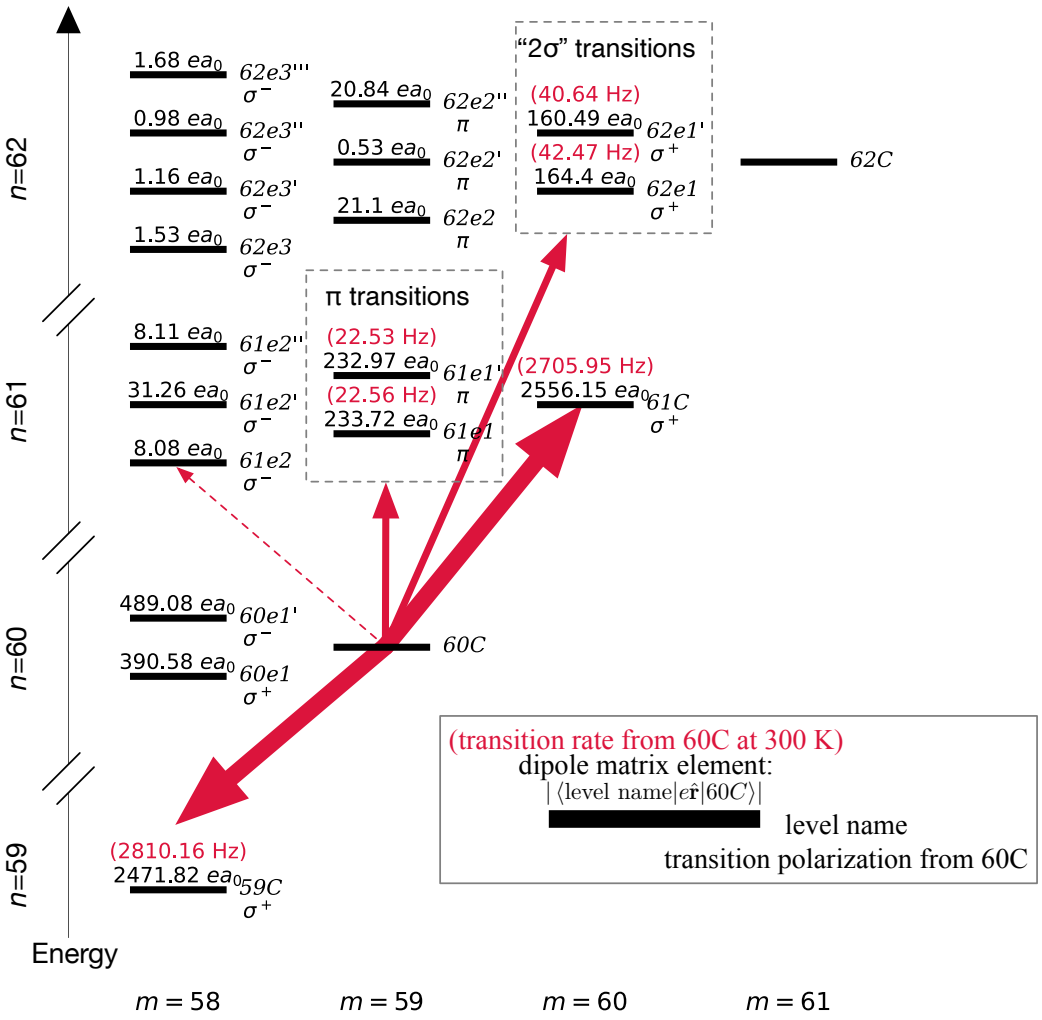

Fig. 2.11 *All the Rydberg levels satisfying* $|n - 60| \leq 2$ *and* $m \geq 58$ *under a small Stark field. Level energy is not to scale. All levels except for* $|62C\rangle$ *are selection-rule allowed dipole transitions from* $|60C\rangle$*. The transition dipole matrix element values are shown in black. The notable transition rate values at 300 K are shown in red (for levels without the transition rates, the corresponding rates are either* $< 1\,\text{Hz}$ *or* $\ll 1\,\text{Hz}$*). The arrows show a few representative room temperature decay transitions from* $|60C\rangle$*. The absolutely dominant decay channels are the two* σ^+ *transitions drawn in thick arrows, compared to which the* π*-polarized decays are negligible (<1% contribution in the total decay rate of* $|60C\rangle$*), and the* σ^-*-polarized decays even more negligible (in dashed arrow). This trend is true for all the CRAs we prepare or observe (mostly with* n *from 50 to 60) in this work.*

emission $nC \to (n-1)C$ takes place and a photon of energy $\hbar\omega_n$ is emitted. The emission power P can be estimated by the Larmor formula:

$$P = \hbar\omega_n/\tau_n = \frac{2}{3}\frac{e^2a^2}{4\pi\epsilon_0 c^3} \propto a^2, \tag{2.33}$$

where a is the acceleration of the electron. In the semi-classical picture, the orbiting electron's acceleration is given by $a = r_n\omega_n^2$, where $r_n = n^2a_0$ is the radius of the atom of Bohr, a quantity that scales as n^2. The emission frequency ω_n follows from the Rydberg equation $\omega_n \propto 1/(n-1)^2 - 1/n^2$. At the very large n we consider, $\omega_n \propto n^{-3}$ to the first order in $1/n$. Taking the scaling of r_n and ω_n back into Eq. (2.33), we get[8]:

$$\tau_n \propto n^5 \quad (\text{at } 0 \text{ K}) \quad , \tag{2.34}$$

The longer lifetime at high n is consistent with the classical interpretation: the larger the orbiting radius of the electron, the less the orbiting acceleration, the atom radiates less power and is more long-lived. The same lifetime scaling can be also found in the spontaneous emission rate in Eq. (2.28) which we obtained from the FGR. The lifetime in this case scales as $\tau_n \propto \omega_n^{-3}D_n^{-2} \propto n^5$, with $\omega_n \propto n^{-3}$ as mentioned above and the $nC \leftrightarrow (n-1)C$ dipole matrix element $D_n \propto n^2$.

To examine the CRA's lifetime at 300 K, we add the ingredient of thermal photons. The downward decay rate $\Gamma_{n\downarrow}$ from nC is the spontaneous emission rate enhanced by the thermal photons, therefore (neglecting the negligible spontaneous emission) $\Gamma_{n\downarrow} \propto \omega_n^3 D_n^2 n_{\text{th}} \propto n^{-5}n_{\text{th}}$. The BBR at room temperature is very well in the Rayleigh-Jeans limit: $k_{\text{B}}T \gg \hbar\omega_n$. In this limit, $n_{\text{th}} = k_{\text{B}}T/\hbar\omega_n \propto \omega_n^{-1} \propto n^3$. It follows that $\Gamma_{n\downarrow} \propto n^{-2}$. The upward BBR-induced transition rate $\Gamma_{n\uparrow}$ to the next circular state has the same scaling[9], therefore the lifetime $\tau_n = 1/(\Gamma_{n\downarrow} + \Gamma_{n\uparrow})$ at room temperature scales as:

$$\tau_n \propto n^2 \quad (T \gg 1\,\text{K} \text{ and } n \gtrsim 50\ ) \quad , \tag{2.35}$$

We note that since $k_{\text{B}}/\hbar = (2\pi)\times 20.8\,\text{GHz/Kelvin}$, for the CRAs we work with (typically with $n > 50$ with decay transition frequencies $\lesssim 50\,\text{GHz}$), a few Kelvins is enough to achieve $k_{\text{B}}T > \hbar\omega_n$. At $\simeq 10\,\text{K}$ the BBR can already reach a good "high temperaure" Rayleigh-Jeans limit. The more detailed analysis by R. G. Cortiñas [69] suggests that the behavior of the limit can manifest starting from $< 5\,\text{K}$. It is thus crucial to reach $< 1\,\text{K}$ to benefit from the $\propto n^5$ scaling of lifetime in Eq. (2.34) for the CRAs with $n \gtrsim 50$.

Finally, in table 2.1 we give the theoretical lifetimes of some of the CRAs we have prepared or observed in this work:

[8] For the low-ℓ Rydberg states at 0 K, $\tau_n \propto n^3$ [97].

[9] At this point we are able to express the 300 K BBR-induced transition rate in terms of only the matrix element and the transition frequency. If we deviate from the dominant circular-to-circular transitions and consider, for example, the transition rate Γ_{ce} from a circular to an elliptical state. We find that $\Gamma_{ce} \propto \omega_{ce}^2 D_{ce}^2$ with the contribution of the thermal photons already included. This allows us to understand the slightly larger 2σ transition rates compared to those of the π transitions in Fig. 2.11: Even when the former transitions have relatively smaller dipole matrix elements, it is compensated by an almost doubled transition frequency which makes the decay channel's mode density $\simeq 4$ times larger. We can also see that even the rf decay channels $60C \to 60e_1$ and $60C \to 60e_1'$ have dipole matrix elements similar in magnitude to that of the π transition, nevertheless the decay rates of the rf channels should be at least 10000 times smaller, which is the square of $\simeq 100$ times difference in the transition frequencies between the rf decay within one manifold and the MW decay crossing two manifolds.

Table 2.1: The theoretical free space lifetimes of the circular states relevant in this work. The different lifetime scalings at 0 K and 300 K is a manifestation of their different scaling laws ($\propto n^5$ vs $\propto n^2$)

CRA (nC)	**0 K lifetime** (ms)	**300 K lifetime** (μs)
60C	71	177
59C	66	171
58C	60	166
57C	55	160
56C	50	154
55C	46	149
54C	42	144
53C	38	138
52C	34	133
51C	32	128
50C	29	123

2.4.4 Lifetime of the CRA Between Two Mirrors

In this subsection, we first study the decay rate modification of a CRA in an ideal capacitor (subsection 2.4.4.1). We show the difference in the capacitor's modifications to the σ transitions and to the π transitions. In particular we identify the capacitor's first order cutoff below which the CRA's major σ^+ decay channels in free space are completely inhibited.

We then turn to analyze the effect of the next leading decay rates at room temperature after the inhibition of the σ^+ channels (subsection 2.4.4.2). In this case the π and 2σ transitions dominate the lifetime of the CRA, and the π transfers set a fundamental limit to the best possible room temperature lifetime of a capacitor-inhibited CRA.

In the end, we show the principle of calculating the decay rate modifications in a real capacitor by means of classical electrodynamics.

2.4.4.1 The modified decay rates of the CRA in an ideal capacitor

For a CRA with a well oriented quantization axis, the σ and π transitions are induced by the field modes with the electric component normal and parallel to the quantization axis, respectively. The different transitions are in this sense mode-selective. This mode selection of the CRA is not evident in free space due to the spherical symmetry of the space and the field modes within. For the atomic emission inhibition, the most intuitive mechanism is to create a zero mode density zone in the position of the atoms, as demonstrated in a circular waveguide (Fig. 2.9). In comparison, the global mode density in between a plane parallel capacitor is always non-zero. The spontaneous emission inhibition asset of such a capacitor relies on its breaking of the spatial symmetry together with the mode selection of a CRA.

Using the FGR, given the capacitor's mode structure and the atomic dipole's position and orientation in between the capacitor, one can work out the atom's spontaneous emission rate in the capacitor (an example of this deduction is given in appendix A). For two specific configurations, a dipole transversely oriented and vertically oriented, the corresponding spontaneous emission rates modification factors are given as the dimensionless numbers C_σ

and C_π below [94]:

$$C_\sigma = \sum_{n=0}^{\lfloor 2L/\lambda \rfloor} \frac{3\lambda}{4L}\left[1+\left(\frac{n\lambda}{2L}\right)^2\right]\sin^2\left(\frac{n\pi z}{L}\right) \tag{2.36}$$

$$C_\pi = \frac{3\lambda}{4L} + \sum_{n=1}^{\lfloor 2L/\lambda \rfloor} \frac{3\lambda}{2L}\left[1-\left(\frac{n\lambda}{2L}\right)^2\right]\cos^2\left(\frac{n\pi z}{L}\right) \tag{2.37}$$

The above equations apply to an ideal capacitor (infinite in size and conductivity), the spacing of which is L. The dipole's vertical displacement z can be chosen to start from 0 at the bottom plate and end at L at the top plate. λ is the dipole emission's wavelength in question. The quantities inside the floor brackets on top of the sum signs are to be evaluated to its integer part, e.g. $\lfloor 1.1 \rfloor = \lfloor 1 \rfloor = 1$. In the case of a CRA having the quantization axis perfectly normal to the capacitor plates, the C_σ and C_π respectively modify the CRA's σ and π transition rates relative to those in free space.

In Fig. 2.12, we plot the C_σ (black) and the C_π (red) for a dipole in the center (solid) and at $3/4L$ (dashed) between the ideal capacitor. The total vanishing of C_σ below the circular frequency $\omega_0 = c\pi/L$ is the most important feature that allows the inhibition of the dominant σ^+ transitions from a CRA. This desirable inhibition takes effect only when the CRA's quantization axis is oriented normal to the plates (the capacitor plates can then be conveniently used to apply the quantization axis field). We can, for example, imagine a CRA with the quantization axis parallel to the plates, the non-dominant π transition of the CRA would be inhibited instead, but this is not of practical interest.

This inhibition of a selected transition type of the CRA is associated with the mode structures in the capacitor, on which we gave a first brief introduction in subsection 2.4.2. On top of Fig. 2.12, we show pictorially the transverse and vertical electric amplitudes, denoted respectively by $E_\leftrightarrow$ and $E_\updownarrow$, of the capacitor's $\mathrm{TE}_m/\mathrm{TM}_m$ modes with the mode order index m running from 0 to 3. One sees that the perfect inhibition of the σ^+ transition below ω_0 is because the transverse electric component cannot exist below this first order cutoff at ω_0, which in the following discussion will implicitly be the cutoff we refer to by mentioning "the cutoff" without other context. The only capacitor mode below ω_0 is the TM_0 mode, which sometimes is called the capacitor's TEM mode [51], since both the electric and the magnetic components of this mode are transverse with respect to the its direction of propagation (parallel to the plates), a feature not shared by the rest of the capacitor modes.

The behavior of the dipole coupling with higher order capacitor modes up till a few ω_0 can also be understood intuitively by examining the shape of the corresponding mode structures. For example, in the solid black curve, the second order modes should normally emerge at $2\omega_0$, but the corresponding σ enhancement resonance is missing at this frequency. This is due to the zero coupling of the centered dipole with the centered node of the $E_\leftrightarrow$ component of the $m = 2$ modes. The σ enhancement at $2\omega_0$ is regained by shifting the transversely oriented dipole away from $z = L/2$ (dashed black). This position dependent transition rate modification in a capacitor is most evident within the frequency bound of a few ω_0 that we plot. In particular, if a CRA is positioned very close to either of the two surfaces of the capacitor, it couples very weakly to the $E_\leftrightarrow$ component of any available modes, and the situation approximates that of the single mirror inhibition. This can be of practical interest in real experiments, where below the cutoff the first order modes do not disappear

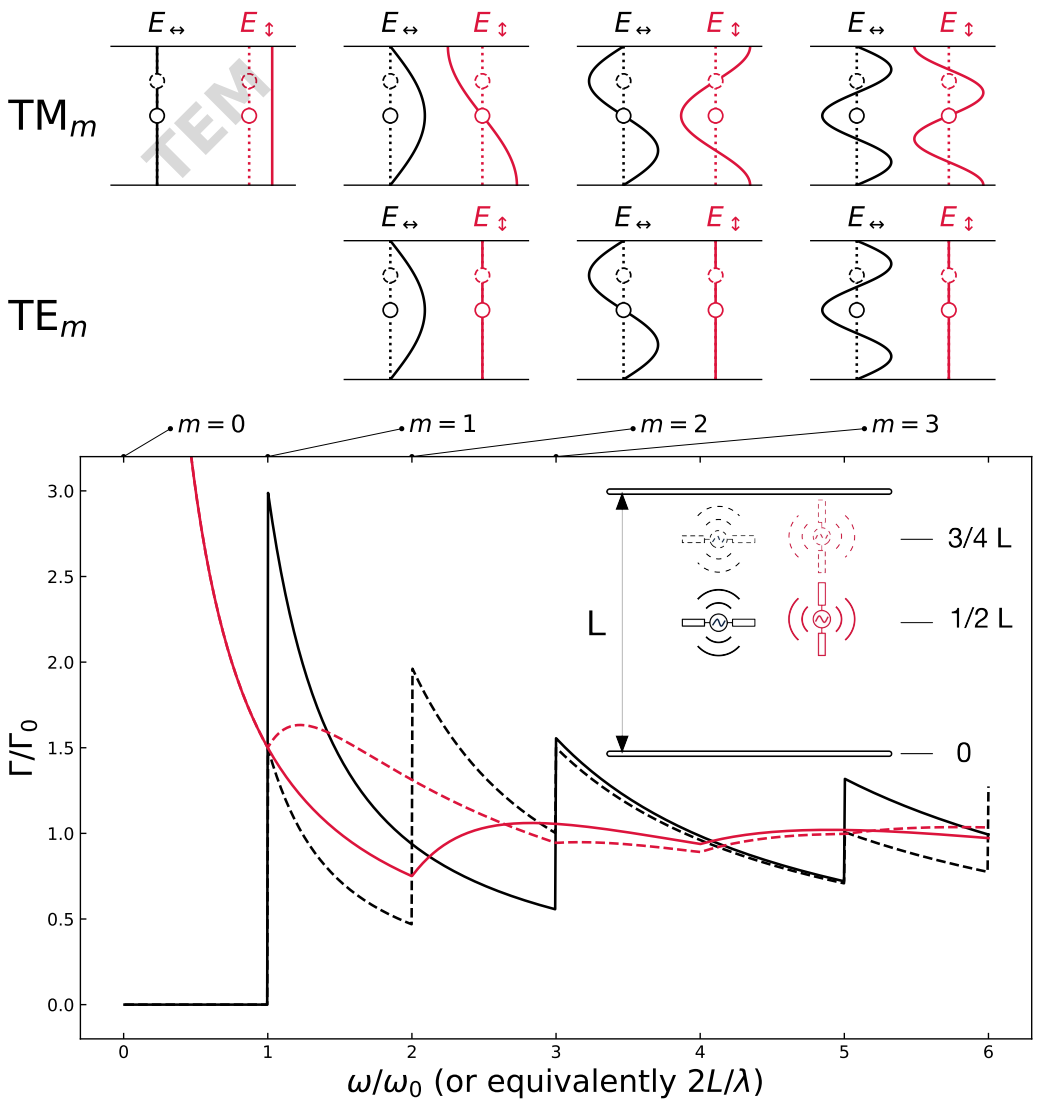

Fig. 2.12 *The main plot at the bottom shows the radiative damping rate of a classical dipole in an fixed ideal capacitor as a function of the dipole radiation frequency (or equivalently as a function of the capacitor separation L for a fixed dipole radiation frequency). The inset shows four dipole configurations yielding the four different rate curves with matched color and style (when the solid line overlaps completely with the dashed line, only the solid is evident). The damping rate $\Gamma(\omega)$ in any configuration has been normalized by the free space damping rate $\Gamma_0(\omega)$ of the dipole. Above the main plot is a grid view of the parallel plate waveguide's first four orders of TE_m, TM_m emerging at equispaced and degenerate cutoff frequencies $m\omega_0$, for $m = 0,1,2,3$. The nodes and antinodes of each mode's transverse (longitudinal) electric field component $E_\leftrightarrow$ ($E_\updownarrow$) are plotted vertically along the capacitor spacing, with the concerned dipole positions marked by empty balls. Two notable exceptions are found at $m = 0$: TE_0 does not exsit; TM_0 is a TEM mode propagating parallel to the plates, with a uniform field distribution along the plate spacing.*

completely, one can then try to move the CRA away from center to gain better σ inhibition. In a numerical simulation of a real capacitor, we find the σ transition rates can be reduced by a factor of two by simply moving the atom from $L/2$ to $3L/4$ (see subsection 3.1.4.3)

2.4.4.2 The room temperature lifetime limit of a CRA in an ideal capcitor

We focus again on the concrete case of the 300 K decay channels of a $60C$, as we did in subsection 2.4.3, but now the CRA is positioned in an ideal capacitor with a 4.1 mm spacing (the parameter of our experiment), as shown in Fig. 2.13.

In the figure, the dominant free space σ^+ transitions from $60C$ to $59C$ and $61C$ are below the ideal cutoff and accept zero population transfers from the initial $60C$. The next leading transitions are then the π and 2σ transitions we introduced before. The 2σ channels can be inhibited by a capacitor with less spacing and is not the fundamental limit of the 300 K lifetime of the CRA. However in real experiments, a cutoff frequency high enough to cover the frequency range of $\Delta n = 2$ requires either a very high n or a very small capacitor spacing L. The former would pose a challenge to the circularization process, the latter could cause difficulty in the field control in a tight space. Therefore, leaving the 2σ channels uninhibited may a compromise in reality such as in our experiment.

After the total ideal inhibition of the circular-to-circular σ^+ decay channels, the next feature we recognize is the modifications to the π transition rates and the 2σ transition rates by the C_π, C_σ factors in Eqs.~(2.36), (2.37). For the π transitions, they are to be put below the cutoff together with the σ^+ upward transition from the initial circular state, as a result, for any capacitor-inhibited CRA, its π transitions are enhanced by at least a factor of 1.5 (the C_π at ω_0). The 2σ transition rates, if not inhibited by a high cutoff, in most cases are also to be consistently enhanced[10]. A detailed analysis has been done regarding the effect of the 2σ decays in the case of a 2 mm ideal capacitor [69] at hight temperature. The analysis shows that for the CRAs from $n = 50$ to $n = 55$, corresponding to the regime where the σ^+ channels are inhibited but the 2σ channels are still open, the 2σ decays dominate the lifetime of the CRA.

If we turn to the even more ideal case when the cutoff is high enough to inhibit the 2σ decays, the only decay channels left of the CRA are the two BBR-induced π transitions. The corresponding transition rates correction C_π increases with n. However one can show that the competition between the increased C_π and the reduced π transition mode density actually reaches a draw: the π transition rate Γ_π below the cutoff does not depend on n [69]:

$$\Gamma_\pi \propto n^0 T \tag{2.38}$$

The above relation shows that there is a fundamental limit for the best lifetime of the CRA that one can achieve in an ideal capacitor at a certain temperature T. This lifetime limit depends on the ideal capacitor's spacing L. At 300 K, the π transfer limited lifetime of any CRA (if the n is sufficiently high) is ≈ 12 ms in a capacitor with $L = 4.1$ mm (the parameter of our setup), and $\simeq 6$ ms for $L = 2$ mm (the parameter in [26]). This reduction in the fundamental 300 K lifetime by switching to a tighter capacitor can be easily understood

[10] In Fig. 2.12, the solid black curve at $2\omega_0$ gives a C_σ of 15/16, corresponds to a negligible inhibition to the 2σ rates which can only be achieved by a CRA with a very high n and its σ^+ transitions barely below the cutoff. However in this situation a relatively large capacitor spacing is already enough to simply inhibit the 2σ completely

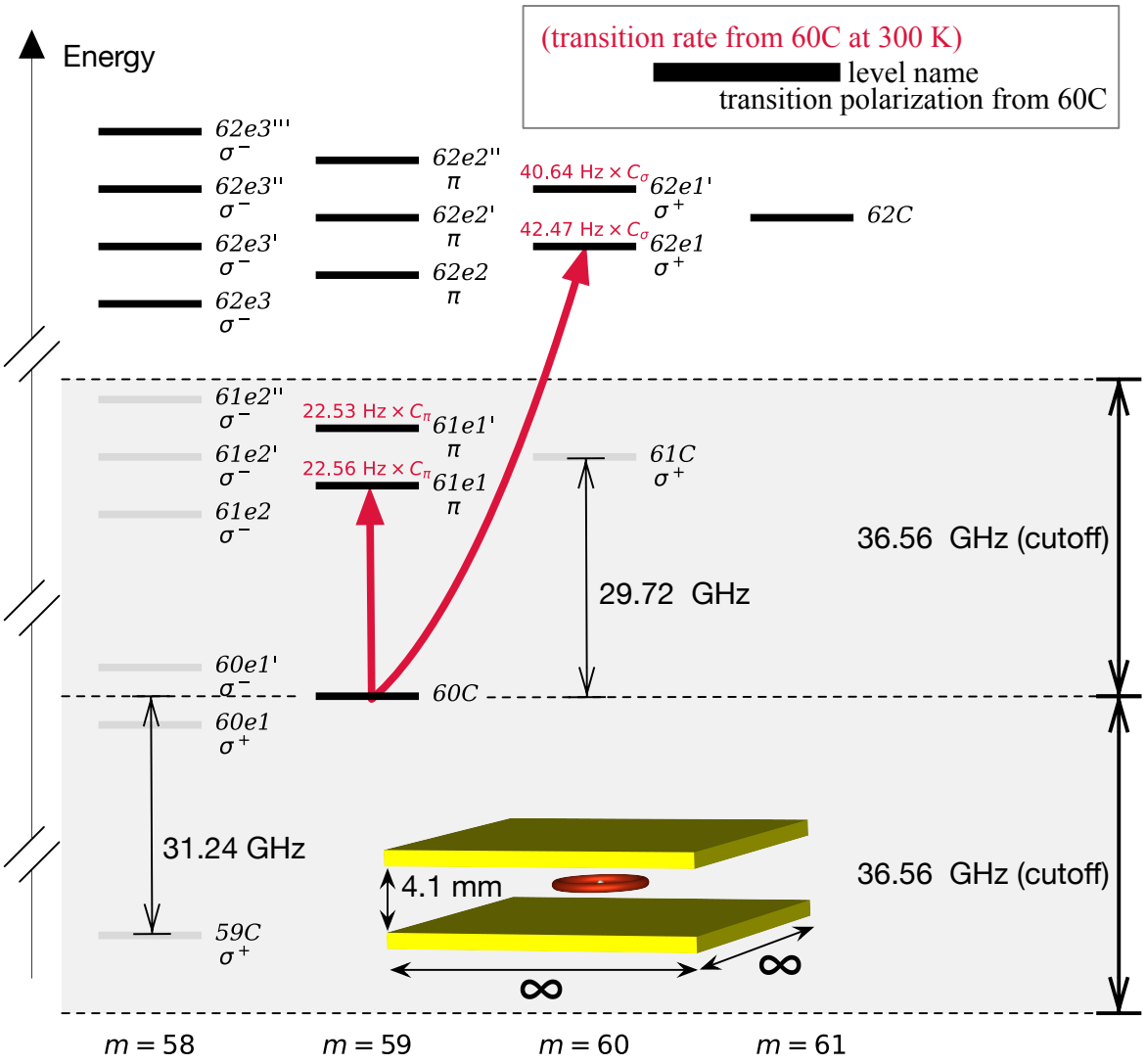

Fig. 2.13 *The dominant decay transfers from $|60C\rangle$ in a 4.1 mm ideal capacitor at 300 K. The CRA in the initial state $|60C\rangle$ and a quantization axis normal to the capacitor plates is positioned in the center of the capacitor (see bottom illustration). Two features are different compared with the free space: 1. Below the cutoff, all σ^+ and σ^- decay channels are completely inhibited (grayed out levels); 2. The dominant BBR transfers (guided by red arrows) are the two π transitions and the two 2σ (high frequency σ^+) transitions. Their corresponding thermal decay rates are modified by the C_π, C_σ factors given in Eqs. (2.36), (2.37) and shown in red. For the other non-inhibited transitions, the corresponding BBR-induced transfer rates (not shown) are all $\ll 1\,\mathrm{Hz}$.*

from Fig. 2.12: below the cutoff, the reduction in L for a fixed transition wavelength λ (of the only non-inhibited π transition) corresponds to a shift towards the left of the plot and hence more enhancement caused by the TEM mode. This gives rise to the interesting conclusion that for a CRA of a certain n at 300 K, there is a best capacitor spacing L that should be small enough to have a large cutoff frequency that puts both the σ and 2σ transitions below, but only barely below to not cause too much the π enhancement. For $60C$ and $50C$, this ideal L to enable their best possible in-capacitor lifetime is $L \approx 2.6\,\text{mm}$ (lifetime $\approx 8\,\text{ms}$) and $L \approx 1.5\,\text{mm}$ (lifetime $\approx 4\,\text{ms}$), respectively.

2.4.4.3 The decay rate modifications in a non-ideal capacitor

The ideal models we have studied allow us to obtain the exact mode structures and decay rate modifications in these models, from which we can identify the main features that also apply to a non-ideal capacitor with finite size, conductivity, and irregular geometries. For the latter case, one has to turn to the numerical simulation to obtain the rate modification.

Since the waveguide modes we treat are fundamentally classical electromagnetic modes and the atomic decays are dipolar. The capacitor's modification to the decay rate of the CRA as formulated in Eqs. (2.36), (2.37) is equivalent to the modification to the damping rate of a radiating dipole, the solution of which can be found purely by classical electrodynamics, which would be a more friendly approach for the numerical simulation.

A classical dipole's radiation field in the presence of a conducting surface can be expressed as the sum of the radiation of the dipole itself and that of its image dipole (the electric image method). A dipole parallel to the surface has its image dipole in phase opposition, and a dipole normal to the surface has its image dipole in the same phase. In between a capacitor, the dipole's radiation reflects successively between the two surfaces, corresponding to the radiation from the image dipoles and images of the image dipoles. This concept is illustrated in Fig. 2.14.

The electric image method in the capacitor problem allows also the treatment of resistive loss on the capacitor surfaces. This can be modeled as the attenuation in the amplitude and shift in the phase from each image dipole (each bouncing of the field). The destructive interference of the images are then not perfect, and the sharp cutoff in Fig. 2.12 is replaced by a smooth drop towards lower frequency [86].

In the simulations we perform, instead of a damping dipole with ever decreasing energy, we model the total radiated power (TRP) in a frequency spectrum of a radiating dipole with an excitation source. The obtained TRP thus corresponds to how much power we need to supply to a radiating dipole in order to prevent it from damping. And the ratio of the dipole's TRP in a structure to that in free space can give us the structure's damping rate modification to a classical dipole, or equivalently the decay rate modification to a CRA.

In Fig. 2.15 (a), we demonstrate the simulated σ transition modification factor C_σ for the transition $48C \leftrightarrow 47C$ in the inhibition regime. The simulation studies the TRP of a very small dipole antenna in the center of two square slabs with very high conductivity ($4.55 \times 10^9\,\Omega^{-1}\text{m}^{-1}$, corresponding to gold at 1 K [98]). We have also performed similar simulations with perfect conductor slabs, and the results are very similar. Therefore the deviation between the solid and the dashed lines we show in Fig. 2.15 (b) demonstrates mainly the finite size effect of the capacitor. Note that the multiple resonances in the blue dashed lines are not the same as the resonances in Fig. 2.12, since the plot span does not

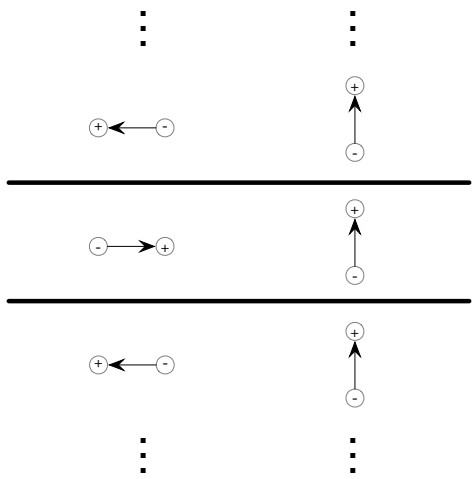

Fig. 2.14 *Principle of the electric image method for calculating the damping rate of a radiating dipole in the center of a capacitor. The zero energy damping of a transversely oriented dipole below the cutoff is understood as the perfect destructive interference of the radiations produced by the collection of phase-opposite dipoles (on the left). And the enhancement of energy damping of a vertically oriented dipole is because its radiation field constructively interferes with its image dipoles oscillating in phase.*

include the second order ideal capacitor modes which appear at $\simeq 150\,\mathrm{GHz}$. The multiple resonances then are to be attributed to the extra modes that cannot exist in an ideal capacitor (e.g. propagation modes in a finite capacitor do not have to travel perfectly parallel to the capacitor plates). These irregular features however do not appear below the cutoff. For the inhibition of $48C \leftrightarrow 47C$ transition shown in the panel (a), the better inhibition is always found at larger capacitor size a and smaller capacitor L (higher cutoff frequency).

The lifetime of $48C$ at $0.4\,\mathrm{K}$ simulated from this capacitor model is $\simeq 2500\,\mathrm{s}$ without considering other loss channels (e.g. collisions with background gas).

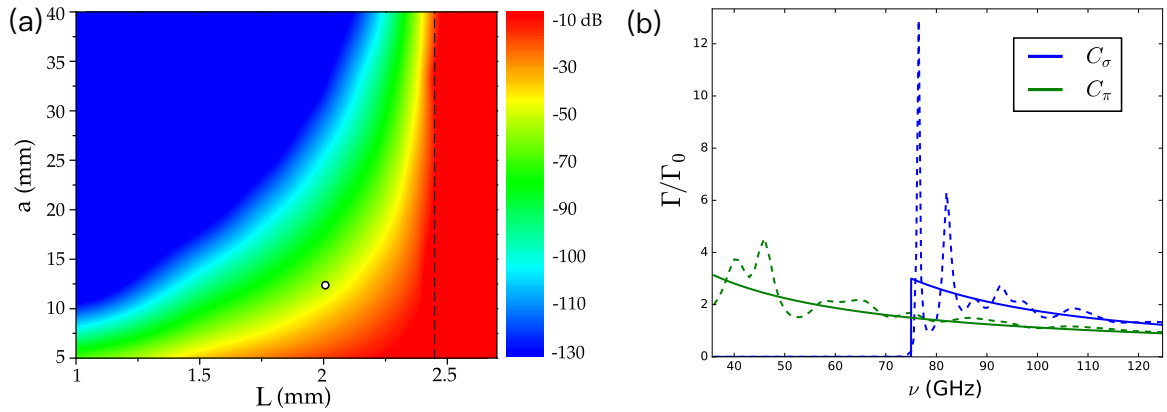

Fig. 2.15 *CST simulation of the C_σ in a capacitor of finite size [26]. The capacitor plates are high-conductivity slabs having the sides of length a. The capacitor spacing is L. (a) The C_σ at 61.407 GHz ($48C \leftrightarrow 47C$ transition frequency) as a function of a and L is plotted on the left. A white dot in the plot corresponds to $a = 13\,\mathrm{mm}$ and $L = 2\,\mathrm{mm}$. (b) The simulated C_σ and C_π in the white dot configuration are plotted in dashed lines. The corresponding solid lines are plotted with the analytical Eqs. (2.36), (2.37) to show the rate modifications in an ideal capacitor of the same $L = 2\,\mathrm{mm}$.*

Chapter 3

The Experiment: Cold CRAs Between Two Parallel Plates

This chapter discusses the experiment setup and its operation.

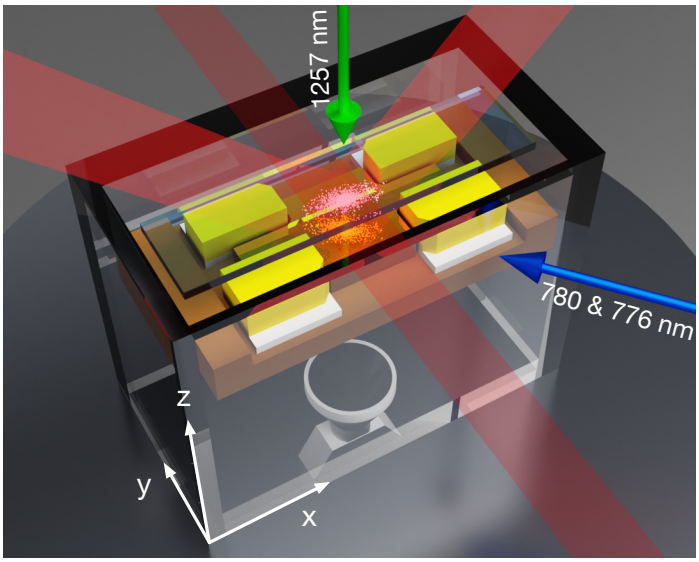

Fig. 3.1 *An artist view of the vapor cell setup. The MOT cloud is prepared in between a capacitor comprised of a transparent top electrode and a reflective bottom electrode that enables a mirror MOT configuration. The MOT atoms are then to be excited to a low-ℓ Rydberg state by a three-stage laser excitaion (arrows). The four transverse electrodes (in yellow) then produce a σ^+-polarized rf field to prepare the CRA. For the end detection, the CRAs are ionized and pushed through a detection hole in the bottom electrode and into the channel electron multiplier below.*

In Fig. 3.1, we show the defining feature of the experiment, a transparent glass cell no larger than the palm of the hand. This cell essentially isolate in space a small volume of vacuum filled with rubidium vapor with complete optical access. The lasers and magnetic field needed for cooling and Rydberg excitation go straight through its glass walls. Inside

this small cell, we fit in an assortment of electrodes, wrapping the slow atoms in their center, a spot where we have full control of the electric field. We then juggle atomic transitions ranging from optical (hundreds of THz) to microwave (tens of GHz) to radio frequency (hundreds of MHz), leading up to the preparation of the long-lived CRAs inside a 4 mm spacing plane-parallel capacitor in a room temperature environment.

In section 3.1, we give a complete description of all the aspects of the experiment setup. In section 3.2, we explain how the cold CRAs are prepared in the setup.

3.1 Experiment Setup Description

In this section we describe the complete experimental system that allows us to create an Ultra High Vacuum (UHV), in which we generate and then slow and trap the rubidium atoms inside a cold cloud, from which we finally prepare, manipulate, and detect the CRAs.

Subsection 3.1.1 presents the non-optical components of our vapor cell experiment. Subsection 3.1.2 introduces the Rydberg excitation lasers. The elements for the creation of the MOT are detailed in subsection 3.1.3. At last, in subsection 3.1.4, we present a series of simulation studies of the inhibition capacitor, which is the heart of the experiment.

3.1.1 A Room Temperature Vapor Cell Setup

The energy difference between two neighboring Rydberg manifolds is typically in the range of microwaves. Therefore, at room temperature, a Rydberg atom's lifetime is always severely limited by the 300 K blackbody radiation thermal photons in the microwave range, which cause a population redistribution across the adjacent Rydberg manifolds.

For a low-ℓ Rydberg atom, since its many spontaneous emission channels limit its room temperature lifetime as much as the stimulated decays caused by the BBR, the benefit of suppressing the number of MW thermal photons is noticeable but may not be enough to justify the need for a costly and high-maintenance cryostat. In fact, before the demonstration by Gallagher and Cooke [80] of a factor of three's reduction, caused by the 300 K BBR, in the radiative lifetime of the 17 P and 18 P states of sodium, the lifetime reduction effect of the room temperature BBR on the low-ℓ Rydberg atoms had been, according to their report, "ignored".

For the CRA however, since it has only one relatively weak spontaneous emission channel, at room temperature the BBR induced transfer rates are absolutely dominant, and typically surpass the spontaneous emission rate by a factor of 100 to 200. As a result, it is conventional to experiment with the CRA in a cryogenic temperature environment. In a ^{4}He cryostat, the lifetime of the $|52C\rangle$ is measured to be 3.7 ms [48], a huge factor of $\simeq 30$ higher than its corresponding theoretical lifetime of 133 µs at 300 K. This measured lifetime at low temperature is moreover limited by the modest 10 K cryostat temperature. A 10 ms-lived $|52C\rangle$ is expected in a 4 K environment.

In this work, our CRAs are prepared in a room temperature environment. The motivation is to demonstrate that, instead of a room-sized cryogenic system, we can use a thumb-sized plane-parallel capacitor to attain the same goal: to prepare a long-lived CRA. With the same result achieved by a far more economical system, we demonstrate a factor of six's increase in the CRA's radiative lifetime, reaching a millisecond-lived CRA at room temperature.

3.1.1.1 The Vacuum

Being a room temperature experiment, our setup can be made compact in size, as shown on the right in Fig. 3.2(a). In this full vacuum setup view, several 316L stainless steel tubes connected via CF40 flanges extend along the y direction. Horizontally, their full length in y is $\approx 500\,\mathrm{mm}$. Vertically, the height of the setup in z is $\approx 400\,\mathrm{mm}$. Below the glass cell on top, a few obviously larger flanges are of size CF63 to allow room for enclosing the electronic components and their supporting structure.

The vacuum in the setup is maintained by a turbo pump (HiPace 80, pumping speed $67\,\mathrm{L\,s^{-1}}$ for N_2) with its associated forepump pumping from the $+y$ end of the setup. The constantly operating turbo pump maintains the vacuum pressure at typically $\simeq 3\times10^{-9}\,\mathrm{mbar}$ as measured by a BA gauge immediately before the turbo pump inlet. This is one order of magnitude higher than the ideal datasheet final pressure $5\times10^{-10}\,\mathrm{mbar}$ of our turbo pump. This UHV is achieved after a full setup bake-out at $150\,^{\circ}\mathrm{C}$ for three days.

We do not have any pressure gauge close to the glass cell to directly measure the residual gas pressure inside. But the pressure difference between the cell and the turbo pump can be estimated given the pipe conductance in between. While the conductance of a vacuum pipe construct is often obtained via computer simulation, for a rough estimation, we use the well-known empirical formula by S. Dushman for estimating the room temperature conductance of a cylindrical tube of air in the molecular flow regime. With this formula, we estimate the effective pumping speed of the turbo pump to be $S = 22\,\mathrm{L\,s^{-1}}$ and the pipe conductance from the pump to the cell to be $C = 8\,\mathrm{L\,s^{-1}}$. Given the measured pressure at the turbo pump inlet $p_{\mathrm{inlet}} = 3\times10^{-9}\,\mathrm{mbar}$, the gas throughput is $Q = p_{\mathrm{inlet}}\times S = 66\times10^{-9}\,\mathrm{mbar\,L\,s^{-1}}$. With the above values, the pressure difference $\Delta p = p_{\mathrm{cell}} - p_{\mathrm{inlet}}$ between the cell and the pump inlet is given by Ohm's law $\Delta p = Q/C \simeq 8\times10^{-9}\,\mathrm{mbar}$. This puts the cell pressure at $p_{\mathrm{cell}} \simeq 1.1\times10^{-8}\,\mathrm{mbar}$. Knowing that the Dushman formula tends to overestimate the conductance, the pressure in the cell should be very well in the $10^{-8}\,\mathrm{mbar}$ regime.

The feedthroughs in the UHV are necessary for the generation, manipulation, and detection of the atoms. These three functions are fulfilled by the following electronic components inside the vacuum:

1. The electrodes (four rf electrodes and two capacitor plates) for rf-driven circularization, Stark field control, and field ionization.
2. The channeltron (also called channel electron multiplier) for atomic signal detection.
3. The rubidium dispenser for rubidium vapor generation.

These feedthroughs into the vacuum are connected to the outside via the SMA ports on the different flanges as shown in Fig. 3.2(a). We also summarize all the electronic components inside the UHV and their respective feedthroughs in the table below.

Components in UHV	**Feedthroughs**
4 rf electrodes	4 coaxial cables (potential control)
2 capacitor plates	2 coaxial cables (potential control)
1 channeltron	1 high voltage (-2.3 kV) input
	1 signal output (anode)
	1 voltage divider output
2 dispensers	2 thin copper rods (DC supply)

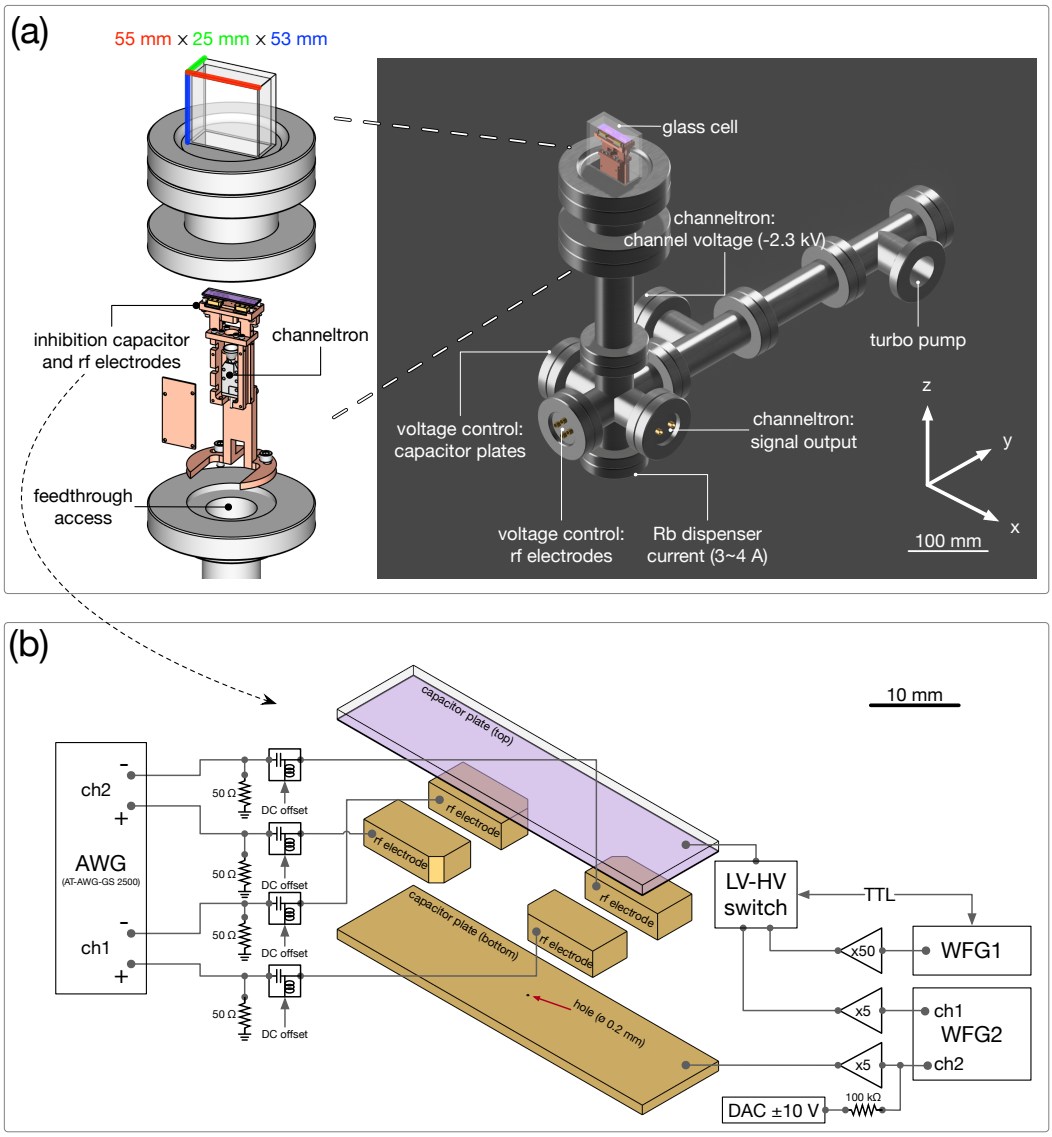

Fig. 3.2 *(a) On the right: the vacuum system. Its size is* ≈ 500 mm *in the y direction and* ≈ 400 mm *in the z direction. On the left: with the glass cell and its attached CF63 tube set opened, we can see the copper supporting structure for the inhibition capacitor on top and the channeltron below it. This copper support is screwed on the CF63 flange at its bottom. The hole in the center of this bottom flange allows the access of all the feedthroughs (coaxial cables and copper rods), which are not shown in this figure but can be seen in Fig. 3.5. In both views (left and right), the flange screws and screw holes are omitted for clarity. (b) The schematic of the electronic connections to the two capacitor plates and the four rf electrodes. The four* 50 Ω *resistors are installed to match the* 50 Ω *port impedance of the AWG. The AWG's outputs are DC-biased via four bias-tees. Regarding the 3D components: They are simplified in shape for clarity. The capacitor spacing has been greatly exaggerated. The capacitor plate on top is a transparent piece of glass, but with a conductive bottom surface (to be discussed in subsection 3.1.4), which is emphasized by a fake tint in purple.*

The items listed above are either commercial products designed to work in the UHV (Allectra coaxial cables, Saes Getter dispensers, Sjuts channeltron), or metal and glass pieces thouroughly cleaned beforehand. The cleaning procedure includes four ultrasound baths in the following sequence: an acetone bath, an ethanol bath, a 10% RBS cleaning agent bath, and a de-ionized water bath. Each ultrasound bath lasts 15 minutes, and the pieces are blow-dried with N_2 afterwards.

3.1.1.2 The glass cell

At the very top of the vacuum setup in Fig. 3.2(a) is a rectangular glass cell with its glassless bottom glued to a size-matched rectangular hole drilled through the very topside CF63 flange. This CF63 flange is made of Titanium, which has a thermal expansion coefficient close to that of the glass. The glass cell is made of optical glass (Hellma) transmitting wavelengths between 360 nm to 2500 nm. This cell has outer dimensions 55 mm × 25 mm × 53 mm and inner dimensions 50 mm × 25 mm × 50 mm, making its glass plates' thickness 2.5 mm at four transverse sides and 3 mm on the top side.

The epoxy glue (EPO TEK® H70E-2) applied on the cell-flange interface guarantees the airtight connection between the two. After mixing and sufficient stirring of the two components of the glue, we use a roughing pump to outgass the residual air in the mixture. Afterwards we apply a 1 mm layer of the mixture on the cell-flange interface. The curing of the glue consists in putting the whole cell-flange structure into an oven, taking 30 minutes to linearly reach 150 °C and then baking at this temperature for one hour.

It is our experience that multiple (5 or more) cylclings of the experiment between UHV and ambient pressure (*e.g.* for opening and changing the setup inside) would cause the glued cell-flange interface to gradually develop tiny crackings and eventual leaking. Therefore we note that this setup is ill-suited to experiments involving frequent vaccum breakings. The final data of this thesis is acquired from a setup that has been under the UHV non-stop for two years.

3.1.1.3 The electric field control

The glass cell houses, close to its top, the inhibition capacitor. In the center of the capacitor we trap the atoms (see subsection 3.1.3). The essential geometry of this capacitor is shown in Fig. 3.2(b), together with all its electronic connections.

All electrodes (capacitor plates included) have independent DC voltage control. The four rf electrodes are distributed transversely around the center of the capacitor. With such a layout these electrodes' DC offsets can be tuned to have the zero of the transverse electric field in the center (see subsection 3.2.2). Afterwards the quantization axis field is exclusively controlled by the capacitor's DC voltage.

The capacitor is truly versatile in this experiment, its inhibition asset is to be discussed in subsection 3.1.4. Aside from that, the capacitor plates are used to apply an electric field with fixed direction defining the quantization axis Oz at the different stages of the experiment (see section 3.2): a static field of a few to a few tens of V/m for Stark switching; a decreasing ramp across 100 V/m for adiabatic passage circularization; and an increasing ramp that shoots to more than 200 V/cm for state-selective field ionization. This field control is achieved by two waveform generators (Keysight 33522B), which we term "WFG1" and "WFG2" in Fig. 3.2(b).

In any single experimental sequence, before the final ionization detection, it is the WFG2 that applies a symmetrical pair of positive and negative potentials respectively on the top and the bottom plates, up to an independent voltage offset on the bottom plate. The 16 bits voltage resolution and the 20 V Vpp of WFG2, after a low-distortion 2-channel $\times 5$ amplifier (Keysight 33502A), result in a potential control precision of 1.5 mV on each capacitor plate. Given the 4 mm spacing of the capacitor, we estimate the resulting granular change in the quantization axis field to be 0.75 V/m, corresponding to a stepwise change in the WFG2's symmetrical output.

A finer field adjustment is provided by a 100 kΩ resistance connected in series to the internal 50 Ω resistance of the channel 2 in the WFG2. A computer controlled 12-bit DAC (output range ± 10 V) connected to the other end of the 100 kΩ resistance can then finely offset the channel 2's output voltage. In practice with this DAC field control we are able to tune any sequence's field globally by less than 0.1 V/m, and see its effect by the resonance of the rf with the CRA (see subsection 3.2.2.2). It is by this resonance that we detect the daily field's slow drift (if any), which is then to be compensated by the DAC field control. In this way it is assured that the same field condition is reproduced from day to day.

In addition to the small field control, the large field generation is also needed, first for ionizing the Rydberg states, subsequently for pushing the ions through the ø0.2 mm diameter hole drilled on the bottom plate [see Fig. 3.2(b)] to the channeltron below for detection. The 0.2 mm diameter is one order of magnitude smaller than the atomic decay transition wavelengths of the CRAs with $n > 50$ (wavelengths >5 mm). In this sense our drilled bottom plate is no different from a holeless mirror, both providing the same microwave mode structures for the CRAs prepared in this work.

The large field generation by the WFG2 is limited by its corresponding $\times 5$ amplifier, the output of which is bounded at ± 25 V. This limit of 50 V potential drop across the capacitor creates a max field of 125 V/cm. The lowest circular state this field can ionize in theory is $|52C\rangle$, but in practice we find the lowest in our setup to be $|53C\rangle$, $|52C\rangle$'s detection efficiency being too low. This field is thus not enough for ionizing all the populated circular states in our experiment which can be as low as $|46C\rangle$. Nevertheless we use the WFG2 for fast partial ionizations during the CRA preparation, as the WFG2 has a bandwidth of 30 MHz and can retract to a stable small field within a few µs after a large ionization field [1].

This stronger ramp is provided by the WFG1 in Fig. 3.2(b). The ramp waveform from the WFG1 is amplified by a factor of 50 (Falco Systems WMA-300) and applied on the top capacitor plate. This high voltage ramp overrides the low voltage signal from the WFG2 via a fast home-made high-low voltage switch [100]. The timing for switching to high voltage is controlled by a TTL signal that simultaneously triggers the WFG1 ramp. The final detection ramp we use as measured by the voltage drop between the capacitor increases from 0 V to 125 V in 75 µs. An ionization signal produced with such a ramp is shown in Fig. 3.19.

[1] This lack of ionization power was not intended for this experiment by design. Initially we worked with a 2 mm spacing capacitor (as proposed in [26]), inside which an ionization field twice as strong as in the current 4 mm capacitor could be achieved under the same setting. However, the rf field from the four transverse electrodes was heavily screened by the 2 mm capacitor and could not reach the atoms in the center well, making CRA preparation impossible. In addition, the close distance between the atomic cloud and the capacitor surfaces clearly worsened the electric field homogeneity as felt by the atoms. These difficulties could potentially be overcome in a future experiment (see chapter 5), but in our current setup, they forced us to double the capacitor spacing, after which we need a stronger ramp for field ionization in order to detect all the final states.

3.1.1.4 The rf field generation

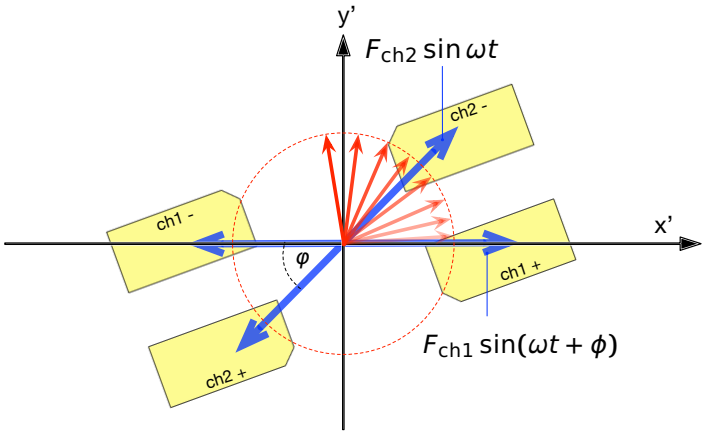

Fig. 3.3 *The illustration of the circular-polarized rf generation. The four rf electrodes are viewd from the top. The $x'y'$ is a Cartesian frame, different from the xyz coordinate convention elsewhere, with the x' axis chosen to coincide with the linear rf polarization generated by the channel 1 of the AWG. The AWG's channel 1 applies sinusoidally oscillating voltage on both electrodes lying on the x' axis. These two diagonally opposite electrodes' signals are π out of phase, creating in the center a linear polarized field $F_{\mathrm{ch1}} \sin(\omega t + \phi)$ in the x' direction. In the same fashion, the channel 2 generates in the center a linear polarized field $F_{\mathrm{ch2}} \sin \omega t$ but rotated by an angle φ. These two linear polarizations are shown by the blue arrows in the figure. To give perfectly circular polarized rf field in the center (the red arrows), the two channels' phase difference ϕ is found to be $\pi - \varphi$, and the two blue arrows' magnitudes have to be the same, i.e. $F_{\mathrm{ch1}}/F_{\mathrm{ch2}} = 1$. Note that the resulting magnitude of the circular polarization is always less than those of the two linear polarizations, because the latter are not normal to each other.*

The four rf electrodes around the atoms in Fig. 3.2(b) are designed to create a circular-polarized rf field with respect to the quantization axis in the z direction. This is an essential procedure for our Rydberg circularization process [70]. Physically, it is the circular-polarized rf that provides the σ^+-polarized photons, which keep increasing the angular momentum along Oz of the initial low-m Rydberg state until it reaches the circular state, which by definition has the highest magnetic quantum number within one n-manifold, *i.e.* $m = n - 1$.

The rf generation and waveform shaping is achieved by a high bandwidth Arbitrary Waveform Generator (Active Technologies AT-AWG-GS 2500). This AWG's 2.5 GS/s sampling rate is more than enough for generating our typically used rf frequencies (no more than 300 MHz). Within the 2 V Vpp limit, the rf envelope is freely programmable. As a result, this one device saves us the need for the complex mixing schemes involving rf synthesizers and low bandwidth AWGs, such as those found in other similar 4-electrode rf circularization setups in our group [59, 69].

The AWG has two channels, each channel has two analog outputs designed to be always opposite in polarity. The two channels' four rf outputs are DC-biased through four bias-tees before connecting to the four electrodes, as shown in Fig. 3.2(b). The four DC biases

are set to cancel out any stray electric field in the transverse directions, as introduced in subsection 3.1.1.3.

The two channels then essentially each generates in the center of the electrodes a linear polarized rf in two different transverse directions, as shown in Fig. 3.3. These two linear oscillations have the general forms $F_{\mathrm{ch1}} \sin(\omega t + \phi)$ and $F_{\mathrm{ch2}} \sin \omega t$, in which $F_{\mathrm{ch1,ch2}}$ is the electric field amplitude of the linear rf, ω the angular frequency of the rf, and ϕ the phase difference between the two channels. The angle φ between the two polarizations is determined by the geometry of the electrodes. To combine the two linear rf's into a perfectly circular polarized rf with amplitude F_{σ^+}, the following equality is to be satisfied:

$$F_{\sigma^+} \begin{pmatrix} \cos \omega t \\ \sin \omega t \end{pmatrix} = \begin{pmatrix} 1 & \cos \varphi \\ 0 & \sin \varphi \end{pmatrix} \begin{pmatrix} F_{\mathrm{ch1}} \sin(\omega t + \phi) \\ F_{\mathrm{ch2}} \sin \omega t \end{pmatrix} \tag{3.1}$$

Based on Eq. (3.1), one finds that the two channels' linear polarizations should have a constant phase difference $\phi = \pi - \varphi$, and should have equal magnitudes $F_{\mathrm{ch1}}/F_{\mathrm{ch2}} = 1$. Experimentally, the purest σ^+-polarized rf is found by tuning ϕ and $F_{\mathrm{ch1,ch2}}$ to minimize the population transferred to the elliptical state $|n, m = n - 2, k = 1\rangle$ after an adiabatic rapid passage (see subsection 3.2.3). One thus never needs to know the electrodes' geometry parameter φ *a priori*.

We note that the two linear polarized rf (the two blue arrows in Fig. 3.3) can be as well generated with only two electrodes (e.g. by suppressing the "ch1 +" and "ch2 +" electrodes in Fig. 3.3). The benefit of using all four electrodes in our experiment is twofold:

1. It improves the homogeneity of the rf field as felt by the atoms in the center.
2. The induced parasitic rf oscillations on the capacitor plates by any one rf electrode is largely canceled out by the other with the opposite polarity.

At the AWG's power limit (2 V Vpp), with optimized σ^+-polarized rf, we find a resonant rf Rabi frequency of 9.2 MHz along the lowest diagonal in the 52 manifold, as shown in Fig. 3.4. This corresponds to a F_{σ^+} of 1.47 V/m.

3.1.1.5 The source of the atoms

The *vapor cell MOT* experiments [101] such as ours have the luxury of loading a MOT directly from the low velocity class atoms in a low-pressure alkali vapor, without the need for atom pre-slowing (e.g. by a Zeeman slower).

Our source of rubidium atoms is the commonly used alkali metal dispenser from Saes Getters. This dispenser contains within a chromate of rubidium $Rb_2\,Cr\,O_4$ and two reducing agents Zr and Al. At high temperature and *in vacuo*, the reduction reaction generates pure rubidium[2], which vaporizes into the vacuum. Moreover, the reducing agents are also getters: at high temperature they are capable of absorbing common gases [102]. This getter property should at least partly explain the observed decrease in our UHV's pressure (from 6×10^{-9} mbar to 3×10^{-9} mbar) when the dispenser is being heated.

[2]For example, with the reducing agent Zr, pure Rb is obtained by:

$$4\,Rb_2CrO_4 + 5\,Zr \longrightarrow 2\,Cr_2O_3 + 5\,ZrO_2 + 8\,Rb$$

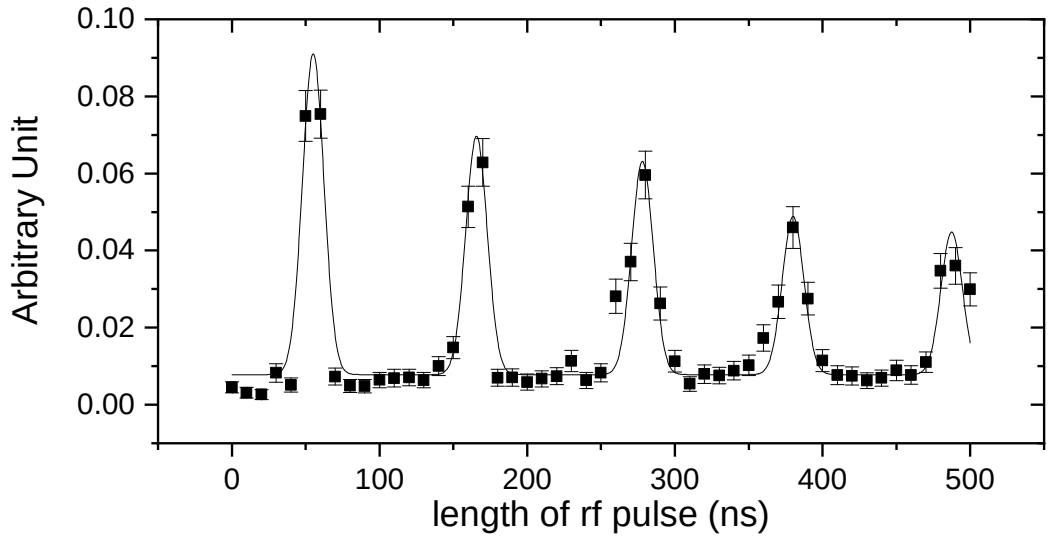

Fig. 3.4 *The σ^+-polarized radio frequency Rabi oscillation starting from $|52, m = 2\rangle$ along the lowest diagonal in the 52-manifold. The plot shows the amount of the $|50C\rangle$ transferred by a two-photon microwave π-pulse from the $|52C\rangle$ at the end of a resonant rf Rabi pulse in the 52-manifold as a function of the duration of this rf pulse. This oscillation gives a Rabi frequency of 9.2 MHz. The obtained $|50C\rangle$ has been normalized by a concurrent ionization signal to mitigate the shot-to-shot fluctuation, hence the "arbitray unit".*

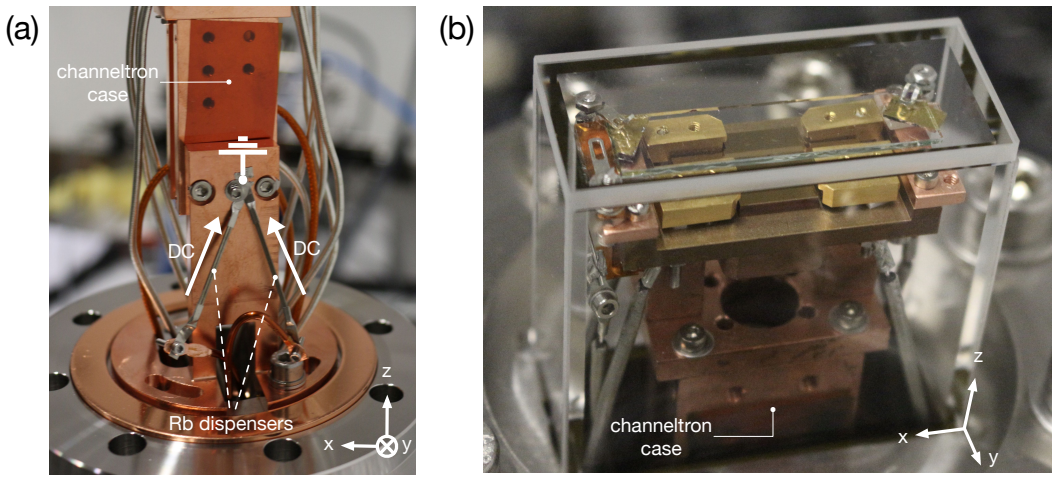

Fig. 3.5 *(a) The exposed inside of the experiment before closing the setup. This view is focused on the two rubidium dispensers installed below the channeltron case (the grounded case screens the undesirable large electric field generated by the channeltron). (b) After closing the setup, a close view at the inhibition structure and other visible parts through the glass cell.*

We installed two Rb dispensers immediately below the channeltron case, as shown in Fig. 3.5(a). The two dispensers have independent current supplies. At all times, only one dispenser is active, and the other serves as a backup. The DC current through the dispenser heats it up, first to start the reduction reaction, subsequently to evaporate the generated pure rubidium. The deposition of the rubidium vapor on surfaces such as those of the cell glass, the capacitor, and the electrodes is not visible to the eyes. However the deposition's effect can be observed from two aspects:

1. The loss of reflected laser beam power: The bottom capacitor plate is a gold-plated mirror. As shown in Fig. 3.10(b), a 780 nm laser beam (one of the cooling beams) incident at 45° from the top of the cell will be reflected at 45° and come out from the top of the cell. The reflectivity given by these two beams drops from 83% to 54% after one day's use of the dispenser, given a new cell and a new capacitor to start with. The reflectivity however stablizes at the low value afterwards, implying the saturation of the Rb deposition on the series of surfaces (glass, ITO coating, and gold) in the way of the laser beam.

2. The change in the electric field: A change of 0.1 A to 0.2 A in the dispenser current, hence the Rb dispensing rate, leads to the immediately noticeable field drift of approximately 1 V/m per hour. If the dispenser current is to be kept constant after the initial change, this field drift slows down after one or two days. Greater change in the dispenser current would naturally lead to a more dramatic drift in the electric field.

Due to the second effect above, our dispenser's current is kept constant at all times, unless the atom dispensing rate drops noticeably (the cold cloud becomes dilute, less atoms detected, etc.). The constant DC current we apply on a new dispenser gradually increased from 2.8 A to 3.2 A over the course of 10 months. The highest current applied corresponds to a dispenser temperature of 450 °C, according to the dispenser's manual.

3.1.2 Laser System

The laser system used for the Rydberg excitation and the MOT creation is mostly inherited from the previous works in our group. While many details and discussions regarding the system's previous states can be found in [103–106], this subsection explains the parts relevant to this thesis' work in their current states.

3.1.2.1 The three-stage excitation

To reach a low-ℓ Rydberg state, we use a well established three-stage excitation scheme [107] to bring the atoms from the ground state $5^2S_{1/2}$ to the 58 F state of ^{85}Rb. The three laser wavelengths used are (in the order of the three stages):

$$
\begin{aligned}
780\,\text{nm} &\qquad 5^2\mathrm{S}_{1/2}, F = 3 \longrightarrow 5^2\mathrm{P}_{3/2}, F' = 4 \\
776\,\text{nm} &\qquad 5^2\mathrm{P}_{3/2}, F' = 4 \longrightarrow 5^2\mathrm{D}_{5/2}, F'' = 5 \\
1257\,\text{nm} &\qquad 5^2\mathrm{D}_{5/2}, F'' = 5 \longrightarrow 58\,\mathrm{F}, m = 2
\end{aligned}
$$

The first stage transition serves at the same time as the MOT cooling transition. In addition, for the MOT a repumper is used to prevent the atoms from accumulating in the ground state hyperfine level $5^2S_{1/2}, F = 2$ (see the level scheme in Fig. 3.6). In other words we use the common rubidium D_2 line for cooling and trapping.

3.1.2.2 The frequency stabilization

All three excitation lasers are locked by the Pound-Drever-Hall technique [110], which entails a phase modulation (equivalent to frequency modulation) applied to the laser in order to create an error signal for the frequency stabilization. This modulation is applied as shown in Fig. 3.7 by EOM (Electro-Optic Modulator) #1~#3 respectively on the 780 nm, 776 nm and 1257 nm laser beams. Before leaving the table, these three excitation lasers have their AOM (Acousto-Optic Modulator) diffracted beams coupled into the output fibers. The rf-pulsed control of the AOM diffraction allows us to apply $\simeq 1\,\mu s$ excitation pulses at the beginning of each experimental sequence: the 780 and 776 nm lasers are pulsed by the same AOM #3, the 1257 nm laser by AOM #6.

The 780 nm laser is locked on a saturated absorption spectroscopic signal from Rb vapor cell #1. The actual frequency of the 780 nm laser after locking is 100 MHz below the first-stage transition frequency due to the effect of AOM #1 [103, p.48]. Therefore, when this red-detuned 780 nm laser co-propagates with the 776 nm laser in Rb vapor cell #2, the latter laser excites the same velocity class as the former, and finds itself locked at the same detuning, *i.e.* 100 MHz red-detuned from the second-stage transition. Excitation beams at 780 nm and 776 nm have their red detunings with respect to their target excitations fully compensated by AOM #3 (+100 MHz) before being sent into the experiment. The bottom right branch of the 780 nm laser in Fig. 3.7 is under-compensated by AOM #2 (+80 MHz), allowing at the output fiber a beam detuned by $\delta \simeq -20\,MHz$, a few times the natural line width ($\simeq 6\,MHz$ [111]) of the D_2 transition, to be fed into a fiber port cluster, and then to be further separated into the four mirror MOT beams (see subsection 3.1.3.1).

The final Rydberg excitation laser at 1257 nm is locked on a tunable standard, such that this laser can reach its target Rydberg state shifted in energy at various electric fields. It also allows the selection of different n-manifolds[3]. This tunable standard is a Fabry-Pérot cavity with a tunable length, serving as a *transfer cavity*. The cavity's length is stabilized by an EOM-modulated branch of the 776 nm beam, and once stabilized, the cavity itself is used as a standard for locking the final 1257 nm laser. In addition, the 776 nm branch for cavity stabilization goes through a "double pass" AOM configuration (AOM #5 in fig. 3.7) before reaching the cavity. This allows the fine-tuning of the 776 nm laser frequency by several tens of MHz, which, through the transfer cavity, can be used to tune the stabilized 1257 nm laser frequency by the same order of magnitude, a useful feature we use to overcome small laser frequency drifts.

The repumper laser, unlike all other ones, is not locked on an EOM-modulation-generated error signal, but on one that is generated by a light wave beat between the 780 nm and the repumper lasers. For this reason, the beams at these two wavelengths, separated by $\simeq 3\,GHz$ when both correctly locked, co-propagate before entering a high frequency photodiode used

[3]For the result of this thesis, we consistently operate the Rydberg excitation laser at 1257.1 nm. But in practice, we made many other studies operating at 1258.4 nm, 1257.1 nm, 1256.1 nm, etc. to reach respectively 52 F, 58 F, 65 F, etc.

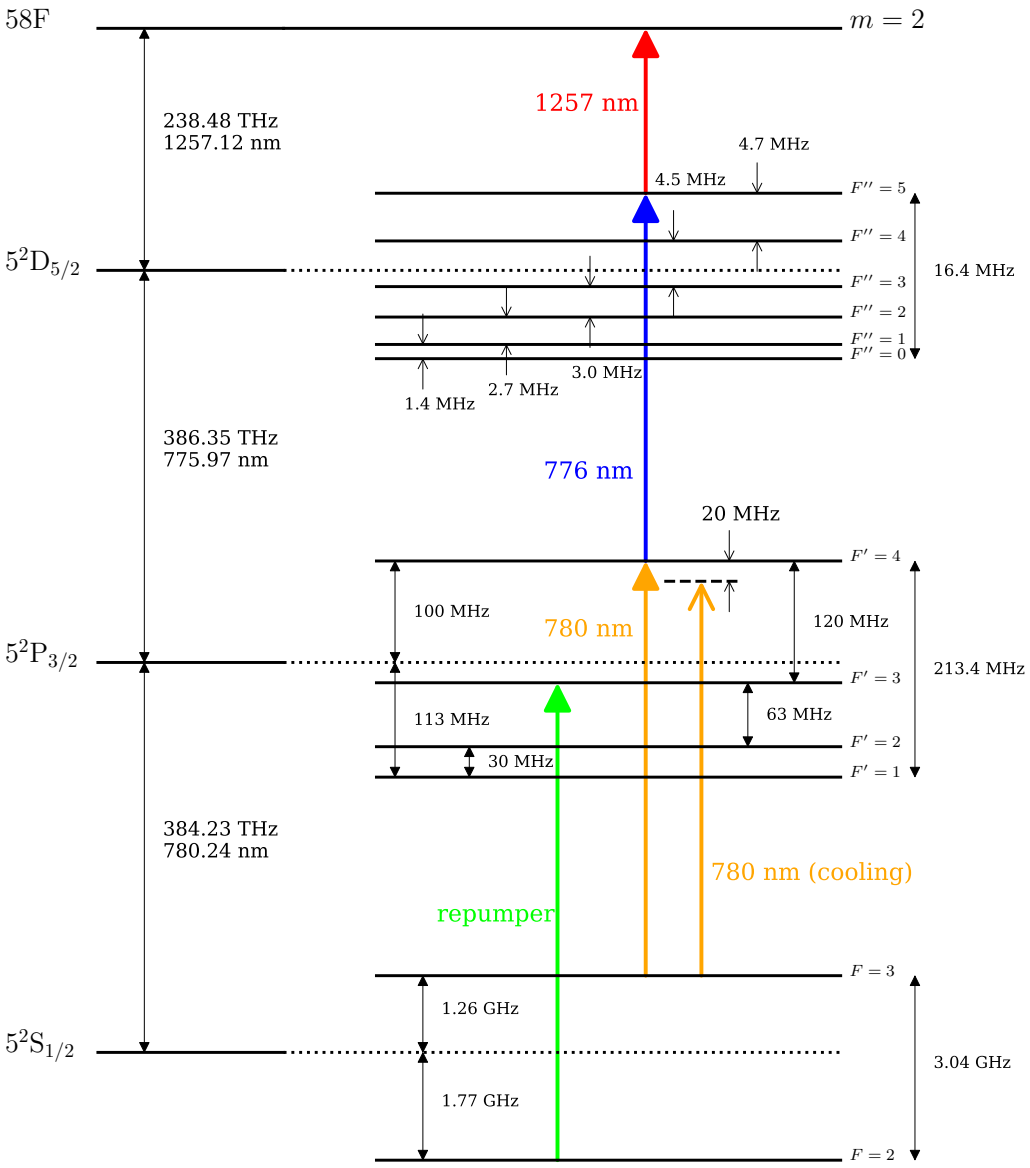

Fig. 3.6 *Level scheme of* ^{85}Rb. *We show as colored arrows the MOT's cooling and repumping transitions as well as the three excitation stages to reach the Rydberg level* $|58\,\mathrm{F}, m = 2\rangle$ *at a small Stark switching field. The transition values are taken from [108, 109]. The hyperfine level splittings are exaggerated.*

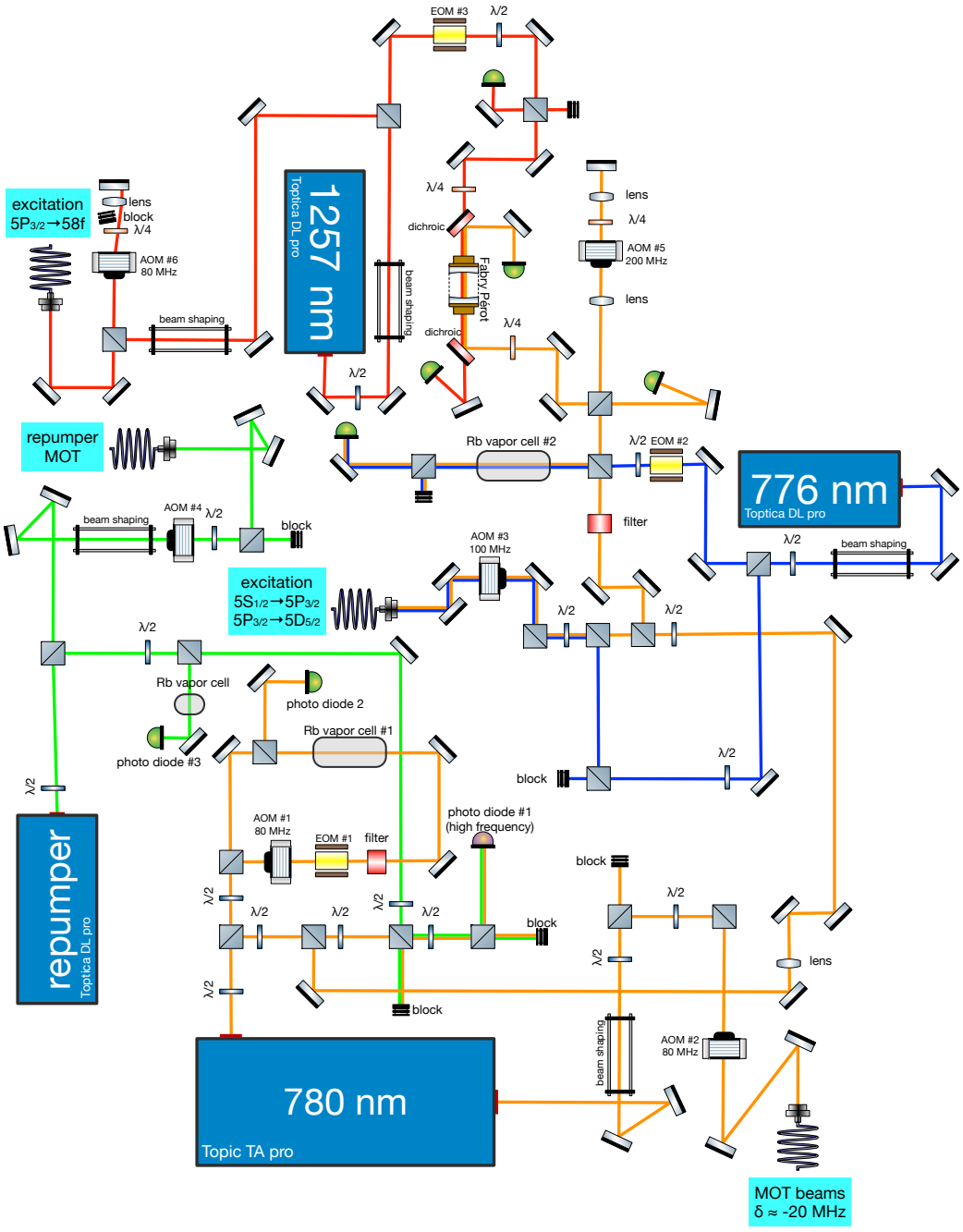

Fig. 3.7 *Laser (optical table) scheme. In ascending order of the wavelength, the 776 nm, the repumper, the 780 nm, and the 1257 nm beams are assigned the colors blue, green, orange, and red, respectively. Arrows of the matching colors in level scheme Fig. 3.6 show these lasers' corresponding transitions. The cyan text blocks mark positions of output laser fibers and their usage in experiment.*

to register this beat (photodiode #1 in Fig. 3.7). Once the 780 nm laser is locked, scanning the repumper laser will cause their beat frequency to also scan relative to a YIG frequency standard. The final mixing of the beat and the YIG frequencies produces the error signal for the repumper laser, for details see [106, p.104].

All lasers introduced above, after shaping and locking, are coupled into polarization-maintaining optical fibers that connect to the six output beam collimators around the glass cell (see Fig. 3.10). Among these six beams, four are for MOT cooling (see subsection 3.1.3.1), two are for Rydberg excitation (see subsection The excitation beams).

3.1.2.3 The excitation beams

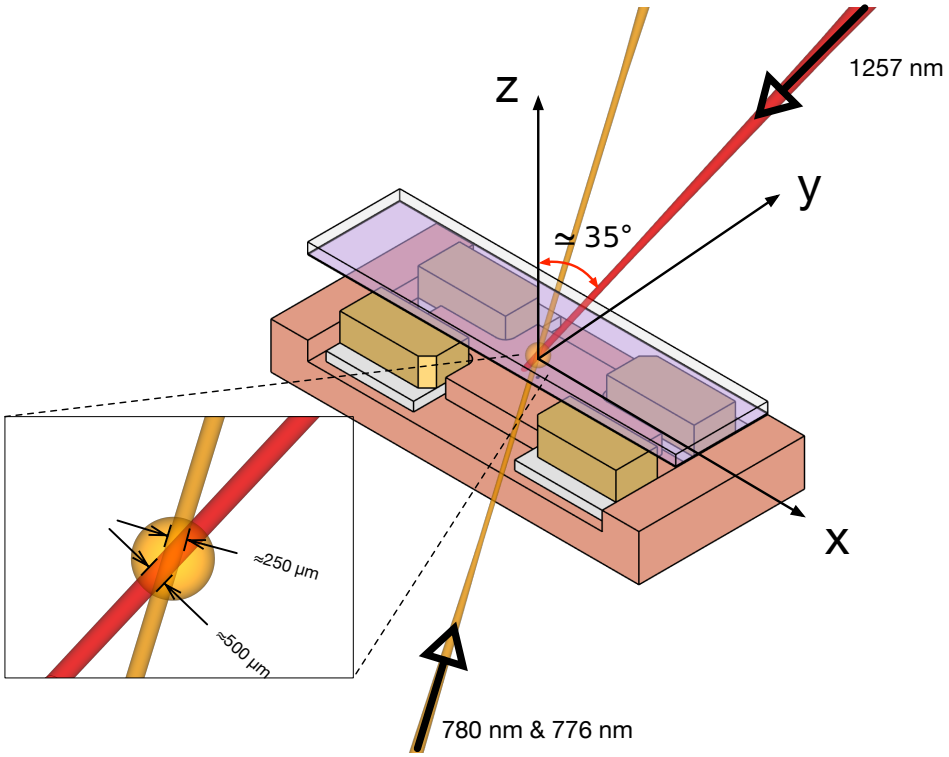

Fig. 3.8 *The isometric configuration of the two exication beams around the capacitor. The surface of the laser beams is chosen to be at the FWHM of the beams' transverse Gaussian intensity profile. The 780 nm and the 776 nm lasers copropagate in one single beam (orange) in the xy plane. The 1257 nm laser beam (red) shoots from the top, making a $\simeq 35°$ angle with the Oz axis in the xz plane. The two exictation beams overlap in the center of the capacitor where their Gaussian diameters coincide within the atomic cloud region, which is represented by a orange sphere with a 1 mm radius.*

The 780 nm and the 776 nm lasers, responsible for the first and second stage excitations, exit as one single beam from the collimator aiming at the capacitor spacing and arrive at the atoms following a horizontal path in the xy plane. This horizontal beam is polarized in the z direction, parallel to the quantization axis, and therefore both the 780 nm and

the 776 nm lasers carried within are π-polarized. The 1257 nm beam, responsible for the last-stage excitation, exits from a collimator positioned above the cell. The resulting beam makes a $\simeq 35^\circ$ angle with respect to the Oz axis and lies in the xz plane. This top beam is circular polarized in an attempt to create as much σ^+-polarized excitation as possible, which can in turn excite the most $|58\,\mathrm{F}, m = 2\rangle$ and the least $|58\,\mathrm{F}, m = -2\rangle$, the former being the starting level of our circularization by a rapid adiabatic passage (see subsection 3.2.3). The aforementioned $\simeq 35^\circ$ tilting angle of the 1257 nm beam is necessary to have an unblocked beam path to reach the atoms. Making the top beam completely vertical in the Oz direction would create the purest σ^+-polarized 1257 nm light possible, but unfortunately in our setup this ideal beam path is blocked by the MOT coil above the cell (the blue coil in Fig. 3.11).

We note that the above polarizations of the excitation lasers are not pure due to our setup limitations. However since our circularization procedure selects only $|58\,\mathrm{F}, m = 2\rangle$, atoms not excited to this state cannot connect to the circular states in the end, and can thus be cleared by a partial ionization that finally removes all but the CRAs.

The horizontal beam's Gaussian diameter is measured to be $\simeq 250\,\mu\mathrm{m}$. In this beam, the 780 nm and 776 nm laser powers are maintained respectively at $250\,\mu\mathrm{W}$ and $600\,\mu\mathrm{W}$. The 1257 nm beam from the top has a Gaussian diameter of $500\,\mu\mathrm{m}$ and laser power of $3\,\mathrm{mW}$. The stepwise increase in three lasers' power is to compensate for the decrease in dipole matrix elements coupling increasingly higher atomic levels. In the end, the two beams are set to converge to their Gaussian diameters in the center of the capacitor, where they overlap and define in the atomic cloud an excitation volume of approximately $250 \times 500 \times 250\ \mu\mathrm{m}^3$ up to a rotation.

3.1.3 Magneto-Optical Trap

A Magneto-Optical Trap (MOT) is used in this experiment to allow the measurement of the lifetime of the CRAs *in situ* within a $\simeq 1\,\mathrm{ms}$ time scale. Technically, this means the atoms need to be slow enough so that the Rydberg atoms prepared from these slow atoms during the $\simeq 100\,\mu\mathrm{s}$ CRA preparation time and the following $\simeq 1\,\mathrm{ms}$ decay time do not diffuse considerably. In practice, a hard upper limit also exists on the velocity of an atom initially centered in the capacitor: it should not escape from the effective detection region limited by the ø0.2 mm hole [see Fig. 3.2(b)] through the center of the bottom mirror. For ^{85}Rb, such a travel distance of 0.2 mm within 1 ms approximately translates into a MOT temperature of half a milli-Kelvin, well within the cooling capability of a typical MOT. As a result, we choose to create a MOT directly in the geometric center of the inhibition capacitor.

In Fig. 3.9 we show some typical sizes of the atomic cloud. The conditions that differ in these images include the rubidium dispensing rate (the dispenser current), the quality of the vacuum, and the intensity of the cooling beams. The magnetic gradient however stays the same across all the images. From these images we estimate that the diameter of our atomic cloud ranges from 1 mm to 2 mm. In all scenarios, the cloud is to be kept in the center of the gap, from which the CRAs are prepared and detected.

3.1.3.1 The MOT beams

In a conventional plane parallel capacitor, to allow 3 pairs of counter-propagating MOT beams access to the atomic cloud region, holes need to be drilled on the capacitor. These holes ideally should be millimeter-sized to preserve the integrity and hence the inhibition

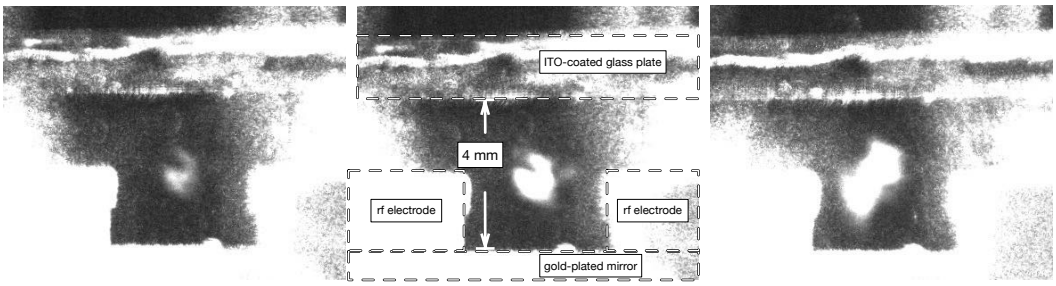

Fig. 3.9 *The atomic cloud trapped in a Magneto-Optical Trap in the center of the inhibition capacitor as viewed by a CCD camera aiming at the gap of the capacitor. From left to right we showcase three different sizes of the atomic cloud from small to big. We typically work with the size in the center, where we have labeled the inhibition capacitor's visible components and the 4 mm spacing between the two conductive planes.*

asset of the capacitor. However, reducing the MOT beams' diameter (twice their Gaussian beam waist) to millimeter proves challenging, due to fast decrease of the number of trapped atoms in this small-beam regime [112]. Experimentally we were able to create a millimeter-size-beam 3D MOT in freespace (without the capacitor) in our glass cell setup, however the time and effort involved to find and maintain such a small MOT, on a daily basis, practically left no room for other experimental activities.

To work with thick MOT beams, we use as the top piece of our plane parallel capacitor a glass plate with a conductive surface coating of Indium-Tin-Oxide(for its discussion see subsection 3.1.4). Since ITO is optically transparent, there is no size limit for beams passing through the top of the capacitor. In addition, we use a standard mirror MOT configuration [see Fig. 3.10 (b)]: In the xz plane, we apply two MOT beams incident at 45º with respect to the mirror plane. The result is that each one of the 45° MOT beams, after reflection on the mirror, counter-propagates with the other incident beam. We thus obtain, in the overlap region between the incident and reflected beams, two pairs of counter-propagating beams, orthogonal to each other, in the xz plane. One last pair of counter-propagating beams goes across the spacing between the capacitor along the y axis, fulfilling all the 6 MOT beams required.

We show in Fig. 3.10 the configuration of the mirror MOT beams. All optical components, together with the MOT coils and the imaging cameras are installed on a 30 cm × 30 cm breadboard, which is screwed at the level of the cell flange. The one cooling laser beam at the bottom right of Fig. 3.7 is divided through a fiber port cluster (Schäfter + Kirchhoff FPC-069) into four beams which are led by polarization-maintaining fibers into four collimators (Thorlabs F810APC-780), labeled by numbers #1 through #4 in Fig. 3.10(a). These four collimators provide the four thick MOT beams (Gaussian beam diameter 7.5 mm). All the collimators and the beam deflecting mirrors in their light paths are installed on the 2-axis mounts, this ensures that there are enough adjustable degrees of freedom to make relevant light beams completely overlap as well as pass through any designated point within the capacitor. Considering the symmetry of the setup, the natural choice is to make the 45° beams from collimator #1 and #2 overlap and target the center of the bottom mirror, then make the beams from collimator #3 and #4 (in the xy plane) overlap and pass through the

middle of the capacitor. With the help of the diaphragms before all the four collimators, we are able to constrain the MOT beams' size to millimeter, and perform the beam alignment with precision.

The power balance between the counter-propagating beams are ensured by direct measurement through an optical power meter. The four cooling beams' exact power values are often tuned by a small amount for MOT position maintenance, but in general, the two 45° cooling beams have their powers close to the saturation intensity of the rubidium's D2 cycling transition ($1.67\,\mathrm{mW/cm^2}$), while the two cooling beams in the xy plane have powers at half of this saturation intensity.

After the above procedures for cooling beam alignment and power balancing, the only cooling beam adjustment we perform is via the fiber port cluster to control the power balance between all cooling beams. The cluster provides enough degrees of freedom for us to move the atomic cloud by a few millimeters in all three directions merely by adjusting the relative cooling beam powers.

3.1.3.2 The MOT coils

Fig. 3.11 shows the six coils we use to generate the quadrupole field for the MOT. In addition to creating the magnetic gradient, the more than usual number of coils allow them to double as compensation coils: they provide complete degrees of freedom for moving the quadrupole field in space. To simulate the quadrupole field, we record the dimensions, the relative distances, and the applied current values of the real coils, and create in the simulation similar coil geometries bearing these parameters as shown in Fig. 3.11(a). Then we perform a finite element simulation [113] to obtain the spatial distribution of the magnetic field generated by them, using the coil current values shown in the cyan text boxes in Fig. 3.11(a). These current values are experimentally found to make the MOT optimally centered in the capacitor. They are also the persistent current values used during the collection of the data published in [49].

In Fig. 3.11(a), the origin of the coordinate frame is set to coincide with the geometric center point of the capacitor, around which the MOT should ideally reside. The two yellow coils are in a *Helmholtz configuration*, generating a magnetic field in the $-x$ direction at the origin. On the other hand, the top blue coil generates at the origin a field in the $+x$ direction. The cancellation of these two fields creates a quadrupole field with its zero point around the origin, and its largest magnetic gradient in the xz plane. The two red coils are in an *anti-Helmholtz configuration*, they create the magnetic fields equal in magnitude and opposite in direction at the origin, where their largest gradient is along the y direction. We note that the two yellow coils are connected in series and thus always have to bear the same current from the same current source. The two red coils however have independent current sources and can bear different currents. The fact that these two red coils coincide in their current values when the MOT is optimally centered is a consequence of the symmetry of the setup.

By fine-tuning the currents in these coils, we can adjust the zero point of the quadrupole field, hence the MOT's position, in all directions. The competition between the blue and the yellow coils lead to a controlled displacement of the zero field point along the z axis; the imbalance between the two red coils' currents lead to an adjustable displacement along the y axis. The last adjustment along the x axis is provided by the green coil, which corresponds to the one that is wired closely around the bottom of the glass cell.

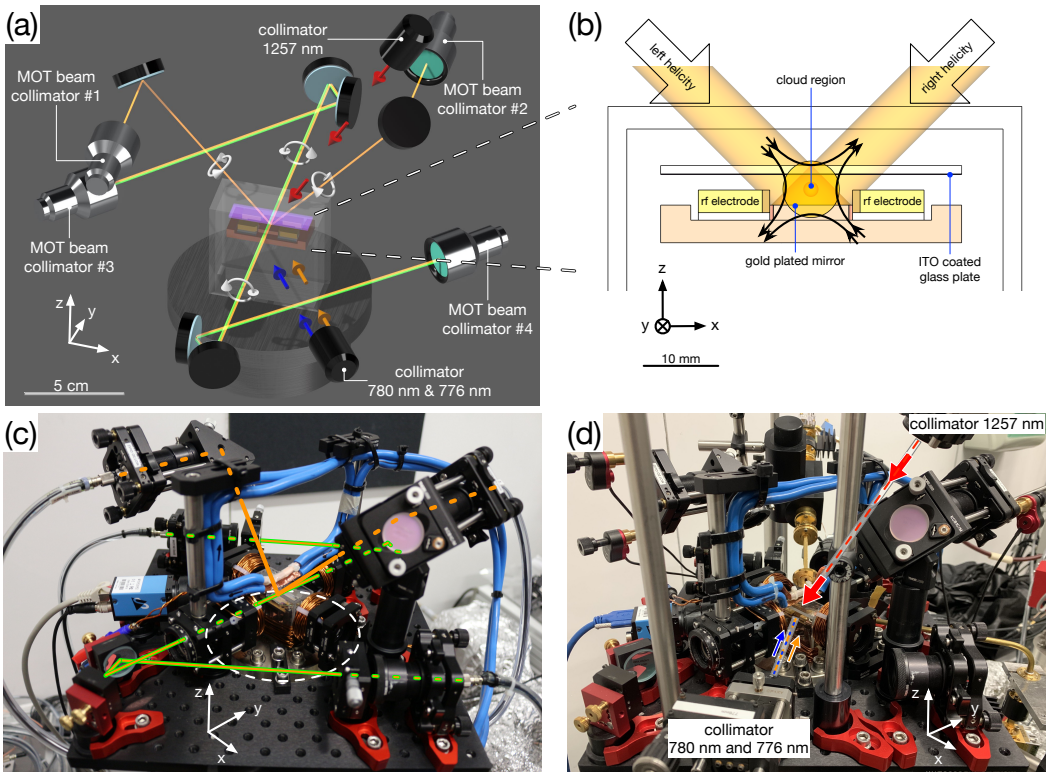

Fig. 3.10 *The laser beam configuration around glass cell. (a) The isometric model showing only essential laser components with all other parts removed. The Always-on MOT cooling and repumping beams are respectively represented by the orange and the green lines, the pulsed excitation beams by colored straight arrows. Four white arrow loops give the polarizations of the four MOT cooling beams traveling* towards *the cell. Note that thinner-than-real-beam lines are used to help clearly trace the cooling and repumping beams. (b) Shown in the xz plane is the capacitor illuminated by the MOT beams represented in their* 7.5 mm *diamater Gaussian beam sizes. Two 45° beams are in the xz plane, two horizontal beams travel perpendicularly in and out of the page. The four beams' overlapping defines the region where the MOT can reside. (c) A photograph of the laser components around the cell. On a small* 30 cm × 30 cm *breadboard, only MOT-related components are installed (no Rydberg excitation beams). In the geometric center of the bread board, a circular hole (traced by white dashed line) is made to allow the insertion of the glass cell. The MOT cooling beam paths are shown in orange lines, with green border when copropagating with repumper beam. Lines are dashed when line paths are blocked from direct view. (d) A photograph of the final setup with excitation beam collimators installed. Shown in colored arrows are the paths of excitation beams.*

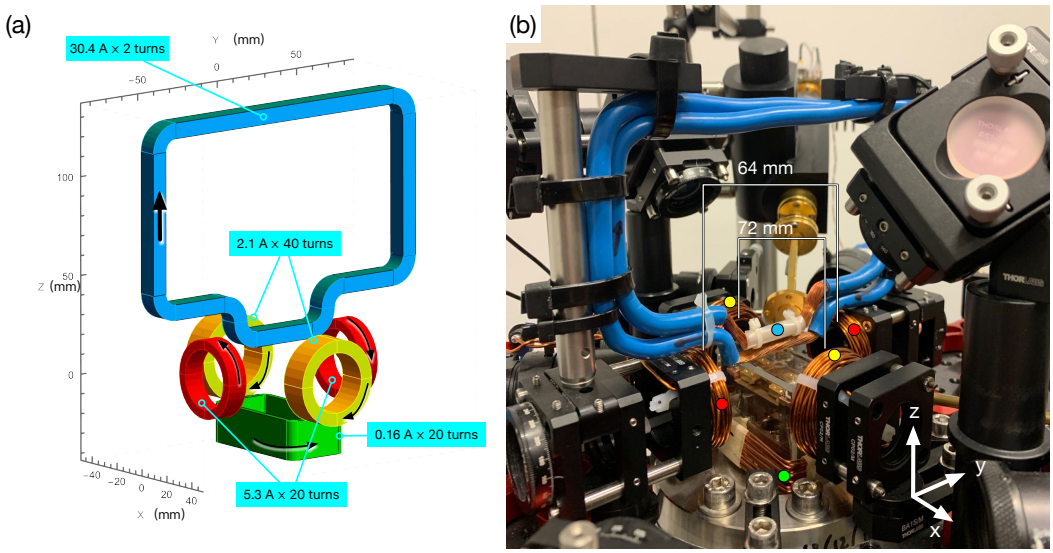

Fig. 3.11 *The configuration of the MOT coils. (a) Isometric view of the current carrying geometries used in the magnetic field simulation. The current directions are given by the black arrows, the current values and number of wire turns are given by the cyan text boxes. The center of the capacitor (not shown in figure) is defined as the origin of the coordinates. (b) A photograph showing the coils from the same view angle. Each coil has been labeled by their corresponding color with respect to (a). The distances between the Helmholtz coils (yellow) and the anti-Helmholtz coils (red) are given. The thick blue coil above the glass cell is made with a multi-strand, 6 gauge copper wire capable of carrying a maximum current of* 100 A. *The bottom part of the blue coil has been stripped of the thick wire skin and stretched down in order to be as close to the cell as possible (*$\simeq$ 2 mm *away from the top of the glass cell and* $\simeq$ 13 mm *away from the center of the capacitor). The rest of the coils are made with single-strand copper wires with a diameter of 1.25 mm.*

We show the resulting simulated quadrupole field with no free parameters in Fig. 3.12. While the current values given in 3.11(a) produce in the experiment an optimally centered atomic cloud, we see that they do not reproduce a quadrupole field centered precisely at the origin of coordinates in the simulation. However the size of our atomic cloud is typically in the range of 1 mm to 2 mm (see Fig. 3.9), such a cloud if assumed to be centered perfectly at the zero point of the quadrupole field in Fig. 3.12 can still include in its volume's span the origin of coordinates. In other words, the MOT's position obtained from this simulation would in reality bring atoms to the x,$y \in [-0.1\,\text{mm}, 0.1\,\text{mm}]$ range delimited by the ion inlet hole at the bottom mirror, and hence yield non-zero ion counts upon ionization. Experimentally this is a critical criterion for us to determine whether the MOT is centered in the xy plane. The simulation thus represents a good enough agreement with the experiment. In practice, the quadrupole field's discrepancy from the origin in such a sub-millimeter scale can easily arise from the imperfect shapes and positions of the real coils. Earth's magnetic field (0.25 Gauss to 0.65 Gauss) also can lead to a sub-millimeter shift to the magnetic zero [see panel (b) and (e) of Fig. 3.12]. Moreover, it is common for the atomic cloud to be located

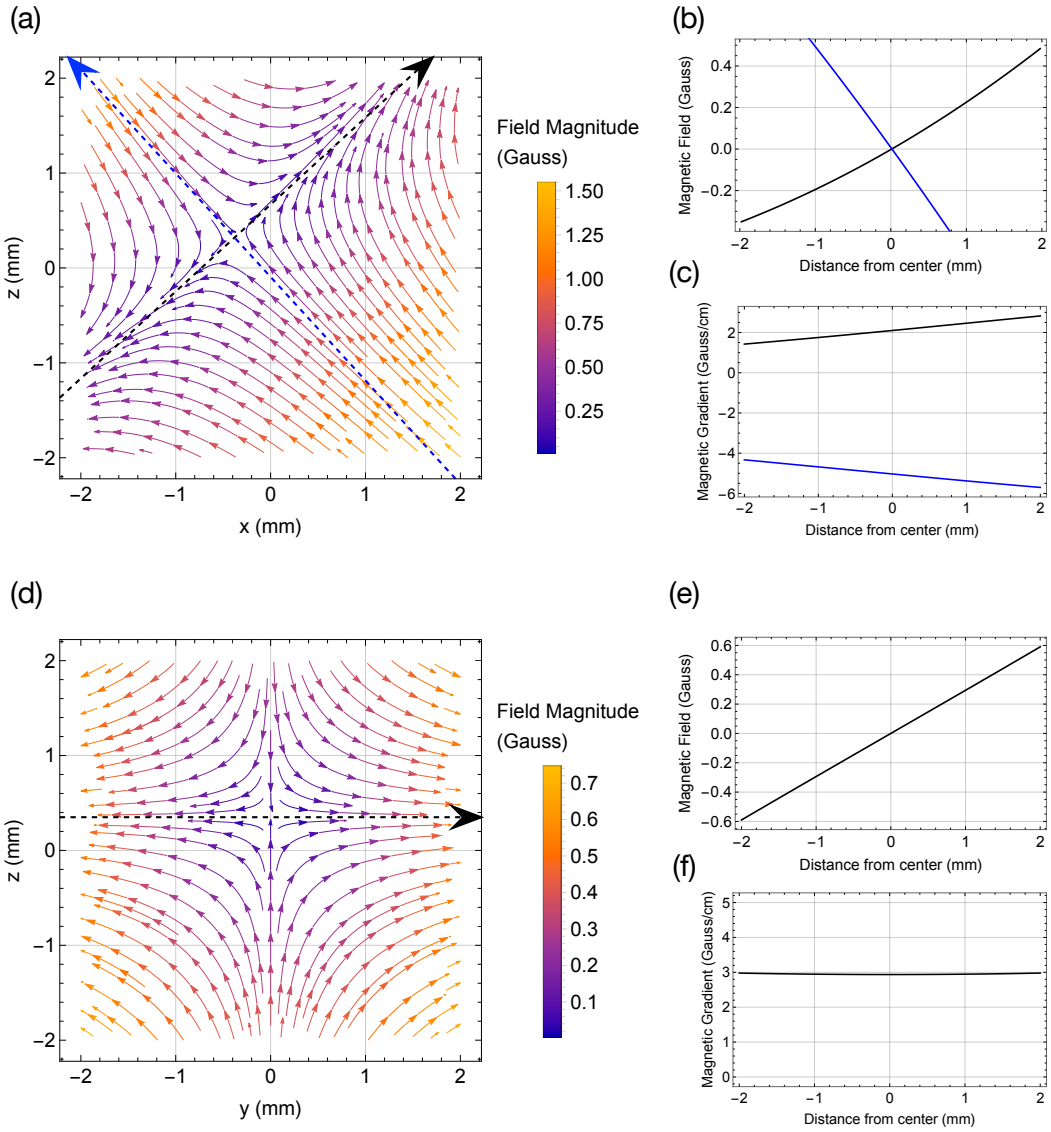

Fig. 3.12 *The simulated quadrupole field. (a) The magnetic field lines and magnitude in the xz plane that includes the origin of the frame in Fig. 3.11. The black and blue dashed lines intersect at the center of the quadrupole field and are orthogonal to each other, as the cooling beams should be in this plane. (b) The magnetic fields along the black (the weak axis) and the blue (the strong axis) dashed lines. The corresponding positive directions are indicated by the color-matching arrows in (a). (c) The corresponding magnetic field gradient. (d) The simulated quadrupole field in the yz plane that cuts at the intersection of the dashed lines in (a). (e) The magnetic field along the black dashed line (the second strong axis). (f) The corresponding magnetic field gradient.*

away from the absolute zero point of the quadrupole field, due to the imbalance between the intensities of the counter-propagating MOT beams.

The panel (c) and (f) of Fig. 3.12 show the simulated magnetic gradient along the three major gradient axes of the MOT. The strongest axis is the blue axis in the panel (a). The gradient along this axis at the quadrupole center is 5 Gauss/cm. The other two axes, the black axes in the panel (a) and (d), have respectively the gradient values 2 Gauss/cm and 3 Gauss/cm at the quadrupole center. From the sum of the gradients along the two weaker axes one obtains the gradient along the strong axis. To estimate the Zeeman shift in our experiment, assuming an unlikely bad scenario when the atom is located 1 mm away from the magnetic zero along the strongest gradient axis. For two states separated by $\Delta m = 1$, the Zeeman shift between them is given by $\mu_B/h = 1.4\,\mathrm{MHz/Gauss}$. The assumed bad scenario then brings a mere 0.7 MHz Zeeman shift per $\Delta m = 1$, negligible compared to the linear Stark shift at hundreds of MHz per $\Delta m = 1$ that we apply in the experiment.

3.1.4 Inhibition Capacitor

This subsection focuses on the numerical simulation of the lifetimes of the in-capacitor CRAs under various conditions.

We first explain the numerical simulation model capacitor (subsection 3.1.4.1), with which we simulate the lifetimes of the CRAs we prepare in the experiment capacitor.

The transparent top capacitor electrode is a important feature of this work, we introduce its properties in subsection 3.1.4.2 and investigate the influence of its resistivity on the lifetimes of the CRAs in the capacitor.

The lifetimes of the in-capacitor CRAs can also depend on its vertical position in between the two surfaces. The simulation of this position dependence is analyzed in subsection 3.1.4.3.

Finally, we see through simulations that the measured lifetimes of the CRAs have a large tolerance to the potential skewness of the parallel plates.

3.1.4.1 The modeled experiment capacitor

The inhibition capacitor shown in Fig. 3.5 (b) is produced from the same 3D design with which we numerically simulate of the atomic decay rates modification. The principles of the simulation was introduced in subsection 2.4.4.3.

We carry out the TRP simulation with the commercial software CST Studio Suite®, which is a multiphysics simulation software capable of numerically solving for the GHz field in the presence of lossy materials. Other similar software include COMSOL® and Ansys HFSS®.

The simulation model is shown in Fig. 3.13. In this 3D model, the bottom capacitor and the four transverse electrodes are set to have the room temperature conductivity of gold, corresponding to the gold plating applied to the real components. The bulk glass plate is assigned the dielectric properties of the lead glass. At the bottom surface of the glass plate, we set an ohmic sheet to mimic the conductive ITO coating (see subsection 3.1.4.2) applied on the corresponding real glass plate. In our simulations, the sheet resistance is either set as $8\,\Omega$/square or $10\,\Omega$/square. The former is our measured number, the latter is the typical number given in the datasheet. However, we found this difference in resistivity produces at most a few percent of difference in the simulated lifetimes of the inhibited circular states. This lifetime difference is no larger than the errorbars of our measured lifetimes, therefore

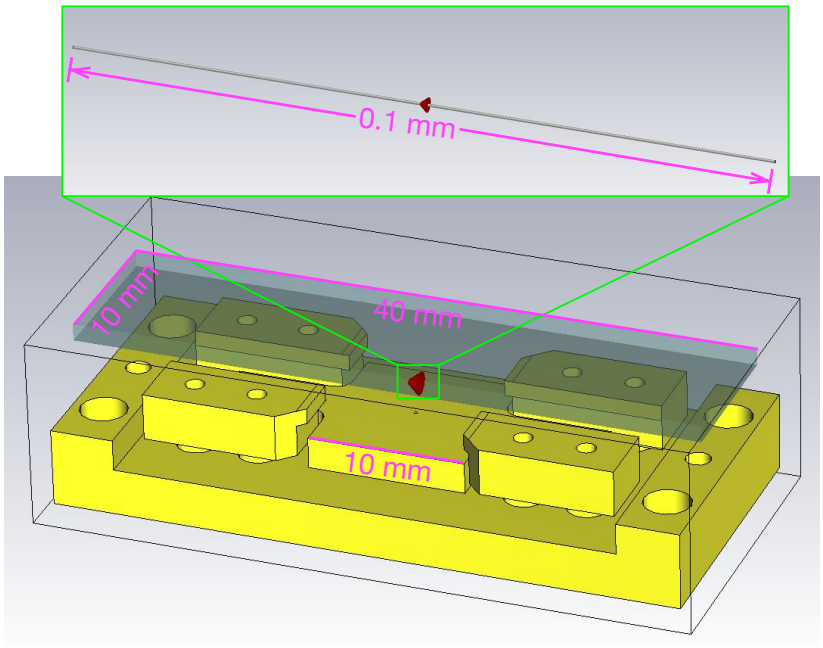

Fig. 3.13 *The 3D capacitor model realized in the CST Studio. With this model we perform all the relevant simulations. The capacitor is comprised of a transparent top plate electrode and an opaque bottom plate electrode (gold). In between the capacitor, four transverse rf electrodes (gold and no contact with the capacitor) surround a central mirror platform. In the very center of the capacitor is a small dipole antenna as the source of the radiation field in the simulation. From the gold surface below the antenna to the glass surface above it, the distance is 4.10 mm.*

the resistivity of the ITO does not stand as a very sensitive parameter within a reasonable range.

The field source of our TRP simulation is a small dipole antenna in the center of the capacitor. The two antenna rods are set to be perfect conductors and have a combined length of 0.1 mm. Other arbitrary small length l can be equally chosen as long as the limit $kl \ll 1$ (k is the wave number of the emission field) is ensured so that the antenna approximates a Hertzian dipole. As a side note: real experiments with large antennas that do not approximate well the dipole limit have been performed, but the measured radiation power from the antenna in between two plates still reproduces the essential inhibition and enhancements features [114].

The 3D model in Fig. 3.13 evidently leaves many screw holes open. For example, the glass plate and the four transverse electrodes are floating in the vacuum without the screw supports we apply in the real setup. However, we have modeled a more detailed 3D structure in an effort to resemble the experiment capacitor as much as possible down to the screws and nuts. The simulations with the more detailed model produce only marginal differences compared to the ones with the gross structure model in Fig. 3.13. Therefore the gross structure model is enough to produce the main mode structures in the capacitor, and all the simulations we present come from this simpler model[4].

[4]However, we note that if we try to moderately exaggerate some details in the model, which do not

The spacing of the real capacitor was measured by a vernier caliper to be 4.10 mm, a fixed parameter in the simulation (see appendix C). This spacing corresponds to a sudden cutoff at 36.56 GHz in an ideal capacitor that can inhibit the σ decay channels of the CRAs with $n \geq 57$. The simulated decay modification factors C_σ and C_π for a CRA in the geometric center of the capacitor are shown in Fig. 3.14.

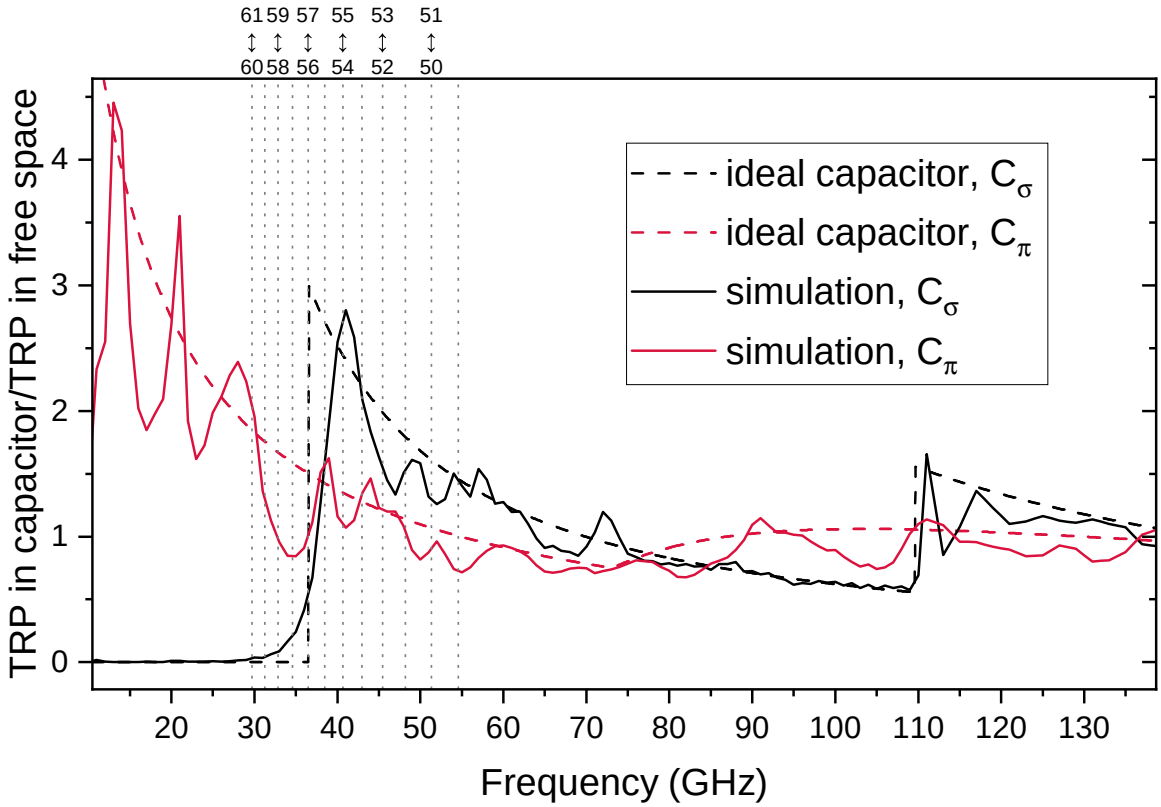

Fig. 3.14 *The C_σ and C_π of from the simulated capacitor (solid) in Fig. 3.13 and the ideal capacitor (dashed). Both are set to have the same spacing of 4.1 mm. The simulated ITO sheet resistance is 8 Ω/square. The vertical dotted lines give the circular-to-circular transition frequencies relevant in this work. The simulation curves are in steps of* 1 GHz. *A wide frequency range is chosen to reveal both the first and the third order cutoffs.*

In this figure, the simulated C_σ and C_π are obtained with the dipole antenna oriented transversely and vertically, respectively. These two TRP ratios clearly restore the main features of the ideal capacitor, including the two cutoffs corresponding to the first and third propagation modes of the capacitor, and the enhancement of the TEM mode below the cutoff.

exist in the real setup, such as adding extra screws and teflon spacers very close to the dipole (but not invading the central 10 mm × 10 mm square mirror region), we can obtain a much greater enhancement at the cutoff resonance, which in magnitude is similar to the experimentally measured enhancement that the simple model can not produce. This suggests, for this compact capacitor design, some mode structures can be highly sensitive to the in-capacitor components. Inside the real capacitor, some modes could indeed be fairly different from the ones in the simulation, which in the end can only approximate the reality.

3.1.4.2 The Indium-Tin-Oxide coating

The Indium-Tin-Oxide (ITO) is one of the most used conductive coating for the transparent electrodes. It is a doped semiconductor with a very high density of mobile charge carriers. The transparency of ITO coating is due to its relatively low plasma frequency (250 THz to 300 THz [115]) than the common metallic conductors. In our experiment, this transparency is essential, allowing the optical access of a pair of mirror MOT laser beams (see subsection 3.1.3). The ITO coating is also central in other proposed plans using exclusively transparent capacitor electrodes to inhibit the decays of the CRAs, while allowing the access of the optical tweezers to trap single CRAs at the same time [46].

The conductivity of ITO can be modeled by the Drude theory, which expresses the optical conductivity $\sigma(\omega)$ of a good conductor in the following general form:

$$\sigma(\omega) = \frac{\sigma_{\mathrm{dc}}}{1 - i\omega/\Gamma} \tag{3.2}$$

where σ_{dc} is the conductor's DC conductivity, ω is the circular frequency of the electromagnetic wave incident on the conductor, Γ is the Drude relaxation rate characterizing how frequently a charge carrier is scattered in the solid. For the ITO, Γ is in the 10 THz range [116]. Therefore in Eq. (3.2), the ratio ω/Γ would be negligible if $\omega/2\pi$ is in the range of tens of GHz, corresponding to our CRA's decay transition frequencies. This allows us to treat the response of the ITO in our MW simulations as frequency-independent: $\sigma(\omega) \approx \sigma_{\mathrm{dc}}$, an assumption we use throughout the whole of subsection 3.1.4. Beyond this simple Drude model argument, the ITO's frequency independence in the tens-of-GHz regime has also been experimentally tested [46].

The ITO coated glass plate we use in the experiment is a customized product manufactured by Techinstro. The bulk plate has the dimensions 40 mm × 10 mm × 1.1 mm. The ITO coating has a thickness of 180 nm to 200 nm, allowing an optical transmittance of $\geq 90\%$. The conductivity of this coating inferred from the thickness and sheet resistance is 0.5×10^6 S/m to 0.7×10^6 S/m. For comparison, the conductivity of the gold plating for the other electrodes is 44×10^6 S/m (room temperature), and a potential Rb desposit layer [117] (conductivity 8.3×10^6 S/m) on the ITO would make its surface more conductive. Finally, the microwave reflectivity of the ITO coating in the range of 45 GHz to 65 GHz is estimated to be 86%~93%. This value is inferred from the finesse of a cavity comprised of the ITO glass plate and a spherical copper mirror.

To understand the effect of the ITO resistance to the lifetime of the CRA, we survey the simulated 300 K in-capacitor lifetimes of the relevant CRAs assuming an exaggerated variation of tens of Ω/square in the sheet resistance of the ITO. This simulation is shown in Fig. 3.15. In panel (a), we see that the lifetimes for any sufficiently inhibited CRA have a moderate dispersion of $\simeq 10\%$ under the different ITO resistance values. In the inset we highlight the lifetime of $60C$ as a function of the chosen resistance values.

It is interesting to observe that the lifetime of $60C$ peaks at $\simeq 20\,\Omega$/square, while the intuitive expectation is that the lower the resistance, the more the approximation to an ideal capacitor, and the better the lifetime under the inhibition. The cause of this peak lifetime resistance is explained by the competition between the σ^+ and the π transitions of $60C$ (2σ decays play a minor role in this particular case). For this highly inhibited circular state, its σ^+ decay rates is almost equal to its $\pi + 2\sigma$ decay rates, modification to the latter rates then brings appreciable change in the resulting lifetime. The detail of this competition is

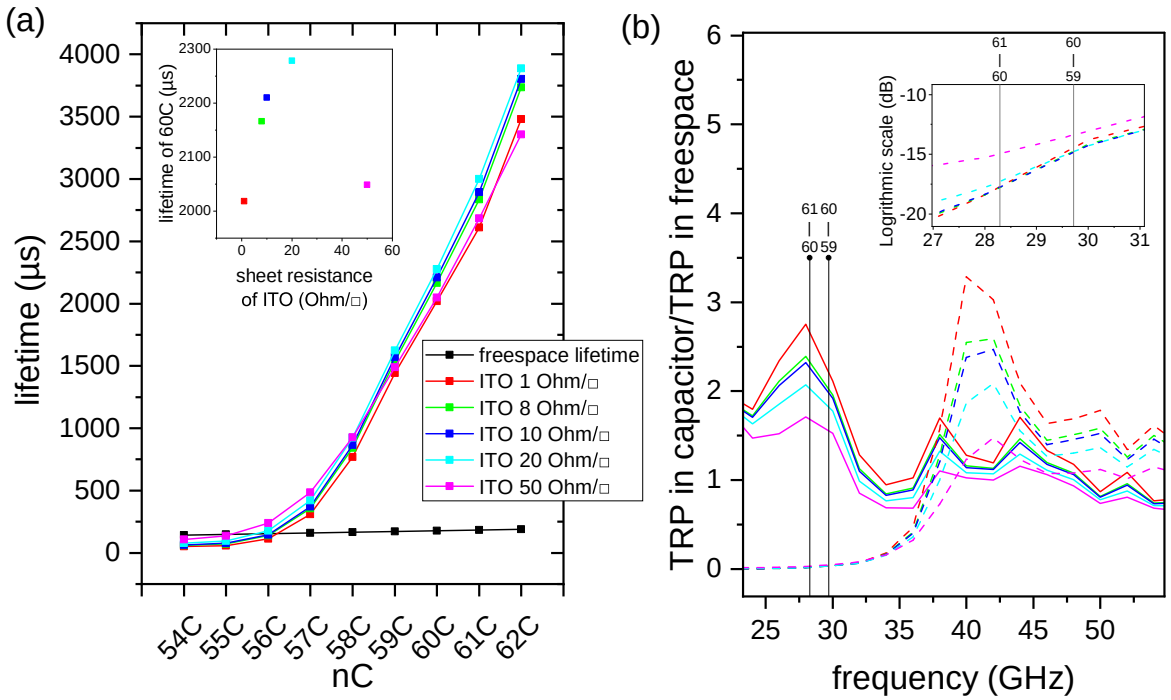

Fig. 3.15 *The dependence of the simulated lifetimes of the CRAs on the sheet resistance of ITO coating. (a) The lifetimes of* $54C$ *to* $62C$ *simulated with the capacitor in Fig. 3.13 with varying sheet resistance of the ITO coating. (b) The simulated TRP ratios with the varying ITO resistance. Solid lines are the simulated* C_π*, dashed lines the simulated* C_σ*. Inset is a log scale plot of* C_σ *focused on the* σ^+ *transition frequencies of* $60C$*. The color code between (a) and (b) is shared.*

shown in panel (b), which gives the simulated C_σ and C_π modifications for the surveyed resistance values. In this TRP ratio plot, we mark the two transition frequencies of the two σ^+ decay channels of the $60C$, knowing that under a moderate Stark shift the two π transitions ($60C \rightarrow 61e_1/61e_1'$) would only be $\simeq 100\,\mathrm{MHz}$ away from the $60C \leftrightarrow 61C$ transition frequency and therefore can be represented by the same vertical mark line. From $1\,\Omega$/square to $20\,\Omega$/square, we see in the main plot of (b) a 25% decrease of π transition rates (equal to the TRP ratio), while in the inset of (b), the corresponding σ^+ transition rates barely increase in this resistance range. We thus observe from $1\,\Omega$/square to $20\,\Omega$/square a $\simeq 15\%$ increase in the simulated lifetime of $60C$. This case study shows us the complication incurred in the transition from the simple σ^+-dominated lifetime to the lifetime determined by multiple comparable decay channels.

In reality, the ITO coating of our transparent electrode has a batch-to-batch dispersion of at most $7\,\Omega$/square to $12\,\Omega$/square. We further confirmed the DC sheet resistance of our sample by the Van der Pauw method (a four-terminal measurement). The measured sheet resistance is $7.9\,\Omega$/square as shown in Fig. 3.16.

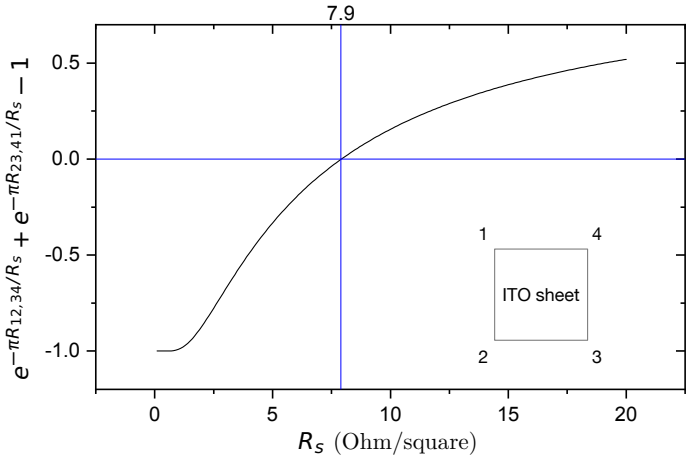

Fig. 3.16 *The Van der Pauw method measurement of the sheet resistance of the sample of our transparent electrode. The four corners of the sample plate are numbered (inset) and attached to four terminal wires. The notation* $R_{12,34} \equiv V_{34}/I_{12}$ *is a resistance quantity defined as the ratio of the voltage measured between the terminals 3, 4 to the current applied between the terminals 1, 2. The measured sheet resistance* $R_{\rm s}$ *is found when the Van der Pauw equation* $(e^{-\pi R_{12,34}}/R_{\rm s}) + (e^{-\pi R_{23,41}}/R_{\rm s}) - 1 = 0$. *For the measurement curve in the plot:* $V_{12} = 93.33\,\text{mV}$, $I_{34} = 53\,\text{mA}$, $V_{41} = 92.85\,\text{mV}$, $I_{23} = 53\,\text{mA}$.

3.1.4.3 A dipole not in the center of the capacitor

Inside an ideal capacitor, there are well defined propagation modes. For the several low order modes, their node structures have only a few transverse electric nodes and antinodes across the two capacitor surfaces. Thus as a transversely positioned dipole is moved from one surface to the other, it switches between the max coupling and the zero coupling to the low order modes, the resulting dipole damping rate changes drastically as a function of the dipole's vertical position in the capacitor. This was demonstrated in subsection 2.4.4.1. In the simulation with the experiment model capacitor, this position dependent decay rate modification is also evident.

In Fig. 3.17, we show the simulated C_σ and C_π for a dipole in the center and shifted by $\pm 1\,\text{mm}$ from the center. Although the experiment capacitor model does not have up-down symmetry, the simulation results from the $+1\,\text{mm}$ and $-1\,\text{mm}$ configurations appear to be very similar. In particular, we see in panel (a) the expected emergence of the second order resonance at twice the first order cutoff frequency for the $\pm 1\,\text{mm}$ configurations.

The panel (b) in log scale focuses on the inhibition cutoff of panel (a). The most striking feature in plot (b) is that: by simply raising or lowering the dipole by 1 mm, it experiences a uniform reduction of C_σ by half in the whole regime of the cutoff resonance peak, from the enhanced to the inhibited frequency regions. This is clearly the behavior of the dipole coupling with the first order capacitor modes. And unlike in the case of the ideal capacitor, the first order modes do not abruptly disappear, but gradually weaken towards low frequencies, resembling the resonator mode of a highly damped cavity. In the ideal capacitor model, the first order modes have only one transverse antinode across the height L of the capacitor

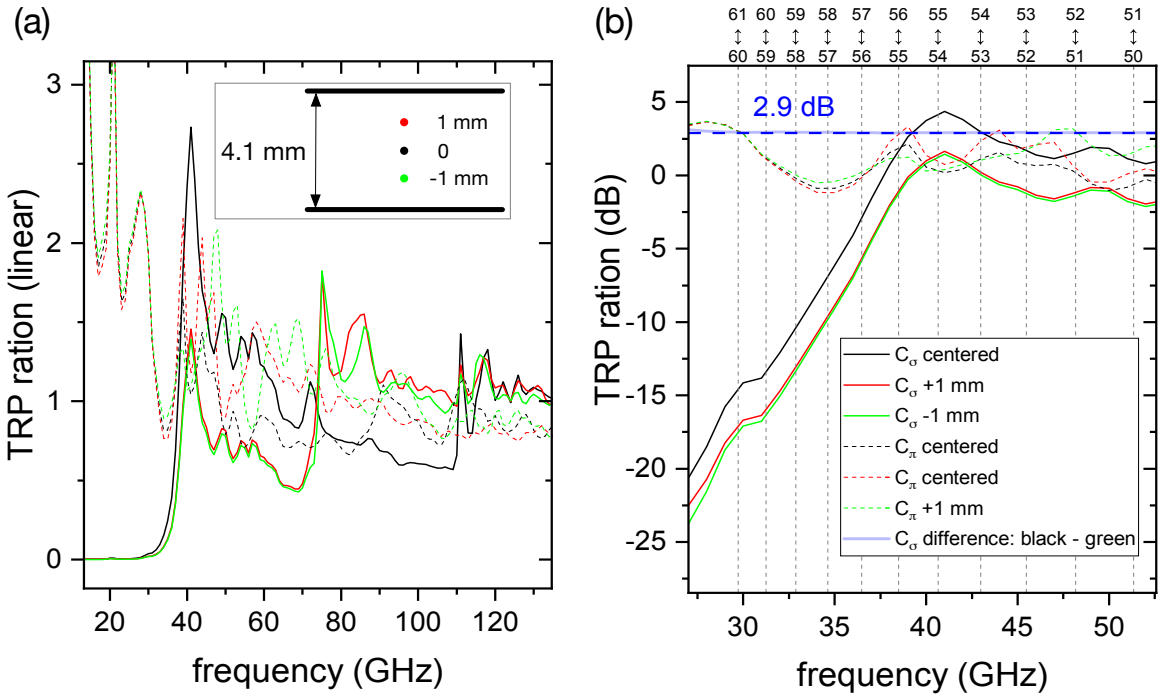

Fig. 3.17 *The TRP ratios simulated with the model in Fig. 3.13 as the vertical position of the in-capacitor dipole antenna is varied. The two panels show the same curves with the same color code plotted only in different scale and range. (a) The C_σ (solid) and C_π (dashed) generated by three different dipole positions are plotted: in the center, $+1$ mm and -1 mm from the center (see inset). (b) The log view focuses on the inhibition cutoff. The dashed lines mark the frequencies of the relevant circular-to-circular transition frequencies in this work. The difference of the black (C_σ centered) and the green (C_σ -1 mm) is plotted as a translucent blue line. A constant 2.9 dB dashed line is given and matches well the translucent line. The simulation uses an ITO sheet resistance of* 10 Ohm/square.

(see Fig. 2.12), a transverse dipole at $L/4$ or $3L/4$ thus couples at exactly the $\pi/4$ or $3\pi/4$ position of a half wave, the resulting emission power is half [$\sin^2(\pi/4) = 1/2$] of the power generated by the dipole at $L/2$, where the dipole-mode coupling is max. In Fig. 3.17 (b), the slightly less than 3 dB reduction of the C_σ simply reflects the fact that a 1 mm shift from the center is still slightly less than a perfect $L/4$ shift in the simulated capacitor with the spacing of $L = 4.1$ mm.

In our experiment, although the MOT cloud has a millimeter size, but the CRAs prepared from the MOT are only localized within a small volume defined by the Rydberg excitation beams (see subsection 3.1.2.3). The 780 and 776 nm beam defines a Rydberg ensemble region in the center within $\Delta L = \pm 100\,\mu$m with respect to the capacitor center, plus a $\approx 100\,\mu$m expansion of the CRA ensemble during the course of one experiment sequence, we do not expect most of the prepared CRAs to deviate by more than 0.2 mm from the capacitor center during the course of the experiment. The position dependent rate modification is then not significant in the experiment, and the CRAs are considered to be centered for all of our

lifetime measurements.

Although the simulation in Fig. 3.17 suggests that a centered CRA (σ^+ inhibited) in the capacitor has the shortest lifetime out of all other positions, it benefits from a large distance from both capacitor surfaces which in our experiment proves to be important for a homogeneous field control. We however note that this conceptually easy reduction of C_σ by moving the atoms up and down could prove useful in other similar experiments when the target CRA's σ^+ decay channels can not be sufficiently inhibited. It could also be used to reduce the spurious C_σ cutoff resonance that enhances the 2σ decay rates and therefore limit the lifetime of the CRAs that could have the σ^+ channels already well inhibited.

3.1.4.4 The lifetime sensitivity to imperfect parallel plate configurations

To investigate the efficiency of the CRA decay inhibition given a necessarily imperfect parallel plate configuration in reality, we simulate the lifetimes of the relevant CRAs while the transparent top electrode of the capacitor is rotated or translated differently. The simulation model is still the one in Fig. 3.13, and the simulation result is summarized in Fig. 3.18.

In the panel (a) and (b), the possible rotation deviations of the ITO plate are introduced in the simulation. The simulated lifetimes of the CRAs in between two capacitor plates with a small angle, compared with the zero angle scenario, are lower for the decay-inhibited CRAs, and higher for decay-enhanced CRAs. This is simply the consequence of the partial loss of the first order capacitor modes, which reduces the contrast of the C_σ cutoff. The panels (c) and (d) show the more mundane consequence as the top plate is gradually slipped away, and the capacitor modes transition into the free space modes. The encouraging conclusion from these simulations is the lifetimes' relative insensitivity to a faulty capacitor plate position: even at unrealistically large deviation from the perfect parallel plate configuration, such as a 5° rotation or a 2 mm translation of the ITO plate, the expected lifetime for a highly inhibited $60C$ state suffers from at most a $\simeq 10\%$ loss in lifetime. Our measured $60C$ lifetime in the real capacitor is well below this 10% bound, therefore its shorter than expected lifetime is not limited by a potentially skewed capacitor plate.

3.2 CRA Preparation

In this section, we detail the main elements of our experimental preparation of the CRAs.

All our experimental activities focus on the manipulation of these atomic states. Therefore, the successful detection of the states is the prerequisite to the rest of the work. It is then appropriate to first introduce our detection technique: the state-selective ionization (section 3.2.1). All the analyses involving the experimental data are based on the discussion of the detected ionization signals.

Next, in subsection 3.2.2, we explain how we prepare a relatively stable electric field environment for the atoms and for the CRA preparation.

We use an adiabatic rapid passage to prepare the CRAs. The optimizations of this method are described in subsection 3.2.3.

Finally, in subsection 3.2.4, we show the complete sequences and schemes to prepare all the initial circular states involved in this work.

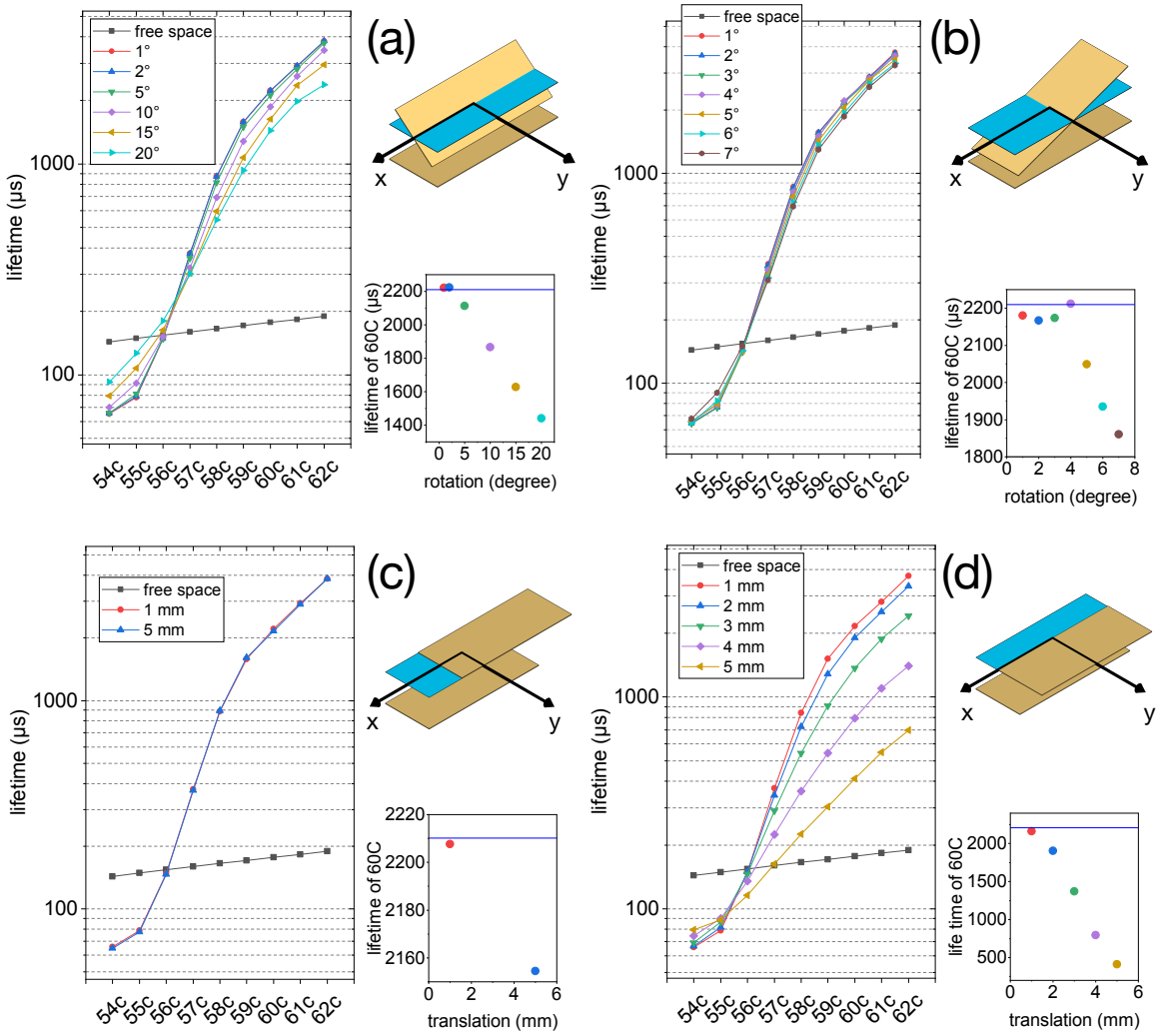

Fig. 3.18 *The simulated lifetimes of the CRAs in an capacitor with some imperfect parallel plates configurations. All the simulations share a common ITO sheet resistance of* 10 Ohm/square. *On the top right of each panel is shown an illustration of the type of top plate transformation investigated, with a blue phantom plate marking the perfect parallel plate position. (a) and (b) are the lifetimes of the relevant CRAs given the different rotation angles of the top plate around the Ox and Oy axes; (c) and (d) are the same lifetimes given the different translation lengths of the top plate along the two axes. The small plot for each panel shows the lifetime of* 60*C under the corresponding configurations. The blue horizontal line in these small plots marks the lifetime of* 60*C in a perfect parallel plate configuration.*

3.2.1 State-selective ionization of the CRA

This subsection focuses on the detection of the circular atoms.

The principle of the state selective ionization is described in subsection 3.2.1.1. The technique can effectively resolve the populations of different CRAs.

In subsection 3.2.1.2, we use a simple model to calculate the ionization signals of hydrogen in a ramp of electric field.

3.2.1.1 The ionization signal and its selectivity

In the experiment, the Rydberg atoms in the end of a sequence are detected by the technique of state-selective field ionization [97]: we apply a fast electric ramp across the capacitor to strip the slow Rydberg atoms of their outer electrons. They become ions and gain momentum in the ionization ramp field, and subsequently travel through the small detection hole pierced in the mirror [see Fig. 3.2 (b)] and reach the channeltron below, a device which allows the detection of individual ions. Every counted ion corresponds to one atom detected. The state selectivity of this approach relies on the different ionization thresholds for the CRAs of different principal quantum number n. The CRAs of different n's are ionized at different field thresholds along the field ramp, and are consequently detected at different times in the experiment sequence. The counted ions give a typical time-resolved signal as shown in Fig. 3.19. The magnitude of this signal is in the unit of counts (number of ions) per microsecond per detection. Integrating the signal produces the total number of atoms detected per detection. In this case the complete signal yields an integration of 0.06858 counts per detection. Considering the 36000 detections performed, this signal is constructed by 2469 detected ions.

This signal exhibits the multiple BBR populated circular states inside our room temperature capacitor, for the initial state $|54C\rangle$ and a waiting time of 900 µs. In this signal we see the successive CRA peaks ionized at increasing electric field as the ramp develops in time. The last discernible ionization peak is that of $|46C\rangle$, however, this is still well below the ionization limit of this detection ramp that continues up to 75 µs . The loss of peak contrast at low n is not due to the loss of detection efficiency, but rather caused by the fact that the corresponding levels are not noticeably populated by the BBR induced transfers during the experiment.

In the signal, the circular states from different n-manifolds have large difference in their ionization thresholds, therefore can be well separated. But within the same manifold, Rydberg levels which are close in both their electric number k and magnetic quantum number m mostly fall into the same detection time window and do not disclose information about their relative populations. In our experiment, most of the time we benefit from the fact that the BBR induced thermal transfer predominantly occurs on the circular-to-circular σ^+ transition (see subsection 2.4.3). But the population of the elliptical states e_1 and e_1' (the "most circular" elliptical states with $m = n - 2$) becomes significant when the σ^+ transition is sufficiently inhibited. An example of the ionization signal of these elliptical states is shown in Fig. 3.20.

In the figure, we see that the $m = n - 2$ elliptical signals have slightly different ionization thresholds than that of the circular ($m = n - 1$). Nevertheless, this difference is much less than that between two circular states with adjacent n's. Suppose the ionization peaks shown in the figure do not correspond to the three separately prepared states, but are one mixture

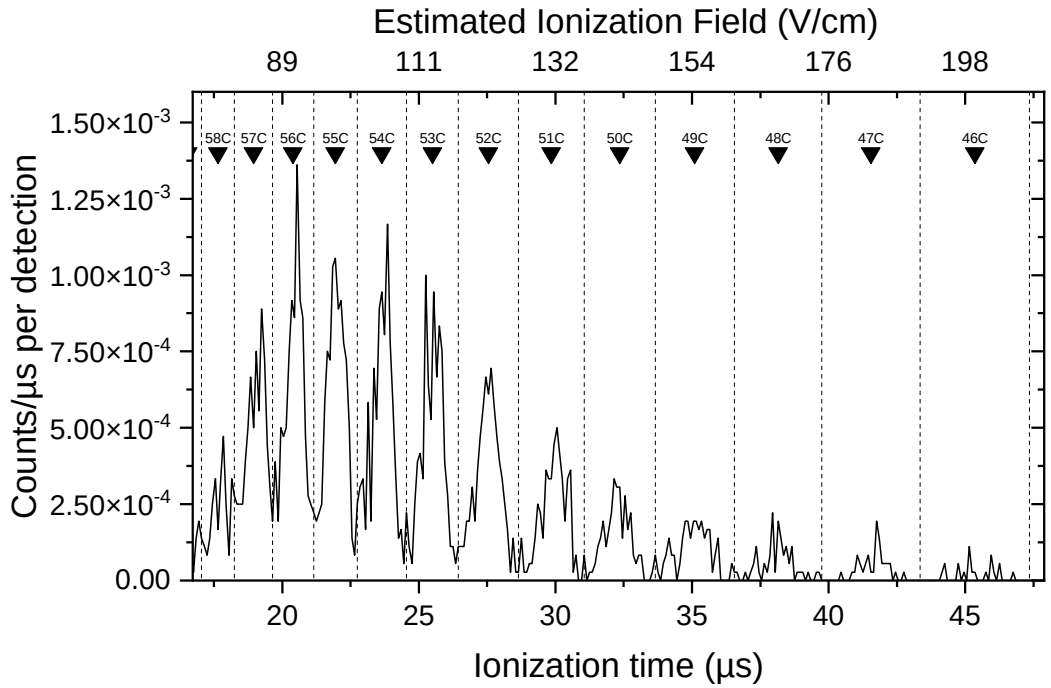

Fig. 3.19 *The ionization signal (also called the arrival time signal) after preparing the intial state* $|54C\rangle$ *and waiting for* 900 µs*. The bottom axis shows the time interval from the beginning of the detection ramp. The time bin size is* 0.1 µs*. The top axis shows the estimated ionization field values at the corresponding ramp time. The time of flight delay due to the ions traveling from the capacitor to the channeltron has already been compensated in this figure. Therefore the signal can be interpreted as the number of atoms detected immediately after their ionization at the corresponding field.*

to be detected as a whole, we would then detect a slightly broadened single peak (dashed line), without being able to tell the exact proportion of the three states. The three states, however, have different linear Stark shifts. Taking advantage of this difference, when we need to resolve the three different states, we use an extra MW π-pulse before the final detection to selectively transfer the population in one state to a different manifold. The single peak then becomes two resolved peaks (or not, if the MW selected state has zero population). A typical application of this MW selection technique is to detect and minimize the elliptical impurities in the CRA preparing sequence, see subsection 3.2.3.2.

When we do not need to discriminate the three states, the detection windows shown in Fig. 3.19 that separate the nC peaks are often enough to also divide well the corresponding ne_1 and ne_1' peaks by their different n's. This is useful, because in our work the BBR-induced transfers can often produce a sizeable amount of $m = n - 2$ elliptical states. Knowing that the detection windows set for different nC states (such as those in Fig. 3.20) also can group different ne_1 and ne_1' states, the population distribution in different n-manifolds can be resolved by one ionization sequence.

In appendix D, some potential techniques to resolve the elliptical states in different

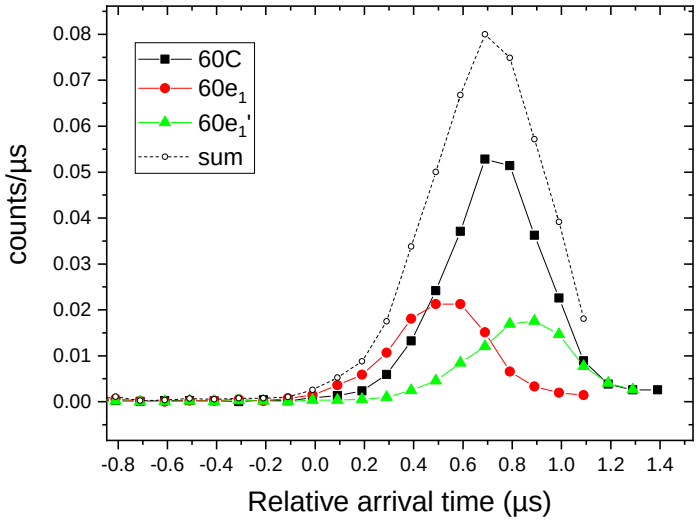

Fig. 3.20 *The ionization signal of the circular state* $60C$ *and the two elliptical states sharing the next highest* m*. Their sum is given in dashed line. All the three states are prepared by MW from a lower manifold. The three states' ion counts falls approximately into a common time window.*

scenarios are discussed.

3.2.1.2 A simplest model to construct the ionization signal

The ionization signals of the Rydberg states we show in subsection 3.2.1.1 all share a common asymmetric peak shape. One might intuitively attribute such a shape to the inhomogeneity and the noise in the ionization field, which certainly does play a part in the broadening of these signals. However, even with an ideal linear ramp with zero field fluctuations, the resulting shape of the ionization signal of a CRA is still intrinsically an asymmetric peak with a finite width. This shape originates fundamentally from the quantum tunneling effect: in an intense electric field, the combined Coulomb-Stark potential barrier is lowered on one side [97], and the electron gains a greatly increased probability to tunnel through the barrier. The "ionization thresholds" we mention in the experiment context is more of a small field range given by the signal width, rather than a clearly defined quantity. There is never a critical "threshold field" across which all the atoms suddenly change into ions, but only a non-zero ionization rate $\Gamma(F)$ as a function of the strong field F.

With a linearly rising ionization ramp $F(t)$, if the form of $\Gamma(F(t))$ is known, the problem of the arrival time signal can be reduced to a rate equation problem. This simple rate equation model is originally proposed in the thesis of J. Hare [118]. It produces ionization signals which at least semi-quantitatively approximate the real signals, and should resemble well an ideal ionization signal with zero broadening mechanisms. Below we reiterate this model and produce some results relevant to the high-n Rydberg states in this work.

We consider there are $N(t)$ atoms all in the same Rydberg level. The only loss mechanism for these atoms is by the field ionization in a ramping field $F(t)$. This assumption is reasonable given the fast ramp we use in the experiment. Then the standard rate equation

for the loss of the atoms reads:

$$\frac{\mathrm{d}N(t)}{\mathrm{d}t} = -\Gamma(F(t))N(t) \tag{3.3}$$

Integrating Eq. (3.3), given the initial number of atoms N_0 at time t_0, we get the number of atoms still not ionized $N(t)$ at any time t:

$$N(t) = N_0 \exp\left[-\int_{t_0}^{t} \Gamma(F(t))\mathrm{d}t\right] \tag{3.4}$$

The magnitude of the arrival time signal $I(t)$ in a time slot Δt is proportional to the number of atoms ΔN ionized within Δt, or $-\,\mathrm{d}N(t)/\mathrm{d}t$. We differentiate Eq. (3.4) and obtain $I(t)$:

$$I(t) = -I_0\frac{\mathrm{d}N(t)}{\mathrm{d}t} = I_0\Gamma(F(t))\exp\left[-\int_{t_0}^{t}\Gamma(F(t))\mathrm{d}t\right] \tag{3.5}$$

where I_0 is a simple normalization parameter (conversion of ion counts to measured signal).

Substituting the perfectly known experiment field ramp for $F(t)$, Eq. (3.5) formally gives the shape of the arrival time peak signal we expect. However, we note that this rate equation argument and hence the resulting signal $I(t)$ from Eq. (3.5) is general for any possible ionization field pattern $F(t)$.

$I(t)$ is to be obtained numerically. The computation needs a last ingredient: the ionization rate of the concerned Rydberg level $\Gamma(F)$. For this we use a semi-emprical formula proposed by Damburg and Kolosov [64, equation (6)]. This formula can approximate well the DC ionization rates of the hydrogen levels. The authors found that for the levels at $n = 7$ the formula yields the DC ionization thresholds [artificially defined as the field for which $\Gamma(F)$ reaches 10^7 Hz] that agree with the exact numerical results within 1.2%. We do not explicitly write down this formula, since we do not intend to discuss it in details. But we point out that this formula needs the perturbative Stark shift terms up to the fourth order [Eq. (2.18)] to produce the reported precision. In Fig. 3.21 we show the calculated ionization thresholds for all the hydrogen levels within $|k| \leq 30$ and $m \geq 0$ in the 60 manifold. The states with $m < 0$ have the same thresholds due to the $\pm m$ symmetry of the Stark structure.

In this figure, our practical definition of the ionization threshold is the field value matching the maximum of the obtained ionization signals. The only free parameter used in generating the figure is the ramp slew rate, which we take from the experimental detection ramp to be 8.26 V/cm/µs. At this magnitude it does not appear to be a sensitive parameter. A factor of two's increase or decrease of the slew rate does not change the obtained ionization thresholds by more than 1%. In the figure, the general thresholds layout matches the physical expectation. The low-ℓ states are easier to ionize than the high-ℓ ones. The circular state has the highest ionization threshold either along the lowest diagonal states, or among all the levels having zero linear Stark shift ($k = 0$). The higher ionization thresholds of the highest diagonal states ($n_2 = 0$) can be intuitively understood from their wave functions [105], which exhibit an electron probability distribution polarized away from the direction of easy ionization. This is exactly opposite to the wave functions of the lowest diagonal states, which are polarized towards the direction of easy ionization.

In Fig. 3.22, we show some selected arrival time peaks calculated with Eq. (3.5). The same ramp slope 8.26 V/cm/µs is used throughout. In panel (a), we obtain respectively for

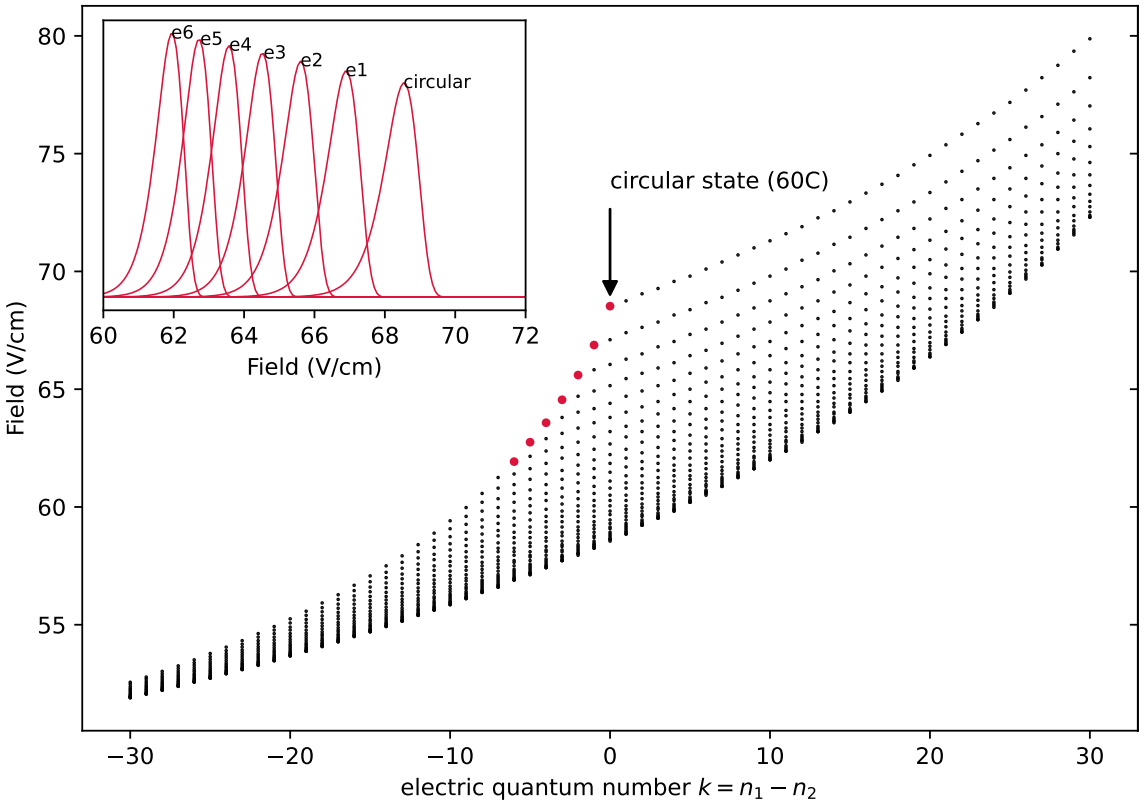

Fig. 3.21 *The calculated ionization thresholds (peak maxima) of the 60 manifold of hydrogen during an ionization with a slew rate of* 8.26 V/cm/µs *(corresponding to our experimental parameters).For each column of points sharing the same electric quantum number k, the state with the higher magnetic quantum number m is always ionized in a higher field. In red points we mark the ionization thresholds of the circular and the first few states along the lowest diagonal of the manifold. The circular state has the highest ionization threshold along the lowest diagonal. In the inset the corresponding ionization peaks are shown. The integration of each ionization peak gives the same area, corresponding to the complete ionization of N_0 atoms.*

the states $51C$ and $50C$ the ionization threshold values 128.6 V/cm and 138.8 V/cm. The two thresholds become lower when the ramp is slower and higher when the ramp is faster. Nevertheless, as we mentioned above, the change is small: the 128.6 V/cm threshold becomes 129.3 V/cm with a twice faster ramp, and becomes 127.9 V/cm with a twice slower ramp. This allows us to compare these stable thresholds with the experimentally measured values of $\approx$ 134 V/cm and $\approx$ 145 V/cm [60]. The resulting difference is only $\approx 5\%$. This shows that the simple rate equation model captures the essential physics in the field ionization process. However, the calculated peak width is clearly smaller than the experimental signal. The nearest neighbor circular states do not overlap at all in panel (a), while the corresponding experimental signals have at least a 5% cross-window contamination. This shows that the calculated peak widths may well represent the ideal limit of the ionization signals. The ramp

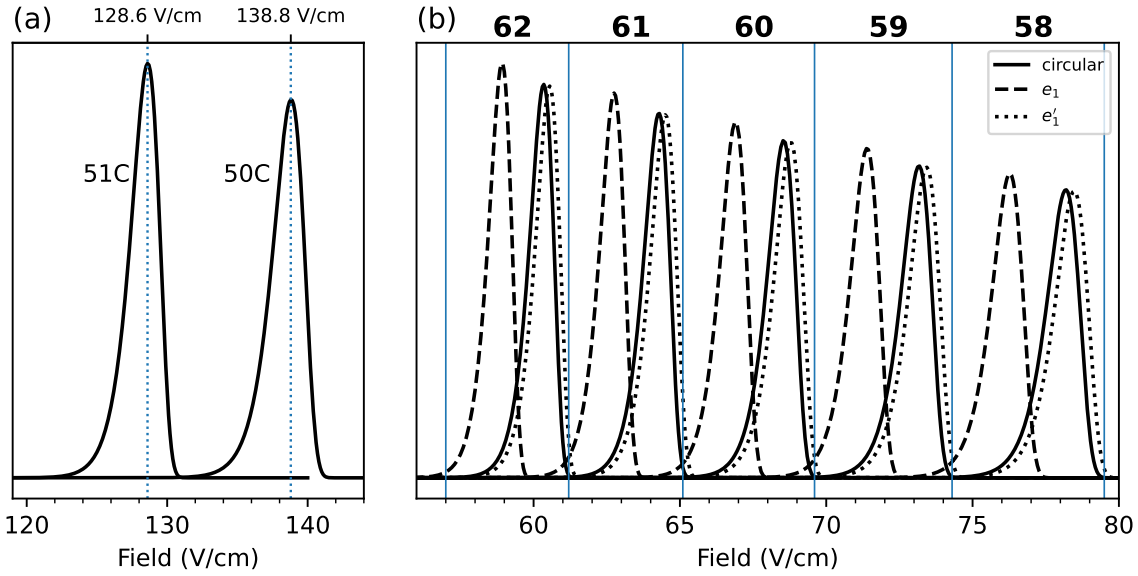

Fig. 3.22 *The calculated ionization signals of some seleted circular and elliptical states during an ionization ramp with a slew rate* 8.26 V/cm/µs *(the experimental parameter). (a) Precision of the calculated ionization thresholds: the theoretical* 51C *and* 50C *thresholds (marked by dotted lines) do not differ from the experiment values by more than 5%. (b) Ionization resolution of the calculated signals. All the circular and elliptical states have the same area. The window dividers are manually selected. They effectively separate the ionization signals of the states from different* n*. Note that in each* n*-window, the three peaks' relative separation resembles that in Fig. 3.20.*

is ideal and ultimately adiabatic due to the DC ionization rate we use in this model. In panel (b), we show the detection window resolution of the ideal signals of the high-n circular states and the two immediate elliptical states. We see that the ideal signals of the states of different n's are well separated and have negligible cross-window contaminations. This is certainly different from what realistically happens (c.f. Fig. 4.1), and can only be regarded as an ideal limit of the resolution of the state-selective field ionization technique using a ramp[5].

3.2.2 Electric field optimization and calibration

In this subsection, we describe how we prepare a controlled DC field for the atoms.

Subsection 3.2.2.1 explains how we minimize the undesired transverse DC field and optimize the field homogeneity.

[5]In addition to peak broadening, one other element that could realistically reduce the peak-to-peak spacings of the state signals is the dispersion in the time of flight of the ions. In an ion trajectory simulation for a cold CRA experiment at a larger scale than the vapor cell experiment of this work, the CRAs 60C and 50C need respectively 34.5 µs and 28.7 µs to reach the detector [private communication, Baptiste Muraz, 2022]. The higher-n CRAs are ionized in a weaker field and the corresponding ions gain less acceleration, taking longer time to travel to the detector. However this ≈ 6 µs of difference is between two CRAs separated by $\Delta n = 10$. The effect is totally negligible for neighboring CRAs in our experiment.

Subsection 3.2.2.2 specifies the calibration we perform to reach a consistent value of the quantization axis field.

3.2.2.1 Cancellation of the stray DC field

The field defining the quantization axis of the CRA in our lifetime measurement sequence is applied across the two plates of the inhibition capacitor. Ideally this vertical directing field should be the only field that the atoms feel, since a tilted quantization axis results in a loss of the σ^+ inhibition. It is then necessary to ensure that the stray DC field in the transverse directions, partly due to the Rb deposits on the electrodes, is minimized. In our setup, the four rf electrodes (see figure 3.2) provide the means to apply a DC offset in any transverse direction.

The line shift and linewidth of a high-n, low-ℓ Rydberg level in a laser excitation spectrum is appropriate for sensing the stray DC field with sub-V/m precision. This follows naturally from fact that the common low-ℓ Rydberg atoms have large electric dipoles and are easily polarized.

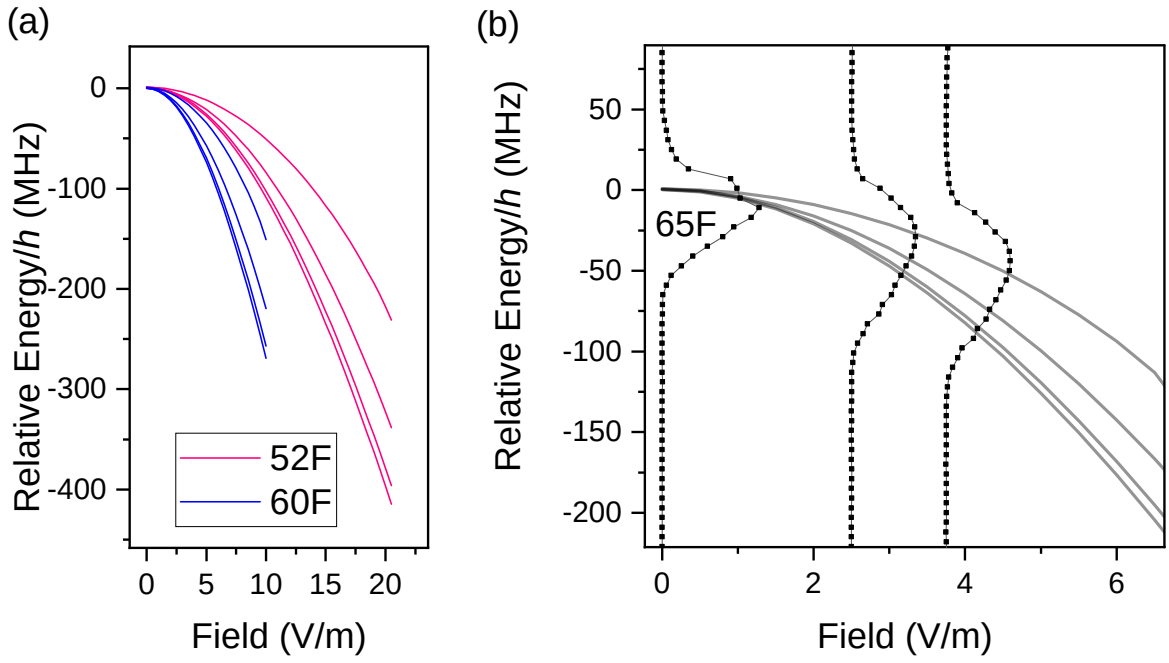

Fig. 3.23 *Rydberg laser spectrum as a figure of merit of electric field minimization. (a) Stark shift of the* 52 F *and the* 60 F *levels in the field range of tens of* V/m*. The two F-multiplicities start from the same reference energy, stop at the field when the* $m = 3$ *level (the highest line in each F-multiplicity) joins the manifold. (b) Experimental laser spectrum of the* $5\,D_{5/2} \rightarrow 65\,F$ *excitation line is compared with the theoretical Stark shift of the 65F multiplicity in the range values lower than* 6 V/m*. Note that the precision of the excitation lines are limited by the wavelength meter used for measurement. It is only meant to demonstrate a field minimization process.*

In Fig. 3.23 we show the principle of this field optimization. In panel (a), we show the

theoretical Stark lines of the 52 F and 60 F multiplicities below 20 V/m. The zero field energy points of the two multiplicities are artificially overlapped. When we deviate from the zero field, we see that the 60 F lines are significantly more downwards shifted than those from the 52 F. This is a manifestation of the $\propto n^7$ scaling of the Rydberg polarizability [97]. In panel (b), we take advantage of this DC field sensitivity by exciting the atoms to the high-lying 65 F state. The excitation laser spectrum shows a 65 F peak that exhibits large line shift and broadening when the residual field is only a few V/m. In this plot, the transverse field is not significant, the field adjusted is the vertical quantization axis field. The magnitude of the adjusted field is inferred from the voltage applied across the inhibition capacitor with a known spacing. The frequency shift of the 65 F excitation line is estimated with a wavelength meter (Angstrom WS-6IR) with a frequency resolution of a few tens of MHz. The plot is thus not meant to be a precise field calibration. However, a clear field minimization process is demonstrated in this plot. A minimized quantization axis field at the position of the atoms is found when the position of the 65 F as a function of the applied voltage across the capacitor is stabilized at a highest frequency. At the same time the 65 F peak width also reaches a minimum.

When this is done, the 65 F peak shape usually still has a noticeable asymmetry, with a longer tail towards low frequencies. This shows that the detected Rydberg ensemble still experiences slightly different Stark shifts from one atom to the other. With the vertical field already minimized, the shifts are mainly caused by the transverse field. We then tune the DC offsets of the four transverse electrodes to reduce the width and asymmetry of the 65 F peak. For the transverse field, two DC offsets are already enough to control its direction, the two extra DC offsets provided by the four electrodes can contribute to the field homogeneity optimization. Following the systematic procedure described in the thesis of R. G. Cortiñas [69], a set of four optimal electrode DC offsets can be found that minimizes the width of the 65 F peak (we fit the peak shape by an asymmetric Gaussian to obtain the width). The two capacitor electrodes also offer one more degree of freedom that can be exploited to tune the field homogeneity in the vertical direction, and their optimal values can be found in the same way as in the transverse optimization.

By minimizing the width of the sensitive F line, we can find the optimal DC offsets of all the six electrodes that represent the best zero field and field homogeneity. From this clean starting point, only the vertical directing field is varied in the experiment sequence, maintaining a straight and non-rotating quantization axis. We note that the MW spectroscopy such as of the transition $nC \rightarrow (n+1)e_1$ takes advantage of the sensitive linear Stark shift. The resulting spectrum peak width is thus a better figure of merit than that of the laser spectrum [69]. However, this approach requires already stable experimental conditions for the preparation of the CRA. In contrast the laser spectrum approach requires only the Rydberg excitation and detection with nothing in between. It is therefore well-suited as a first order optimization. In our experiment, the field homogeneity is limited by the tightly spaced electrodes around the atoms and the known Rb deposit on their surfaces [117].

As a final note, a more concrete way to optimize the field homogeneity is to directly explore the electric gradient along a spatial axis by exciting and detecting the atoms at a few closely spaced points along this axis [69]. This method is not feasible in our setup. Because only the atoms excited directly above the ø0.2 mm detection hole on the bottom mirror can be detected.

3.2.2.2 Calibration of the quantization axis field

The DC field in the capacitor often suffers from a slow daily drift in the order of sub-V/m. The transverse field drift is not significant given the dominant vertical directing field we apply (160 V/m). The vertical field itself can be efficiently calibrated by the linear Stark shift in the 58 manifold.

The calibration starts with a 58C preparation ARP sequence. A good property of the ARP circularization is its insensitivity to a field drift of a few V/m. Unless the field drift is large, the ARP sequence can always prepare a reproducible amount of CRAs in the 58 manifold. The prepared population in $58C$ can be transferred by a subsequent weak σ^+-polarized rf pulse to the low-m states in the lowest diagonal of the manifold. This rf transfer also produces a corresponding transfer in the arrival time signal. When we perform a rf spectroscopy of the weak transfer pulse, the maximum transfer appears when the rf pulse is resonant with the linear Stark shift. If we reproduce the resonance frequency of this rf spectroscopy, we reproduce the same directing field for the atoms. This procedure is shown in Fig. 3.24.

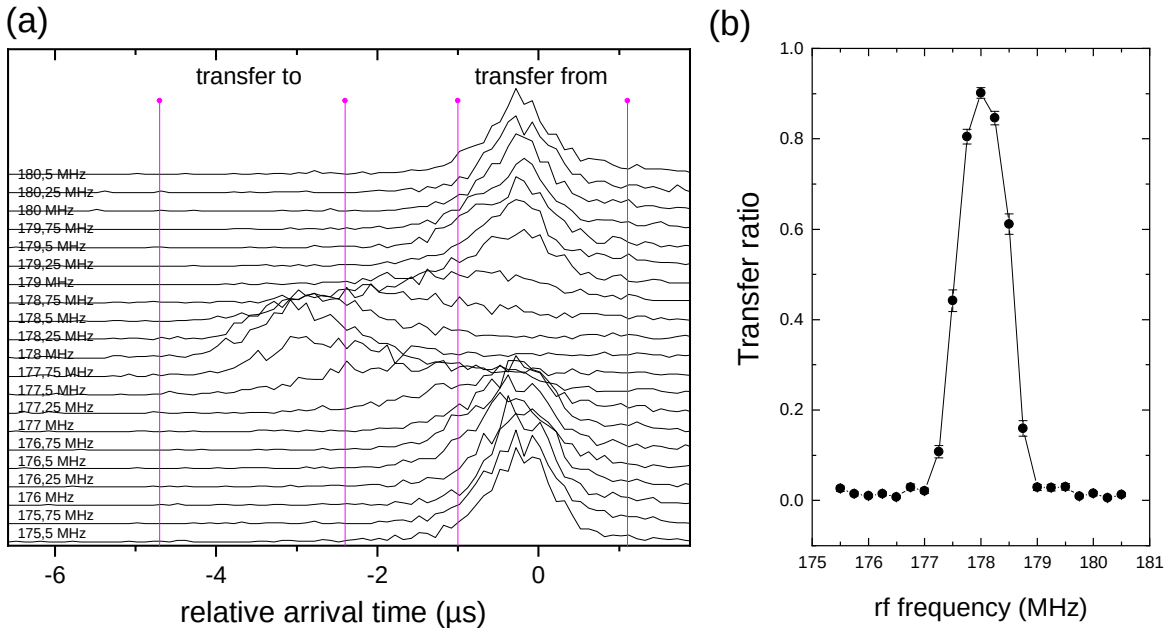

Fig. 3.24 *rf spectroscopy to measure the field along the quantization axis. The σ^+-polarized rf pulse is a* 1 µs *square pulse of ampitude* 0.15 MHz *in terms of Rabi frequency. (a) Series of ionization signals during a rf spectroscopy to transfer the* $58C$ *(highest ionization threshold) to the low-m states with lower ionization thresholds. The signals are vertically offset for different rf frequencies. The transfer window delimiters are shown in magenta. (b) The corresponding transfer ratio obtained from the ionization signals. The rf spectoscopy finds a resonance at* 178 MHz*. This linear Stark shift in the 58 manifold corresponds to a field of* 160 V/m*.*

In this figure, panel (a) shows the full series of the ionization signals during a complete rf spectroscopy. To characterize the change in these signals, we define a transfer ratio, or

simply a "transfer". We define the two detection windows A and B and record the number of atoms N_A and N_B in these windows, then the transfer ratio from window A to window B is defined as $N_B/(N_A + N_B)$. The transfer ratio of the signals in panel (a) is shown in panel (b). The resonance at 178 MHz corresponds exactly to a most shifted ionization signal. This frequency in the 58-manifold is the linear Stark shift that corresponds to a directing field of 160 V/m. When the field drift causes a deviation from this field, we apply the corresponding DC offsets on the capacitor to counterbalance the drift. Therefore, a stable directing field of 160 V/m is ensured during the field-sensitive rf and MW operations, and during the idle time before CRA detection in the lifetime measurement.

3.2.3 Preparation of the circularization adiabatic rapid passage

In this work, the adiabatic rapid passage (ARP) [119, 120] is the only technique we use for the CRA preparation. The ARP is robust against modest field drifts compared to some other techniques that would require a stable Stark shift, hence a precise field [70, 121]. In comparison, the main drawback of the ARP, its long duration, is not a limiting factor in our slow atom experiment. Using it for $\simeq 10\,\mu s$ in our experiment sequences is acceptable.

The principle of the ARP circularization was introduced in section 2.3. The experimental ARP sequence will be detailed in subsection 3.2.4. In this subsection, we focus on two key points in the preparation of our ARP.

In subsection 3.2.3.1, we describe the starting point of an ARP, the Rydberg excitation before the Stark switching.

In subsection 3.2.3.2, we demonstrate how to optimize an ARP in order to improved the purity of the prepared CRAs.

3.2.3.1 The laser excitation before the ARP

The ARP we use to produce the data in [49] is exclusively performed in the 58 manifold. The ideal passage starts from the state $|58\,\mathrm{F}, m = 2\rangle$, ends in the state $58C$. The initial $|58\,\mathrm{F}, m = 2\rangle$ state is reached by a direct laser excitation in a small Stark field of typically 5 V/m to 10 V/m. This Stark field should not be too large, so that the 58F multiplicity does not join the 58 manifold. At a given laser frequency, an optimal Stark field during laser excitation is one that allows the most $|58\,\mathrm{F}, m = 2\rangle$ excited and the most $58C$ prepared. This is demonstrated in Fig. 3.25.

In this figure, the 1257 nm laser frequency is stabilized at ≈ -150 MHz below the zero field excitation frequency of $5\,\mathrm{D}_{5/2} \leftrightarrow 58\,\mathrm{F}$. The Stark field during laser excitation (a small vertical directing field) is varied in the range of $\approx 10 \pm 5$ V/m. In this small field range, the sensitive 58F multiplicity partially reveals its structure in the detection signals. The black curve shows the 58F atoms detected immediately after the excitation. The separation of the $m = 3$ line from the rest of the lines is evident and desirable, since the state $|n\mathrm{F}, m = 3\rangle$ in a circularization ARP connects to the state $58e_1$, which is an impurity in a circularization process. The rest of the lines m = 2,1,0 have poor resolution. However, it is not critical to resolve these three states during the ARP. The states $|n\mathrm{F}, m = 0\rangle$ and $|n\mathrm{F}, m = 1\rangle$ have large detunings from the rest of the lowest diagonal states. Therefore they do not join the ARP at all, and stay as the low-ℓ states which can be well separated from the circular state in the ionization signal. This fact is manifest in the red curve. The red curve plots the resulting amount of CRAs prepared after the ARP when the initially excited 58F states

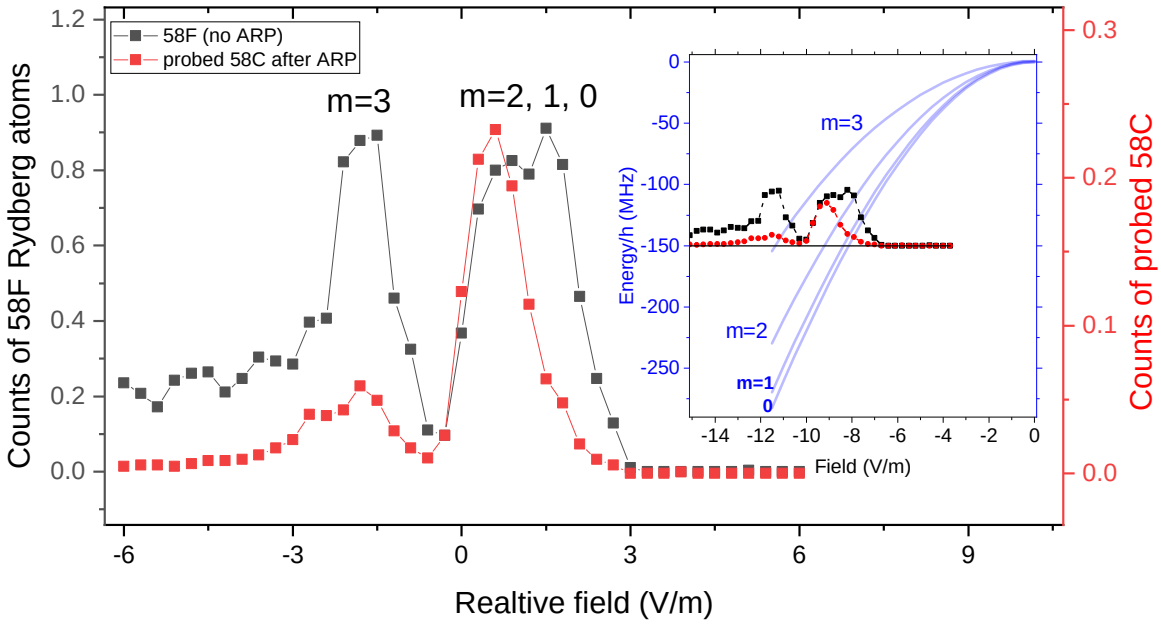

Fig. 3.25 *Detected low-ℓ (black, ARP off) and circular (red, ARP on) Rydberg atoms in the 58 manifold as a function of the Stark field during laser excitation. The CRAs are selectively detected after a MW probe. The probe performs a $58C \rightarrow 56C$ two-photon transfer. The resulting $56C$ population is detected to produce the red curve. The field scale on the x axis is estimated by the voltage applied on the inhibition capacitor with a known spacing. The inset shows the same data, overlapped with the theoretical Stark shift (transluscent blue) of the 58F multiplicity.*

differ in their m's. The CRA signal in the detection is separated from contamination by other spurious high-m states by applying a MW probe pulse to transfer the $58C$ population to $56C$, which has a higher ionization threshold. The red curve clearly shows that the maximum number of CRAs is reached when the ARP starts from a situation in which the population of $|58\,\mathrm{F}, m = 2\rangle$ is maximal. And if we compare the black and the red curves, it is evident that if an unfortunate drift in the laser frequency or the Stark field causes the excitation to produce mostly $|58\mathrm{F}, m = 0\rangle$ and $|58\mathrm{F}, m = 1\rangle$, we would observe a sharp drop in the detected CRAs. We also see that a small amount of CRAs can be prepared starting from $|58\mathrm{F}, m = 3\rangle$, this may be due to the imperfection of the adiabatic passage (e.g. if the ARP is too fast and partially loses its adiabaticity). However, as we noted before, the $m = 3$ line is well separated from that of the $m = 2$. In our experiment, a drift large enough to cause an excitation to $|58\mathrm{F}, m = 3\rangle$ would cause many other problems that cannot escape our noticing.

3.2.3.2 Optimization of the ARP

In subsection 3.2.3.1 we touched on the topic of the imperfection in an ARP and the resulting impurities in the prepared CRAs. The impurities after a circularization ARP are the non-circular states unintentionally prepared at the same time. They can come from two main sources.

1. An impurity in the σ^+-polarization of the rf dressing field
2. An imperfection in the adiabaticity of the ARP

The first defect produces an unwanted σ^- component in the rf dressing field, which couples the Stark levels with $n_1 \neq 0$. This can be pictured as the population "leaking out" from the lowest diagonal states during an ARP. The second defect results in an infidelity in the (ideally) one-to-one connections by the ARP for the states within the lowest diagonal. The small amount of CRAs prepared from $|n\mathrm{F}, m = 3\rangle$ in Fig. 3.25 is an example of the second imperfection.

Experimentally, these two possible imperfections of the ARP can be reduced by minimizing the populations in the states ne_1 and ne_1'. The individual detection of the populations in these two states in addition to that of the circular state is achieved by a MW spectroscopy taking advantage of the differential Stark shift. This is a common optimization procedure. Other descriptions of this technique adopted in different experimental contexts can be found in [59, 104, 105, 122] (thermal beam), [69] (MOT in cryostat), and [93, 106] (atomic fountain).

The linear Stark shift [Eq. (2.15)] is the dominant Stark shift in a moderate electric field. This shift has a dependence on n. The two-photon transition $ne_1 \leftrightarrow (n+2)e_1$ hence to first order has a transition frequency that is detuned by $-3ea_0F$ from the $nC \leftrightarrow (n+2)C$ transition. For the transition $ne_1' \leftrightarrow (n+2)e_1'$, this detuning is $3ea_0F$. These differential Stark shits are dependent on F while independent of n. See Fig. 3.26 for a diagram of the transitions mentioned.

The differential Stark shifts of the three transitions differ in frequency by a few MHz under a typical quantization axis field we apply to the atoms, allowing them to be resolved in a MW spectroscopy. An example of such a MW spectrum is shown in Fig. 3.27.

The figure shows the minimization process of the population in $58e_1'$. The minimization of $58e_1$ (not shown) is similar. A two-photon MW π-pulse of duration $\approx 1\,\mu\mathrm{s}$ is first calibrated to optimize the $58C \rightarrow 56C$ transfer. Since all the three transitions shown in Fig. 3.26 have similar transition matrix elements, scanning the frequency of the calibrated π-pulse constitutes a MW spectroscopy in which we can also observe the efficiently transferred population impurities in $58e_1$ and $58e_1'$. The prominent $58e_1' \rightarrow 56e_1'$ peak shown in the red spectrum in panel (a) is proportional to the $58e_1'$ population prepared after the ARP. It is a clear sign of a non-negligible σ^- component in the rf dressing field, which can be minimized by tuning the phase difference ϕ between the two independent channels of the rf source (see subsection 3.1.1.4). The ϕ tuning process is shown in panel (b). We plot as a function of ϕ the transferred $58C$ and $58e_1'$ populations. The optimal value of ϕ minimizes the unwanted $58e_1'$ population while maximizing that of $58C$. With this optimal ϕ, we obtain the green spectrum in panel (a). It is worth noting that the optimal ϕ also reduces the spurious $58e_1'' \rightarrow 56e_1''$ transfer. This is expected, since all the blue-detuned differential Stark transfers are caused by the spurious σ^- component in the rf (imperfection 1). On the other hand, the $58e1 \rightarrow 56e1$ transfer is not affected before and after the optimization of ϕ. The corresponding impurity is caused by the inefficiency of the ARP (imperfection 2). Other parameters, typically the shape, amplitude, timing, and frequency of the rf dressing, need to be adjusted to minimize the red-detuned differential Stark transfers.

Finally, with the ionization signals of Fig. 3.28, we show the $58C \rightarrow 60C$ π-pulse transfer ratio before and after the optimization shown in Fig. 3.27. The transfer is estimated by comparing the counts on both sides of the central divider set in the figure. The maximum

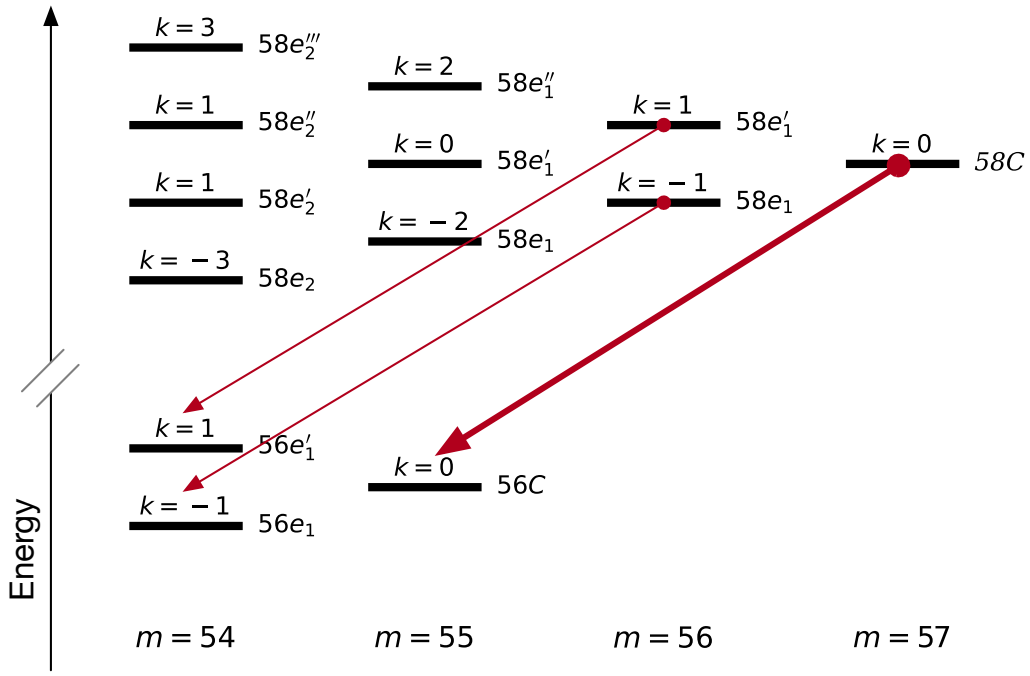

Fig. 3.26 *Illustration of the differential Stark shifts. The energies are relative. The electric quantum number k is proportional to the linear Stark shift of each level. The transitions shown in the figure are $58C \rightarrow 56C$, $58e_1 \rightarrow 56e_1$, and $58e'_1 \rightarrow 56e'_1$. They have respectively differential Stark shifts of 0, $-3ea_0F$, and $3ea_0F$. This figure presents also the MW probing scheme used in Fig. 3.27.*

transfers before and after the ϕ optimization are respectively 50% and 65%. These can be regarded as a coarse estimation of the purity of $58C$ prepared after the ARP (the real purity should be a few percent higher, since it is visible from the plot that some initially prepared $58C$ decays to $57C$, the latter failed to be transferred by the MW). This improved purity is still far from the state of the art of the ARP circularization in a lower manifold [70, 71]. However, this is somewhat expected due to the relatively high-n manifold in which we perform the ARP. The ARP circularization certainly cannot be extrapolated to an arbitrarily high n manifold. As n increases, the neighboring manifolds cross at increasingly small Stark field. The same rf dressing field we use at $n = 58$ was tested to produce purer CRAs at $n = 52$, and less pure CRAs at $n = 60$. The less efficient ARP at $n = 58$ thus may represent a midpoint in the gradual process towards the total breakdown of the ARP at a very high n. In our experiment, the ARP at $n = 58$ is preferred to that at a lower n, because the prepared $58C$ is a decay-inhibited CRA with a measured lifetime of 800 µs. This gives sufficient time for the subsequent rf and MW operations used to distill a more pure circular population in other multiplicities. While there could still be room to improve the efficiency of the ARP in the 58 manifold (see section 5.2), we turn to simply use the partial ionization techniques to remove the non-circular states after the ARP (see subsection 3.2.4).

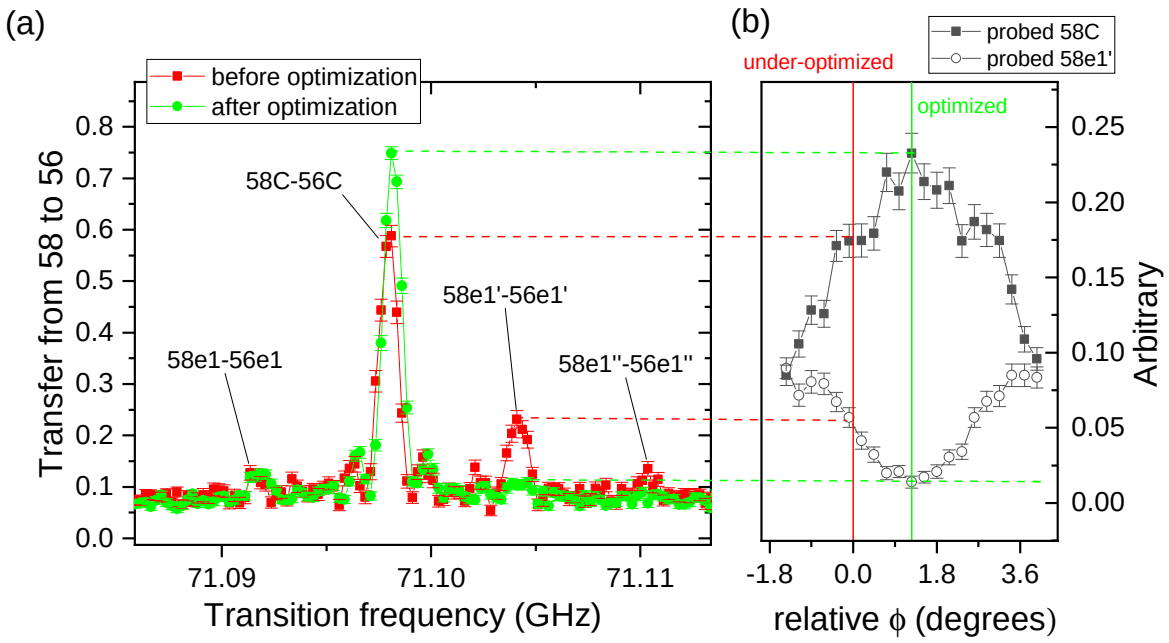

Fig. 3.27 *MW spectroscopy for the optimization of the purity of the σ^+ polarization of the dressing rf field during a circularization ARP in the 58 manifold. (a) Two MW spectrums obtained after the ARP are compared. The MW is a π-pulse with a duration of $\approx 1\,\mu s$. The peak in the center corresponds to the circular-to-circular transfer. Before optimization (red), a peak appears at the detunning of the $58e_1' \rightarrow 56e_1'$ transition, indicating a sizable population impurity in $58e_1'$. This $58e_1'$ population is minimized after the opimization (green). (b) The optimization process in between the red and the green. The parameter tuned is the phase ϕ in Eq. (3.1), which is the phase difference between the two channels of the rf source (AWG).*

3.2.4 Sequences for preparing the CRAs from *60C* to *54C*

We prepare seven initial circular states, from $60C$ to $54C$, for the lifetime measurement. The lifetimes of the CRAs from $56C$ to $60C$ serve to exhibit the gradual increase in the σ^+ inhibition below the cutoff, while those of the $55C$ and $54C$ demonstrate the great σ^+ enhancement of the cutoff resonance. The CRAs with lower n's are not prepared, but the circular states down to at least $51C$ can be sufficiently populated by the BBR transfers during the longest measurement sequences. Therefore our data processing (see chapter 4) also yields well characterized lifetimes with small errors for these unprepared circular states.

Starting from $58C$ prepared by an ARP, a series of MW transfer pulses and rf decircularization pulses, together with several partial ionization ramps are designed to prepare and purify all the concerned CRAs. The sequences are summarized in Fig. 3.29.

The figure shows two sequences, both sharing the same laser excitation, ARP, and first partial ionization (sweeper 1) stage (the sweeper 2 appears shared in the figure, but is technically different in slew rate for different circular states prepared). After a $1\,\mu s$ laser

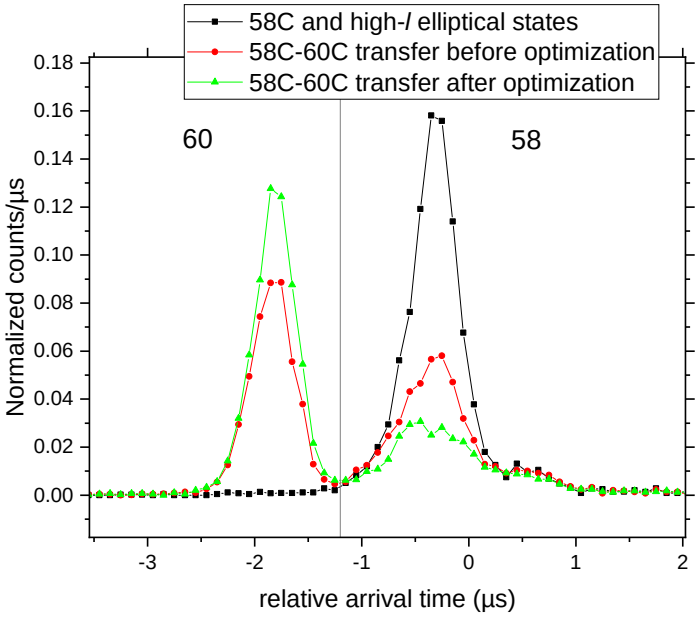

Fig. 3.28 *Ionization signals before and after the ARP optimization in Fig. 3.27. The black signal corresponds to the atoms prepared after the ARP, before the π-pulse.*

excitation (see subsection 3.2.3.1) and before the ARP, a Stark switching[6] increases the field from a few V/m to 195 V/m in 1 µs. After this high field is reached, it is then ramped down in 6 µs to 95 V/m. During the ramping down, the σ^+-polarized rf dressing field is ramped up in 2.5 µs, reaches and maintains a max Rabi frequency (amplitude) of ≈ 6 MHz for 3 µs, and then during another 2.5 µs is ramped down to zero. The precise parameters of this trapezoid dressing field may be subject to changes from time to time. The thesis of A. Larrouy [122] explains the experimental optimization of this dressing field.

The sweeper 1 is calibrated to remove the low-ℓ populations that either do not join the ARP, or are falsely connected to some non-circular states by the imperfect ARP. At the end of the sweeper 1, the $58C$ and some spurious high-m elliptical states are prepared. Starting from here, a circular state $n'C$ with $n' < 58$ can be straightforwardly prepared by one or more MW π pulses followed by a second partial ionization ramp (sweeper 2) to remove any non-circular impurities left in all the manifolds with $n > n'$.

The amplitude calibration of these sweepers guarantees that they do not ionize the $n'C$, but do ionize any state with a lower ionization threshold. This calibration is typically done by varying the sweeper's amplitude while monitoring the population transferred from $n'C$ to a lower $n''C$. For instance, we monitor the counts of $55C$ transferred from $57C$ by a two-

[6]The terminology was originally introduced in the theoretical proposal of Freeman and Kleppner [123] as a way to reach high-ℓ Rydberg states. The scheme was soon realized experimentally to prepare a doubly excited autoionizing Rydberg state of Sr [124]. In these early works, the switching refers to a decrease from high field to zero field. A Stark level in this process adiabatically connects to a high nL level not accessible by laser at zero field. In the context of our work, the switching refers to an increase from low field (during laser excitation) to high field [120]. The $|n\mathrm{F}, m = 2\rangle$ state in this process adiabatically connects to the $|m = 2, n_1 = 1\rangle$ Stark level, the starting level of the following circularization ARP.

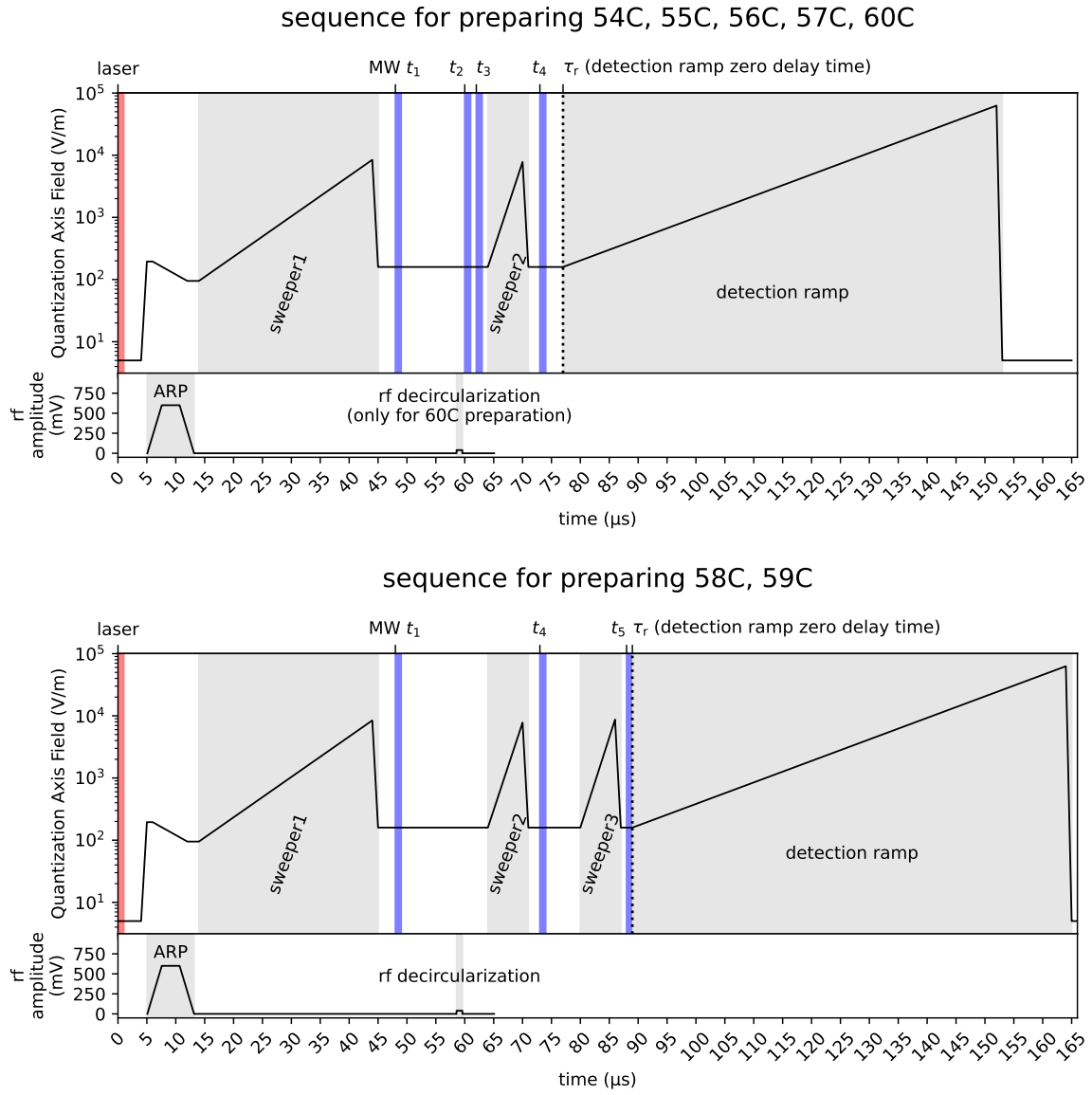

Fig. 3.29 *Sequences for preparing the purified CRAs. The field is estimated from the voltage applied across the capacitor and from the rf spectrum field calibration. The rf amplitude shows the output voltage of the rf source.* 1 V *translates to a rf Rabi frequency of* 10.3 MHz *in the 58 manifold. The gray areas are the partial ionization stages ("sweepers") and the final detection stage. In a lifetime measurement session, the final detection ramp starts at regular time delays* τ_r, $\tau_r + \Delta t$, $\tau_r + 2\Delta t$,.... *The red and blue bars label the laser excitation and MW operation windows, respectively. For the preparation of any specific* nC, *only part of the blue windows are used (see table 3.1). Note that for the sequence on top, the rf decircularization pulse exists only for the prepration of* $60C$.

photon π pulse when we calibrate the sweeper 2 that prepares the pure $57C$. The optimal amplitude of the sweeper is found when it is high enough to start reducing the transferred $55C$, indicating that all the states with the ionization thresholds higher than that of $57C$ were already eliminated.

All the MW π pulses we use share a common duration of $1 \pm 0.2\,\mu s$. The MW pulses are triggered, depending on the specific target state, at five possible time points marked from t_1 to t_5 in Fig. 3.29. The specific MW transfers involved in the preparation of all the nC's are listed in table 3.1.

Table 3.1: MW transfer scheme for the prepration of all the initial circular states involved in our lifetime measurement. Note that for $54C$ and $55C$ there is for each an alternative MW scheme for very short time evolution detection. The data prepared by the alternative schemes are shown in (a) and (d) in Fig. 4.2.

CRA to prepare	MW t_1	MW t_2	MW t_3	MW t_4	MW t_5
$54C$		$58C \rightarrow 56C$	$56C \rightarrow 54C$		
$54C$ (alt.)		$58C \rightarrow 56C$		$56C \rightarrow 54C$	
$55C$		$58C \rightarrow 57C$	$57C \rightarrow 55C$		
$55C$ (alt.)		$58C \rightarrow 57C$		$57C \rightarrow 55C$	
$56C$			$58C \rightarrow 56C$		
$57C$			$58C \rightarrow 57C$		
$58C$	$58C \rightarrow 60C$			$60C \rightarrow 58C$	
$59C$	$58C \rightarrow 60C$			$60C \rightarrow 58C$	$58C \rightarrow 59C$
$60C$	$58C \rightarrow 60C$				

For the preparation of $57C$ and $56C$, only one MW transfer is needed. The transfer takes place at time t_3, immediately before the purifying sweeper 2. This ensures that the prepared $57C$ and $56C$, not possessing enough σ^+ inhibition, do not decay too much in the 300 K thermal field before the final detection ramp (for the zero delay signals in the whole lifetime evolution). For the preparation of $55C$ and $54C$, they are prepared by one additional two-photon MW transfer from $57C$ and $56C$, respectively. The two consecutive MW transfers are triggered at the closely spaced t_2 and t_3 and also immediately before the sweeper 2. But since these two states suffer from the enhanced σ^+ decay rates, both their lifetimes are less than $50\,\mu s$. For these two states we thus use an alternative session, in which the second MW transfer is at t_4. These most short-lived states are thus prepared later in one session by $t_4 - t_3 = 11\,\mu s$ before the detection. This gives us more information about their fast early evolution, and helps us in measuring their lifetime more precisely.

For the preparation of $60C$, one difficulty is that the sweeper technique cannot immediately clean the impurities in the 58 manifold after the $58C \rightarrow 60C$ MW transfer. A sweeper that ionizes the high-m impurities at $n = 58$ must first ionize the prepared $60C$ with a lower ionization threshold. We solve this problem by using a weak σ^+-polarized rf decircularization pulse to tranfer the residual high-m populations to the low-m states, which have a lower ionization thresholds than that of $60C$. This decircularization process is shown in Fig. 3.30.

The rf decircularization pulse applied in the figure has an estimated Rabi frequency of only 0.4 MHz in the 60 manifold. At the same time, the rf pulse is resonant with the 58 manifold and thus detuned from the 60 manifold by more than 6 MHz. This efficient

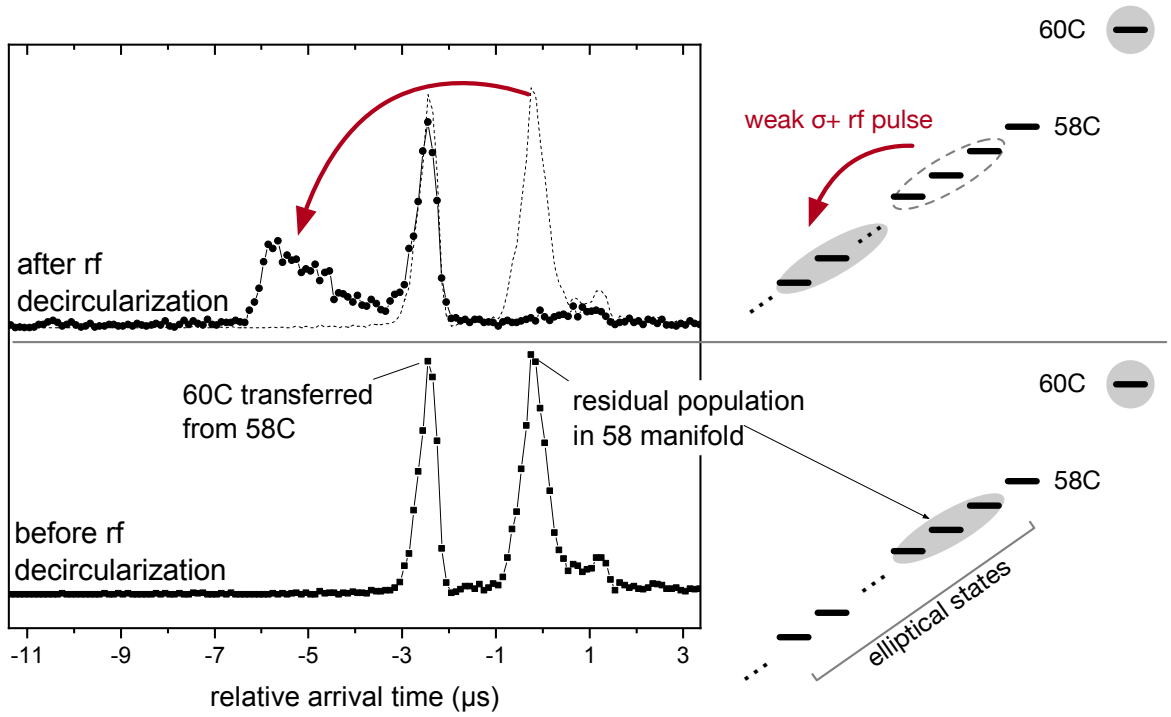

Fig. 3.30 *The rf decircularization for the prepration of* $60C$*. The bottom half shows the* $60C$ *prepared after a* $58C \rightarrow 60C$ *MW transfer. A sizable high-*m *impurities remain at a later arrival time. The top half shows the same ionization signal in dashed line. It also shows the resulting ionization signal after the application of an rf decircularization pulse. The undesirable high-*m *impurities are effectively moved to an earlier arrival time, accessible to the partial ionization technique. The simple illustrations on the right are only qualitative (e.g. the non-circular populations can reside in Stark levels with* $n_1 > 0$*).*

decircularization pulse in the 58 manifold does not perturb the purity of the prepared $60C$ by more than a few percent. Following this rf pulse, the impurity populations are open to a partial ionization sweeper, leaving the prepared pure $60C$ untouched.

The $60C$ prepared in this way is also the starting point for the preparation of the $58C$ state (with a higher purity than that prepared by only the initial ARP) and the $59C$ state. The preparation sequence of these two states is shown in the bottom half of Fig. 3.29. $58C$ is prepared by a $60C \rightarrow 58C$ MW transfer at t_4. Afterwards, a calibrated sweeper 3 clears the residual population in the 60 manifold before the final detection. Ideally, $59C$ should also be prepared in exactly the same way, simply with instead a $60C \rightarrow 59C$ MW transfer. However, the corresponding MW frequency at 31.2 GHz turns out to be below the cutoff (31.391 GHz) of our MW waveguide. Therefore the $59C$ preparation is performed at the end of a $58C$ preparation session by a $58C \rightarrow 59C$ MW transfer at t_5, immediately before the final detection.

Finally, after a CRA preparation sequence is set up, a lifetime measurement session consists in delaying the beginning of the final detection ramp at regular time steps τ_r, $\tau_r + \Delta t$,

$\tau_r + 2\Delta t, \ldots$. The corresponding ionization signals then represent a series of snapshots taken at different time points of the evolution of the initially prepared CRAs. We see in these snapshots the BBR-induced population redistribution among different ionization windows. One can immediately appreciate from these snapshots the stark contrast between the decay-inhibited and the decay-enhanced CRAs. In a comprehensive data analysis in chapter 4, the lifetimes of the prepared CRAs can be inferred from all the transfers in these snapshots.

Chapter 4

The Data: Determination of Lifetime

In chapter 2 we presented the properties of the Rydberg atoms with a strong focus on the theoretical lifetime of the circular Rydberg state. In particular, we discussed that the CRAs are expected to have ideally milliseconds of room temperature lifetime in between a plane-parallel capacitor. In chapter 3, we detailed our vapor cell experiment and the capacitor structure. We concluded by showing the preparation sequences for seven different circular states inside the capacitor.

In this chapter, we present the results obtained by following the time evolutions of the initially prepared CRAs for $\approx 1\,\text{ms}$.

In section 4.1, we present the ionization signal datasets, the snapshots of the CRA's population distribution. In section 4.2, these datasets are analyzed through a comprehensive rate equation fitting, based on which we report the millisecond-lived CRAs in our room temperature setup. Section 4.3 shows our efforts in the reduction of the GHz environment noise, which negatively affect the lifetime of the CRAs. Finally, in section 4.4, two alternative rate equation models are compared with the one we used in section 4.2 and [49].

4.1 Arrival Time Data

The arrival time signals of the initial circular states (zero detection delay) prepared by the sequences introduced in subsection 3.2.4 are shown in Fig. 4.1. The ion counts for each curve are normalized by their sum over the whole curve, so that an integration of any curve yields an area of one. This makes the purity of the initially prepared circular states immediately comparable between different n's. From the heights of these zero-delay detection signals, we see the evident increase of the σ^+ transfer rate as n decreases. The states $55C$ and $54C$, for example, populate their neighboring circular states so fast that it is not possible to prepare them with a high purity. In this figure, the most long-lived and most short-lived states are respectively $60C$ and $54C$. For these two states, we also give in dashed lines the corresponding ionization signals after $900\,\mu\text{s}$.

The signals shown in Fig. 4.1 are chosen from the arrival time data collection in Fig. 4.2. This full collection of data is used for the rate equation data fitting (section 4.2). The collection contains 16 datasets: a $300\,\mu\text{s}$ evolution and a $900\,\mu\text{s}$ evolution for each of the prepared circular states from $54C$ to $60C$. In addition, for the very short-lived $54C$ and $55C$, a $150\,\mu\text{s}$ short time evolution dataset is acquired using the alternative MW transfer

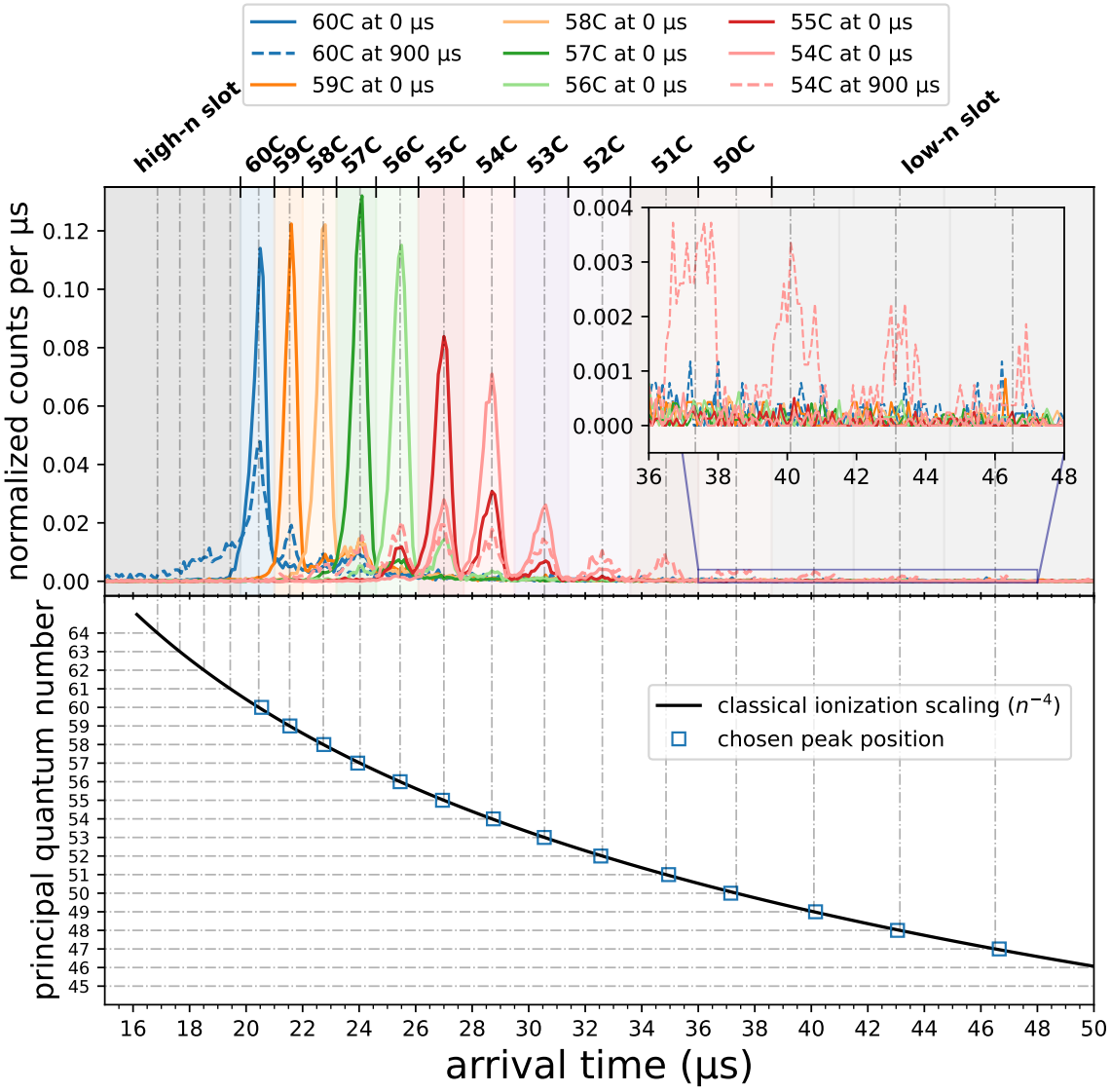

Fig. 4.1 *Normalized ionization signals of all the circular states prepared in this work. Solid lines show the zero detection delay signals chosen from (c), (f), (h), (j), (l), (n), (p) in Fig. 4.2. Dashed lines show the selected* 900 µs *delay signals from (c) and (p). All the signals have a time bin size of* 0.1 µs*. The detection window selections used in the data fitting in Fig. 4.4 are shown on top of the frame. The inset is an enlarged view of the low signals of the BBR populated circular states. The bottom panel shows in squares the manually chosen ionization peak positions in the arrival time. The black line is a fit of the points using the scaling of the classical ionization field.*

scheme shown in table 3.1 to reduce the time between their preparation and detection by 11 µs. These two datasets are shown in plots (a) and (d) of the figure. The two 150 µs heatmaps at zero delays have higher residual populations at early arrival time than the corresponding 300 µs and 900 µs versions. This is caused by the lack of a partial ionization sweeper before the final detection. On the other hand, the two maps have a slightly better contrast at zero delay between the prepared nC and the BBR populated $(n-1)C$ due to the earlier detection without the sweeper.

Two constraints cause us to collect the data in such a combination:

1. The field waveform generator is limited to store a max of 31 different delays for the detection ramp. Therefore, using all available scan points, the delay scans up to 900 µs, 300 µs, and 150 µs correspond to increasingly finer delay step sizes of 30 µs, 10 µs, and 5 µs. Starting from zero delay, the 900 µs datasets allow us to observe the corresponding population distribution at a very late time, a regime where the BBR induced redistribution has slowed down and a fine time scan in detection is not necessary. The 300 µs and 150 µs datasets, on the other hand, can take frequent snapshots of the fast initial thermal transfer dynamics.

2. Given certain peculiarities of our measurement sequence and program, it is more fault-tolerant to change the time steps than to change the zero-delay detection time τ_r in Fig. 3.29. If setting τ_r was an easy operation, we could imagine collecting segmented evolutions and combining them afterwards. This could reduce some redundancy in the data collection (e.g. the zero-delay ionization signal for each nC does not need to be acquired multiple times). But for practical convenience, all our datasets start from zero detection delay.

The ionization signals presented in Fig. 4.2 are already normalized at each detection delay by the signal sum. This is the same normalization as in Fig. 4.1. After this normalization, it is as if we detected one and only one atom at each delay. The lost information is the fluctuation of the total atom number, which is an irrelevant input for the rate equation fitting procedure. The BBR induced inter-level transition rates cause only relative population transfers among the levels. They do not lead to a change in the magnitude of the total population.

Note that, without the normalization, we observe in all the datasets a gradual loss of the total atom number as the detection delay increases. This is an expected behavior in our setup. When the ground state atoms are turned into the CRAs, they are not slowed by the cooling beams anymore. Therefore the prepared CRA ensemble starts to expand. The expansion eventually leads to an incomplete detection of the ensemble, since the outer rim of the ensemble at long times extends to outside of the detection diameter. These expansion-induced losses are not the only ones. In each session, the fast repetition of excitation and ionization rapidly removes atoms from the MOT cloud, which does not have time to replenish from the surrounding vapor at the beginning of a session. As the session progresses, the atom loss rate, being proportional to the decreasing atom number in the MOT, would eventually become equal to the MOT replenishment rate to reach an equilibrium. From the beginning of a session to the equilibrium, the typical time scale is a few seconds, during which we would have scanned through a few delay points already. For this reason, the "MOT depletion loss", just like the expansion loss, becomes more significant at larger detection delays. However, unlike the expansion loss, this is not a true delay dependency, but rather a concurrence of

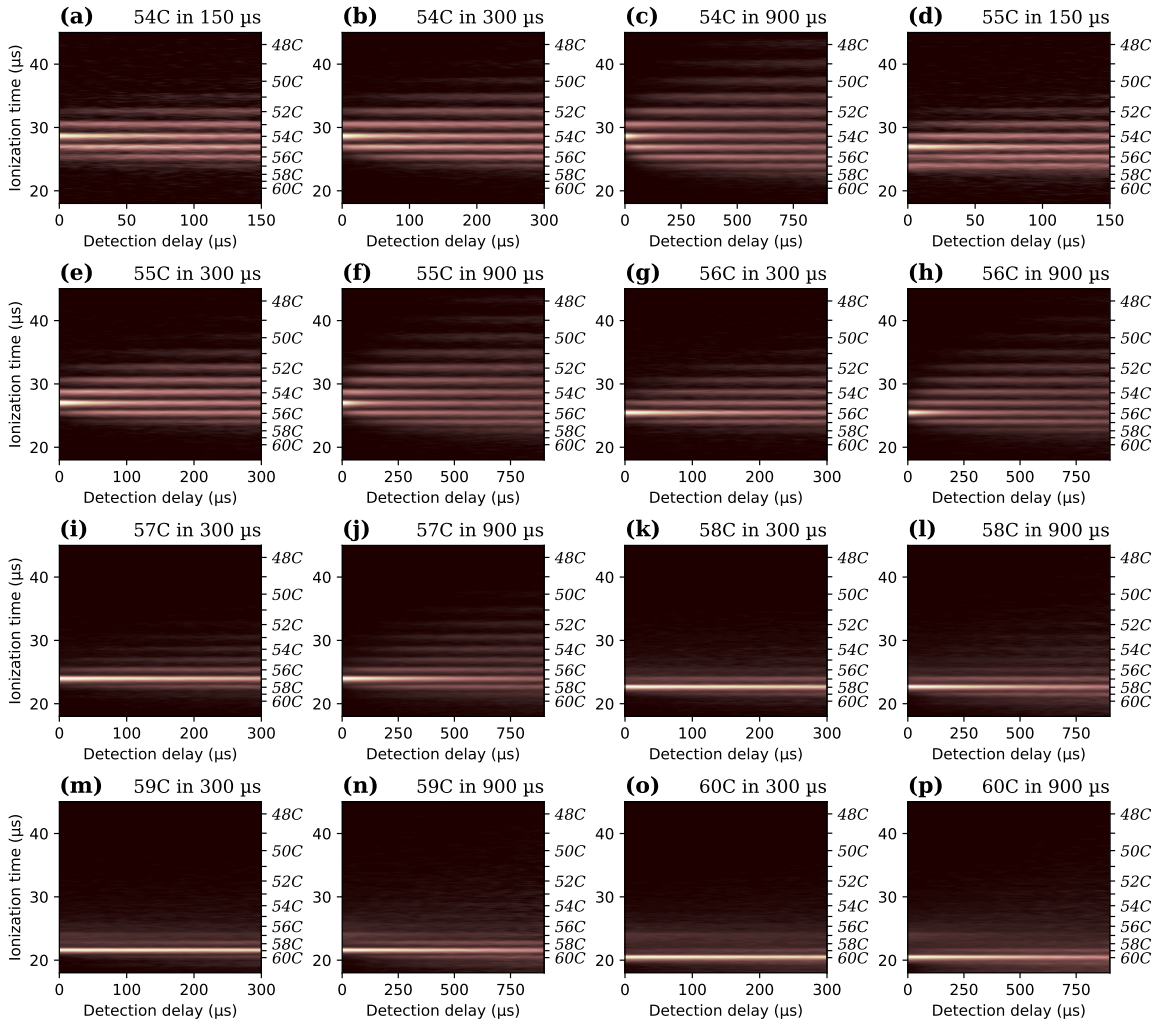

Fig. 4.2 *Arrival time signals of all the prepared CRAs at linearly spacely detection delays. The same 31 delay points are used for all the datasets. The vertical axis, the ionization time, always has a bin size of* 0.1 µs*. The zero point of the vertical axis is the onset of the final detection ramp. For each heatmap, the color scale is normalized to the maximum value on the map. The center positions of the circular states' ionization peaks, whether they are visible or not in a map, are marked on the right side of each map (one tick every n, one label every two n's). During the data acquisition, a* 6 dB *attenuation was applied to a known source of GHz noise (analysis of this noise is in section 4.3). Note that (a) and (d) are prepared by the alternative MW schemes in table 3.1.*

MOT depletion and delay increments. This effect is experimentally tested to contribute to 30% of loss factor in all the datasets. The 900 µs datasets naturally see the greatest atom loss, the loss factors varying in the range from 2.88 (j) to 4.36 (n). From these, we deduce the expansion-only loss factors to be around 2 to 3, for 900 µs.

We give a brief statistical profile of this data collection. For the zero detection delay, we detect per ionization at most 0.295 atoms (o), at least 0.129 atoms (n). For the final detection delay of the 900 µs datasets, these two numbers are respectively 0.0946 (j) and 0.0296 (n). We perform more detections for the sessions with a longer time evolution, in order to even out the effects of low counts at long times. The 150 µs, 300 µs, and 900 µs datasets are obtained respectively after 9000, 18000, and 36000 detections at every delay. If we pick from this data collection a random ionization signal, i.e. a random column in any plot in Fig. 4.2, it is constructed by at least 1066 detected atoms [the end delay of (n)], at most 9812 detected atoms [the zero delay of (j)].

Without any post analysis, we can already appreciate visually from these raw data maps the clear contrast between the long-lived and the short-lived CRAs. The $54C$ is the most short-lived circular state (lifetime 43 µs) in our inhibition capacitor (in free space at 300 K, the circular state with a comparable lifetime is $30C$). It is experimentally challenging to prepare a large initial $54C$ population without considerable BBR-induced transfers to the neighboring $55C$ and $53C$ states. In heatmap (c), the population visibly diffuses consecutively down to as low as $48C$, but the same trend does not extend to the upward transitions. The circular state windows beyond $58C$ stay dark, indicating an increasingly weakened σ^+ transfers at high n. This relative lack of upward transfers does not improve when the initial CRA is a $56C$ (h) or a $57C$ (j). Starting from the initial state $58C$, the population diffusion in time becomes much less conspicuous. The $60C$ barely reveals in the heatmaps any downward transfers. Throughout all these heatmaps, the inhibition cutoff region above $58C$ appears as an inaccessible zone when the initial population is prepared outside, and an inescapable zone when the initial population is prepared inside.

4.2 Fitting Data with Rate Equations

The 300 K BBR-induced transfers shown in the ionization data presented in section 4.1 are governed by the physically well-defined inter-level decay rates. The nature of these constant rates was developed in section 2.4. Consequently, the observed population redistributions can be fully described by a set of coupled rate equations.

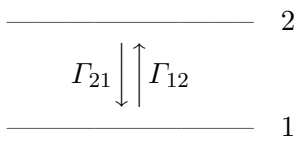

Fig. 4.3 *A two level rate equation model.*

As a concrete example, we consider a minimal two-level rate equation model, described in Fig. 4.3. The populations of level 1 and level 2 as a function of time are denoted by $p_1(t)$, $p_2(t)$, respectively. The population transfers can only be in directions $1 \to 2$ and $2 \to 1$, the corresponding constant transition rates are denoted by Γ_{12}, Γ_{21}, respectively. The system's

coupled rate equations then take the form:

$$\frac{\mathrm{d}}{\mathrm{d}t}\begin{pmatrix} p_2(t) \\ p_1(t) \end{pmatrix} = \begin{pmatrix} -\Gamma_{21} & \Gamma_{12} \\ \Gamma_{21} & -\Gamma_{12} \end{pmatrix} \begin{pmatrix} p_2(t) \\ p_1(t) \end{pmatrix} \tag{4.1}$$

A diagonalization of the square matrix above decouples the homogeneous system, then the evolution of the populations, given the initial $p_1(0)$, $p_2(0)$, is known at any time t. For a larger system with more levels, one simply diagonalizes a bigger matrix.

Above we described how we can obtain the population evolution with a set of known input rates. In the experiment, we face the inverse problem: we measure as ionization signals the population evolutions, from which we want to extract a set of decay rates to characterize the lifetimes of the CRAs. This can be achieved by firstly building a rate equation model with the rates to be determined, and secondly using this model to directly fit the evolution data to obtain the set of least squares rates.

For performing the rate equation model fitting, the raw ionization signal data in Fig. 4.2 need to be grouped into well divided time windows. The ions summed up in different windows represent the populations detected in different manifolds. The borders of these windows are naturally chosen to be at the minimum counts positions in Fig. 4.1, and shown in the figure as the top ticks. The states above $60C$ and below $50C$ are not significantly populated during the time scale of the experiment. We hence do not try to discriminate the inter-level transfers for the states with $n \geq 61$ and $n \leq 49$, and instead set two wide detection windows (the high-n and low-n slots) for their signals. The windowed ion counts plotted as a function of detection delays are shown in Fig. 4.4. The solid curves are the corresponding rate equation fit.

In this figure, we see a high level of agreement between the data points and the fit curves. It is even more remarkable to realize that the 16 plots are showing the results of not 16 fits, but *one* fit. From one plot to the other, the same set of window-to-window transfer rates are shared. Only the initial populations are varied. The excellent fit is a demonstration of the validity of the rate equation model in our problem. A pictorial explanation of the rate equation model used in Fig. 4.4 is shown in Fig. 4.5.

The first thing we have to take note of is that the transfers in our model are to be interpreted as inter-window transfers, rather than inter-level transfers. This follows from the limitation of our detection by state-selective ionization (see subsection 3.2.1). In Fig. 4.5 (a), we show the breakdown of the concept of levels vs. windows. In our data, different nC states are well separated in time windows as shown in Fig. 4.1. The elliptical states ne_1 and ne_1' have similar ionization thresholds to that of the nC, therefore they both fall into the nC window during a detection. In free space, the BBR induced dynamics is limited to a chain of circular levels, due to the dominant σ^+ decay rates between the neighboring circular states. In this situation, the difference between a window and a level is not critical, since by detecting the ions in one window, we detect the population in one level. However, when the σ^+ decays are inhibited by the capacitor, from an initially prepared nC, the non-inhibited π and 2σ upward decay rates become comparable with the inhibited upward σ^+ rate. As a consequence, by detecting the ions in the $(n+1)$-window in Fig. 4.5 (a), we detect a sizable non-circular populations.

At room temperature, there are hundreds of thermal photons per mode in the transition frequency range of the circular states we consider (tens of GHz). As a result, the spontaneous emission contributes to less than 1% difference between the transition rates of $nC \to (n+1)C$

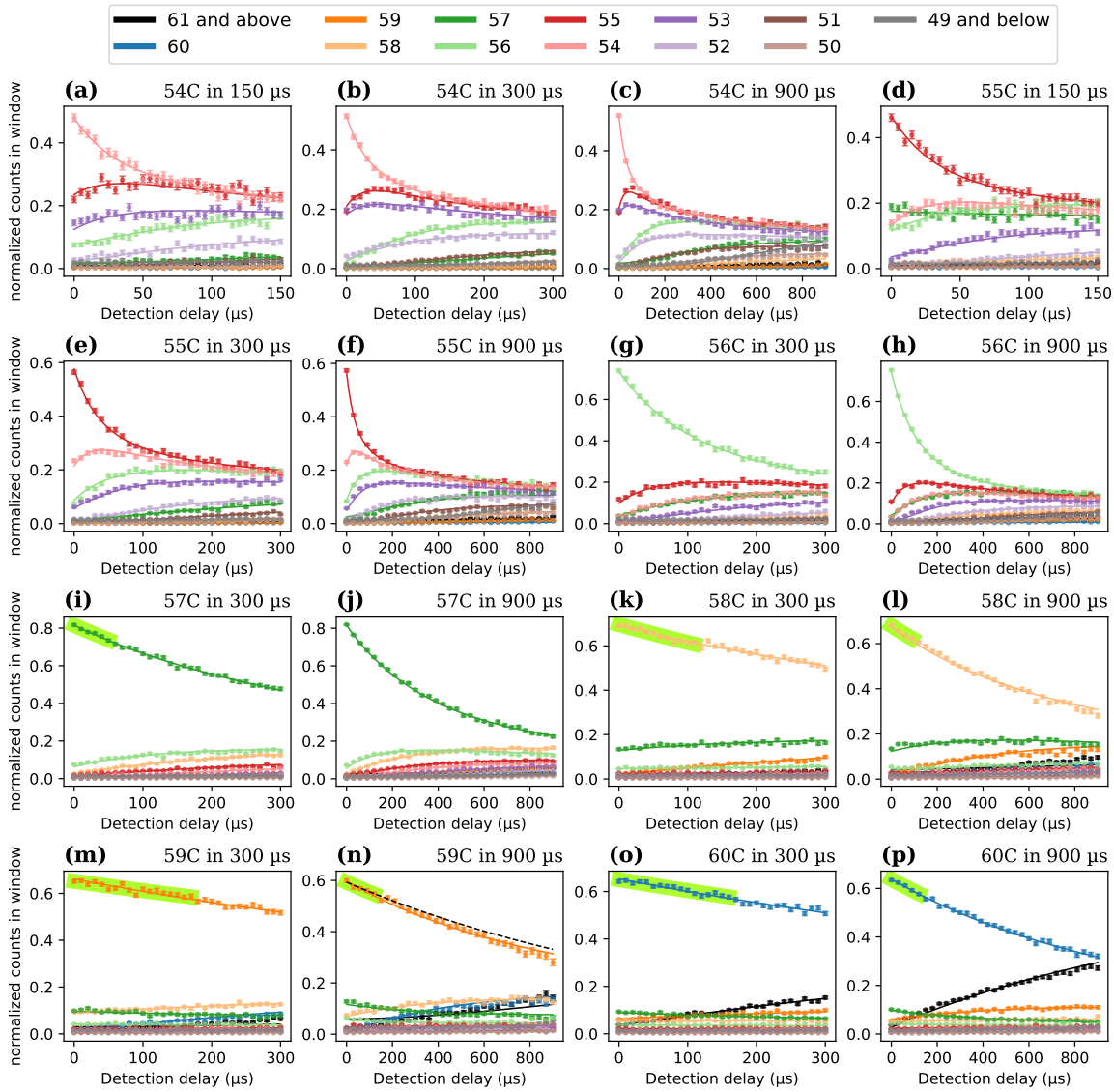

Fig. 4.4 *Windowed ion counts from Fig 4.2. The 16 datasets are fitted as a whole with the balanced model as illustrated in Fig. 4.5 (b). The error bars are poissonian errors based on the raw counts of each point. They represent the statistical fluctuations, but are not used to weight the fit. The green highlighted sections are used to obtain the short time exponential t_1 points in Fig. 4.7. In panel (n), the black dashed line gives the long time exponential decay using an optimistic t_1 plotted in Fig. 4.7 (the highest green empty ball).*

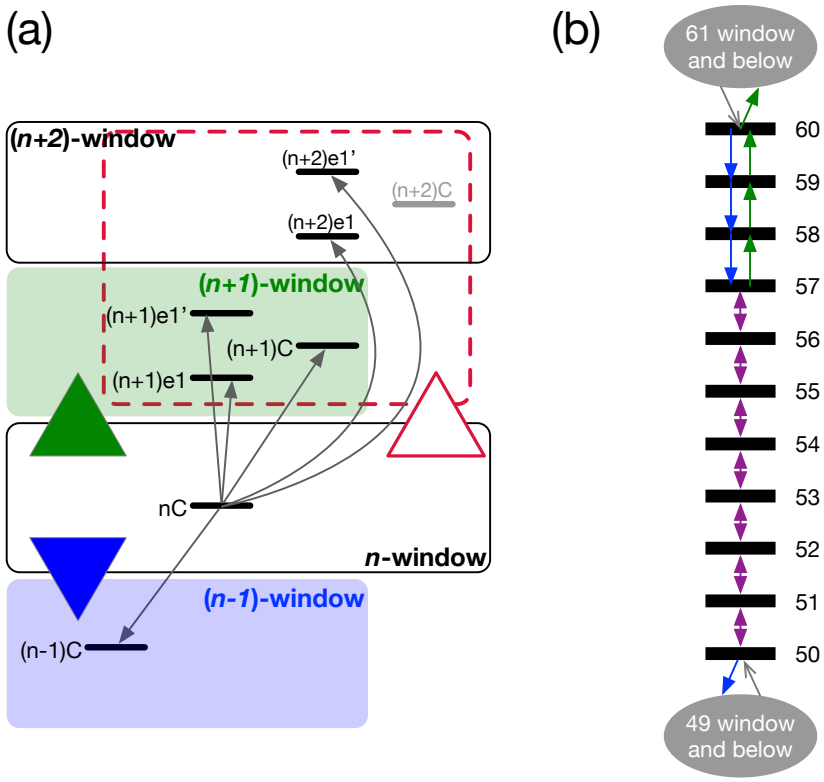

Fig. 4.5 *Rate equation model used in Fig. 4.4. (a) The gray arrows show all the 300 K decay channels with decay rates* $\gg 1\,\mathrm{Hz}$ *(c.f. Fig. 2.11) starting from a circular state. The big green and blue triangles represent the global inter-window transfers included in the model. The empty triangle represents a global transfer from the initial nC to the two next windows combined. This transfer is not modeled in the blanced model in (b). These triangle styles are reused to indicate the transfer types in Fig. 4.6. (b) Transfer scheme of the "balanced" rate equation model (more models are discussed in section 4.4). The detection windows are shown as the black levels and the gray balls. Every arrow, single or double headed, represents one fitting parameter in the model.*

and $(n+1)C \to nC$. This is less than our measurement errorbars, allowing us to ignore the spontaneous emission. Therefore, when there is no strong σ^+ inhibition, the transfer rates on the $nC \to (n+1)C$ and $(n+1)C \to nC$ transitions are considered equal. We can safely call these window transfer rates the $nC \leftrightarrow (n+1)C$ transition rates, for we are essentially observing the stimulated emission and absorption between in a two level system. However, when there is an effective σ^+ inhibition, we have to take into consideration that the n-window $\to (n+1)$-window decay rate is physically the sum of multiple rates combined $[nC \to (n+1)C,\ nC \to (n+1)e_1$, and $nC \to (n+1)e_1']$, which has to be noticeably larger than the observed $(n+1)$-window $\to n$-window rate. The determination of the latter rate in our rate equation fitting relies predominantly on the initially prepared $(n+1)C$, which exhibits a $(n+1)$-window $\to n$-window transfer rate that is the same as the $(n+1)C \to nC$ decay rate, a single-channel σ^+ rate.

In Fig. 4.5 (a), starting from a prepared nC in the n-window, the inter-window transfers are labeled with big triangles, while the inter-level transfers are labeled with gray arrows. In panel (b) we show the rate equation fitting model that we shall call the "balanced model" in the following text. The arrows in this scheme only stand for the inter-window transfers, as we have discussed above. However, outside of the effective σ^+ inhibition regime ($C_\sigma < 1/5$), the population redistribution is predominantly confined in the chain of circular levels. Consequently, the inter-window transfers below $n = 57$ are effectively $nC \leftrightarrow (n+1)C$ transfers. For each of these transfers we use a double-headed arrow to represent the only one rate parameter needed: the value of the identical stimulated emission and absorption rates between the neighboring circular levels. For the neighboring windows above $n = 57$, the σ^+ circular-to-circular transition rate does not overwhelm the non-inhibited π rate anymore. For these transfers, we use the single-headed arrows to represent the two separate upward and downward rate parameters. Finally, the wide detection windows, the high-n and low-n slots in Fig. 4.1, are represented by the two gray ellipses. We set different rate parameters for the transfers into and out from these slots for the model to be consistent. But the return rates from these slots, represented by the gray arrows, are not needed for the lifetime calculation. The return rates from these high and low states, too difficult to resolve individually, are simplified into one total return rate.

We have so far omitted the 2σ decay rate. If we consider it to be non-negligible, the total upward transfer rate should physically be the sum of the rates from the n-window to the combined two windows upwards (the big empty triangle). However, without considering this, our balanced model shown in Fig. 4.5 (b) already yields a good fit as shown in Fig. 4.4, which might be an indication that for the most σ^+-inhibited CRA we have prepared, the upward σ^+ and π rates combined are still larger than the sum of the 2σ rates. Moreover, as we will mention, the 2σ can be taken into consideration in a more complex model, which agrees with the balanced model for the measured lifetimes.

The shared set of rates that fit the 16 evolutions in Fig. 4.4 is plotted in Fig. 4.6. The data points (with errorbars) are the balanced model's input rates that best describe the whole data collection. These data points have a one-to-one correspondence with the arrows in Fig. 4.5 (b), the latter give the directions of these transfer rates. The rest of the points show the theoretical rates, these are connected by lines. The line-connected gray points are the theoretical 300 K free space inter-window transfer rates, which for our concern have only one rate value for every point. If we try to discriminate the different upward and downward transfer rates, we find that their difference in this plot is smaller than the size of the gray points. The line-connected colorful points are the capacitor-modified inter-window transfer rates obtained using the C_π and C_σ parameters in Fig. 3.14. We recall that the upward rates, denoted by the green and the red triangle points, refer to the sum of rates from multiple decay channels, which is illustrated in Fig. 4.5 (a). Since it is impossible to plot against a single transition frequency an upward transition rate which results from the sum of multiple decay channels, we use a complex bottom axis for this figure. However, to focus on the main effect, the modification to the σ^+ decay rates among those between an n-window and an $(n+1)$-window, we put on the top axis the corresponding σ^+-polarized $nC \leftrightarrow (n+1)C$ transition wavelengths and frequencies. Note that these transition parameters on top *do* associate uniquely with the matching downward rates (blue triangles), since only one channel (circular-to-circular) contributes to any downward decay from an initially prepared circular state.

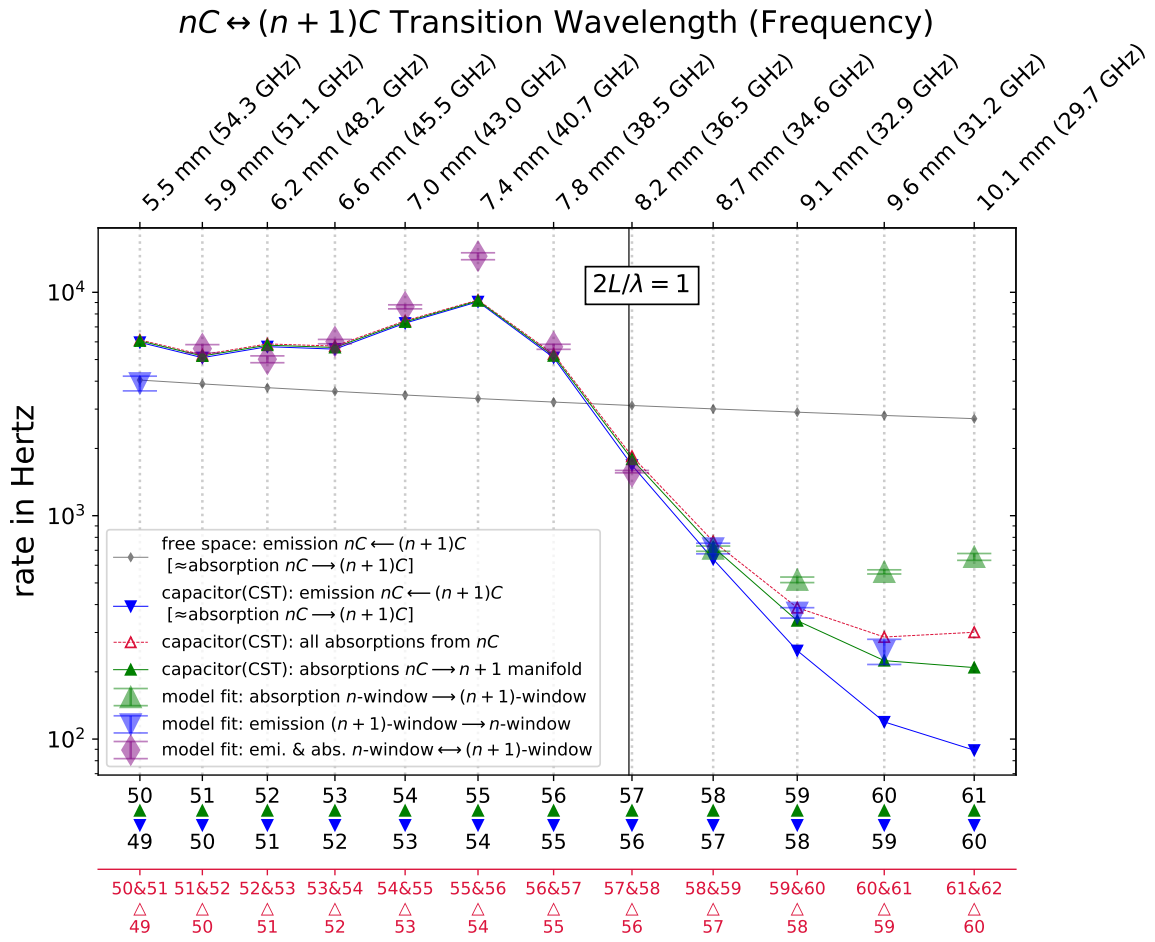

Fig. 4.6 *Plot of the rates. The model rates, determined by the fit as shown in Fig. 4.4, are given by markers with errorbars. The other markers are theoretical. The rate points are plotted against the corresponding $n \leftrightarrow n+1$ window transfers they are responsible for ($n \rightarrow n+1$ & $n+2$ for the empty red triangle points). The filled green and filled blue triangles (both with or without errorbars) and the empty red triangle stand for different inter-window transfer rates as illustrated in Fig. 4.5. Outside of the effective σ^+ inhibition regime, the purple diamonds stand for the common rate for $n \rightarrow n+1$ and $n+1 \rightarrow n$ transfers. The small gray points are the theoretical 300 K free space decay rates from $(n+1)C$ to nC. On the top, we show the corresponding $nC \leftrightarrow (n+1)C$ transition wavelengths and frequencies. A vertical solid line is put at the cutoff wavelength of an ideal 4.1 mm capacitor.*

The first feature we notice in Fig. 4.6 is a drop of the obtained rates towards the right of the plot. A technical inhibition is already reached after the ideal cutoff line at $2L/\lambda = 1$: the $56 \leftrightarrow 57$ transfer rate is lower than the corresponding theoretical rate in free space by a factor of two. For the next pair of windows, $57 \leftrightarrow 58$, the inhibition increases to a factor of 4.2. However this is still not enough to make transitions other than the σ^+ ones dominant. The obtained $57 \rightarrow 58$ rate is $714 \pm 39\,\mathrm{Hz}$, and the $58 \rightarrow 57$ transfer rate is $712 \pm 19\,\mathrm{Hz}$. We specifically discriminate in this balanced model the independent upward and downward transfer rates at $57 \leftrightarrow 58$ to demonstrate that this is the critical point where the σ^+ is still dominating. For the next pair of windows, $58 \leftrightarrow 59$, the non-reciprocity between the up and down rates emerges. The $58 \rightarrow 59$ and $59 \rightarrow 58$ transfers have respectively rates of $517 \pm 15\,\mathrm{Hz}$ and $368 \pm 20\,\mathrm{Hz}$. The lower rate gives the measured σ^+ transition rate. Compared with the theoretical free space rate, this $58C \leftrightarrow 59C$ transition rate at 300 K has been inhibited by a factor of 7.9. We hence deduce that a σ^+ inhibition factor of ≈ 5 is necessary to observe the emergence of the usually σ^+-overwhelmed π transitions. We note that this "effective inhibition threshold" could be setup-specific, since the C_π enhancement varies greatly from one capacitor design to another. For example, the C_π of an ideal capacitor is always an enhancement factor (> 1) below the cutoff, but the C_π of a real capacitor could be an inhibition factor (< 1) under the same condition (see Fig. 3.14).

The initial break of the up-down reciprocity at $58 \leftrightarrow 59$ is also observed in the simulated theory points. However, it is also at this point that the data rates deviate noticeable from the theory points. The higher rates obtained from the data could be due to the limitation of the longest evolution time (900 µs only): it is less than the lifetime of the $59C$ and $60C$ obtained from these rates (observing longer evolution proved too time consuming to undertake due to the greatly reduced detection efficiency caused by the expansion of the Rydberg ensemble). The errorbars produced from the Levenberg-Marquardt fitting algorithm appear significantly larger for these most inhibited transfer rates at $58 \leftrightarrow 59$ and higher. As a result, we turn to use a more sensible type of errorbar for the rate points: a simple standard error. As we mentioned in section 4.1, each of the 16 evolution datasets is acquired after 9000, 18000, or 36000 repetitions. We divide these repetitions into 5 equal subsets. The balanced model by fitting these subsets generates 5 sets of rates. The unbiased standard errors calculated from these subset rates provide the errorbars in Fig. 4.6. Since the complete data acquisition took a few days, the errorbars produced in this way are an indication of the reproducibility of our measurement. The other reason for the disagreement between the inhibited data rates and theory rates could be the imperfections of the CST simulation. In particular, the simulation results show that the inclusion of the transverse electrodes into the capacitor increases C_σ (a reduction in the σ^+ inhibition). The increased ΔC_σ also keeps increasing towards low frequency. For the $58C \leftrightarrow 59C$ transition, this increase is $\approx 3\,\mathrm{dB}$, with which we calculate the corresponding theoretical rates. If the electrode effect is underestimated, the real electrodes may result in a higher ΔC_σ, the theory rates would be in better agreement with the data rates. Finally, we note that a large data-theory disagreement also happens for the $54 \leftrightarrow 55$ transfer. At this cutoff resonance point, both the data and the theory correctly find their highest points, however the former is a factor of 1.6 that of the latter. Given that this rate is outside of the effective σ^+ inhibition regime, there is no complication involved in measuring the simple circular-to-circular transfer rate. It is hence more likely that the CST simulation underestimates the cutoff resonance. The increased resonance can also be attributed to the lowered ITO resistance due to Rb deposits, or to the heated disperser operating at 750 K,

which increases the temperature of the BBR.

The fitted rates we show in Fig. 4.6 characterize the departure rates, either through single channel or through multiple channels, from the initial circular states we prepare. We can thus obtain the lifetime of an nC by calculating the inverse of the sum of two transfer rates: $n \to n+1$ and $n \to n-1$. The corresponding lifetimes of the circular states are shown in Fig. 4.7.

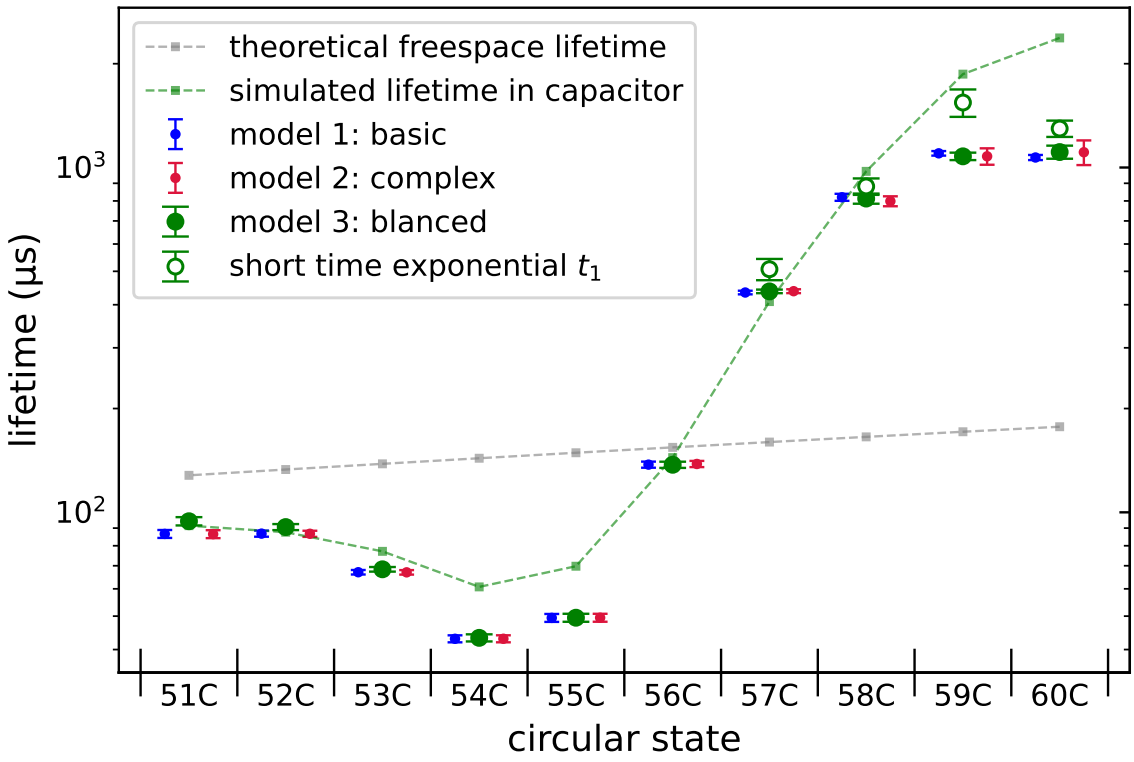

Fig. 4.7 *Lifetimes of the CRAs from* $51C$ *to* $60C$*. In each* nC *slot there are at least 5 different lifetime points: theoretical 300 K free space lifetime (gray square), CST simulation predicted lifetime (green square), the lifetimes calculated from three different data fitting models (filled balls), in which the green filled balls are calculated from the rates in Fig. 4.6. The blue and red balls are side shifted to prevent overlapping. For* $n \geq 57$*, we give in green empty balls a sixth lifetime estimation: the* t_1 *of the short time exponential fit* ($y_0 = 0$) *of the initially prepared population.*

In this figure, we plot the lifetimes of all the prepared CRAs from $60C$ to $54C$. We also include the lifetimes of $53C$, $52C$ and $51C$, because the uninhibited BBR-induced σ^+ transfers can populate sufficiently these levels starting from the states we prepare. The 900 μs evolution time also allows us to monitor their population redistribution over the course of multiple lifetimes, during which only the simple circular-to-circular transfers take place. Hence we can determine their lifetimes well.

In the figure, we plot as green filled balls the lifetimes calculated from the balanced model rates of Fig. 4.6. The lifetime errorbars are propagated from the statistical errors

of the rates. The values of these lifetimes are also given in table 4.1. For comparison, we plot also the lifetimes obtained from two additional rate equation fitting models. We will cover these two other models in section 4.4. For now the comparison only serves to leave a clear impression that the obtained lifetime values do not change drastically as we add reasonable corrections to the fitting model. The measured lifetimes follow the trend of the CST-predicted lifetimes well. The disagreements of lifetimes at $60C$, $59C$, $55C$, and $54C$ follow from the corresponding disagreements in the transfer rates, as we discussed above.

Table 4.1: Lifetimes obtained from the balanced rate equation fitting model. The corresponding data points are shown in green filled balls in Fig. 4.7.

CRA	lifetime from balanced model
60C	$1109 \pm 48\,\mu s$
59C	$1078 \pm 27\,\mu s$
58C	$813 \pm 27\,\mu s$
57C	$437 \pm 5\,\mu s$
56C	$137 \pm 3\,\mu s$
55C	$49 \pm 1\,\mu s$
54C	$43 \pm 1\,\mu s$
53C	$68 \pm 1\,\mu s$
52C	$91 \pm 2\,\mu s$
51C	$94 \pm 3\,\mu s$

For the circular states from $57C$ to $60C$, due to their long lifetimes, we can prepare their initial states without the significantly BBR-populated neighboring windows. It is then possible to obtain from their single window evolution a short time exponential decay, with a time constant t_1, which in principle is not significantly impacted by the repopulations from the neighboring windows. We choose the short time durations that correspond to a 10% drop in the initially prepared circular population. The chosen data points in this range are highlighted in green in Fig. 4.4. We then fit these highlighted points with an exponential Ae^{-t/t_1}, with the free parameters A and t_1. The t_1 obtained for $60C$, for instance, is the weighted average of the two t_1's from (o), and (p). In the same way, the t_1 for $59C$ is from (m) and (n), the t_1 for $58C$ is from (k) and (l). The $57C$ is an exception, its t_1 is obtained from a single fit in (i). (j) is not used, because by fitting a drop of less than 10% of initial population in this plot, we only fit two points. The four short time exponential t_1's obtained without the rate equation model corroborate the lifetimes obtained from the model. They are shown as green empty balls in Fig. 4.7. These t_1's reproduce the same trend as the corresponding rate equation lifetimes. However, the t_1 of $59C$ is evidently too optimistic. To show this, in Fig. 4.4 (n), we explicitly plot in a black dashed line the 900 µs exponential decay using the optimistic short time exponential t_1. This dashed line is above all the $59C$ population points at long times, indicating that the short time fit of only a few points fail to give a better lifetime characterization than a full rate equation that takes into account all the data points. The imprecision of the short time t_1 of $59C$ is also evident by the fact that it should ideally predict a faster decay rather than a slower decay at long times when the repopulation process slows down the loss of the population from the 59-window. The fluctuations of the first few points can thus lead to a large uncertainty in these t_1's, as shown

in their large errobars. This also suggests that the rate equation could equally benefit from fitting evolutions longer than 900 µs.

4.3 Transfer Rate Sensitivity to non-BBR Noise

The rather small uncertainties in the lifetimes in table 4.1 come from the equally small uncertainties of the rates in Fig. 4.6. These simple statistical uncertainties demonstrate the ability of a comprehensive rate equation fitting to overcome local noise in the data collection. With these precisely measured rates, we are able locate a non-BBR noise source in our experiment.

The noise source is a MW frequency multiplier (millitech AMC-19-RFH00), which is a powered frequency mixer. For generating the CRA preparation MW pulses, the mixer has to stay operational even when no MW pulse is triggered. The GHz white noise from the mixer outputs through the MW waveguide pointing at the glass cell, adding to the background 300 K BBR. This noise leads to a global increase in the observed inter-window transfer rates. The reduction of this noise, on the hand, leads to a global decrease of the observed rates.

Using a tunable, direct reading MW attenuator (millitech DRA-19-C), we are able to quantitatively reduce the mixer noise. The precision of the attenuator is first tested by attenuating a MW Rabi pulse at 40.7 GHz, resonant with the $55C \leftrightarrow 54C$ Rabi oscillations. We incrementally set a series of MW attenuation values from -3 dB to -25 dB, and record the corresponding Rabi frequency before (Ω_{before}) and after (Ω_{after}) each attenuation increment. The squared ratio $(\Omega_{\text{after}}/\Omega_{\text{before}})^2$ gives us the reduction in the MW power as felt by the atoms. The atom-felt attenuation values are plotted against the hand-set attenuation values in Fig. 4.8. We see in this figure that the attenuator can impose a precise attenuation to the MW output towards the atoms.

We then prepare the same complete data collection as in Fig. 4.2, but at different hand-set MW attenuation values of 0 dB, -1.25 dB, -3 dB, -6 dB, and -18 dB. At each value, the MW source power is increased accordingly to compensate for the attenuation, in order to still prepare the CRAs using the MW transfer schemes introduced in subsection 3.2.4. At the same time, the mixer noise at different attenuations experiences a reduction of respectively 0%, 25%, 50%, 75%, until almost 100%.

The only data collection we show in this manuscript (Fig. 4.2), thouroughly discussed in the previous sections, was acquired under an attenuation of -6 dB. For the other data collections, we show only the resulting rates from the rate equation data fitting. The rates under different mixer noise attenuations are compared in Fig. 4.9. In this figure, we plot the $n \leftrightarrow n+1$ transfer rates from $51 \leftrightarrow 52$ to $57 \leftrightarrow 58$. Lower windows are not sufficiently populated, higher windows correspond to lower transition frequencies, which are outside of the attenuator's working range[1]. In addition, as the upward and downward rates are equal within errorbars for $57 \leftrightarrow 58$, we can use less rate points to make a clear comparison.

In the figure, we see clearly that the obtained inter-window rates are consistently lower when a larger attenuation is applied. This is certainly the expected behavior, well picked up

[1]However, the mixer noise does not affect the lifetimes of the inhibited CRAs with $n \geq 58$. In this high-n regime, the small transition frequencies are close to the cutoff of the output waveguide. The mixer noise in this frequency range is heavily attenuated, and does not reach the atoms.

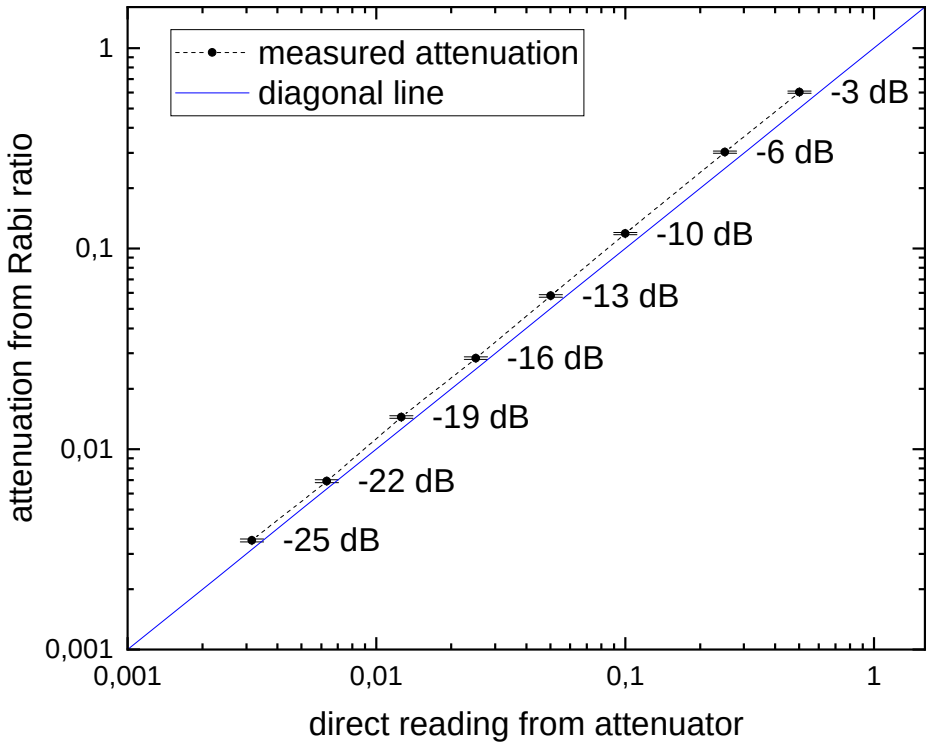

Fig. 4.8 *The reduction of MW power caused by a tunable MW attenuator. At each increase of the hand-set attenuation, the attenuation value displayed in the reading window of the attenuator is the x value of the data point (also shown in decibel numbers inside the plot). The attenuation inferred from the reduction in the $55C \leftrightarrow 54C$ Rabi frequency is the y value. The errobars are propagated from the fitting uncertainties of the Rabi frequencies. A diagonal line when the hand-set and the atom-felt attenuations perfectly agree. The attenuator's working range is* 40 GHz *to* 60 GHz *(U band), the attenuated frequency in the figure is* 40.7 GHz.

through the rate equation fitting. It shows that any noise source inducing a change larger than the experiment fluctuations, characterized by the rates' statistical errorbars, can be detected globally in all the inter-window transfers. The rates we obtain by fitting all these transfers are thus precise within the statistical errorbars. This is especially evident when we notice the excellent linear drop of rate points at $55 \leftrightarrow 56$ and $56 \leftrightarrow 57$. This is because, given the linearly spaced the attenuation values, when the statistical errorbars are sufficiently smaller than the rate decrease caused by each linear increase of the attenuation, the drops in the detected rates appear as linear steps.

Ideally, the attenuation should be applied in its full, removing the non-BBR mixer noise in its whole. However, this attenuation also applies to the MW transfer pulses we use to prepare the circular states. At a global attenuation of -18 dB, the MW pulse at low frequencies become too weak in power to induce enough transfer within reasonable time in an experiment sequence. Therefore, we choose a MW attenuation of -6 dB to acquire the main data presented in section 4.1. With this attenuation, we can reduce most of the non-BBR noise induced spurious rates. Further spurious rates reduction at -18 dB would

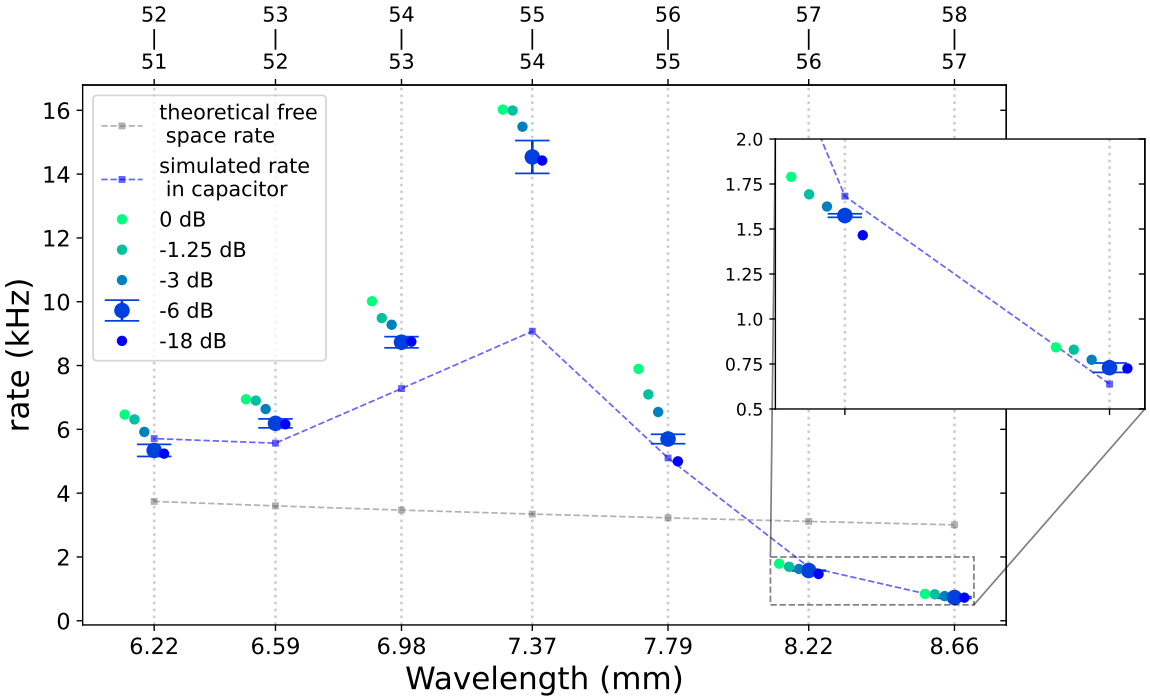

Fig. 4.9 *Response of the measured rates to the controlled attenuation of a MW noise source. The rates obtained under different attanuations are side shited differently to prevent overlapping. Only the* -6 dB *rates have the statistical errors calculated by fitting multiple data subsets. The other rates should have comparable statistical erros.*

be marginal.

4.4 Alternative Rate Equation Models

The balanced rate equation model we show in Fig. 4.5 (b) is the main model we analyzed in section 4.2. There are two other rate equation models we used to fit the data in Fig. 4.2, and their corresponding lifetimes were shown in Fig. 4.7. The transfer schemes of these two models are shown in Fig. 4.10.

The basic model is actually the complete rate equation model needed for a free space CRA. The model considers only the 300 K BBR-induced stimulated emission and absorption, equal in value, between the neighboring circular states. Hence one rate parameter is enough between any two neighboring windows. This model is valid for a CRA experiment time scale of at least 10 ms in a cryostat [40], or below 3 ms to 5 ms at 300 K. The BBR-induced population redistribution in the end always extends outside of the circular level chain, but the untrapped CRAs cannot reach such a high experiment time scale. In our longest 900 µs evolution, the basic rate equation model would also be enough in the absence of the σ^+ inhibition.

However, the balanced model found a higher upward transfer rate when the σ^+ transition is effectively inhibited. This drove us to add more physical decay channels on top of the

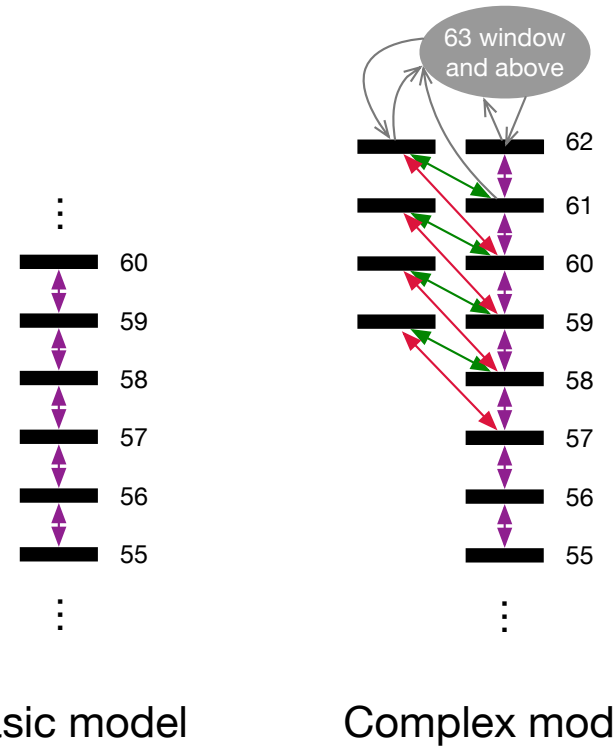

Fig. 4.10 *The transfer schemes of two other rate equation models. The basic model ignores the non-σ^+ transitions. The complex model considers the π (green) and the 2σ (red) transfers.*

balanced model. We then reach the complex model. This model is only more complex than the balanced model, but actually less complex than the real physical process. From window 59 to window 62, in addition to the circular level chain of the basic model, we explicitly add one single elliptical level which accepts the BBR-stimulated π and 2σ transfers from the prepared circular levels. At 59 and above, the population in the detection window is the sum of the "elliptical" and the "circular" populations. For the window 63 and above, we use again a wide detection window to maintain a population-conserving rate equation. Making an exact physical model to consider both of the $m = n-2$ elliptical states is possible, but this model would be overfitting the data when the detected ionization signals cannot resolve these elliptical states. Besides, we did not see the complex model producing different lifetimes than the balanced model.

When we compare the fits performed on the same data collection using the different models, we see that the basic model has the highest χ^2, the balanced model has a relative χ^2 reduction of 18%, and the complex model shows no further reduction in χ^2. This suggests that the balanced model has already captured the essential dynamics that can be resolved from the inter-window transfers in the ionization signal. The discrepancies among these three models appear only at the 58-window and above. The relevant fitting comparisons are shown in Fig. 4.11.

In the figure, the datasets (j), (l), (n), and (p) are selected from Fig. 4.4. They correspond to the 900 µs evolutions of the initially prepared $57C$, $58C$, $59C$, and $60C$. The fit curves of

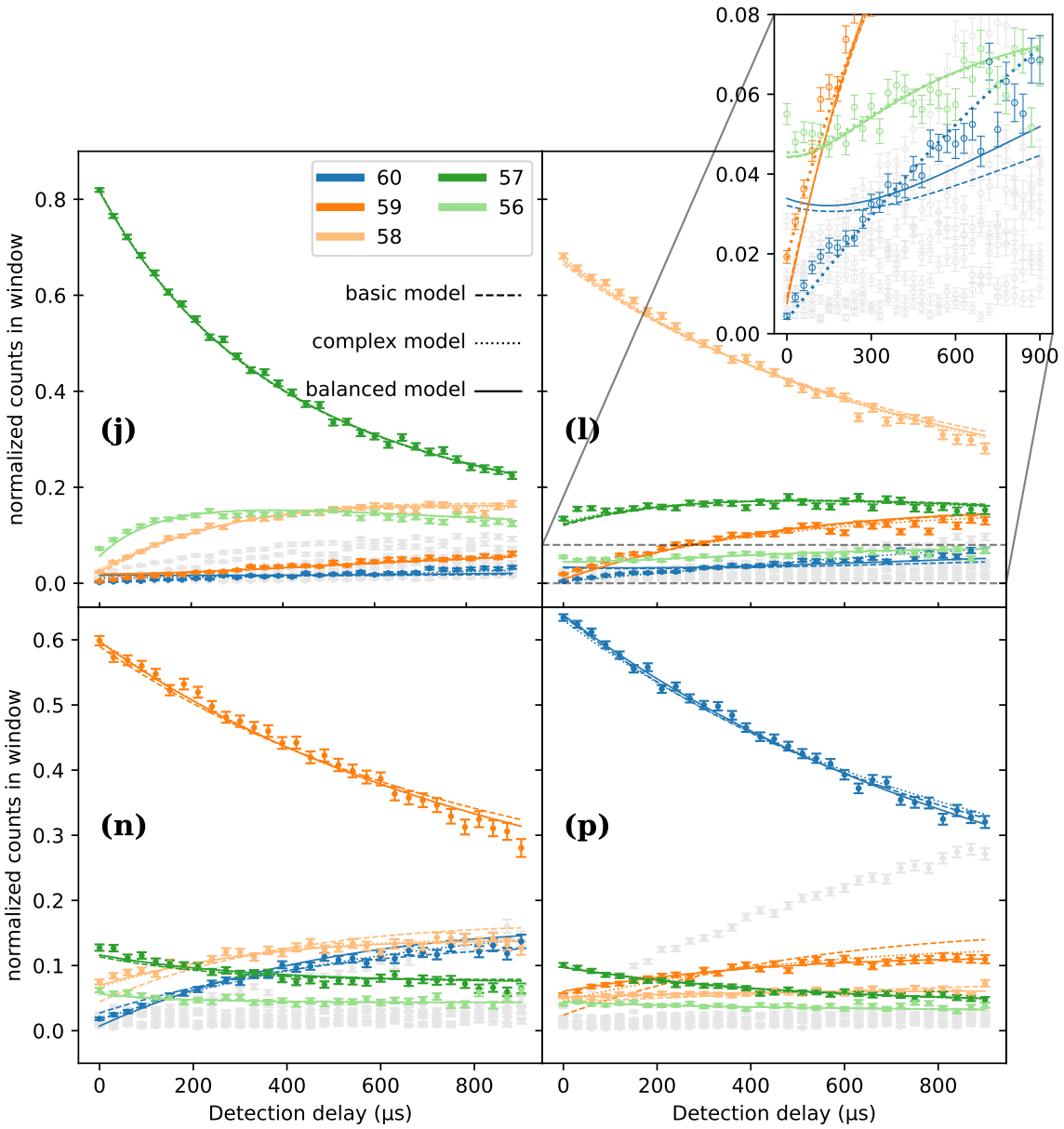

Fig. 4.11 *Discrepancies of the three models. The (j), (l), (n), and (p) frames show the same data as the corresponding plots in Fig. 4.4. The fit curve comparison is focused on the windows from 56 to 60. Data points from the other windows are grayed out, without the corresponding fit curves. The inset enlarges the low populations and the corresponding fit curves. The complex model (dotted) has a* $58 \to 60$ 2σ *channel, hence finds the best fit for the slow but steady rise of the 60.*

the three models are plotted respectively as dashed, dotted, and solid lines. The comparison is limited to the windows from 56 to 60, because for the windows below, all the models have the same transfer scheme. The plot (j) shows the excellent agreement of all three models. This corroborates our observation in Fig. 4.6 that the $57 \to 58$ and $58 \to 57$ transfers are the last pair of reciprocal transfers with equal rates before the effective σ^+ inhibition regime.

In plot (l), small discrepancies between the three models can be noticed. In particular we see that the complex model fits the low-lying 60-window population (blue) much better than the other two models. This shows that the complex model correctly registers the 2σ transfers from the initially prepared $58C$, which directly populates the 60-window at short delays. The other two models require the 59-window to be sufficiently populated first to start transferring noticeable population to the 60-window. They therefore fail to fit correctly the slight rise of the low-lying $n = 60$ population. The complex model obtains a series of 2σ transfer rates: $58C \to 60$, $59C \to 61$, $60C \to 62$ transfers have respectively the rates of 120 Hz, 115 Hz, and 200 Hz. These fitted rates agree qualitatively with the corresponding simulation predictions of 89 Hz, 104 Hz, and 119 Hz. Here each simulated rate is the sum of the two 2σ rates $[nC \to (n+1)e_1$ and $nC \to (n+1)e_1']$.

In the next plots (n) and (j), the basic model cannot fit the data points well anymore, while the balanced and complex models can still maintain a relatively decent fit. In the end, the balanced model is preferred for its lower number of fitting parameters.

The three very different models produce similar lifetimes in Fig 4.7. We give a qualitative explanation to this outcome. To obtain the least squares fit, a model has to prioritize a good fit of the evolution of the dominant initial population. In plot (p), for example, the basic model clearly overestimates the $60 \to 59$ rate. However, this is compensated by an underestimated $60 \to 61$ rate (fit curve not shown in plot). In this way, the decrease of the 60-window population, the greatest population change during this 900 µs, can be fit well by the model. The calculated lifetime of $60C$ then stays relatively stable given an increased decay rate through one channel and an decreased one through the other.

Chapter 5

Conclusion and Prospective

5.1 Conclusion

The main result of this work is the inhibition of the BBR-induced 300 K emission and absorption from a circular Rydberg state. As we discussed in section 2.4, our inhibition mechanism is identical to that of the inhibition of spontaneous emission proposed and demonstrated in some early pioneering works [50, 51]. However, our experiment is realized inside a small-scaled vapor cell with laser-cooled atoms in between a centimeter-sized capacitor. In this compact and economical setup, millisecond-lived CRAs are observed and carefully characterized. The observed maximum lifetimes are one order of magnitude larger than in free space and comparable to those observed in a cryogenic environment [48].

The ITO-coated transparent electrode (subsection 3.1.4.2) as the top capacitor plate proves to be instrumental in this work. In this experiment, it not only maintains the structural integrity of a parallel plate waveguide, but also let through thick laser beams to easily create a MOT inside the plates. This would be a difficult task inside two opaque capacitor plates spaced necessarily millimeters away to enable practical inhibition. Our proof-of-principle experiment shows that transparent, conductive electrodes provide a large inhibition while offering a wide optical access to the atoms. One can thus envision circular atoms laser-trapped [40] in complex arrangements of optical tweezers [46, 47] inside an inhibition capacitor made up of two transparent electrodes. These results thus open the way for a widespread use of circular atoms in existing and future Rydberg experiments.

5.2 Limitations and Solutions

This experiment suffers from limited circularization efficiency. We estimate at least 30% high-ℓ impurities that could not connect to the circular state after the ARP (see the residual population in the 58 window in Fig. 3.28). It is worth noting that these impurities have a random long-term fluctuation in magnitude, and could generally not be further reduced by the common optimization techniques we introduced in subsection 3.2.3.2. However, we use the partial ionization and rf decircularization techniques to remove most of the spurious population before the final detection. Furthermore, the remaining non-circular impurities are mostly in the high-ℓ Stark levels. As a result, they introduce negligible bias in the rate equation fitting procedure due to their similar transition matrix elements to those of the

circular states.

Nevertheless, in hindsight, the circularization efficiency could possibly have been improved by two ways without any setup modification. First, if the ARP efficiency is limited by a non-reducible σ^- rf component, we could apply a vertical magnetic field. This field is easily implementable by the green coil in Fig. 3.11. The field would introduce m-dependent Zeeman shifts to the Stark levels to lift the degeneracy of the σ^+ and σ^- rf transitions within a Stark manifold. In our setup we estimate the Zeeman-induced energy difference between these two transitions could easily reach a few MHz (The controlled competition between the magnetic gradient and the cooling beam intensity could dislodge the atomic cloud from the quadrupole center by a few millimeters to experience a magnetic field of a few Gauss). In the ARP, this reduces the parasitic σ^- rf coupling, which transfers population away from the ARP-related levels. In fact, even without any controllability in the polarization of the rf, a magnetic field of $\approx 20\,\text{Gauss}$ alone is already enough to select only the σ^+ couplings in a circularization ARP [120]. Second, if the ARP efficiency is limited by its adiabaticity which tends to deteriorate at a high n, we could possibly improve it by switching to a lower rf dressing frequency, as suggested in section 2.3.

A few realistic upgrades could considerably improve the field conditions of this experiment. The large residual field gradients in the capacitor likely originate from rubidium or impurity deposits [117] emanating from the nearby atom dispensers. They could be removed in a setup using a slow atomic beam to load the MOT (see section 5.3). In such a low-field environment [48, 125], state of the art fidelity (above 99%) can be reached by a careful optimization of the circularization process [70, 71]. The preparation fidelity could be improved by a better control of stray fields and the use of advanced quantum control techniques for the circularization process [71]. Field-ionization detection could be replaced by a direct optical detection of the circular atoms through a transfer back to the ground state or through the use of the optically active electron of an alkaline earth circular state.

5.3 A New Experiment: Inhibition of Spontaneous Emission of Single Atoms

After the first demonstration of the decay inhibition of the CRA [50], the community has been constantly reminded of this powerful tool, which frequents numerous experiment proposals [26, 46, 47, 126]. However, up until now, the relevant experimental realizations are few. This makes new experiments in this direction interesting.

A new inhibition setup is planned in our lab. It operates in a cryostat with an optical system to load individual atoms into the inhibition capacitor. The plan of the new experiment is shown in Fig. 5.1.

The cryostat is a historical one capable of reaching a BBR temperature of 0.8 K [92]. At this temperature and for CRAs with $n \approx 50$, $n_{\text{th}} \ll 1$, thus the spontaneous emission becomes the main decay mechanism. The CRAs at 0.8 K already possess a free space lifetime in the millisecond range. With an ideal 100% σ^+ inhibition, the theoretical lifetime limit of the CRA is in the $\simeq 10\,\text{second}$ range. This limit is mainly set by the non-zero π transitions (the 2σ transitions become less significant in this low temperature regime). To reach this π-dominated regime, the σ^+ transitions need to be reduced by a factor of 1000.

The new experiment also features a clean scheme for atom supply. The Rb atom source is

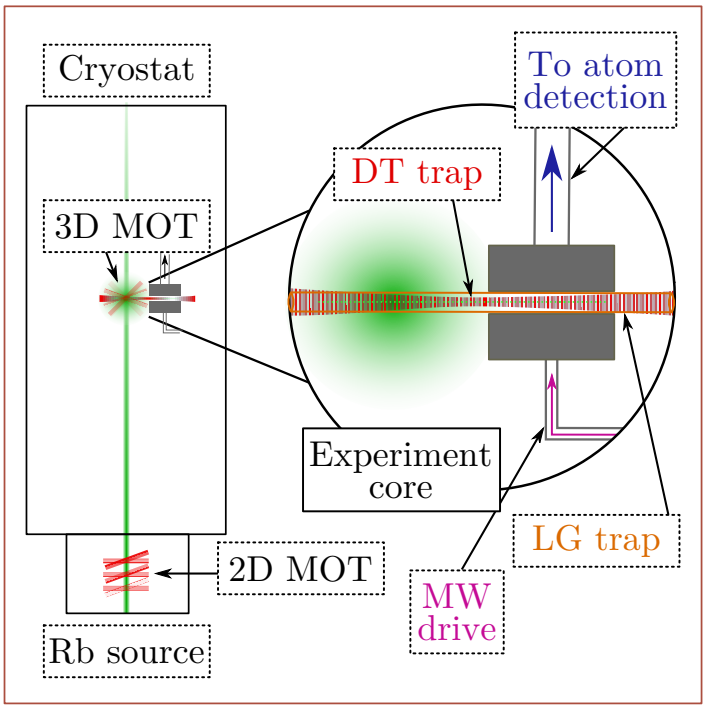

Fig. 5.1 *Concept of the new inhibition experiment. The atoms are generated from an upward 2D MOT stream. They are captured in a 3D MOT. Two counter-propagating laser beams form standing wave dipole potentials to trap single atoms inside. The conveyor belt beam translates the trapped atoms from free space into the inhibition capacitor. Upon detection, the Rydberg atoms are ionized by the capacitor. The ions are sent through a 0.2 mm diameter hole at the top.*

a 2D MOT, which produces a stream of atoms into a 3D MOT above for further cooling. Two counter-propagating beams of wavelength 820 nm are far-detuned from the D2 transition (780 nm). They form standing wave dipole traps, which not only can load a prescribed number of individual atoms from the MOT [127], but also can adiabatically transport the loaded atoms along the dipole trap beams by adjusting the mutual detuning between the two beams. This technique is known as the optical conveyor belt [128], and can be combined with individual site imaging [129]. In practice the conveyor belt technique has a limited range (millimeters), therefore it is assisted with focus-tunable lenses [130] to achieve the required centimeters of translation (the characteristic size of the capacitor).

After an atom is placed in the capacitor, the dipole trap is switched off transiently. The atom is excited to the Rydberg state. The subsequent circularization is performed with four electrodes surrounding the capacitor, in a similar fashion to the work of this thesis. Since the Rydberg state is too far-detuned from the optical frequency, the dipole trap has to be change to a ponderomotive trap, where the CRA is trapped in the light field minimum. To trap the CRA, the original dipole trap beam (after a fringe shift) is switched back on to confine the atoms in the direction of the beam. An additional Laguerre-Gauss hollow beam [40] overlaps with the dipole trap beam, to provide the confinement in the transverse directions.

The < 1 K cryogenic environment would potentially allow a CRA to live for seconds. The

individually trapped CRAs are well localized, minimizing the spurious field gradient effect. In the long term, this inhibition experiment could be developed into a spin model simulation platform based on the proposal in [26].

Appendices

Appendix A

Obtain Spontaneous Emission Rates from Fermi's Golden Rule

Starting from Eq. (2.27), i.e. the spontaneous emission rate expressed in a FGR format in the dipole approximation limit, the spontaneous emission rates in two ideal scenarios are obtained in this appendix: a dipole in free space; a transversely oriented dipole in the center of an ideal plane-parallel capacitor.

A.1 Spontaneous Emission Rate in Free Space

In free space the field eigenmodes have the plane wave form, each mode is identified by a unique pair of $(\mathbf{k}, \varepsilon)$, where $\mathbf{k}$ is the wave vector, and $\varepsilon = 1,2$ is an index to denote the two orthogonal polarizations for an electromagnetic field mode. We choose a random cube volume $V = L^3$ in space to set the periodic boundary conditions. These boundary conditions lead to the quantization of the $\mathbf{k}$ vector according to:

$$k_l L = 2\pi n_l, \quad l \in \{x,y,z\}, \tag{A.1}$$

where k_l is the wave vector projections on the three Cartesian axes, and $n_l = 1,2,\ldots$ gives the number of the periods repeated along the axis l.

The possible combinations of (n_x, n_y, n_z) thus form a regular 3D lattice in the reciprocal space where each node (n_x, n_y, n_z) with twofold polarization degeneracy represents one mode for $\varepsilon = 1$ and another for $\varepsilon = 2$. It follows that a volume in the "n-space" is equal to the number of nodes (modes) contained in this volume. We then consider the number of modes for a certain ε in a small volume $\Delta n_x \Delta n_y \Delta n_z$, which with Eq. (A.1) is evaluated to $\Delta n_x \Delta n_y \Delta n_z = \Delta k_x \Delta k_y \Delta k_z \times V/(2\pi)^3$. Represented in a spherical frame in the $\mathbf{k}$-space, the number of modes $\mathrm{d}n$ is $\mathrm{d}n(k, \theta, \varphi, \varepsilon) = k^2 \sin\theta \mathrm{d}\theta \mathrm{d}\varphi \mathrm{d}k \times V/(2\pi)^3$, where $k = |\mathbf{k}|$, and θ, φ are the polar and azimuthal angles of the spherical frame, respectively. Knowing the free space dispersion relation $kc = \omega$, the number of modes of photon frequency ω in an azimuth circle (θ fixed φ varying) is $\mathrm{d}n(\omega, \theta, \varepsilon) = \omega^2 \sin\theta \mathrm{d}\theta \mathrm{d}\omega \times V/(2\pi)^2 c^3 \equiv \rho(\omega,\theta,\varepsilon)\mathrm{d}\theta\mathrm{d}\omega$. The mode spectral density $\rho(\omega, \theta, \varepsilon)$ is the density of the plane wave modes of the polarization family ε which fall within the circular frequency continuum interval $\omega \to \omega + \mathrm{d}\omega$ and polar angle interval $\theta \to \theta + \mathrm{d}\theta$:

$$\rho(\omega, \theta, \varepsilon) = \frac{V}{(2\pi)^2 c^3} \omega^2 \sin\theta \tag{A.2}$$

For sanity check, integrating $\rho(\omega,\theta,\varepsilon)\mathrm{d}\theta \times 2$ (factor of 2 for two polarizations)with θ from 0 to π yields the familiar free space mode density $\rho_{\mathrm{fs}}(\omega)/V = \omega^2/\pi^2c^3$.

The dipole interaction we consider has the dipole matrix element $\mathbf{D}_{ij}$ pointing to the $+z$ direction. $\mathbf{D}_{ij}$ couples to all the free space plane wave eigenmodes, each reads:

$$\boldsymbol{\alpha}_{\mathbf{k},\varepsilon}(\mathbf{r}) = \frac{1}{\sqrt{V}}\hat{\boldsymbol{\alpha}}_{\mathbf{k},\varepsilon}e^{i\mathbf{k}\cdot\mathbf{r}} \tag{A.3}$$

where $\hat{\boldsymbol{\alpha}}_{\mathbf{k},\varepsilon}$ is the unit vector giving the direction of polarization of the plane wave. The two polarizations $\varepsilon = 1{,}2$ can always be chosen so that one is always perpendicular to the dipole $\mathbf{D}_{ij}$ and has zero coupling, as shown in Fig. A.1. We thus only need to consider the non-zero coupling mode with polarization index $\varepsilon = 1$, the corresponding coupling term has the form:

$$\left|\mathbf{D}_{ij}\cdot\boldsymbol{\alpha}_{\mathbf{k},\varepsilon=1}(\mathbf{r}=0)\right|^2 = D_{ij}^2\cos^2\left(\frac{\pi}{2}-\theta\right)\frac{1}{V} \tag{A.4}$$

where $D_{ij} = |\mathbf{D}_{ij}|$, and the atomic dipole is chosen to be at $\mathbf{r} = 0$.

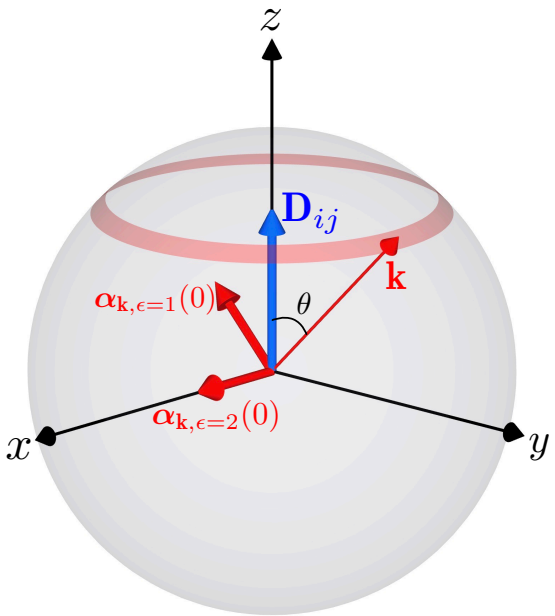

Fig. A.1 *The coupling between a dipole* $\mathbf{D}_{ij}$ *and two plane wave modes* $\boldsymbol{\alpha}_{\mathbf{k},\varepsilon=1,2}$ *sharing an arbitrary* $\mathbf{k}$ *in free space. We choose the plane containing* Oz *and* $\mathbf{k}$ *as the* yOz *plane of a Cartesian fame. At the frame origin, field mode direction* $\boldsymbol{\alpha}_{\mathbf{k},\varepsilon=1}(\mathbf{r}=0)$ *can be chosen to be in the* yOz *plane, the other orthogonal field mode direction* $\boldsymbol{\alpha}_{\mathbf{k},\varepsilon=2}(\mathbf{r}=0)$ *then has to be along the* x *axis. With this choice, the mode* $\boldsymbol{\alpha}_{\mathbf{k},\varepsilon=2}$ *always has zero coupling to the dipole:* $\mathbf{D}_{ij}\cdot\boldsymbol{\alpha}_{\mathbf{k},\varepsilon=2} = 0$.

Plugging the θ-dependent single dipole-mode coupling term Eq. (A.4) and the corresponding azimuth circle mode density Eq. (A.2) into the spontaneous emission rate evaluation equation (2.27), finally, the free space spontaneous emission rate $A_{ij}^{(\mathrm{fs})}$ is the sum of rates contributed by dipole coupling to all the plane wave modes, with the modes' propagation direction's polar angle θ varying from 0 to π:

$$
\begin{aligned}
A_{ij}^{(\mathrm{fs})} &= \frac{\pi\omega_{ij}}{\hbar\epsilon_0}\sum_{\varepsilon}\int_0^{\pi}\left|\mathbf{D}_{ij}\cdot\boldsymbol{\alpha}_{\mathbf{k},\varepsilon}(\mathbf{r}=0)\right|^2\rho(\omega_{ij},\theta,\varepsilon)\mathrm{d}\theta \\
&= \frac{\omega_{ij}^3 D_{ij}^2}{2\pi\hbar\epsilon_0 c^3}\int_0^{\pi}\cos^2\left(\frac{\pi}{2}-\theta\right)\sin\theta\mathrm{d}\theta \\
&= \frac{\omega_{ij}^3 D_{ij}^2}{3\pi\hbar\epsilon_0 c^3}
\end{aligned}
\tag{A.5}
$$

where there is only the $\varepsilon = 1$ term in the sum, because we imposed that the $\varepsilon = 2$ term is zero. Assuming random polarizations will not change the above result.

A.2 Spontaneous Emission Rate Between Two Ideal Mirrors: a Limited Example

In between two ideal mirrors, a field eigenmode is either a TE mode or a TM mode. For the parallel plate waveguide, the acronym TE(TM) stands for the transverse electric (magnetic) mode which has the electric (magnetic) component exclusively parallel to the plates, so that the electric (magnetic) component normal to the plates is always zero. Since the transverse directions are not confined, each TE/TM mode can propagate transversely with a wave vector $\mathbf{k}$ that can only be parallel to the mirrors.

The considered mirror spacing is L, we choose in between the mirrors a rectangular volume $V = a \times a \times L$ with a random length a for transverse sides to impose periodic boundary conditions. We then set the origin of the Cartesian frame at the bottom mirror, and set the Oz axis pointing perpendicular to the top mirror. In this frame the transverse boundary conditions read:

$$k_l a = 2\pi n_l, \quad l \in \{x,y\} \tag{A.6}$$

where k_l is the wave vector projections on the x,y axes, and $n_l = 1,2,3,\ldots$. This is simply the free space case (see section A.1) reduced to 2D.

To obtain the mode spectral density, we write down the dispersion relation for a parallel plate waveguide:

$$\omega^2 = m^2\omega_0^2 + k^2c^2 \tag{A.7}$$

$$\omega_0 = c\pi/L \tag{A.8}$$

where $k = \sqrt{k_x^2 + k_y^2}$, and ω is the mode's circular frequency. $m = 0,1,2,\ldots$ is the order of the transverse TE/TM modes, both sharing the same dispersion relation Eq. (A.7) and the same first order cutoff frequency ω_0. The dispersion relation Eq. (A.7) written in a different form is:

$$k = \frac{1}{c}\sqrt{\omega^2 - (m\omega_0)^2}, \tag{A.9}$$

from which it is clear that the transverse modes TE_m, TM_m have the (degenerate) cutoff frequency at $m\omega_0$, below which the m-th order transverse electric/magnetic modes disappear.

In this limited example we are to examine the spontaneous emission rate caused only by the coupling between the modes TE_1, TM_1 and a transversely oriented dipole in the center

of the mirrors. However, these are already all the possible couplings for such a dipole below the frequency $3\omega_0$, below which the full spontaneous emission rate can be obtained in this limited example. For the the complete result, the equations (2.36) and (2.37) in the main text give the spontaneous emission rate modifications for both transversely and vertically oriented dipoles, positioned at any height between the mirrors, coupling all modes at any frequency.

In a parallel plate waveguide, for any mode family $\varepsilon = \mathrm{TE}_m$ or TM_m, the mode density always has the same form, because the differential dispersion relation [differentiate both sides of Eq. (A.7)] $\omega \mathrm{d}\omega = c^2 k \mathrm{d}k$ does not depend on the choice of ε. But the modes of different orders have different cutoff frequencies, because Eq. (A.9) has a m dependence. We follow the same reasoning as in the free space argument, and find that the number of modes $\mathrm{d}n$ in the family ε represented in the polar frame coordinates (k, φ) of the 2D $\mathbf{k}$-space is $\mathrm{d}n(\omega,\varphi,\varepsilon) = \omega \mathrm{d}\omega \mathrm{d}\varphi \times V/(2\pi c)^2 L \equiv \rho(\omega,\varphi,\varepsilon)\mathrm{d}\varphi\mathrm{d}\omega$, where we have used the dispersion relation Eq. (A.7) to convert k to ω. The corresponding mode density $\rho(\omega, \varphi,\varepsilon)$ then represents the mode density contributions from the ε modes of photon frequency ω propagating transversely in direction of φ:

$$\rho(\omega, \varphi, \varepsilon) = \Theta\left(\frac{\omega}{\omega_0} - m\right) \frac{V}{L} \left(\frac{1}{2\pi c}\right)^2 \omega = \Theta\left(\frac{\omega}{\omega_0} - m\right) \frac{V\omega_0}{4\pi^3 c^3} \omega \tag{A.10}$$

where we used the Heaviside function[1] Θ to impose the cutoff frequency.

We use $\boldsymbol{\alpha}_{k\varphi,\mathrm{TE}m}(z, \boldsymbol{\varrho})$ and $\boldsymbol{\alpha}_{k\varphi,\mathrm{TM}m}(z, \boldsymbol{\varrho})$ to denote the eigenmode functions of the corresponding TE_m and TM_m modes. The positional arguments $(z, \boldsymbol{\varrho})$ are respectively the vertical displacement z ranging from 0 to L between the two mirrors, and the transverse position $\boldsymbol{\varrho}$ along the mirrors. These eigenmode functions for any order m are [86]:

$$\boldsymbol{\alpha}_{k\varphi,\mathrm{TE}m}(z, \boldsymbol{\varrho}) = \sqrt{\frac{2}{V}} \sin \frac{m\pi z}{L} \hat{\boldsymbol{\varphi}} \times \hat{\mathbf{z}} e^{ik\hat{\boldsymbol{\varphi}}\cdot\boldsymbol{\varrho}} \tag{A.11}$$

$$\boldsymbol{\alpha}_{k\varphi,\mathrm{TM}m}(z, \boldsymbol{\varrho}) = \sqrt{\frac{\beta_m}{V}} \left(\frac{ck}{\omega} \cos \frac{m\pi z}{L} \hat{\mathbf{z}} - i \frac{m\omega_0}{\omega} \sin \frac{m\pi z}{L} \hat{\boldsymbol{\varphi}}\right) e^{ik\hat{\boldsymbol{\varphi}}\cdot\boldsymbol{\varrho}} \tag{A.12}$$

The unit vectors $\hat{\boldsymbol{\varphi}}$ and $\hat{\mathbf{z}}$ are respectively in the $\mathbf{k}$ direction (always parallel to the mirrors with an azimuthal angle φ) and the Oz direction. The normalization factor β_m satisfies:

$$\beta_m = 1 \text{ if } m = 0, \quad \text{else } \beta_m = 2$$

From Eq. (A.11) and Eq (A.12) we obtain the eigenmode functions we need: $\boldsymbol{\alpha}_{k\varphi,\mathrm{TE}1}(z = L/2, \boldsymbol{\varrho} = 0)$ and $\boldsymbol{\alpha}_{k\varphi,\mathrm{TM}1,}(z = L/2, \boldsymbol{\varrho} = 0)$, which are evaluated at the position of the dipole $(z = L/2, \boldsymbol{\varrho} = 0)$ and at the considered emission frequency ω_{ij}:

$$\boldsymbol{\alpha}_{k\varphi,\mathrm{TE}1}(z = L/2, \boldsymbol{\varrho} = 0) = \sqrt{\frac{2}{V}} \hat{\boldsymbol{\varphi}} \times \hat{\mathbf{z}} \tag{A.13}$$

$$\boldsymbol{\alpha}_{k\varphi,\mathrm{TM}1}(z = L/2, \boldsymbol{\varrho} = 0) = \sqrt{\frac{2}{V}} \left(-i \frac{\omega_0}{\omega_{ij}}\right) \hat{\boldsymbol{\varphi}} \tag{A.14}$$

The above modes are coupled with a dipole $\mathbf{D}_{ij}$ chosen to point in the $+x$ direction, as shown in Fig. A.2, the resulting coupling terms read:

[1] Θ is equal to one if its argument is strictly positive, to zero otherwise.

$$|\mathbf{D}_{ij}\cdot\boldsymbol{\alpha}_{k\varphi,\mathrm{TE1}}(z=L/2,\boldsymbol{\varrho}=0)|^2 = D_{ij}^2\frac{2}{V}\cos^2\left(\frac{\pi}{2}-\varphi\right) \tag{A.15}$$

$$|\mathbf{D}_{ij}\cdot\boldsymbol{\alpha}_{k\varphi,\mathrm{TM1}}(z=L/2,\boldsymbol{\varrho}=0)|^2 = D_{ij}^2\frac{2}{V}\left(\frac{\omega_0}{\omega_{ij}}\right)^2\cos^2\varphi \tag{A.16}$$

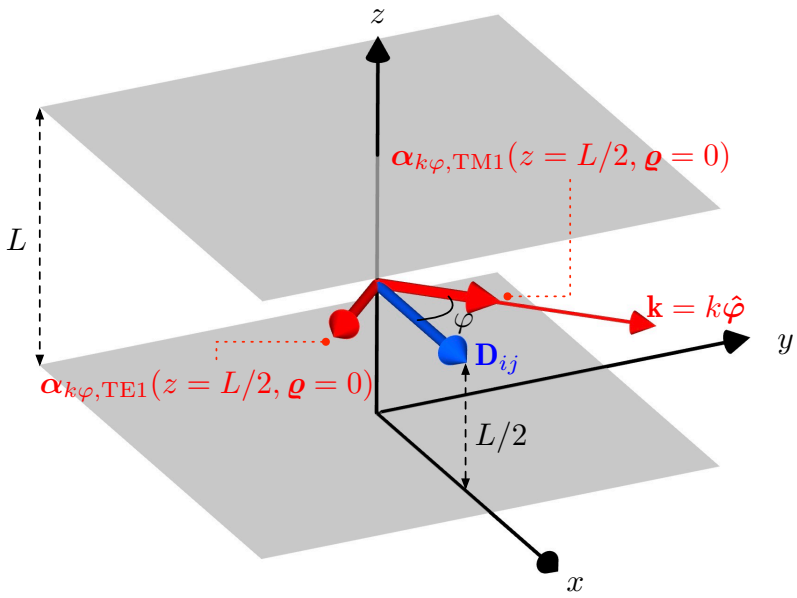

Fig. A.2 *The coupling between a transversely positioned, centered dipole* $\mathbf{D}_{ij}$ *and two propagation modes. The two modes are a* TE_1 *mode and a* TM_1 *mode between two ideal mirrors. They share the same wave vector* $\mathbf{k}$.

Plugging into the spontaneous emission rate evaluation equation (2.27) the φ-dependent single dipole-mode coupling terms Eqs. (A.15), (A.16) and the corresponding mode density Eq. (A.10) for modes propagating in $\hat{\boldsymbol{\varphi}}$, the corresponding spontaneous emission rate $A_{ij,\mathrm{TE1+TM1}}^{(\mathrm{capacitor})}$ is the sum of rates contributed by the dipole couplings with all the TE_1 and TM_1 modes, while the modes' propagation direction angle φ varying from 0 to 2π:

$$\begin{aligned}
A_{ij,\mathrm{TE1+TM1}}^{(\mathrm{capacitor})} &= \frac{\pi\omega_{ij}}{\hbar\epsilon_0}\sum_{\varepsilon=\mathrm{TE1,TM1}}\int_0^{2\pi}|\mathbf{D}_{ij}\cdot\boldsymbol{\alpha}_{k\varphi,\varepsilon}(z=L/2,\boldsymbol{\varrho}=0)|^2\rho(\omega_{ij},\varphi,\varepsilon)\mathrm{d}\varphi \\
&= \Theta\left(\frac{\omega_{ij}}{\omega_0}-1\right)\frac{\omega_{ij}^2\omega_0 D_{ij}^2}{2\pi^2\hbar\epsilon_0 c^3}\int_0^{2\pi}\left[\cos^2\left(\frac{\pi}{2}-\varphi\right)+\cos^2\varphi\left(\frac{\omega_0}{\omega_{ij}}\right)^2\right]\mathrm{d}\varphi \\
&= \Theta\left(\frac{\omega_{ij}}{\omega_0}-1\right)\frac{\omega_{ij}^2\omega_0 D_{ij}^2}{2\pi\hbar\epsilon_0 c^3}\left[1+\left(\frac{\omega_0}{\omega_{ij}}\right)^2\right]
\end{aligned} \tag{A.17}$$

The emission frequency ω_{ij} has to be below $3\omega_0$ for Eq. (A.17) to produce the complete spontaneous emission rate; above $3\omega_0$, more modes are to be coupled, TE_1 and TM_1 are not enough.

Dividing Eq. (A.17) by the free space rate Eq. (A.5), and making the substitution $\omega_{ij}/\omega_0 = 2L/\lambda$, we obtain the exact form of the $n = 1$ term in the sum of Eq. (2.36). When the emission frequency is at the cutoff frequency: $\omega_{ij} = \omega_0$, Eq. (A.17) produces a factor of three's spontaneous emission rate enhancement relative to that of the free space, this is the greatest enhancement that can be produced on a transverse dipole by two ideal mirrors, as shown in Fig. 2.12. This enhancement is caused by only the TE_1 and TM_1 modes.

We stop at the first order waveguide modes only to make a terse and clear example. Evidently, rates caused by higher order modes and hence the complete result given in Eqs. (2.36), (2.37) can be found in exactly the same way.

Appendix B

Global Mode Spectral Density in Two Ideal Models

In free space, given the dispersion relation $\omega = c|\mathbf{k}|$ and the photon frequency range $\omega \to \omega + \mathrm{d}\omega$, one can find in this range the associated number $\mathrm{d}n(\omega)$ of the available plane wave modes. The number $\mathrm{d}n(\omega)$ is twice (for the two orthogonal polarizations of light) of the number of all possible wave vectors $\mathbf{k}$'s in a spherical shell $|\mathbf{k}| \to |\mathbf{k} + \mathrm{d}\mathbf{k}|$ in the $\mathbf{k}$-space. These concepts allow us to formally introduce the *global mode spectral density per volume* $\rho(\omega)/V$ as the number of all existing photonic modes per frequency interval per unit volume:

$$\rho(\omega)/V = V^{-1}\frac{\mathrm{d}n(\omega)}{\mathrm{d}\omega} \tag{B.1}$$

In this thesis, for simplicity, the word *mode density* or *mode spectral density* are used without discrimination to refer to both $\rho(\omega)$ and $\rho(\omega)/V$, but there is no ambiguity in the notation, in the analytical discussions the distinction is always clear.

By the definition in Eq. (B.1), the global free space mode density can be readily worked out through the textbook approach of assuming the periodic boundary conditions in a cube of random volume V. The resulting free space mode density $\rho_{\mathrm{fs}}(\omega)/V$, independent from the choice of V, reads:

$$\rho_{\mathrm{fs}}(\omega)/V = \frac{\omega^2}{\pi^2 c^3} \tag{B.2}$$

In this appendix, the global mode spectral densities are obtained and compared with the free space value [Eq. (B.2)] in two infinite waveguide structures: the circular waveguide (infinite in 1D) and the parallel plate waveguide (infinite in 2D).

B.1 Global Mode Density in Circular Waveguide

The mode density shown in Fig. 2.9 is given in this section.

Consider a zero-resistivity circular waveguide in the vacuum, its length is infinite and its radius is r. The dispersion relation of the fundamental mode in this ideal waveguide reads $k = \sqrt{\omega^2 - \omega_0^2}/c$. In this expression, k is the wave vector along the length of the waveguide, ω is the circular frequency associated with the wave vector, and $\omega_0/2\pi$ the cutoff frequency of the fundamental waveguide mode (TE_{11}). As in the free space case, the dispersion relation

plus the periodic boundary condition $kL = 2\pi n$ allow one to express as a function of ω the number of allowed photonic modes $n(\omega)$ below frequency ω. Afterwards, by using directly the definition Eq. (B.1) and taking the random volume as a cylindrical section $V = \pi r^2 \times L$, the mode density $\rho_0(\omega)/V$, independent from the choice of section length L, of the fundamental waveguide mode is found to be:

$$\rho_0(\omega)/V = \frac{2\omega_0^2}{\zeta c^3} \frac{\omega}{\sqrt{\omega^2 - \omega_0^2}} \quad (\text{for } \omega > \omega_0) \tag{B.3}$$

The equation above gives the $\rho_0(\omega)$ for $\omega > \omega_0$. As for $\omega < \omega_0$, it is simply the case of below cutoff, where $\rho_0(\omega) = 0$. The singularity at cutoff frequency $\omega = \omega_0$ is a feature of the ideal waveguide, but would not appear for real waveguides with finite size and conductivity. In Eq (B.3), $\zeta = (\chi'_{11}\pi)^2 = 33.4\ldots$ is a dimensionless constant [the χ notation is introduced shortly below in Eq (B.5)]. The geometry information is contained in the cutoff frequency ω_0, which depends on the transverse radius of the waveguide.

To obtain the total mode density $\rho_{\mathrm{g}}(\omega)$ of all allowed waveguide modes, it consists only in adding the contributions of all the waveguide modes together:

$$\rho_{\mathrm{g}}(\omega)/V = \frac{2\omega_0^2}{\zeta c^3} \sum_j \frac{\omega}{\sqrt{\omega^2 - \omega_j^2}} \tag{B.4}$$

In Eq. (B.4), ω_j is the cutoff frequency of the j-th waveguide mode. And just like in Eq. (B.3), when below the j-th cutoff frequency, $\omega < \omega_j$, the contribution of the corresponding j-th term in the sum is zero. For an ideal circular waveguide in vacuum, all possible ω_j's are given by:

$$\omega_{mn}^{\mathrm{TE}} = \chi'_{mn} c/r \tag{B.5}$$

$$\omega_{mn}^{\mathrm{TM}} = \chi_{mn} c/r \tag{B.6}$$

where $\omega_{mn}^{\mathrm{TE,TM}}$ represents the cutoff frequency of the corresponding TE_{mn}, TM_{mn} modes, r is the radius of the cross-section of the circular waveguide. χ_{mn} and χ'_{mn} are the positions of the n-th zero point of the m-th order Bessel function and Bessel function derivative, respectively.

With all the ω_j's given by Eq. (B.5) and Eq. (B.6), the mode density $\rho_{\mathrm{g}}(\omega)$ in an ideal circular waveguide can be obtained via Eq (B.4). To examine its inhibition and enhancement relative to the free space mode density $\rho_{\mathrm{fs}}(\omega)$, it helps to calculate the ratio $R_{\mathrm{g}}(\omega/\omega_0)$ of the two quantities (the random volume V then are assumed to be identical in both cases):

$$R_{\mathrm{g}}\left(\frac{\omega}{\omega_0}\right) = \frac{\rho_{\mathrm{g}}(\omega)}{\rho_{\mathrm{fs}}(\omega)} = \frac{2\pi^2}{\zeta}\left(\frac{\omega}{\omega_0}\right)^{-1} \sum_j \left[\left(\frac{\omega}{\omega_0}\right)^2 - \left(\frac{\omega_j}{\omega_0}\right)^2\right]^{-1/2} \tag{B.7}$$

Because we parametrize ω/ω_0 as the independent variable of $R_{\mathrm{g}}(\omega/\omega_0)$, its radius dependence contained in ω_0 is lost, therefore the mode density modification $R_{\mathrm{g}}(\omega/\omega_0)$ is general and applies to an ideal circular waveguide of arbitrary size.

The plots of $R_{\mathrm{g}}(\omega/\omega_0)$ is shown in Fig. 2.9, which reproduces the only figure in the Kleppner paper. Panel (a) plots the mode density up until $2.5\omega_0$. In this range, distinct

enhancement peaks appear at the onsets of the low order waveguide modes, which we label on the top. It is then clear, for instance, that the mode density at $1.1\omega_0$ is associated only with photons in TE_{11} mode, whereas the mode density at $2\omega_0$ has the contributions of three modes: TE_{11}, TM_{01}, and TE_{21}. In panel (b) we plot the mode density up until $20\omega_0$, twice as high as in the original figure of Kleppner. We did not apply any singularity truncations as Kleppner did, it is because with our choice of plotting points in (b), i.e. linearly spaced 1001 points in the range of $\omega \in [0,20\omega_0]$, it so happens that we do not encounter any enhancements $\gg 1$.To see the reduced significance of singularities at $\omega \gg \omega_0$, we consider the mode density value of the j-th waveguide mode at a small normalized frequency $\Delta x = \Delta\omega/\omega_0$ to the right of the j-th singularity at $x_j = \omega_j/\omega_0$, we keep the terms to first order in $\Delta x/x_j$, and find that the mode density yielded by the j-th waveguide mode at a fixed $\Delta x/x_j$ away from the j-th singularity scales as x_j^{-2}. This means that the singularity peaks will become increasingly narrower at higher frequencies, as a result, very high enhancements will only be localized in fleetingly small frequency zones.

B.2 Global Mode Density in Parallel Plate Waveguide

We follow the same parallel plate structure described in section A.2.

From the dispersion relation Eq. (A.9), we see that the m-th order modes belonging to the TE_m and TM_m families exist only above their mutual cutoff frequency $m\omega_0$. At the frequency ω, the number of propagation mode families between the plates are:

$$1 + 2\left\lfloor \frac{\omega}{\omega_0} \right\rfloor \tag{B.8}$$

where any number in the floor brackets is evaluated to its integer part, e.g. $\lfloor 1.1 \rfloor = \lfloor 1 \rfloor = 1$. The one always existing mode family is the TM_0 that cuts off at DC. Going up in frequency ω, after each frequency interval of ω_0 [Eq. (A.8)], one new TE family and TM family add to the number of propagation families.

Differentiating both sides of the dispersion relation Eq. (A.7), we get the relation $\omega \mathrm{d}\omega = c^2 k \mathrm{d}k$ independent from the order m, the mode number counted in $\mathbf{k}$-space is thus converted to the frequency spectrum by the same relation for any mode family TX_m (a TE_m or TM_m), the corresponding single mode spectral density ends up being always Eq. (A.10). Each mode family TX_m thus has the single family mode density $V\omega_0\omega/2\pi^2c^3$ which is the integral of Eq. (A.10) over 2π. The global mode density $\rho_\mathrm{p}(\omega)$ in between the plates is the single family mode density multiplied by the number of families given in Eq. (B.8):

$$\rho_\mathrm{p}(\omega)/V = \frac{\omega_0\omega}{2\pi^2c^3}\left(1 + 2\left\lfloor \frac{\omega}{\omega_0} \right\rfloor\right) \tag{B.9}$$

The parallel plate mode density can then be compared with the free space mode density by the ratio of Eq. (B.9) to Eq. (B.2):

$$R_\mathrm{p}(\omega/\omega_0) = \frac{\rho_\mathrm{p}(\omega)}{\rho_\mathrm{fs}(\omega)} = \frac{1}{2}\left(\frac{\omega}{\omega_0}\right)^{-1}\left(1 + 2\left\lfloor \frac{\omega}{\omega_0} \right\rfloor\right) \tag{B.10}$$

$R_\mathrm{p}(\omega/\omega_0)$ is plotted in Fig. 2.10.

Appendix C

Lifetime Sensitivity to Capacitor Spacing

We show in this appendix that, based on the comparison between the measured and simulated 300 K lifetimes of the CRAs, the real capacitor spacing respects well the measured value of 4.10 mm.

In subsection 3.1.4, the presented simulation results are based on a 4.10 mm capacitor spacing obtained by the direct measurement with a vernier caliper. The measurement instrument itself has a minimum reading of 0.01 mm. However, a slight capacitor spacing shift in this magnitude is already enough to induce a 5% difference for the σ decay rate modification factor C_σ along the simulated cutoff. If the manual error involved in the measurement of the real capacitor spacing is a few tens of microns, the simulated lifetime then should not be directly comparable to the measured lifetime.

To dismiss this concern, we simulate the lifetimes of a series of the CRAs with their σ^+ transition frequencies distributed along the cutoff of the capacitor in Fig. 3.13, varying the spacing of the capacitor from 3.9 mm to 4.3 mm in 0.1 mm steps. We compare these simulated lifetimes with the measured lifetimes in Fig. 4.7 (the balanced model). The comparison is shown Fig. C.1.

In this comparison, it is clear that the measured lifetimes of the $56C$, $57C$, and $58C$, having their σ^+ decay rates varying successively from barely inhibited (similar to the free space values) to effectively inhibited (σ^+ decays rates reduced by more than a factor of 5), match well only with the simulated lifetimes in a 4.1 mm capacitor. The measured lifetimes of the lower-n CRAs $51C$, $52C$ and $53C$ also match well with those from the 4.1 mm simulation (shown in Fig. 4.7 in the main text), representing a good agreement on the high frequency side of the cutoff resonance. Therefore, the measured lifetimes of these circular states prove to be a good reflection of the sharp features of the cutoff enhancement for a capacitor of 4.1 mm. A deviation of more than 0.01 mm is unlikely.

As for the disagreement between the measured and the simulated lifetimes of the rest of the CRAs, some possible reasons have been discussed in the main text.

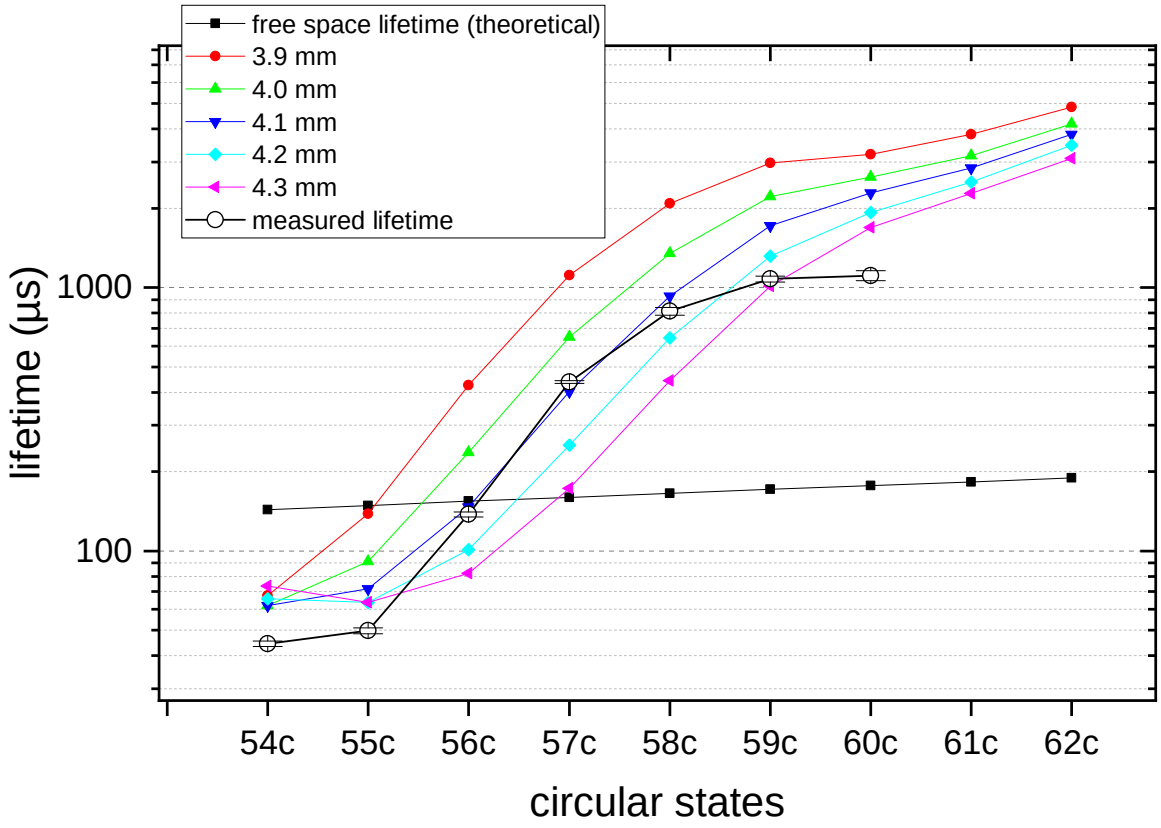

Fig. C.1 *The comparison between the measured lifetimes (those of the balanced model in Fig. 4.7) and the simulated lifetimes of the CRAs that transition successively from decay-enhanced to decay-inhibited. In the simulation, the capacitor spacing is varied by* $\Delta L = \pm 0.2\,\mathrm{mm}$ *from the measured value of 4.1 mm. The optimal match is found at 4.1 mm for the successive states* $56C$, $57C$, *and* $58C$, *which undergo the gradual transition from under-inhibited to effectively-inhibited, corresponding to the sharp feature of the capacitor cutoff which can be sensitive to a deviation of 0.01 mm in spacing.*

Appendix D

Potential Elliptical-State-Selective Techniques in Field Ionization Detection

In Fig. 3.20, the three states' ionization peaks have a large overlapping, indicating their similar ionization thresholds. However, we notice that the separation between the tips of e_1 and e_1' is comparable to the width of the circular state peak. This means when the circular state's population is not dominant, the sum of the three peaks, comparable in their widths, would define a lumped shape with double the width of the circular only signal. The ionization thresholds of different "lumps" are not different enough to separate them well in a ramped ionization field. Just imagine the circular state only signal in Fig. 3.19, with every peak broadened by a factor of two.

The ne_1 peak is more separated from the nC peak than the ne_1' peak in both the theory (see Fig. 3.22) and the detection (see Fig. 3.20, see also the thesis of E. K. Dietsche [59, Figure 2.8]). As a result, the long tail of the ne_1 peak towards the left would cause a considerable contamination in the $n+1$ detection window located at earlier arrival time. This signal merging between $(n+1)C$ and ne_1 becomes inignorable when the populations in these two levels are comparable. A situation like this can happen in a capacitor when the BBR transfers become π and 2σ dominated (see subsection 2.4.4). Experimentally, after 900 µs evolution of an initially prepared $60C$ (the blue dashed line in Fig. 4.1), we observe the peak shaped ionization signal to the right of $60C$, but lumped signal to the left. This is an indication that the elliptical populations in the 61 manifold and above may have surpassed that of the circular.

When one wishes to clearly identify the decay rates of the three upward decay channels (σ^+, π, 2σ), it is desirable to further resolve the ne_1, ne_1, and nC populations from the lumped signal. Two potential techniques are discussed in the child sections. With these techniques used singularly or combined, when the BBR dynamics is limited only to the circular and a few high-m elliptical states, in principle it is possible to unequivocally determine the Rydberg level populations at any detection time. The overlapping between the circular and the elliptical level signals and the cross-window contaminations do not seem to impose an insurmountable challenge in the selectivity of the ramp detection[1].

[1]Experimentally we also tried to program a step-shaped ionization ramp to gain a controllable time

D.1 RF De-Circularization

The rf-decircularization was already demonstrated in the main text (Fig. 3.24 and Fig. 3.30). This technique transfers a high-m state, circular or elliptical, to a low-m state within the same manifold. In the ionization signal, the corresponding ion counts are moved from a high-field window to a low-field one. This type of transfer could have an application in resolving the 2σ populated $(n+2)e_1^{(\prime)}$ states[2] and the π populated $(n+1)e_1^{(\prime)}$ states by an initially prepared nC under heavy σ inhibition.

The heavy σ inhibition means that the thermal transfer populates the $m = n-2$ states in the next two manifolds as much as it populates the $(n+1)C$ state, if not more. The $e_1^{(\prime)}$ states, as mentioned in the parent section, have an ionization threshold difference that is enough to make their ionization peaks difficult to resolve. As a result, at long times the BBR-transferred $(n+1)C$, $(n+1)e_1^{(\prime)}$, and $(n+2)e_1^{(\prime)}$, comparable in their populations, would appear as a merged whole in the ionization signal (e.g. the blue dashed line in Fig. 4.1, in the high-n slot). In this scenario, an rf decircularization resonant with the $n+1$ or $n+2$ manifold could move the corresponding state signals to an earlier arrival time for separate detection. The previously blurred manifold resolution is regained.

We did not implement this technique in the experiment, because we initially wrote a rf control software capable of only one waveform per sequence. The two rf pulses in Fig. 3.29 are implemented as one 60 µs long waveform with zero amplitude between the two pulses. To add one additional rf de-circularization pulse after $\simeq$ 1 ms before detection, we would need a millisecond long waveform, which is beyond the hardware limit. We could upgrade the rf control software to allow several different waveforms per sequence, but this was not done due to the project time limit.

D.2 MW Redistribution Pulses

In subsection 3.2.1.1, we mentioned the method of resolving the ne_1, ne_1', and nC populations by MW π-pulse selection. If we use a two-photon MW pulse to transfer, for example, ne_1 to $(n+2)e_1$, the transferred population ne_1 is immediately known only when the initial populations in $(n+2)e_1$, $(n+2)e_1'$, and $(n+2)C$ are all negligible. If initially there is a mixture of the three states, without any MW selection we already have a lumped signal in the $(n+2)$-window during ionization. After the $ne_1 \rightarrow (n+2)e_1$ MW pulse, we get a different lumped signal in $(n+2)$-window. How much ne_1 is transferred is not immediately known.

Situations like the above can realistically arise in this work. It would be useful to resolve the population in a specific circular or elliptical state after a long time of BBR-induced population redistribution. However the thermal field leads in the end to a wide spread of

separation of peak signals. It appears effective for the CRAs of different n's and thus different enough ionization thresholds. However for the CRAs a simple ramp already provides a good enough signal separation without the time consuming threshold field calibration. Moreover, the stair ramp is not very promising for separating the high-m elliptical signals. A good separation of ne_1 from nC is experimentally challenging. The DC ionization field needs to be in a precise range: high enough to ionize all the ne_1 within a few microseconds in a room temperature experiment, but also low enough to at most ionize a few percent of the nC during this time. The separation of ne_1' from nC by DC ionization steps is not feasible due to their very similar ionization thresholds.

[2] $e_1^{(\prime)}$ means e_1 and e_1'.

population in the circular states, and in the $m = n-2$ elliptical states too in the σ inhibition regime. It becomes difficult to find a clean manifold to transfer the population to in order to be resolved individually during the field ionization. However one could use before the detection a few carefully planned MW π-pulses to intentionally redistribute the ion counts in different detection windows, followed by some post analysis comparing the signals before and after the redistribution pulses to infer the original population distribution.

To give a toy example of such an analysis, we consider a BBR redistribution dynamics limited to four levels. However the four levels fall into only two detection windows: we can only detect the population sum of level 1, 2 in window 1, and the population sum of level 3, 4 in window 2. We assume, at the end of an experimental sequence, the BBR causes among the four levels a reproducible final population distribution of $\begin{pmatrix} p_1 & p_2 & p_3 & p_4 \end{pmatrix}^{\mathrm{T}}$, a vector we do not know and will set out to find out. Our partial information is the detected window populations $P_1 = p_1 + p_2$ and $P_2 = p_3 + p_4$. To gain another half of the information, we conduct the same experiment, but at the end apply a π-pulse between level 1 and level 3 to exchange their population, and obtain a different set of detected window populations $P_1' = p_3 + p_2$, $P_2' = p_1 + p_4$. A transformation between the detected window populations and the individual level populations can then be given below:

$$\begin{pmatrix} P_1 \\ P_2 \\ P_1' \\ P_2' \end{pmatrix} = \begin{pmatrix} 1 & 1 & 0 & 0 \\ 0 & 0 & 1 & 1 \\ 0 & 1 & 1 & 0 \\ 1 & 0 & 0 & 1 \end{pmatrix} \begin{pmatrix} p_1 \\ p_2 \\ p_3 \\ p_4 \end{pmatrix} \tag{D.1}$$

It is straightforward to introduce the cross-window population contaminations into the equation above. To this end, we assume the populations in level 1 and 4 are well separated in the two detection windows. But for the population in level 2, a small proportion ϵ_{12} escapes window 1 and is detected in window 2. For level 3, a small proportion ϵ_{21} is detected in window 1. The transformation Eq. (D.1) then becomes:

$$\begin{pmatrix} P_1 \\ P_2 \\ P_1' \\ P_2' \end{pmatrix} = \begin{pmatrix} 1 & 1-\epsilon_{12} & \epsilon_{21} & 0 \\ 0 & \epsilon_{12} & 1-\epsilon_{21} & 1 \\ \epsilon_{21} & 1-\epsilon_{12} & 1 & 0 \\ 1-\epsilon_{21} & \epsilon_{12} & 0 & 1 \end{pmatrix} \begin{pmatrix} p_1 \\ p_2 \\ p_3 \\ p_4 \end{pmatrix} \tag{D.2}$$

Assuming the detection window contamination coefficients ϵ_{12}, ϵ_{21} to be constant, they could be experimentally estimated. An inverse of the matrix in Eq. (D.2) can then lead to the desired Rydberg level distribution $\begin{pmatrix} p_1 & p_2 & p_3 & p_4 \end{pmatrix}^{\mathrm{T}}$.

In our experiment, for the high-n CRAs in the heavy σ^+ inhibition regime, their inter-manifold transition frequencies are $< 30\,\mathrm{GHz}$, which lies below the operating range of our MW instruments (waveguide cutoff, frequency multiplier bandwidth, and the inhibition capacitor cutoff). We detect the Rydberg levels in the 61 manifold and above as a whole, and do not try to resolve the transfers among these levels.

Bibliography

[1] A. Aspect, P. Grangier and G. Roger; "Experimental Realization of Einstein-Podolsky-Rosen-Bohm *Gedankenexperiment* : A New Violation of Bell's Inequalities"; Physical Review Letters **49**(2), pp. 91–94 (1982). Cited page 1

[2] J.-G. Ren, P. Xu, H.-L. Yong, L. Zhang, S.-K. Liao, J. Yin, W.-Y. Liu, W.-Q. Cai, M. Yang, L. Li, K.-X. Yang, X. Han, Y.-Q. Yao, J. Li, H.-Y. Wu, S. Wan, L. Liu, D.-Q. Liu, Y.-W. Kuang, Z.-P. He, P. Shang, C. Guo, R.-H. Zheng, K. Tian, Z.-C. Zhu, N.-L. Liu, C.-Y. Lu, R. Shu, Y.-A. Chen, C.-Z. Peng, J.-Y. Wang and J.-W. Pan; "Ground-to-Satellite Quantum Teleportation"; Nature **549**(7670), pp. 70–73 (2017). Cited page 1

[3] S.-K. Liao, W.-Q. Cai, W.-Y. Liu, L. Zhang, Y. Li, J.-G. Ren, J. Yin, Q. Shen, Y. Cao, Z.-P. Li, F.-Z. Li, X.-W. Chen, L.-H. Sun, J.-J. Jia, J.-C. Wu, X.-J. Jiang, J.-F. Wang, Y.-M. Huang, Q. Wang, Y.-L. Zhou, L. Deng, T. Xi, L. Ma, T. Hu, Q. Zhang, Y.-A. Chen, N.-L. Liu, X.-B. Wang, Z.-C. Zhu, C.-Y. Lu, R. Shu, C.-Z. Peng, J.-Y. Wang and J.-W. Pan; "Satellite-to-Ground Quantum Key Distribution"; Nature **549**(7670), pp. 43–47 (2017). Cited page 1

[4] M. A. Nielsen and I. L. Chuang; *Quantum Computation and Quantum Information*; 10. anniversary ed edition (Cambridge Univ. Press, Cambridge, 2010); ISBN:978-1-107-00217-3. Cited page 1

[5] D. J. Wineland; "Nobel Lecture: Superposition, Entanglement, and Raising Schrödinger's Cat"; Reviews of Modern Physics **85**(3), pp. 1103–1114 (2013). Cited page 1

[6] S. Haroche; "Nobel Lecture: Controlling Photons in a Box and Exploring the Quantum to Classical Boundary"; Reviews of Modern Physics **85**(3), pp. 1083–1102 (2013). Cited page 1

[7] W. Wasilewski, K. Jensen, H. Krauter, J. J. Renema, M. V. Balabas and E. S. Polzik; "Quantum Noise Limited and Entanglement-Assisted Magnetometry"; Physical Review Letters **104**(13), p. 133601 (2010). Cited page 1

[8] W. Muessel, H. Strobel, D. Linnemann, D. B. Hume and M. K. Oberthaler; "Scalable Spin Squeezing for Quantum-Enhanced Magnetometry with Bose-Einstein Condensates"; Physical Review Letters **113**(10), p. 103004 (2014). Not cited.

[9] O. Hosten, N. J. Engelsen, R. Krishnakumar and M. A. Kasevich; "Measurement Noise 100 Times Lower than the Quantum-Projection Limit Using Entangled Atoms"; Nature **529**(7587), pp. 505–508 (2016). Cited page 1

[10] S. Massar and E. S. Polzik; "Generating a Superposition of Spin States in an Atomic Ensemble"; Physical Review Letters **91**(6), p. 060401 (2003). Cited page 1

[11] H. W. Lau, Z. Dutton, T. Wang and C. Simon; "Proposal for the Creation and Optical Detection of Spin Cat States in Bose-Einstein Condensates"; Physical Review Letters **113**(9), p. 090401 (2014). Not cited.

[12] T. Tanaka, P. Knott, Y. Matsuzaki, S. Dooley, H. Yamaguchi, W. J. Munro and S. Saito; "Proposed Robust Entanglement-Based Magnetic Field Sensor Beyond the Standard Quantum Limit"; Physical Review Letters **115**(17), p. 170801 (2015). Cited page 1

[13] V. Giovannetti, S. Lloyd and L. Maccone; "Quantum-Enhanced Measurements: Beating the Standard Quantum Limit"; Science **306**(5700), pp. 1330–1336 (2004). Cited page 1

[14] M. H. Devoret, B. Huard, R. Schoelkopf and L. F. Cugliandolo (editors); *Quantum Machines: Measurement and Control of Engineered Quantum Systems*; first edition edition (Oxford University Press, Oxford, United Kingdom, 2014); ISBN:978-0-19-968118-1. Cited page 1

[15] L. Henriet, L. Beguin, A. Signoles, T. Lahaye, A. Browaeys, G.-O. Reymond and C. Jurczak; "Quantum Computing with Neutral Atoms"; Quantum **4**, p. 327. 2006.12326 (2020). Cited page 1

[16] S. Ebadi, A. Keesling, M. Cain, T. T. Wang, H. Levine, D. Bluvstein, G. Semeghini, A. Omran, J.-G. Liu, R. Samajdar, X.-Z. Luo, B. Nash, X. Gao, B. Barak, E. Farhi, S. Sachdev, N. Gemelke, L. Zhou, S. Choi, H. Pichler, S.-T. Wang, M. Greiner, V. Vuletić and M. D. Lukin; "Quantum Optimization of Maximum Independent Set Using Rydberg Atom Arrays"; Science **376**(6598), pp. 1209–1215 (2022). Cited pages 1 and 3

[17] F. Arute, K. Arya, R. Babbush, D. Bacon, J. C. Bardin, R. Barends, R. Biswas, S. Boixo, F. G. S. L. Brandao, D. A. Buell, B. Burkett, Y. Chen, Z. Chen, B. Chiaro, R. Collins, W. Courtney, A. Dunsworth, E. Farhi, B. Foxen, A. Fowler, C. Gidney, M. Giustina, R. Graff, K. Guerin, S. Habegger, M. P. Harrigan, M. J. Hartmann, A. Ho, M. Hoffmann, T. Huang, T. S. Humble, S. V. Isakov, E. Jeffrey, Z. Jiang, D. Kafri, K. Kechedzhi, J. Kelly, P. V. Klimov, S. Knysh, A. Korotkov, F. Kostritsa, D. Landhuis, M. Lindmark, E. Lucero, D. Lyakh, S. Mandrà, J. R. McClean, M. McEwen, A. Megrant, X. Mi, K. Michielsen, M. Mohseni, J. Mutus, O. Naaman, M. Neeley, C. Neill, M. Y. Niu, E. Ostby, A. Petukhov, J. C. Platt, C. Quintana, E. G. Rieffel, P. Roushan, N. C. Rubin, D. Sank, K. J. Satzinger, V. Smelyanskiy, K. J. Sung, M. D. Trevithick, A. Vainsencher, B. Villalonga, T. White, Z. J.

Yao, P. Yeh, A. Zalcman, H. Neven and J. M. Martinis; "Quantum Supremacy Using a Programmable Superconducting Processor"; Nature **574**(7779), pp. 505–510 (2019). Cited page 1

[18] M. H. Devoret and R. J. Schoelkopf; "Superconducting Circuits for Quantum Information: An Outlook"; Science **339**(6124), pp. 1169–1174 (2013). Cited page 1

[19] R. P. Feynman; "Simulating Physics with Computers"; International Journal of Theoretical Physics **21**(6-7), pp. 467–488 (1982). Cited page 1

[20] J. Billy, V. Josse, Z. Zuo, A. Bernard, B. Hambrecht, P. Lugan, D. Clément, L. Sanchez-Palencia, P. Bouyer and A. Aspect; "Direct Observation of Anderson Localization of Matter Waves in a Controlled Disorder"; Nature **453**(7197), pp. 891–894 (2008). Cited page 1

[21] J. F. Sherson, C. Weitenberg, M. Endres, M. Cheneau, I. Bloch and S. Kuhr; "Single-Atom-Resolved Fluorescence Imaging of an Atomic Mott Insulator"; Nature **467**(7311), pp. 68–72 (2010). Cited page 1

[22] M. Saffman, T. G. Walker and K. Mølmer; "Quantum Information with Rydberg Atoms"; Reviews of Modern Physics **82**(3), pp. 2313–2363 (2010). Cited page 2

[23] H. Weimer, M. Müller, I. Lesanovsky, P. Zoller and H. P. Büchler; "A Rydberg Quantum Simulator"; Nature Physics **6**(5), pp. 382–388 (2010). Not cited.

[24] P. Schauss; "Quantum Simulation of Transverse Ising Models with Rydberg Atoms"; Quantum Science and Technology **3**(2), p. 023001 (2018). Not cited.

[25] C. S. Adams, J. D. Pritchard and J. P. Shaffer; "Rydberg Atom Quantum Technologies"; Journal of Physics B: Atomic, Molecular and Optical Physics **53**(1), p. 012002 (2019). Not cited.

[26] T. L. Nguyen, J. M. Raimond, C. Sayrin, R. Cortiñas, T. Cantat-Moltrecht, F. Assemat, I. Dotsenko, S. Gleyzes, S. Haroche, G. Roux, Th. Jolicoeur and M. Brune; "Towards Quantum Simulation with Circular Rydberg Atoms"; Physical Review X **8**(1), p. 011032 (2018). Cited pages 2, 3, 4, 34, 38, 44, 108, and 110

[27] D. Jaksch, J. I. Cirac, P. Zoller, S. L. Rolston, R. Côté and M. D. Lukin; "Fast Quantum Gates for Neutral Atoms"; Physical Review Letters **85**(10), pp. 2208–2211 (2000). Cited page 2

[28] L. Isenhower, E. Urban, X. L. Zhang, A. T. Gill, T. Henage, T. A. Johnson, T. G. Walker and M. Saffman; "Demonstration of a Neutral Atom Controlled-NOT Quantum Gate"; Physical Review Letters **104**(1), p. 010503 (2010). Cited page 2

[29] N. Schlosser, G. Reymond, I. Protsenko and P. Grangier; "Sub-Poissonian Loading of Single Atoms in a Microscopic Dipole Trap"; Nature **411**(6841), pp. 1024–1027 (2001). Cited page 2

[30] F. Nogrette, H. Labuhn, S. Ravets, D. Barredo, L. Béguin, A. Vernier, T. Lahaye and A. Browaeys; "Single-Atom Trapping in Holographic 2D Arrays of Microtraps with Arbitrary Geometries"; Physical Review X **4**(2), p. 021034 (2014). Cited page 2

[31] D. Barredo, S. de Léséleuc, V. Lienhard, T. Lahaye and A. Browaeys; "An Atom-by-Atom Assembler of Defect-Free Arbitrary Two-Dimensional Atomic Arrays"; Science **354**(6315), pp. 1021–1023 (2016). Cited page 2

[32] D. Barredo, V. Lienhard, S. de Léséleuc, T. Lahaye and A. Browaeys; "Synthetic Three-Dimensional Atomic Structures Assembled Atom by Atom"; Nature **561**(7721), pp. 79–82 (2018). Cited page 2

[33] W. Tian, W. J. Wee, A. Qu, B. J. M. Lim, P. R. Datla, V. P. W. Koh and H. Loh; "Parallel Assembly of Arbitrary Defect-Free Atom Arrays with a Multi-Tweezer Algorithm"; (2022); 2209.08038. Not cited.

[34] K.-N. Schymik, B. Ximenez, E. Bloch, D. Dreon, A. Signoles, F. Nogrette, D. Barredo, A. Browaeys and T. Lahaye; "*In Situ* Equalization of Single-Atom Loading in Large-Scale Optical Tweezer Arrays"; Physical Review A **106**(2), p. 022611 (2022). Cited pages 2 and 3

[35] H. Bernien, S. Schwartz, A. Keesling, H. Levine, A. Omran, H. Pichler, S. Choi, A. S. Zibrov, M. Endres, M. Greiner, V. Vuletić and M. D. Lukin; "Probing Many-Body Dynamics on a 51-Atom Quantum Simulator"; Nature **551**(7682), pp. 579–584 (2017). Cited page 2

[36] C. J. Turner, A. A. Michailidis, D. A. Abanin, M. Serbyn and Z. Papić; "Weak Ergodicity Breaking from Quantum Many-Body Scars"; Nature Physics **14**(7), pp. 745–749 (2018). Cited page 2

[37] S. Ebadi, T. T. Wang, H. Levine, A. Keesling, G. Semeghini, A. Omran, D. Bluvstein, R. Samajdar, H. Pichler, W. W. Ho, S. Choi, S. Sachdev, M. Greiner, V. Vuletić and M. D. Lukin; "Quantum Phases of Matter on a 256-Atom Programmable Quantum Simulator"; Nature **595**(7866), pp. 227–232 (2021). Cited page 2

[38] D. Bluvstein, H. Levine, G. Semeghini, T. T. Wang, S. Ebadi, M. Kalinowski, A. Keesling, N. Maskara, H. Pichler, M. Greiner, V. Vuletić and M. D. Lukin; "A Quantum Processor Based on Coherent Transport of Entangled Atom Arrays"; Nature **604**(7906), pp. 451–456 (2022). Cited page 2

[39] P. Scholl, M. Schuler, H. J. Williams, A. A. Eberharter, D. Barredo, K.-N. Schymik, V. Lienhard, L.-P. Henry, T. C. Lang, T. Lahaye, A. M.

Läuchli and A. Browaeys; "Quantum Simulation of 2D Antiferromagnets with Hundreds of Rydberg Atoms"; Nature **595**(7866), pp. 233–238 (2021). Cited page 2

[40] R. G. Cortiñas, M. Favier, B. Ravon, P. Méhaignerie, Y. Machu, J. M. Raimond, C. Sayrin and M. Brune; "Laser Trapping of Circular Rydberg Atoms"; Physical Review Letters **124**(12), p. 123201 (2020). Cited pages 3, 102, 107, and 109

[41] D. Barredo, V. Lienhard, P. Scholl, S. de Léséleuc, T. Boulier, A. Browaeys and T. Lahaye; "Three-Dimensional Trapping of Individual Rydberg Atoms in Ponderomotive Bottle Beam Traps"; Physical Review Letters **124**(2), p. 023201 (2020). Cited page 3

[42] J. T. Wilson, S. Saskin, Y. Meng, S. Ma, R. Dilip, A. P. Burgers and J. D. Thompson; "Trapping Alkaline Earth Rydberg Atoms Optical Tweezer Arrays"; Physical Review Letters **128**(3), p. 033201 (2022). Cited page 3

[43] I. Cong, H. Levine, A. Keesling, D. Bluvstein, S.-T. Wang and M. D. Lukin; "Hardware-Efficient, Fault-Tolerant Quantum Computation with Rydberg Atoms"; (2021). Cited page 3

[44] Y. Alexeev, D. Bacon, K. R. Brown, R. Calderbank, L. D. Carr, F. T. Chong, B. DeMarco, D. Englund, E. Farhi, B. Fefferman, A. V. Gorshkov, A. Houck, J. Kim, S. Kimmel, M. Lange, S. Lloyd, M. D. Lukin, D. Maslov, P. Maunz, C. Monroe, J. Preskill, M. Roetteler, M. J. Savage and J. Thompson; "Quantum Computer Systems for Scientific Discovery"; PRX Quantum **2**(1), p. 017001 (2021). Cited page 3

[45] K.-N. Schymik, S. Pancaldi, F. Nogrette, D. Barredo, J. Paris, A. Browaeys and T. Lahaye; "Single Atoms with 6000-Second Trapping Lifetimes in Optical-Tweezer Arrays at Cryogenic Temperatures"; Physical Review Applied **16**(3), p. 034013 (2021). Cited page 3

[46] F. Meinert, C. Hölzl, M. A. Nebioglu, A. D'Arnese, P. Karl, M. Dressel and M. Scheffler; "Indium Tin Oxide Films Meet Circular Rydberg Atoms: Prospects for Novel Quantum Simulation Schemes"; Physical Review Research **2**(2), p. 023192 (2020). Cited pages 3, 4, 62, 107, and 108

[47] S. R. Cohen and J. D. Thompson; "Quantum Computing with Circular Rydberg Atoms"; PRX Quantum **2**(3), p. 030322 (2021). Cited pages 3, 107, and 108

[48] T. Cantat-Moltrecht, R. Cortiñas, B. Ravon, P. Méhaignerie, S. Haroche, J. M. Raimond, M. Favier, M. Brune and C. Sayrin; "Long-Lived Circular Rydberg States of Laser-Cooled Rubidium Atoms in a Cryostat"; Physical Review Research **2**(2), p. 022032 (2020). Cited pages 3, 19, 40, 107, and 108

[49] H. Wu, R. Richaud, J.-M. Raimond, M. Brune and S. Gleyzes; "Millisecond-Lived Circular Rydberg Atoms in a Room-Temperature Experiment"; (2022); 2209.11654. Cited pages 3, 5, 19, 55, 77, and 87

[50] R. G. Hulet, E. S. Hilfer and D. Kleppner; "Inhibited Spontaneous Emission by a Rydberg Atom"; Physical Review Letters **55**(20), pp. 2137–2140 (1985). Cited pages 25, 27, 107, and 108

[51] D. Kleppner; "Inhibited Spontaneous Emission"; Physical Review Letters **47**(4), pp. 233–236 (1981). Cited pages 3, 24, 25, 27, 32, and 107

[52] R. C. Teixeira, A. Larrouy, A. Muni, L. Lachaud, J.-M. Raimond, S. Gleyzes, 1 and M. Brune; "Preparation of Long-Lived, Non-Autoionizing Circular Rydberg States of Strontium"; Physical Review Letters **125**(26), p. 263001. 2006.15921 (2020). Cited page 4

[53] A. Muni, L. Lachaud, A. Couto, M. Poirier, R. C. Teixeira, J.-M. Raimond, M. Brune and S. Gleyzes; "Optical Coherent Manipulation of Alkaline-Earth Circular Rydberg States"; Nature Physics **18**(5), pp. 502–505 (2022). Cited page 4

[54] J. A. Sedlacek, A. Schwettmann, H. Kübler, R. Löw, T. Pfau and J. P. Shaffer; "Microwave Electrometry with Rydberg Atoms in a Vapour Cell Using Bright Atomic Resonances"; Nature Physics **8**(11), pp. 819–824 (2012). Cited page 4

[55] H. Fan, S. Kumar, J. Sedlacek, H. Kübler, S. Karimkashi and J. P. Shaffer; "Atom Based RF Electric Field Sensing"; Journal of Physics B: Atomic, Molecular and Optical Physics **48**(20), p. 202001 (2015). Cited page 4

[56] A. Facon, E.-K. Dietsche, D. Grosso, S. Haroche, J.-M. Raimond, M. Brune and S. Gleyzes; "A Sensitive Electrometer Based on a Rydberg Atom in a Schrödinger-cat State"; Nature **535**(7611), pp. 262–265 (2016). Cited page 4

[57] E. K. Dietsche, A. Larrouy, S. Haroche, J. M. Raimond, M. Brune and S. Gleyzes; "High-Sensitivity Magnetometry with a Single Atom in a Superposition of Two Circular Rydberg States"; Nature Physics **15**(4), pp. 326–329 (2019). Cited pages 4 and 10

[58] S. Haroche; *La lumière révélée: de la lunette de Galilée à l'étrangeté quantique* (Odile Jacob, Paris, 2020); ISBN:978-2-7381-5171-1. Cited page 7

[59] E.-K. Dietsche; *Quantum Sensing with Rydberg Schrödinger Cat States*; Ph.D. thesis; l'Université Paris 6 (2017). Cited pages 10, 13, 15, 45, 79, and 125

[60] S. Haroche and J.-M. Raimond; *Exploring the Quantum: Atoms, Cavities and Photons*; Oxford Graduate Texts (Oxford University Press, Oxford ; New York, 2006); ISBN:978-0-19-850914-1. Cited pages 10, 12, 14, 23, 28, and 72

[61] T. L. Nguyen; *Study of Dipole-Dipole Interaction between Rydberg Atoms - Toward Quantum Simulation with Rydberg Atoms*; Ph.D. thesis; l'Université Paris 6 (2016). Cited pages 11, 20, and 28

[62] M. Gross and J. Liang; "Is a Circular Rydberg Atom Stable in a Vanishing Electric Field?"; Physical Review Letters **57**(25), pp. 3160–3163 (1986). Cited page 11

[63] M. L. Zimmerman, M. G. Littman, M. M. Kash and D. Kleppner; "Stark Structure of the Rydberg States of Alkali-Metal Atoms"; Physical Review A **20**(6), pp. 2251–2275 (1979). Cited page 12

[64] R. J. Damburg and V. V. Kolosov; "A Hydrogen Atom in a Uniform Electric Field. III"; Journal of Physics B: Atomic and Molecular Physics **12**(16), pp. 2637–2643 (1979). Cited pages 12 and 71

[65] H. A. Bethe and E. E. Salpeter; *Quantum Mechanics of One- and Two-Electron Atoms*; Dover Books on Physics; dover ed edition (Dover Publ, Mineola, N.Y, 2008); ISBN:978-0-486-46667-5. Cited page 12

[66] S. P. Alliluev and I. A. Malkin; "Calculations of the Stark Effect in Hydrogen Atoms by Using the Dynamical Symmetry 0(2, 2) x 0(2)"; (p. 6) (1974). Cited page 12

[67] H. J. Silverstone; "Perturbation Theory of the Stark Effect in Hydrogen to Arbitrarily High Order"; Physical Review A **18**(5), pp. 1853–1864 (1978). Cited page 12

[68] S. Haroche and J.-M. Raimond; "Bohr's Legacy in Cavity QED"; in "Niels Bohr, 1913-2013", , volume 68, edited by O. Darrigol, B. Duplantier, J.-M. Raimond and V. Rivasseau; (pp. 103–146) (Springer International Publishing, Cham, 2016); ISBN:978-3-319-14315-6 978-3-319-14316-3. Cited page 13

[69] R. G. Cortiñas; *Laser Trapping of Cold Circular Rydberg Atoms for Quantum Simulation*; Ph.D. thesis; PSL University (2020). Cited pages 16, 28, 30, 34, 45, 75, and 79

[70] A. Signoles, E. K. Dietsche, A. Facon, D. Grosso, S. Haroche, J. M. Raimond, M. Brune and S. Gleyzes; "Coherent Transfer between Low-Angular-Momentum and Circular Rydberg States"; Physical Review Letters **118**(25) (2017). Cited pages 16, 45, 77, 80, and 108

[71] A. Larrouy, S. Patsch, R. Richaud, J.-M. Raimond, M. Brune, C. P. Koch and S. Gleyzes; "Fast Navigation in a Large Hilbert Space Using Quantum Optimal Control"; Physical Review X **10**(2), p. 021058 (2020). Cited pages 16, 80, and 108

[72] F. Assemat, D. Grosso, A. Signoles, A. Facon, I. Dotsenko, S. Haroche, J. M. Raimond, M. Brune and S. Gleyzes; "Quantum Rabi Oscillations in Coherent and in Mesoscopic Cat Field States"; Physical Review Letters **123**(14), p. 143605 (2019). Cited page 18

[73] W. Gornik, D. Kaiser, W. Lange, J. Luther, H. H. Radloff and H. H. Schulz; "Lifetime Measurements Using Stepwise Excitation by Two Pulsed Dye Lasers"; Applied Physics **1**(5), pp. 285–286 (1973). Cited page 18

[74] T. F. Gallagher, S. A. Edelstein and R. M. Hill; "Radiative Lifetimes of the S and D Rydberg Levels of Na"; Physical Review A **11**(5), pp. 1504–1506 (1975). Cited page 18

[75] F. Gounand, P. Fournier, J. Cuvellier and J. Berlande; "Determination of Natural Radiative Lifetimes for Highly Excited P States in Rubidium"; Physics Letters A **59**(1), pp. 23–24 (1976). Cited page 18

[76] I. I. Beterov, I. I. Ryabtsev, D. B. Tretyakov and V. M. Entin; "Quasiclassical Calculations of Blackbody-Radiation-Induced Depopulation Rates and Effective Lifetimes of Rydberg n S , n P , and n D Alkali-Metal Atoms with n $\leq$ 80"; Physical Review A **79**(5), p. 052504 (2009). Cited pages 18 and 19

[77] M. Archimi, M. Ceccanti, M. Distefano, L. Di Virgilio, R. Franco, A. Greco, C. Simonelli, E. Arimondo, D. Ciampini and O. Morsch; "Measurements of Blackbody-Radiation-Induced Transition Rates between High-Lying S , P , and D Rydberg Levels"; Physical Review A **105**(6), p. 063104 (2022). Cited page 19

[78] M. Archimi, C. Simonelli, L. Di Virgilio, A. Greco, M. Ceccanti, E. Arimondo, D. Ciampini, I. I. Ryabtsev, I. I. Beterov and O. Morsch; "Measurements of Single-State and State-Ensemble Lifetimes of High-Lying Rb Rydberg Levels"; Physical Review A **100**(3), p. 030501 (2019). Not cited.

[79] E. Robertson, N. Šibalić, R. Potvliege and M. Jones; "ARC 3.0: An Expanded Python Toolbox for Atomic Physics Calculations"; Computer Physics Communications **261**, p. 107814 (2021). Cited page 19

[80] T. F. Gallagher and W. E. Cooke; "Interactions of Blackbody Radiation with Atoms"; Physical Review Letters **42**(13), pp. 835–839 (1979). Cited pages 19 and 40

[81] N. Šibalić, J. D. Pritchard, C. S. Adams and K. J. Weatherill; "ARC: An Open-Source Library for Calculating Properties of Alkali Rydberg Atoms"; Computer Physics Communications **220**, pp. 319–331 (2017). Cited page 19

[82] P. A. M. Dirac; *The Principles of Quantum Mechanics*; The International Series of Monographs on Physics; 4. ed. (rev.) edition (Clarendon Press, Oxford, 1978); ISBN:978-0-19-851208-0. Cited page 19

[83] J. J. Sakurai and J. Napolitano; *Modern Quantum Mechanics*; 3rd ed edition (Cambridge University Press, Cambridge, 2021); ISBN:978-1-108-47322-4. Cited page 19

[84] C. Cohen-Tannoudji; "Introduction to Quantum Electrodynamics"; in "New Trends in Atomic Physics, Les Houches Summer School Session XXXVIII", , edited by G. Grynberg and R. Stora (North Holland, Amsterdam, 1984). Cited page 20

[85] J. Dalibard, J. Dupont-Roc and C. Cohen-Tannoudji; "Vacuum Fluctuations and Radiation Reaction : Identification of Their Respective Contributions"; Journal de Physique **43**(11), pp. 1617–1638 (1982). Cited page 20

[86] S. Haroche; "Cavity Quantum Electrodynamics"; in "Fundamental Systems in Quantum Optics, Les Houches Summer School, Session LIII", , edited by J. Dalibard, J.-M. Raimond and J. Zinn-Justin; (p. 767) (North Holland, Amsterdam, 1992). Cited pages 20, 22, 24, 36, and 116

[87] W. Jhe; "QED Level Shifts of Atoms between Two Mirrors"; Physical Review A **43**(11), pp. 5795–5803 (1991). Not cited.

[88] D. Meschede, W. Jhe and E. A. Hinds; "Radiative Properties of Atoms near a Conducting Plane: An Old Problem in a New Light"; Physical Review A **41**(3), pp. 1587–1596 (1990). Cited page 20

[89] E. M. Purcell; "Spontaneous Emission Probabilities at Radio Frequencies"; Physical Review **69**, p. 681 (1946). Cited page 21

[90] J.-M. Raimond; "Atoms and Photons"; (2016). Cited page 21

[91] G. Grynberg, A. Aspect and C. Fabre; *Introduction to Quantum Optics: From the Semi-Classical Approach to Quantized Light* (Cambridge University Press, Cambridge, UK ; New York, 2010); ISBN:978-0-521-55112-0. Cited page 22

[92] S. Gleyzes, S. Kuhr, C. Guerlin, J. Bernu, S. Deléglise, U. Busk Hoff, M. Brune, J.-M. Raimond and S. Haroche; "Quantum Jumps of Light Recording the Birth and Death of a Photon in a Cavity"; Nature **446**(7133), pp. 297–300 (2007). Cited pages 23 and 108

[93] F. Assémat; *Manipulation d'états quantiques de la lumière par l'intermédiaire d'un atome de Rydberg unique*; Ph.D. thesis; Sorbonne Université (2019). Cited pages 23 and 79

[94] E. Hinds; "Cavity Quantum Electrodynamics"; in "Advances In Atomic, Molecular, and Optical Physics", , volume 28(pp. 237–289) (Elsevier, 1990); ISBN:978-0-12-003828-2. Cited pages 24 and 32

[95] W. L. Barnes; "Fluorescence near Interfaces: The Role of Photonic Mode Density"; Journal of Modern Optics **45**(4), pp. 661–699 (1998). Cited page 24

[96] A. G. Vaidyanathan, W. P. Spencer and D. Kleppner; "Inhibited Absorption of Blackbody Radiation"; Physical Review Letters **47**(22), pp. 1592–1595 (1981). Cited page 27

[97] T. F. Gallagher; *Rydberg Atoms*; number 3 in Cambridge Monographs on Atomic, Molecular, and Chemical Physics; digitally print. 1. pbk version edition (Cambridge Univ. Press, Cambridge, 1994); ISBN:978-0-521-38531-2 978-0-521-02166-1. Cited pages 30, 68, 70, and 75

[98] D. R. Lide and H. P. R. Frederikse; *CRC Handbook of Chemistry and Physics: A Ready Reference Book of Chemical and Physical Data*; 75th ed edition (CRC, Boca Raton Ann Arbor London [etc.], 1994); ISBN:978-0-8493-0475-0. Cited page 36

[99] R. Richaud; "Implémentation d'impulsions RF optimisées pour la préparation d'états de Rydberg"; *Technical report*; LKB (2018). Not cited.

[100] B. Ravon; *Préparation et Piégeage d'atomes de Rydberg Circulaires Individuels Pour La Simulation Quantique*; Ph.D. thesis; PSL University (2022). Cited page 44

[101] C. Monroe, W. Swann, H. Robinson and C. Wieman; "Very Cold Trapped Atoms in a Vapor Cell"; Physical Review Letters **65**(13), pp. 1571–1574 (1990). Cited page 46

[102] P. della Porta, C. Emili and S. J. Hellier; "Alkali Metal Generation and Gas Evolution from Alkali Metal Dispensers"; in "IEEE Conference on Tube Techniques", (New York, 1968). Cited page 46

[103] E.-K. Dietsche; "Preparation of Circular Rydberg Atoms in a Superconducting Cavity"; *Technical report* (2012). Cited pages 48 and 49

[104] A. Signoles; *Manipulations cohérentes d'états de Rydberg elliptiques par dynamique Zénon quantique*; Ph.D. thesis; l'Université Paris 6 (2015). Cited page 79

[105] A. Facon; *Chats de Schrödinger d'un Atome de Rydberg Pour La Métrologie Quantique*; Ph.D. thesis; l'Université Paris 6 (2016). Cited pages 71 and 79

[106] D. Grosso; *Des atomes froids pour sonder et manipuler des photons piégés*; Ph.D. thesis; l'Université Paris 6 (2017). Cited pages 48, 52, and 79

[107] P. Filipovicz, P. Meystre, G. Rempe and H. Walther; "Rydberg Atoms"; Optica Acta: International Journal of Optics **32**(9-10), pp. 1105–1123 (1985). Cited page 48

[108] E. Arimondo, M. Inguscio and P. Violino; "Experimental Determinations of the Hyperfine Structure in the Alkali Atoms"; Reviews of Modern Physics **49**(1), pp. 31–75 (1977). Cited page 50

[109] X. Maitre; *Une Paire d'atomes Intriqués : Expériences d'électrodynamique Quantique En Cavité*; Ph.D. thesis; Université Paris 6 (1998). Cited page 50

[110] E. D. Black; "An Introduction to Pound–Drever–Hall Laser Frequency Stabilization"; American Journal of Physics **69**(1), pp. 79–87 (2001). Cited page 49

[111] D. A. Steck; "Rubidium 85 D Line Data"; (2013). Cited page 49

[112] G. W. Hoth, E. A. Donley and J. Kitching; "Atom Number in Magneto-Optic Traps with Millimeter Scale Laser Beams"; Optics Letters **38**(5), p. 661 (2013). Cited page 54

[113] O. Chubar, P. Elleaume and J. Chavanne; "A Three-Dimensional Magnetostatics Computer Code for Insertion Devices"; Journal of Synchrotron Radiation **5**(3), pp. 481–484 (1998). Cited page 55

[114] F. B. Seeley, J. E. Alexander, R. W. Connatser, J. S. Conway and J. P. Dowling; "Dipole Radiators in a Cavity: A Radio Frequency Analog for the Modification of Atomic Spontaneous Emission Rates between Mirrors"; American Journal of Physics **61**(6), pp. 545–550 (1993). Cited page 60

[115] C.-W. Chen, Y.-C. Lin, C.-H. Chang, P. Yu, J.-M. Shieh and C.-L. Pan; "Frequency-Dependent Complex Conductivities and Dielectric Responses of Indium Tin Oxide Thin Films From the Visible to the Far-Infrared"; IEEE Journal of Quantum Electronics **46**(12), pp. 1746–1754 (2010). Cited page 62

[116] T. Wang, M. Zalkovskij, K. Iwaszczuk, A. V. Lavrinenko, G. V. Naik, J. Kim, A. Boltasseva and P. U. Jepsen; "Ultrabroadband Terahertz Conductivity of Highly Doped ZnO and ITO"; Optical Materials Express **5**(3), p. 566 (2015). Cited page 62

[117] C. Hermann-Avigliano, R. C. Teixeira, T. L. Nguyen, T. Cantat-Moltrecht, G. Nogues, I. Dotsenko, S. Gleyzes, J. M. Raimond, S. Haroche and M. Brune; "Long Coherence Times for Rydberg Qubits on a Superconducting Atom Chip"; Physical Review A **90**(4), p. 040502 (2014). Cited pages 62, 75, and 108

[118] J. Hare; *Étude théorique et expérimentale des Atomes de Rydberg Circulaires: vers une mesure directed de la Constante de Rydberg en unités de fréquence*; Ph.D. thesis; l'Université Paris 6 (1991). Cited page 70

[119] R. G. Hulet and D. Kleppner; "Rydberg Atoms in "Circular" States"; Physical Review Letters **51**(16), pp. 1430–1433 (1983). Cited page 77

[120] P. Nussenzveig, F. Bernardot, M. Brune, J. Hare, J. M. Raimond, S. Haroche and W. Gawlik; "Preparation of High-Principal-Quantum-Number "Circular" States of Rubidium"; Physical Review A **48**(5), pp. 3991–3994 (1993). Cited pages 77, 82, and 108

[121] S. Patsch, D. M. Reich, J.-M. Raimond, M. Brune, S. Gleyzes and C. P. Koch; "Fast and Accurate Circularization of a Rydberg Atom"; Physical Review A **97**(5), p. 053418 (2018). Cited page 77

[122] A. Larrouy; *Manipulation d'atomes de Rydberg par contrôle quantique*; Ph.D. thesis; Sorbonne Université (2020). Cited pages 79 and 82

[123] R. R. Freeman and D. Kleppner; "Core Polarization and Quantum Defects in High-Angular-Momentum States of Alkali Atoms"; Physical Review A **14**(5), pp. 1614–1619 (1976). Cited page 82

[124] W. E. Cooke, T. F. Gallagher, S. A. Edelstein and R. M. Hill; "Doubly Excited Autoionizing Rydberg States of Sr"; Physical Review Letters **40**(3), pp. 178–181 (1978). Cited page 82

[125] A. Browaeys and T. Lahaye; "Many-Body Physics with Individually Controlled Rydberg Atoms"; Nature Physics **16**(2), pp. 132–142 (2020). Cited page 108

[126] J. Mozley, P. Hyafil, G. Nogues, M. Brune, J.-M. Raimond and S. Haroche; "Trapping and Coherent Manipulation of a Rydberg Atom on a Microfabricated Device: A Proposal"; The European Physical Journal D **35**(1), pp. 43–57 (2005). Cited page 108

[127] D. Frese, B. Ueberholz, S. Kuhr, W. Alt, D. Schrader, V. Gomer and D. Meschede; "Single Atoms in an Optical Dipole Trap: Towards a Deterministic Source of Cold Atoms"; Physical Review Letters **85**(18), pp. 3777–3780 (2000). Cited page 109

[128] D. Schrader, S. Kuhr, W. Alt, M. Müller, V. Gomer and D. Meschede; "An Optical Conveyor Belt for Single Neutral Atoms"; Applied Physics B **73**(8), pp. 819–824 (2001). Cited page 109

[129] S. Kuhr, W. Alt, D. Schrader, I. Dotsenko, Y. Miroshnychenko, W. Rosenfeld, M. Khudaverdyan, V. Gomer, A. Rauschenbeutel and D. Meschede; "Coherence Properties and Quantum State Transportation in an Optical Conveyor Belt"; Physical Review Letters **91**(21), p. 213002 (2003). Cited page 109

[130] J. Léonard, M. Lee, A. Morales, T. M. Karg, T. Esslinger and T. Donner; "Optical Transport and Manipulation of an Ultracold Atomic Cloud Using Focus-Tunable Lenses"; New Journal of Physics **16**(9), p. 093028 (2014). Cited page 109

Haiteng WU **8 décembre 2022**

Sujet : Atomes de Rydberg Circulaires Vivant plus d'une Milliseconde dans une Expérience à Température Ambiante

Résumé : Les états de Rydberg circulaires sont des outils idéaux pour les technologies quantiques, avec d'énormes interactions mutuelles et des durées de vie extrêmement longues de l'ordre de quelques dizaines de millisecondes, deux ordres de grandeur plus grandes que celles des états de Rydberg accessibles au laser. Cependant, de telles durées de vie ne sont observées qu'à température nulle. À température ambiante, les transferts induits par le rayonnement du corps noir annihilent cet atout essentiel des états circulaires, qui ont donc été principalement utilisés jusqu'à présent dans des expériences cryogéniques spécifiques et complexes. Dans ce travail, nous démontrons, sur un échantillon atomique refroidi par laser, une durée de vie d'état circulaire de plus d'une milliseconde à température ambiante pour un nombre quantique principal de 60. La structure d'inhibition est un simple condensateur plan parallèle qui inhibe efficacement le rayonnement du corps noir. -transferts induits. L'une des électrodes du condensateur est entièrement transparente et offre un accès optique complet aux atomes, une caractéristique essentielle pour les applications. Cette expérience ouvre la voie à une large utilisation des atomes circulaires de Rydberg pour la métrologie quantique et la simulation quantique.

Mots clés : mécanique quantique, atomes froids, atome de Rydberg, atome de Rydberg circulaire, émission spontanée, simulation quantique, métrologie quantique

Subject : Millisecond-lived Circular Rydberg Atoms in a Room Temperature Experiment

Abstract: Circular Rydberg states are ideal tools for quantum technologies, with huge mutual interactions and extremely long lifetimes in the tens of milliseconds range, two orders of magnitude larger than those of laser-accessible Rydberg states. However, such lifetimes are observed only at zero temperature. At room temperature, blackbody-radiation-induced transfers annihilate this essential asset of circular states, which have thus been used mostly so far in specific, complex cryogenic experiments. In this work we demonstrate, on a laser-cooled atomic sample, a circular state lifetime of more than one millisecond at room temperature for a principal quantum number 60. The inhibition structure is a simple plane-parallel capacitor that efficiently inhibits the blackbody-radiation-induced transfers. One of the capacitor electrodes is fully transparent and provides complete optical access to the atoms, an essential feature for applications. This experiment paves the way to a wide use of circular Rydberg atoms for quantum metrology and quantum simulation.

Keywords : quantum mechanics, cold atoms, Rydberg atom, circular Rydberg atom, spontaneous emission, quantum simulation, quantum metrology